ABSTRACT

Title of dissertation: CHARACTERIZATION OF THE REGIONAL, CRUSTAL, AND GLOBAL DISTRIBUTION AND ABUNDANCE OF THE HEAT PRODUCING ELEMENTS AND THEIR GEONEUTRINO FLUX

Scott Alan Wipperfurth
Doctor of Philosophy, 2019

Dissertation directed by: Professor William F. McDonough
Department of Geology

The amount and distribution of radiogenic power generation from the heat producing elements (HPE) U, Th, and K in the Earth is not well constrained. Compositional estimates of these elements vary by a factor of three in the bulk-Earth and 30 in the mantle after removal of the continental crust contribution. Understanding the total power derived from these elements is critical to understanding the power driving the Earth as they supply fuel to the geodynamo and mantle convection. The decay of HPE's produce particles called geoneutrinos and the measurement of the geoneutrino flux reveals the frequency of decay and the abundances of these elements in the Earth. The total geoneutrino flux can be categorized into three major contributors: the dominant component from the nearest 500 km of continental crust surrounding the detector and slightly smaller sub-equal contributions from the remaining global continental crust and the mantle.

The negligible amount of HPE's within the core was tested by a mass-balance of the Th/U derived from Pb isotopes (κ_{Pb}). Each Earth layer was attributed a κ_{Pb} from representative samples with associated weighting factor from the estimated mass of U in each reservoir. The radiogenic power in the core from U and Th was constrained to ~0.03 terra-watts (median), emphasizing the core's negligible geoneutrino luminosity.

To unravel the contribution from the inaccessible mantle to the signal at a detector one must build a physical and chemical description of the local and global crust. The 50×50 km regional geoneutrino flux surrounding the SNO+ detector (Sudbury, Canada) was modeled. 112 geologic samples were analyzed for their U, Th, K abundances and combined with a 3D physical model of the region. To supplement this, the methodology of *Huang et al.* (2013) was applied to an updated geophysical model for the bulk-crust to predict the global crustal signal at SNO+ and other detectors. Variable correlation is addressed and uncertainties from density, seismic velocity, crustal thickness, and abundances propagated.

This dissertation explores the amount and distribution of HPE's within the Earth and their geoneutrino flux through geochemical and geophysical modeling on regional, crustal, and global scales. Together, the results update our understanding of the Earth's geoneutrino flux and the uncertainties still in the system.

Characterization of the regional, crustal, and global distribution and abundance of the heat producing elements and their geoneutrino flux

by

Scott Alan Wipperfurth

Dissertation submitted to the Faculty of the Graduate School of the
University of Maryland, College Park in partial fulfillment
of the requirements for the degree of
Doctor of Philosophy
2019

Advisory Committee:
Professor William F. McDonough, Chair
Associate Professor Ricardo Arevalo, Jr.
Associate Professor Fabio Mantovani
Professor Alice Mignerey, Dean's Representative
Assistant Professor Nicholas C. Schmerr

Dedication

This dissertation and the work put in during the preceding five years are dedicated to my parents, John and Janet Wipperfurth, for their support and acceptance of the continually changing paths I have chosen to walk.

Table of Contents

List of Tables

List of Figures

Chapter 1: Introduction

Estimated at 47 ± 2 terra-watts (TW) (*Davies and Davies*, 2010), the Earth's radiant heat is primarily comprised of two sources: primordial heat remaining from planetary assembly and core formation, and radiogenic heat produced during nuclear decay of the heat-producing elements (HPE: uranium (U), thorium (Th), and potassium (K)). The isotopes of these elements — ^{238}U (99.3% g/g of U), ^{235}U (0.7%), ^{232}Th (100% g/g of Th), ^{40}K (0.012% g/g of K) — presently account for 99% of Earth's radiogenic heat due to their long half-lives and high abundances relative to other radiogenic elements.

There are three categories of models which predict the abundance of the HPE's in the bulk-silicate Earth (BSE; crust + mantle (∼0.5% and ∼67% of Earth by mass, respectively)) and therefore the radiogenic heat production within the BSE. Models which predict low heat flux (Q) from radiogenic decay (≈ 10 TW) are derived from observations of isotopic similarities between Earth and enstatite chondrite (a type of meteorite)(*Javoy*, 1999; *Javoy et al.*, 2010) or from models of early Earth collisional erosion of an HPE-enriched crust (*O'Neill and Palme*, 2008). Medium-Q models (≈ 20 TW) are derived from combining observations from chondrites and mantle melting trends of terrestrial samples (*McDonough and Sun*, 1995; *Palme and O'Neill*,

2014). Finally, High-Q models (≈ 30 TW) are derived from simple parameterized mantle convection models (*Turcotte and Schubert*, 2014). There is inconclusive data to critically evaluate the veracity of each of these three BSE models, therefore there is currently not a precise understanding of the composition and thermal evolution of our planet. The Earth's stable isotopic composition is most similar to enstatite chondrites (low-Q model), and yet it falls outside of the chondritic defined end-members in a Fe-Mg-Si plot, indicating Earth is not comprised of a single type of chondrite nor a two component mixture (*McDonough*, 2017). Furthermore, the use of terrestrial samples and observed conservation of chondritic ratios in terrestrial samples yields a BSE composition (medium-Q model) with refractory element abundances (including U and Th, but not K) double that estimated from enstatite chondrites alone. Finally, neither the low- or medium-Q BSE models satisfy some simple parameterized convection models of the Earth which require larger amounts of radiogenic power to avoid a totally molten mantle for a significant amount of Earth history (high-Q model)(*Schubert et al.*, 1980; *Davies*, 1980). Overall, the range of heat production in BSE models differ by a factor of three (10 to 30 TW). With the consideration of uncertainties and the removal of the HPE contribution from the accessible and HPE enriched continental crust (∼7 ±1 TW)(*Huang et al.*, 2013), these models differ by a factor of thirty in estimates of the radiogenic power in the modern mantle.

Radiogenic heating in the Earth's core is more constrained than that in the BSE. There is a long-standing observation that the ratios of elements with high nebular condensation temperatures and which readily combine with oxygen — called

refractory lithophile elements and include U and Th — in the BSE are consistent with ratios observed in chondrites (*McDonough and Sun*, 1995). A core containing significant amounts of U or Th must also contain significant quantities of other refractory lithophile elements or disturb the conserved chondritic ratio of these elements in the mantle (*McDonough*, 2017). Similarly, if K is sequestered into the core, other large-ion elements, such as rubidium, would also be sequestered, and this is not observed in estimates of the BSE. Furthermore, a mass balance of the Earth's time-integrated Th/U value, where U but not Th has been suggested to partition into the core, documents that negligible amounts of U or Th is present in the core (*Wipperfurth et al.*, 2018). It is reasonable to conclude from these studies that the BSE contains the budget of the Earth's HPE's.

For more than a decade, particle physicists have detected and reported on the Earth's geoneutrino flux — electron anti-neutrinos ($\bar{\nu_e}$) of terrestrial origin produced during β- decay ($n \rightarrow p^+ + e^- + \bar{\nu_e}$)(*Araki et al.*, 2005). The intensity of this flux is proportional to the concentration and distribution of HPE's inside the Earth relative to the detector's location. These elusive particles are exceedingly difficult to detect as they are charge-less leptons with negligible interaction cross sections ($\sim 10^{-44}$ cm^2)(*Dye*, 2012). Measurement of the geoneutrino flux requires large, underground, scintillation detectors which use the inverse beta decay (IBD) detection process ($\bar{\nu_e} + p^+ \rightarrow n + e^+$). The IBD reaction creates two flashes of light, separated in time ($\sim$200 μs) and space ($\sim$30 cm), which uniquely classifies the event and provides an energy tag identifying the specific geoneutrino source isotope. The IBD reaction requires an $\bar{\nu_e}$ kinematic threshold energy of 1.806 MeV due to the larger mass of the

products relative to the reactants in the production of $\bar{\nu}_e$'s. Consequently, only $\bar{\nu}_e$'s emitted by the decay of U and Th are detectable (*Bellini et al.*, 2013). Detectors are located at ~1-2 km deep in the upper crust to shield from cosmogenic muons — the primary background source. Geoneutrino signals are measured in terrestrial neutrino units (TNU), with one TNU equal to one detection per 10^{32} free protons ($\propto$ one kton of liquid scintillator) in one year with 100% detection efficiency of a geoneutrino detector. This unit accounts for differences in detector size and efficiency.

Geoneutrino detectors are presently counting at KamLAND (Kamioka, Japan; 1 kton) and Borexino (Gran Sasso, Italy; 0.3 kton); future detectors include SNO+ (1 kton; online 2019) in Sudbury, Canada, JUNO (20 kton; online 2022) in Guangdong, China, and Jinping (4 kton; unknown start date) in Sichuan, China. Although the Earth is emitting ~10^6 $\bar{\nu}_e/\mathrm{cm}^2/\mathrm{s}$, few events are detected annually at KamLAND (14/yr) and Borexino (4/yr) because of the combined effects of the inverse square law (intensity $\propto 1/\mathrm{distance}^2$) and the neutrino's small interaction cross section. Of these detected events, *Araki et al.* (2005) estimated that 50% are derived from U and Th in the HPE-enriched upper continental crust within ~500 km of the detector (known as near-field crust). The remaining signal comes sub-equally from the rest of the continental crust (i.e. the far-field crust; >500 km) and the mantle. Consequently, the signal from the crust (~35 km thick) overpowers that from the more massive mantle (~2900 km thick). In order to determine the mantle contribution to the geoneutrino flux — and therefore the amount of U and Th within the mantle — it is necessary to have precise and accurate estimates of the crustal contribution, particularly the near-field signal.

Endeavors to understand the near- and far-field crustal signal constitute the dominant effort in geoneutrino research. On a regional scale, studies adopt high-resolution seismic, gravity, and surface exposure data to create a 3D physical model of the local upper crust, including thickness and density of locally relevant geologic units. Combined with this model are geochemical data for each unit. Composite regional models (physical + chemical) provide an estimate of the ∼50% of the total geoneutrino signal expected from the near-field crust and as such the precision on the estimate of the total geoneutrino signal mimics that from the regional model. Detailed regional models with local data have been constructed for KamLAND (*Enomoto et al.*, 2007), Borexino (*Coltorti et al.*, 2011), and SNO+ (*Huang et al.*, 2014), with similar models needed for JUNO and Jinping. The regional geochemical surveys of the near-field crust used in these models often highlight heterogeneity of HPE abundances. While geophysical data are available to determine the general physical conditions of a region, rarely is it with enough resolution to constrain the boundaries of HPE heterogeneity with depth.

Models of the global crust, with resolutions of 2×2 or 1×1 degrees, employ a combination of global and regional seismic and gravity data with extrapolation to areas with minimal available data. Similarly, geochemical data from global compilations representative of sediment, upper, middle, and lower crustal layers are combined with these physical models. These joint models make simplifying assumptions regarding the bulk composition of each layer of the continental crust. Only recently did these geochemical model estimates include lateral and vertical spatial variability, although not in all layers of the crust (e.g. *Huang et al.* (2013)). A further

confounding issue is that there exist different geophysical models of the bulk-crust and each yields slightly different geoneutrino estimates. From the variance between these models and lack of direct measurement, it is unclear which model provides a more accurate representation of the crust. Compositional models with lateral variability in HPE abundances rely specifically on estimates of the compressional seismic velocity (Vp) in the crust, which differs between these geophysical models. Present global crustal models do not have chemical spatial variability in the HPE-enriched upper crust, thereby they neglect any local heterogeneity in the crust and perhaps poorly represent the variability in the layer with the most dominant geonuetrino signal.

Interpretation of simulation results involving HPE abundances, distribution, and geoneutrino flux depend on uncertainties propagated in these models. Attribution and propagation of uncertainty is the greatest modeling difficulty. Many geophysical studies of the crust do not include uncertainty, which requires conservative assumptions of uncertainty when applying them to geoneutrino modeling. HPE abundance variability, which generally contributes the most uncertainty to the predicted signal, is difficult to minimize due to the inherent compositional heterogeneity within the continental crust, particularly at small scales. Generally, authors have propagated uncertainty through Monte Carlo methods to accommodate normal, log-normal, and non-gaussian input distributions. Unlike the regional and crustal models, the uncertainty on the measured geoneutrino flux is dependent on counting statistics. As these detectors continue counting the photons from the IBD reaction, the measurement uncertainty decreases due to counting statistics. Recently,

Šrámek et al. (2016) estimated that current and future detectors will have the required statistics to exclude end-member BSE compositional models and provide a low-uncertainty mantle measurement by 2025. However, to provide the uncertainty necessary for this prediction to come to fruition and to take full advantage of the measured signal, high-resolution near-field models around each detector and updated bulk-crustal models need to be refined, and in some cases, constructed.

1.1 Overview of Dissertation

This dissertation addresses topics in the field of neutrino geoscience. Included in this work is a regional and global modeling of geoneutrino fluxes and HPE abundances. Subsidiary work involves modeling of backgrounds expected at a small antineutrino detector, calculation of the Th/U ratio in Earth's layers, and the calculation of heat production from the decay of HPE's. Uncertainty and error propagation are discussed and interpreted where applicable.

Chapter 2 addresses the modeling of particle backgrounds expected at a small antineutrino detector ('miniTimeCube') deployed next to a nuclear reactor, and the efforts to mitigate these backgrounds in situ. This study provided me with knowledge on the propagation of particles through matter as well as the techniques used in the detection of these particles (including geonuetrinos). The project has resulted in two publications related to the miniTimeCube detector and include estimates of backgrounds (*Li et al.*, 2016, 2018). The text of this chapter focuses in-depth on the backgrounds — measured and simulated — next to the nuclear reactor at

the National Institute of Standards and Technology (NIST). This chapter is under preparation for submission to peer review.

Chapter 3 pertains to the regional geoneutrino signal at the SNO+ detector in Sudbury, Canada. A previous study (*Huang et al.*, 2014) created a 3D model of the ~500 km radius around SNO+ and identified geologic formations that required further investigation. The present study collected 112 samples from the 50×50 km area surrounding SNO+, which include the problematic units identified by *Huang et al.* (2014). These samples and a gravity based structural interpretation were combined to create a high-resolution geoneutrino model for the area surrounding SNO+ to supplement *Huang et al.* (2014). The contents of this chapter have been previously published as *Strati et al.* (2017).

Chapter 4 includes the fitting of upper crustal HPE abundance to observed surface heat flux to improve current geochemical models. Bulk-crustal geoneutrino models adopt homogeneous heat production for the upper crust as a simplifying assumption. Abundances in the upper crust were calculated by subtracting the mantle and reduced (i.e. lower + middle crust) heat flux from the observed surface heat flux. Relatedly, the bulk-crustal heat production was calculated from models of mantle geotherms derived from seismic and thermodynamic modeling from *Cammarano and Guerri* (2017).

Chapter 5 provides an updated geoneutrino reference model for the bulk-crust. The methods of *Huang et al.* (2013) were applied to three geophysical models of the crust. To ascertain the degree of difference between the signals from these three models, the geoneutrino flux was calculated at current and expected detector

locations. Uncertainty from HPE abundances, Vp, density, and thickness were propagated through Monte Carlo methods and correlated when applicable. Flux and abundance results were compared when using each of these geophysical models. This chapter is under preparation for submission to peer review.

Chapter 6 evaluates the hypothesis that the core contains no U and Th, often assumed from geochemical arguments (*McDonough*, 2014). A mass-balance of the Pb-derived molar Th/U (κ_{Pb}) of the bulk Earth, crust, mantle, and the core was performed. The κ_{Pb} of the bulk-Earth was calculated by weighting each layer by the mass of U expected within, and an assumed a mass of U in the core from 0 to 10 ng/g. The intersection of these results with a meteorite-derived κ_{Pb} for the Earth constrains the amount of U and Th in the core. The contents of this chapter have been previously published as *Wipperfurth et al.* (2018).

Chapter 7 re-evaluates the calculation of heat production from the decay of short- and long-lived radioactive isotopes (beyond simply U, Th, and K). The effect of different decay parameters from the physics and geologic communities on the calculated decay energy are evaluated. Geologic parameters are adopted and combined with models of isotopic abundances in the present and past Earth to calculate the heat production and geoneutrino luminosity during planetary accretion and the following 4.56 Gyr. This chapter is under preparation for submission to peer review.

The characterization of the magnitude and distribution of radiogenic power in the planet through measurement of the Earth's geoneutrino flux is the central topic of geoneutrino science. Due to the conserved ratio of refractory lithophile elements, the assessment of Earth's U and Th abundance also constrains the abundance of

~30 other elements. These results will ultimately validate or reject compositional models of the BSE, place constraints on Earth's thermal evolution, and constrain the power available for mantle convection, plate tectonics, and the geodynamo (*Bellini et al.*, 2013).

Chapter 2: A Shielding Enclosure for Neutrino Detector Development at NIST

[1] K.L. Engel and J.G. Learned designed the shielding Cave. S.A. Wipperfurth created the modeling environment using the graphical user interface 'SWORD' and along with A.L. Hutcheson modeled the gamma and neutron background flux seen outside/inside the Cave. H.P. Mumm performed neutron measurements at NIST and handled construction of the Cave. B.C. Rasco performed gamma measurements at NIST. K.L. Engel, S.A. Wipperfurth, H.P. Mumm, A.L. Hutcheson, B.C. Rasco, and A.T. Dreutzler were involved with data analysis and writing the manuscript.

[2] This chapter is to be submitted as:

Kristi L. Engel, Scott A. Wipperfurth, Andrew T. Druetzler, Craig R. Heimbach, Anthony L. Hutcheson, Emily G. Jackson, Glenn R. Jocher, Thomas J. Langford, John G. Learned, Viacheslav A. Li, William F. McDonough, Kurtis A. Nishimura, Bernard F. Phlips, B. Charlie Rasco, Richard S. Woolf, and H. Pieter Mumm, A Shielding Enclosure for Neutrino Detector Development at NIST, 2019.

2.1 Overview

Previous work at UMD in collaboration with the University of Hawaii, the National Institute of Standards and Technology (NIST), and the Naval Research Laboratory (NRL) designed a shielding Cave to attenuate particle backgrounds seen by a small antineutrino detector (miniTimeCube; see *Li et al.* (2016) and *Li et al.* (2018)). The study described in this chapter is work that was performed as an introduction to particle physics and the methodology involved in the detection of anti-neutrinos.

To test the efficiency of the shielding cave, I simulated backgrounds using "Software for Optimization of Radiation Detectors" (SWORD)(*Novikova et al.*, 2006), a graphical user interface developed for GEANT4 (*Agostinelli and with the GEANT Collaboration*, 2003) by the Naval Research Laboratory. GEANT4 is software developed by CERN for the simulation of particle-matter interaction. We simulated backgrounds from cosmic-ray produced muons, gammas, and neutrons, as well as gammas and thermal neutrons from the nuclear reactor located at NIST. Cosmic muon and gamma energy spectrums were derived from the Cosmic-RaY (CRY) shower library (*Hagmann et al.*, 2007). Cosmic neutron spectra were derived from measurements performed by *Gordon et al.* (2004a). Ambient reactor gamma and thermal neutron spectra and rates were measured within the NIST reactor Guide Hall, where the mTC and shield were located until September 2016. Reactor sources were introduced from every direction within the simulation, while cosmic sources were introduced above the shielding with a $\cos^2(\theta)$ distribution. Figure 2.1

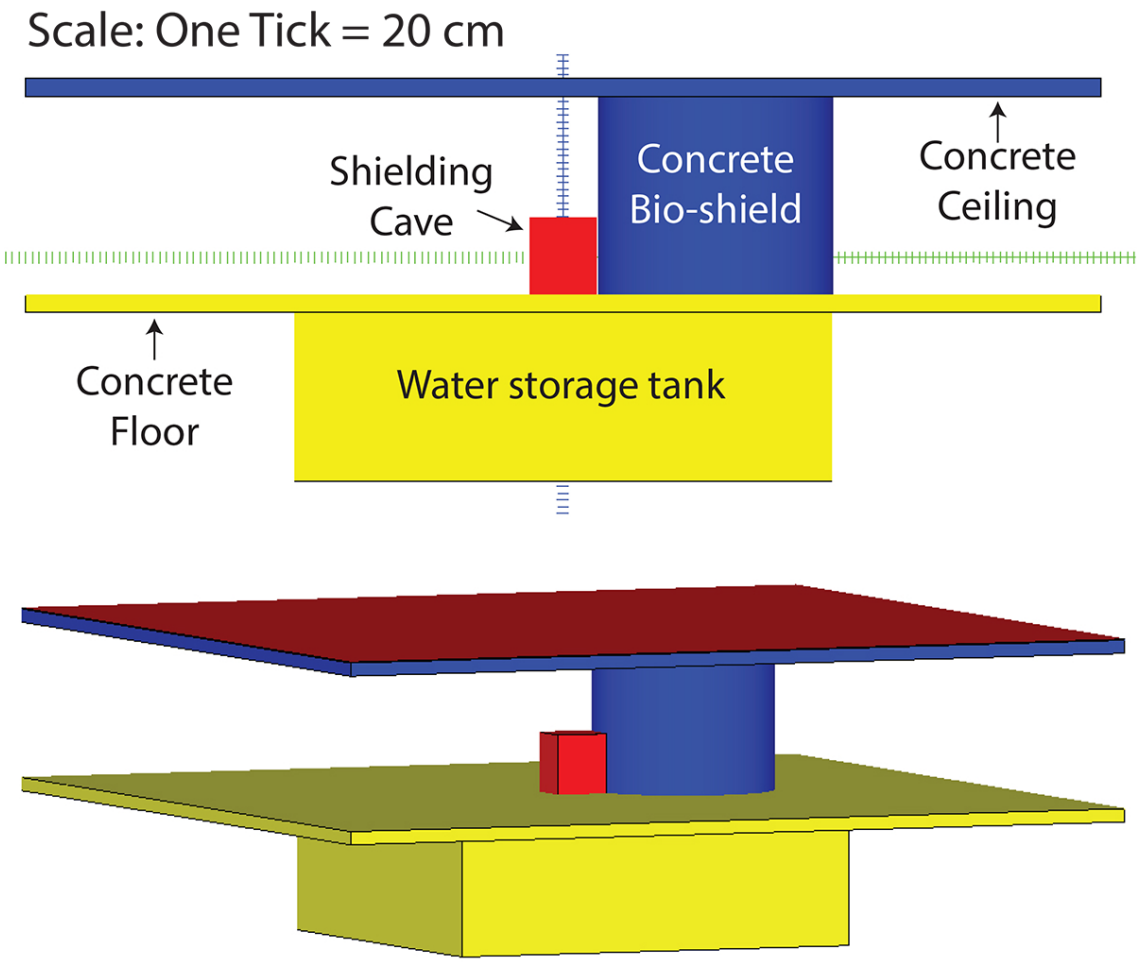

Figure 2.1: Simulation environment in the SWORD software. The top image shows a sideview, while the bottom image shows a rotated viewpoint. Tick marks refer to blue and green ticked x-y lines in the top figure (for quick-reference, the Shielding Cave is 2.2 m high).

and 2.1 show the simulation environment in SWORD.

2.2 Abstract

A 22 ton movable shielding enclosure for neutrino detector prototyping, referred to henceforth as "the Cave", was constructed at the National Institute of Standards and Technology. The Cave is intended to operate as a general-purpose

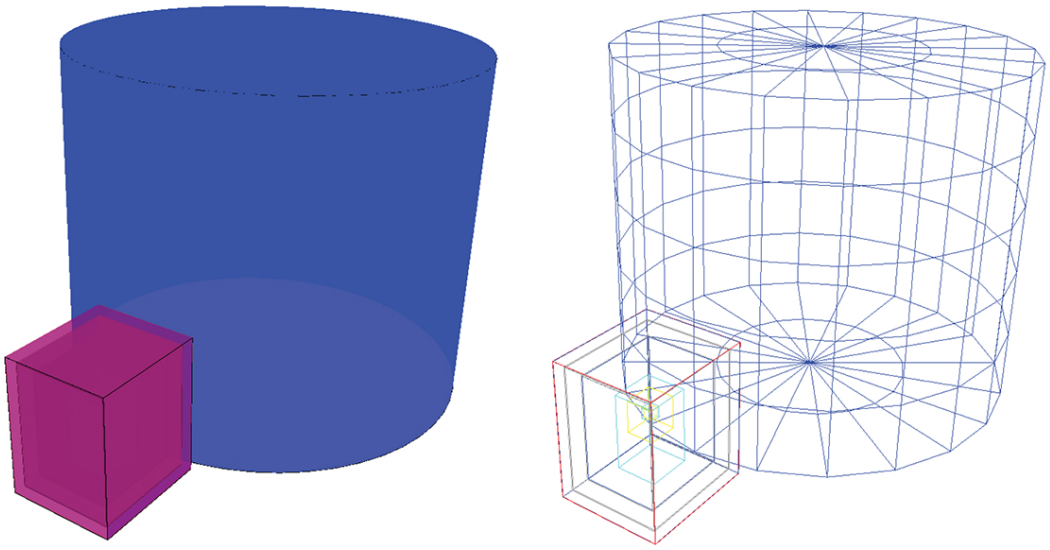

Figure 2.2: Shielding Cave next to the concrete reactor bio-shield. Right image shows the wire-frame view with layers of the Cave exposed.

user facility and can be deployed at modestly different baselines ranging from $\sim$ 4 m to 5.5 m from the reactor core. The Cave is comprised of multiple overlapping layers of borated polyethylene that cover both the interior and exterior walls of a box composed of 1 cm thick steel plates separated by 15 cm of steel shot and paraffin wax. Both natural and reactor-related background attenuations are reported in this paper for gammas, neutrons, and muons, and with comparison of these measurements against Monte Carlo simulation. Noteworthy background characteristics such as temporal variation are also discussed herein.

2.3 Introduction

Low-rate experiments in close proximity to a reactor core (e.g., measurements of reactor antineutrinos) generally require a detailed understanding of local radioactive backgrounds as well as substantial shielding. A general purpose,

well-characterized test facility can potentially provide a number of scientific opportunities, such as improved studies of neutrino oscillations at very short baselines, studies of reactor neutrino spectral shape, and prototyping of emerging technologies (*Vogel et al.*, 2015a). Deployment of short-baseline experiments near a nuclear reactor, where backgrounds can be particularly high due to reactor operation and adjacent neutron–scattering instruments, requires shielding from various backgrounds that could overwhelm or yield signal mimics within the detector volume (e.g., high-energy gammas, thermal neutrons, fast neutrons, cosmic-ray muons and their secondaries). In particular, the reactor-correlated gamma spectrum extends to relatively high energies due to prompt gammas from neutron capture, thus posing additional challenges for shielding.

Originally designed to house the University of Hawai'i miniTimeCube (mTC) $\bar{\nu}_e$ detector (*Li et al.*, 2016), the Cave can also accommodate other modest-scale detectors requiring significant shielding at relatively short baselines.

2.4 NIST Center for Neutron Research

The National Institute of Standards and Technology (NIST) Center for Neutron Research (NCNR) operates the National Bureau of Standards Reactor (NBSR). NBSR is a heavy water (D_2O) cooled, moderated, and reflected tank-type reactor that operates at a thermal power of 20 MW. While lower power than a typical commercial power reactor, the short core-detector baselines roughly compensates in available neutrino flux. The NCNR typically operates the NBSR 250 days per year

with high reliability. During refueling, two spent fuel elements are replaced and the others are reshuffled to maintain an even power distribution. Of the 30 elements, 16 stay in the core for eight cycles and 14 stay in the core for seven cycles. Variations in reactor power (about $\pm 2\%$) are minimized by the automatic movement of a regulating rod. Reactor power is calculated from the rate and temperature difference of the coolant flow, and is known to $\sim 5\%$. The primary source of uncertainty is the temperature measurement.

The Cave is deployed within the NBSR confinement building, immediately adjacent to the biological shield surrounding the core (see Figure 2.3). The biological shield consists of 2.4 m of concrete, lead, and steel shielding. Thus, direct neutron and gamma backgrounds are expected to be small. The location where the Cave is deployed was designed to provide high-flux thermal neutron beams (thermal column), but is currently decommissioned. The moderator and shielding (2 m combination of concrete, lead, and neutron moderation and shielding material) for these beam-lines is still in place however, and result in very low neutron penetration from the core. It must be emphasized that due to the NCNR's primary purpose as a neutron facility, the thermal column area has neutron scattering instruments to either side of the Cave. These are sources of thermal neutrons as well as prompt γ-ray fields arising from neutron capture; both being complex and potentially time-varying in nature. In addition, directly above the thermal column area is a cooling water manifold that is part of the thermal shield cooling system. This is a source of γ-rays from $^{16}\mathrm{O(n,p)}^{16}\mathrm{N}$ that illuminates roughly half of the Cave.

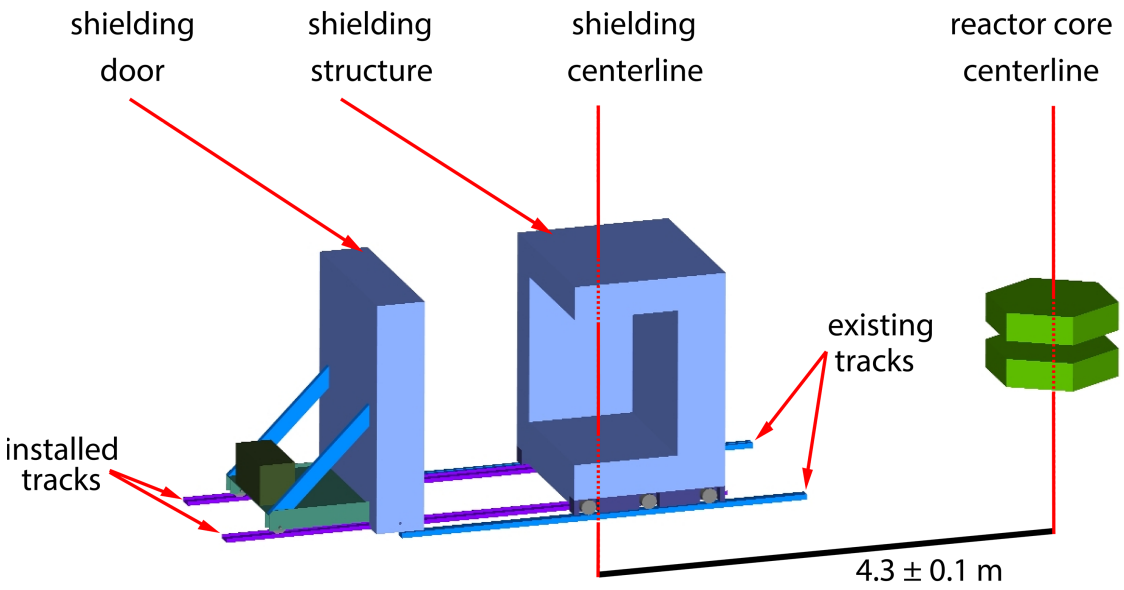

Figure 2.3: Location of the Cave relative to reactor core. The Cave sits on existing tracks (blue), with a movable door on separately installed tracks (purple). The baseline (distance between detector center and reactor core center) displayed was used during mTC analysis (adapted from (*Li et al.*, 2016)).

2.5 Shielding Strategy & Design of The Cave

The Cave is comprised of six nested rectangular boxes, with the outermost dimensions being 2.0 m wide (78") × 2.2 m high (88.5") × 1.8 m deep (70") and an average wall thickness of roughly 0.4 m. The composition of the walls is described in Table 2.1. This leaves an interior cavity, with dimensions 1.2 m wide (47.2") × 1.5 m high (59") × 1 m deep (39"), for housing experiments and associated electronics. The essential features are shown in Figure 2.4.

The materials chosen serve specific particle attenuation roles. Hydrogenous materials, in the form of 5% borated high-density polyethylene (HDPE) and paraffin wax, attenuate < 10 MeV neutrons. Additionally, the borated materials capture thermal neutrons without producing secondary high-energy gammas (neutron cap-

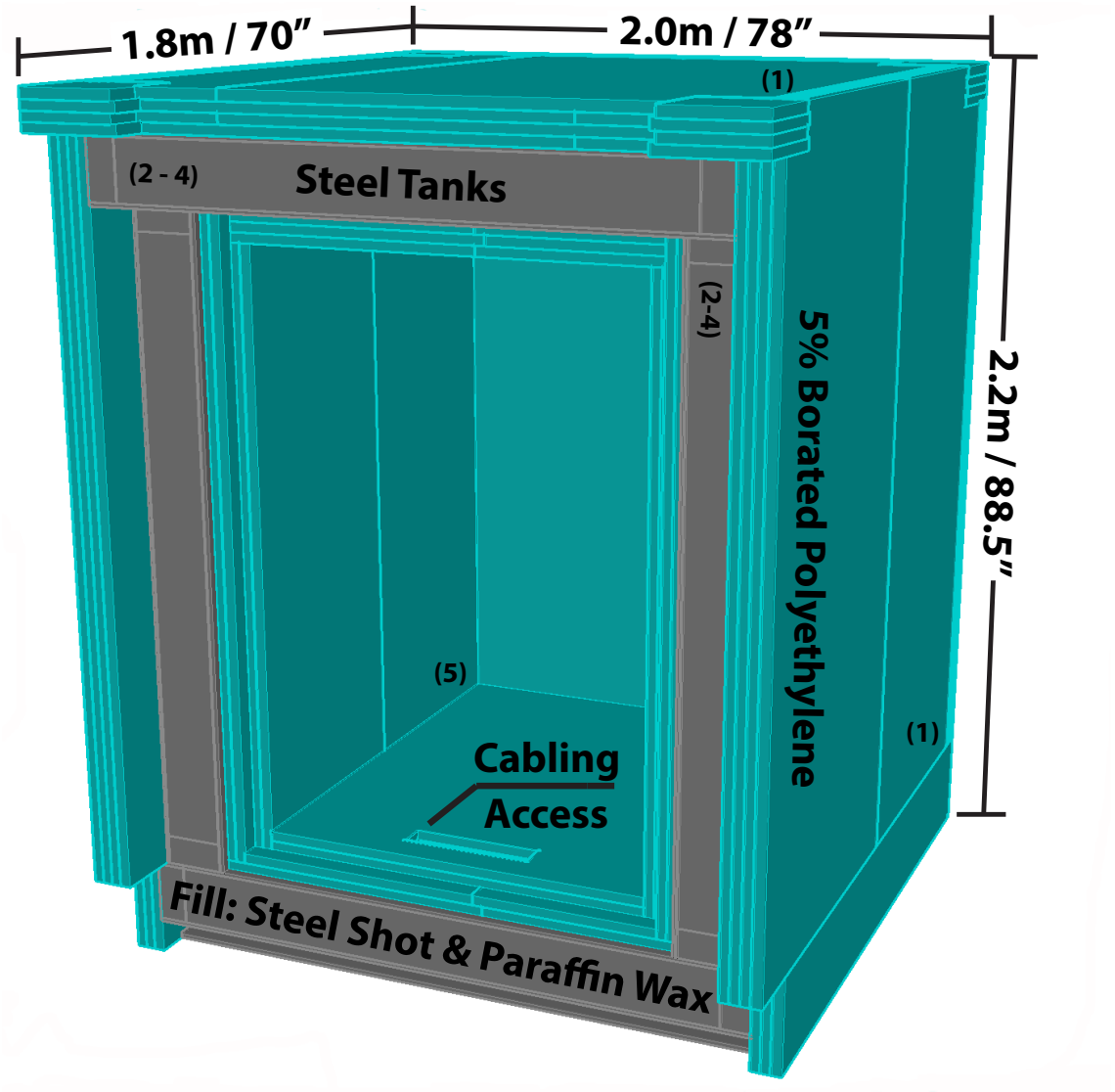

Figure 2.4: AutoCAD rendering of the Cave. Teal sheets (material 1 & 5) are 5% borated polyethylene that cover both the exterior of the Cave as well as the interior cavity, while gray (materials 2 – 4) is the steel-shot/parafin wax mixture enclosed between steel plates that comprises the structural heart of the Cave. See Table 2.1 for more information.

ture on boron yields a 478 keV gamma). This effect is duplicated with the innermost layer of borated HDPE to attenuate and capture spallation-/evaporation- derived neutrons. Lithiated polyethylene was considered, but rejected due to the high cost. High Z materials, in the form of A36 steel walls (98% Fe, 1% Mn) and steel shot,

	Material	Dimension (cm)
1	Borated polyethylene	10
2	A36 steel	1
3	Steel shot & paraffin wax	15
4	A36 steel	1
5	Borated polyethylene	10

Table 2.1: From exterior to interior, composition and dimension of Cave layers. Polyethylene layer used is doped with 5% boron. Steel layer and steel shot are A36 steel. Steel shot & paraffin wax mixture comprised of 75% steel, 25% wax.

attenuate $>$ 10 MeV neutrons and gammas in addition to providing structural support for the Cave. All layers serve to attenuate the muon flux, albeit less efficiently than the neutrons. For the framework of the Cave, 9.5 mm sheets of A36 steel were welded together to form tanks, which were then filled with steel shot and molten paraffin wax (75% steel shot, 25% wax). Four layers of 25 mm borated HDPE sheets were bolted in sets of two layers such that no bolts penetrated the full shielding. All edges were overlapped to prevent line-of-sight to the interior.

The Cave structure (minus the Cave door) is supported by existing rails embedded in the reactor facility floor for the purpose of retracting the thermal column door from the primary shielding structure (Figure 2.3). This allows the Cave to be moved across modestly different baselines ($\sim$ 4 m – 5.5 m from the reactor core) depending on experimental needs. A removable stepped-profile door, of like layering and dimensions, allows access to the interior of the Cave. When closed, there are no direct line-of-sight paths for particles to enter the central cavity. This limits gas-like thermal neutrons from penetrating. There is an opening built into the base of the structure to provide access for cooling and power to the enclosed instrumentation

("Cabling Access", Figure 2.4). During the operation of an experiment, the area around piping and cabling through this opening can be packed with borated HDPE pellets contained in bags to limit thermal neutron penetration.

2.6 Shield Simulations

Monte Carlo-type simulations were employed to model the interaction of incident particles with, and the attenuation efficiency of, the Cave. Benchmarking simulations with in-situ measurements allowed for better understanding of temporally–changing backgrounds from other experiments in the confinement building as well as the ability to study time-correlated backgrounds of relevance to neutrino experiments.

Backgrounds were simulated within the Cave using SWORD (SoftWare for the Optimization of Radiation Detectors (*Novikova et al.*, 2006)), a Naval Research Laboratory initiative that provides a graphical user interface (GUI) to GEANT4 (GEometry ANd Tracking, v.4 (*Agostinelli and with the GEANT Collaboration*, 2003)). GEANT4 is a Monte Carlo particle-matter interaction modeling software for the simulation of the passage of particles through matter (*Agostinelli and with the GEANT Collaboration*, 2003). The implementation of SWORD allowed for ease of modeling and visualization of the modeling environment. Backgrounds simulated included both cosmogenic sources (muons, gammas, and neutrons) and reactor sources (thermal and fast neutrons, gammas). Source energy spectra were obtained from in-situ measurements or literature. Gamma spectra were as measured outside the

Cave (see Section 2.7). Thermal neutron spectra were assumed to follow a Maxwell-Boltzmann flux distribution at 20 °C. The cosmic neutron spectrum was adopted as the flux incident on the roof of the IBM T.J. Watson Research Center in Yorktown Heights, NY (*Gordon et al.*, 2004b). Cosmic muon and gamma spectra were calculated using the Cosmic-RaY (CRY) shower library (*Hagmann et al.*, 2012a).

The simulated geometry includes a rough approximation of the NBSR biological shield, the confinement building ceiling and floor, a water-based spent fuel storage pool beneath the reactor, and the Cave. The biological shield comprises a 3.5 m radius concrete cylinder. The confinement building ceiling and floor is simulated as 0.5 m thick concrete. The spent fuel storage pool is simulated as a 5 m deep pool of water beneath the model. Actual reactor components were not simulated, although fine mechanical structure could potentially alter the particles passing through the center of the reactor.

2.7 Background Measurements

Detailed background surveys have previously been carried out in the Cave location (*Ashenfelter and with the PROSPECT Collaboration*, 2016). This information was combined with more recent measurements to understand the background fields both outside and inside the Cave. The detector suite used for characterization of backgrounds in the Cave as presented in this paper are listed in Table 2.2.

Detector	Type
FaNS-1	Capture gated spectrometer (^{3}He and plastic)
Radpack-GC	^{3}He proportional counter
GammaTracer	Ion chamber
Canberra gamma Detector	HPGe
miniTimeCube	^{10}B-loaded plastic scintillator

Table 2.2: Detectors and primary function as used within this study.

2.7.1 Gammas (γ)

Gamma measurements were carried out using a Canberra High-Purity Germanium (HPGe) detector (Model CPHA7.5-37200S). The crystal is a closed-end coaxial geometry 55 mm in length and 62.5 mm in diameter. The detector is regularly calibrated at NIST and these data are combined with Monte Carlo calculations to determine absolute efficiency as a function of energy. The photo-peak efficiency at 6 MeV is roughly 0.025%.

Significant increases in the gamma background over the reactor-off rates are observed shortly after the reactor starts up. These increase further as adjacent beam-lines are opened. Raw data taken during reactor-on cycles — with adjacent beam lines open — and reactor-off cycles are shown in Figure 2.5. Several location-dependent features are observed depending on line-of-sight to the various sources we have identified above. Strong Fe lines (^{57}Fe and ^{55}Fe) from neutron capture on surrounding shielding and structural materials are seen. Lines due to ^{16}O(n,p)^{16}N reactions in the biological shield cooling system are observed when sufficiently far from the thermal column that the system is not shadowed. Due to the fact that the

data presented in Figure 2.5 was taken in a shadowed location, the line from this reaction is not significant herein. The bulk of the spectrum is, however, a continuum, suggesting that down-scattered Fe captures within rebar–reinforced concrete dominate. Unfolded spectra useful for future modeling work are discussed in Section 2.7.2.

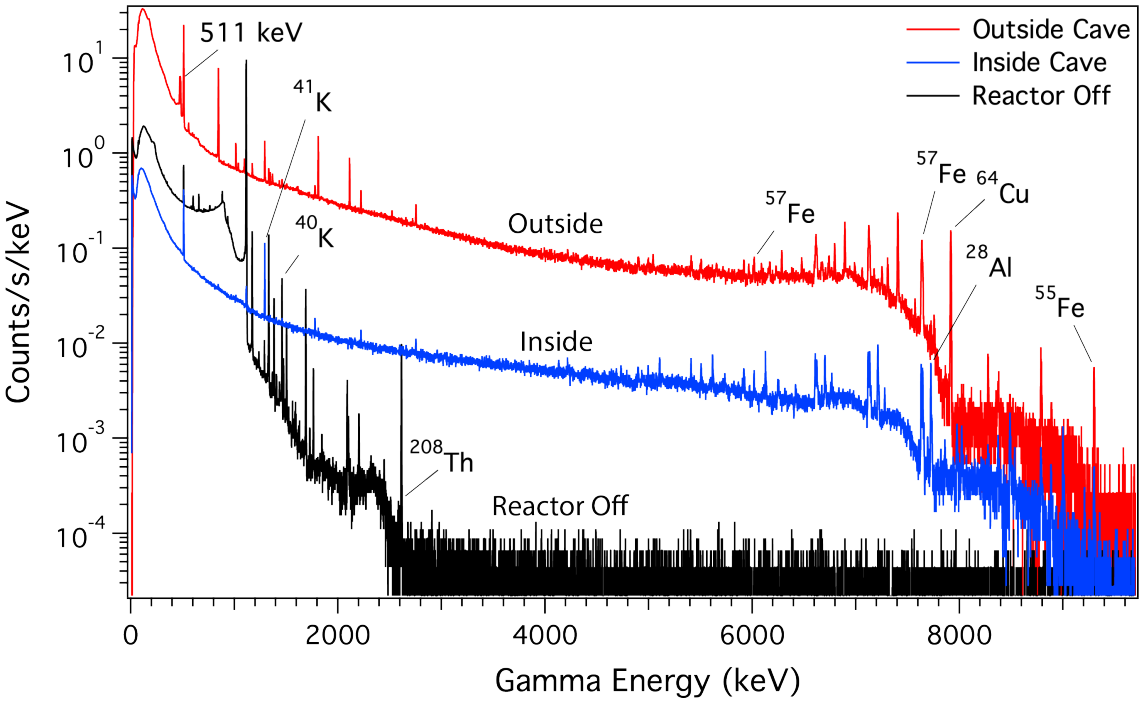

Figure 2.5: Raw gamma spectra acquired using the HPGe detector described in the Section 2.7.1. With the reactor on, the spectrum is dominated by prompt gammas from neutron capture on structural materials (Fe, Cu, and Al) that are subsequently down-scattered. Some of these features are still present within the Cave, with a notable addition being ^{41}Ar produced through neutron capture in the air that diffuses into the Cave during its 1.8 hour half-life. Reactor-off backgrounds (measured outside the Cave) are primarily the result of uranium and thorium decay chains in concrete with the exception of the 1115-keV gamma from ^{65}Zn which has a 244 day half-life and thus persists through reactor refueling cycles.

In order to asses the temporal variation of gamma fields, a GammaTracer (GF1414) was placed between the location of the Cave and the The Multi Axis Crystal Spectrometer (MACS) (*Rodriguez et al.*, 2008) instrument (adjacent to and

west of the Cave) at the approximate neutron beam height to measure the temporal variation of gamma backgrounds. The GammaTracer consists of two detectors and was configured to record the average dose rate over a 10 minute period for each of the detectors and to then compute an average of the two readings. Data due to typical MACS operating conditions is shown in Figure 2.6. Dose rates are observed to vary by about an order of magnitude over hour timescales. The effect is particularly pronounced at the rear (reactor side) of the Cave because of the geometry of the MACS sample-position and detector. In addition to being important in understanding the ultimate effect on potential experiments, this variation makes comparison of background data taken at different times problematic as noted in section 2.7.2.

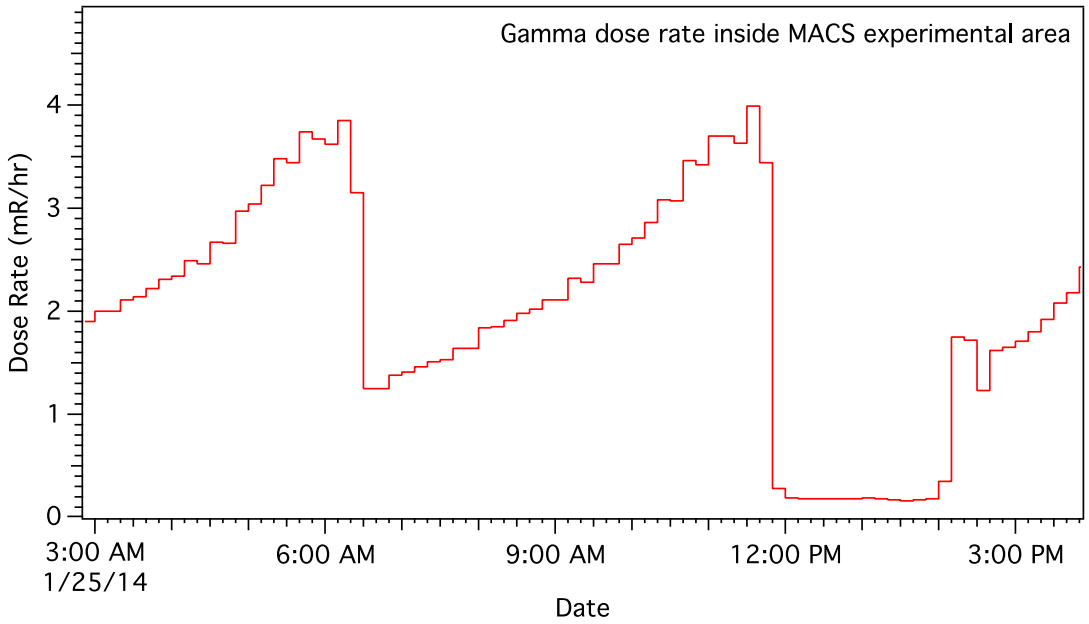

Figure 2.6: A subset of the GammaTracer data showing significant temporal variations in dose rate. The time structure is due to sample position changes in the adjacent MACS spectrometer.

2.7.2 γ-Spectrum Unfolding

The primary purpose of the background characterization is to provide input for Monte Carlo simulation of experiments within the Cave. The problem can be stated mathematically as

$$d_i = \sum_{j=0}^{N} R_{ij} f_j, \tag{2.1}$$

where d_i is the number of counts in the i^{th} data bin, f_j is number of γ-rays with energy E_j, and R_{ij} is the response of the detector in the i^{th} data bin to a given γ-ray with energy E_j. There are several ways to perform such a deconvolution of the measured γ-spectra. The technique we used in this work was originally implemented for astronomical measurements (*Lucy*, 1974), but NaI(Tl) total absorption spectrometers extensively use this technique (*Cano-Ott et al.*, 1999a,b; *Tain and Cano-Ott*, 2007; *Rasco et al.*, 2016). We use the expectation-maximization method described in detail in *Tain and Cano-Ott* (2007), as it is stable, returns only positive feeding fractions, is relatively easy to implement, and does not use other fit parameters that may influence the results.

The results of the HPGe deconvolution of the measured spectrum inside and outside the Cave are shown in Figure 2.7. We show the reduction as a function of energy in Figure 2.8. The ratio of inside to outside the Cave is similar to the ratio obtained by merely scaling up the raw spectrum by the HPGe efficiency. However, the HPGe-efficiency-scaled estimate of the total flux of γ rays not in a HPGe peak is off by an order of magnitude.

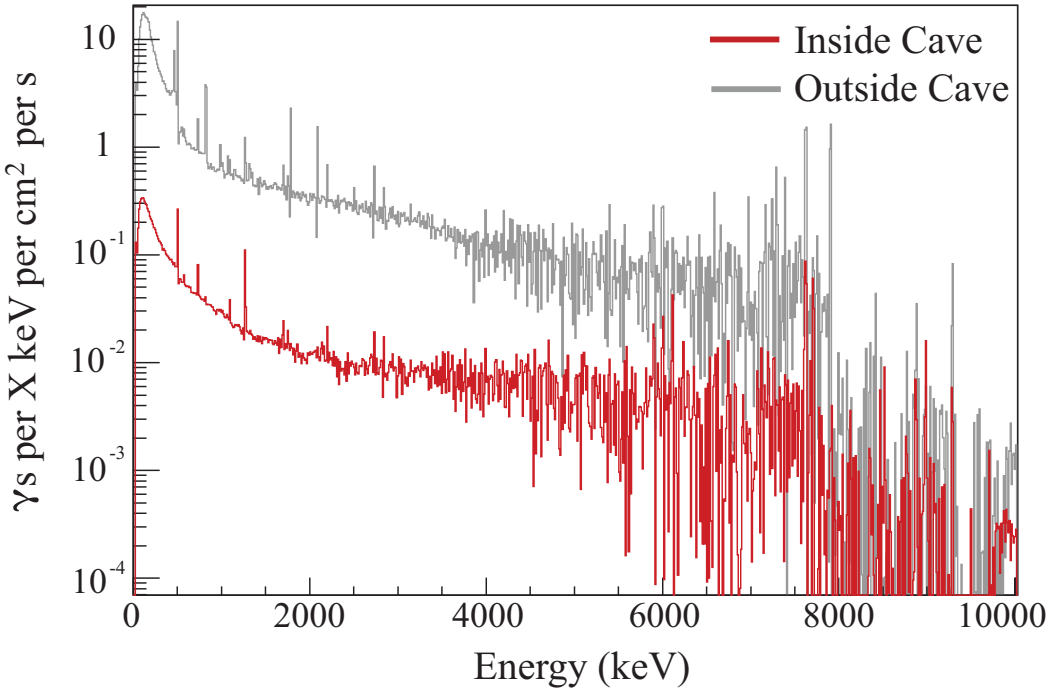

Figure 2.7: Deconvolved HPGe spectra inside (red; lower spectrum) and outside (grey; upper spectrum) of the Cave; measured at NIST.

We have performed two checks on our deconvolved spectra. The first is to input the deconvolved energy spectrum into our simulation and compare the results with the original measured data. We found the results from the simulation to match very well with the measured data. The other check is to compare the estimated HPGe peak efficiencies of particular gammas with the peak efficiencies measured directly by counts in the energy peak. Again, the deconvolved results agree well with the predicted gamma efficiency as a function of energy.

The gamma flux inside the Cave is dominated by gammas incident upon the exterior of the Cave, rather than secondaries produced through neutron or muon interaction within the Cave. Regardless, all gamma sources (primary or secondary)

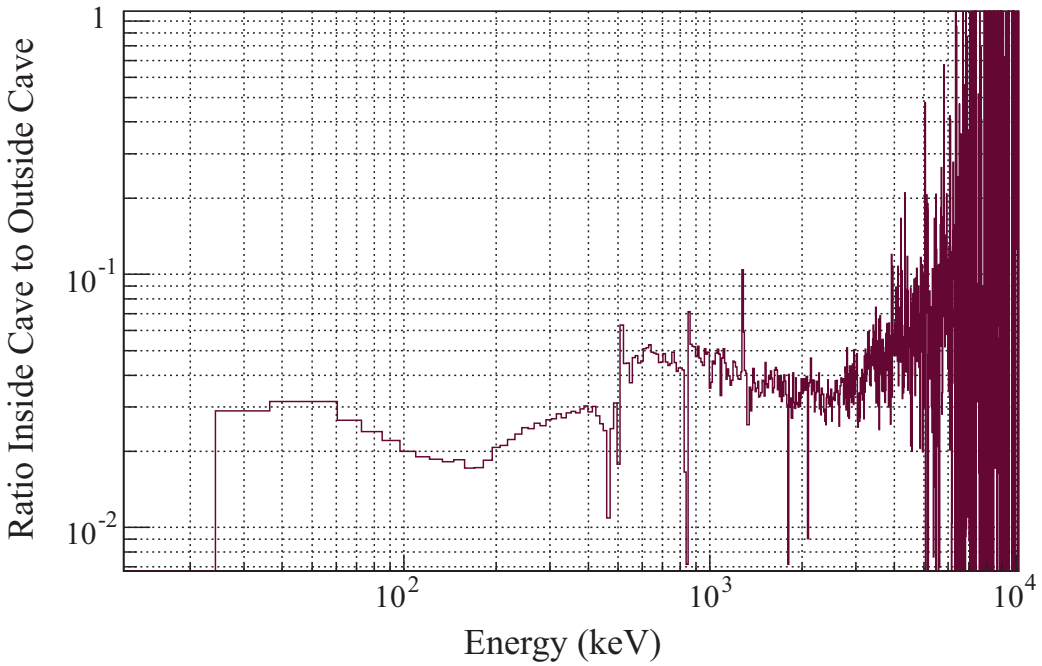

Figure 2.8: Ratio of counts per energy inside the Cave to outside the Cave from HPGe results.

were simulated. A comparison of the measured and simulated spectra show reasonable agreement in terms of spectral shape but an order of magnitude lower flux in the simulated spectra (Figure 2.9). This discrepancy is assumed to be due to the complex gamma fields in the vicinity of the Cave and the fact that it was not possible to measure the incident flux at the location of the Cave interior under the same operating conditions of the adjacent instruments. Thus the measured spectra inside and outside the Cave were not measured concurrently (physically or temporally) and represent different background conditions. However, as the mechanisms for prompt-gamma production remain the same, this difference primarily effects the overall rate. A small dosimeter was used to measure rates in the gap between the Cave and the MACS instrument, which suggested at least a factor of five upward re-

normalization of the background data. Qualitatively this would put the simulation and data in reasonable agreement.

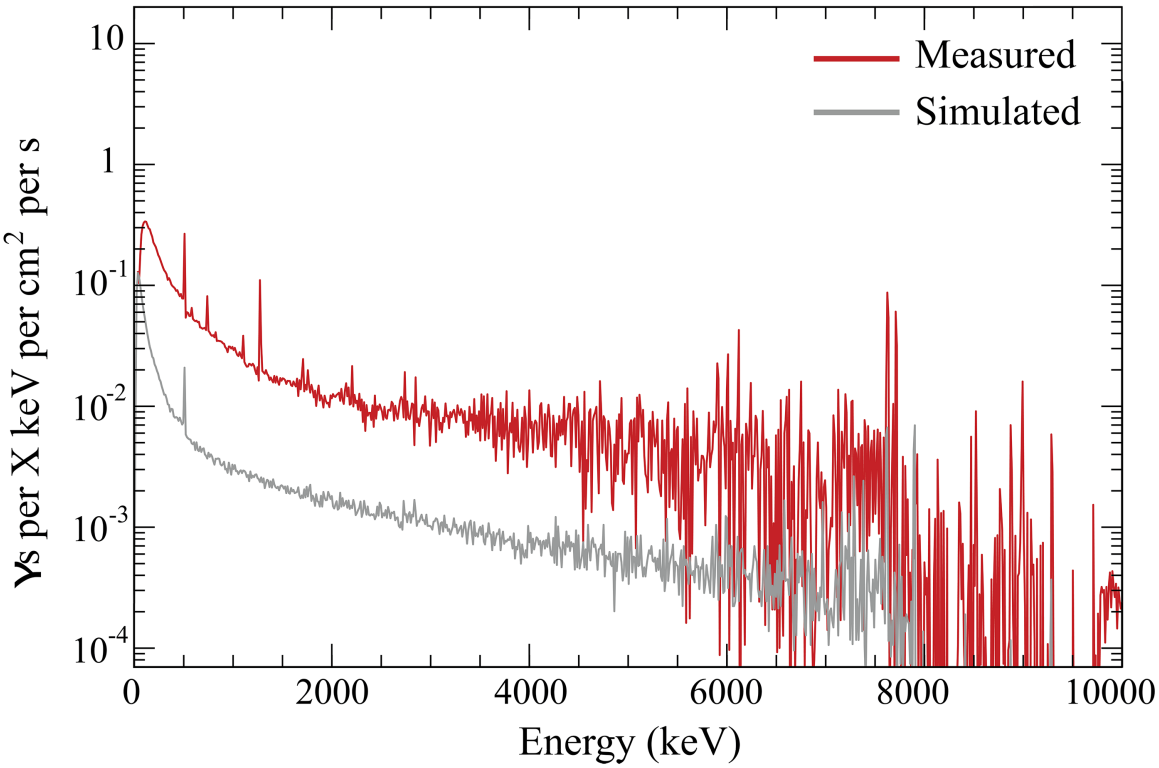

Figure 2.9: Spectral shape comparison of unfolded measured (red; upper spectrum) and simulated (grey; lower spectrum) gamma spectra within the Cave. General agreement over the continuum is seen. A few additional features, most notably a line at 1,293 keV from ^{41}Ar, are due to sources not included in the Monte Carlo.

2.7.3 Fast Neutrons: FaNS-1

Neutrons with energies above 0.5 MeV were measured using the FaNS-1 detector. The FaNS-1 fast neutron spectrometer consists of segments of BC-400 plastic scintillator with ^{3}He proportional counters in between (*Langford et al.*, 2015; *Langford*, 2013). The six 9 cm × 18.5 cm × 15 cm optically-decoupled segments have a total active volume of 15 liters. Pairs of Photo-Multiplier Tubes (PMTs) collect

light from each segment through cylindrical light-guides. Signals from each PMT are split; one half is attenuated by a factor of nine, while the full amplitude pulse is delayed. These pulse pairs are digitized, allowing for the construction of a linear response over a large dynamic range. The six 1" diameter ^{3}He proportional counters are filled with 4.0 bar of ^{3}He and 1.1 bar of natural krypton and have high thermal neutron capture efficiency. All six helium-counter signals were combined in one fan in/out module and digitized.

FaNS-1 operates via the concept of capture-gated spectroscopy. A fast neutron enters the detector, where it may thermalize through multiple (n,p) scatters. After a random walk it can be captured by a ^{3}He counter or it may leave the detector. The signature of a fast neutron is a recoil in the scintillator signal followed ~ 10 μs later by a delayed neutron capture. The neutron energy is determined by the light yield of the scintillator, where non-linearities are reduced through segmentation. By examining the time separation between a scatter-like event and a capture-like event, it is possible to differentiate accidental coincidences, which are uniform in time, and correlated coincidences, which have a distinct exponential distribution. The energy calibration of FaNS-1 was determined with well-calibrated ^{252}Cf, 2.5 MeV, and 14 MeV generator sources, and detailed MCNP models of detector response.

Fast neutron measurements were carried out in a background laboratory space at the NCNR with similar overburden to the confinement building, within the confinement building but outside of the Cave, and inside the Cave as shown in Figure 2.10. A full unfolding of the spectra is complicated by response uncertainties at higher energies (100 MeV) due to cosmic muons. Because of this, to compare

measurements with the expected Cave performance, cosmic fast neutrons with the appropriate spectrum (*Gordon et al.*, 2004b) were propagated in MCNP through the building roof and Cave. Resulting spectra were then used as a source term for the FaNS-1 simulation and integrated counts between 1 MeV and 100 MeV were compared. Integrating the simulated spectrum over this region shows an attenuation factor of 3.6 for the combination of the confinement building structure and the Cave.

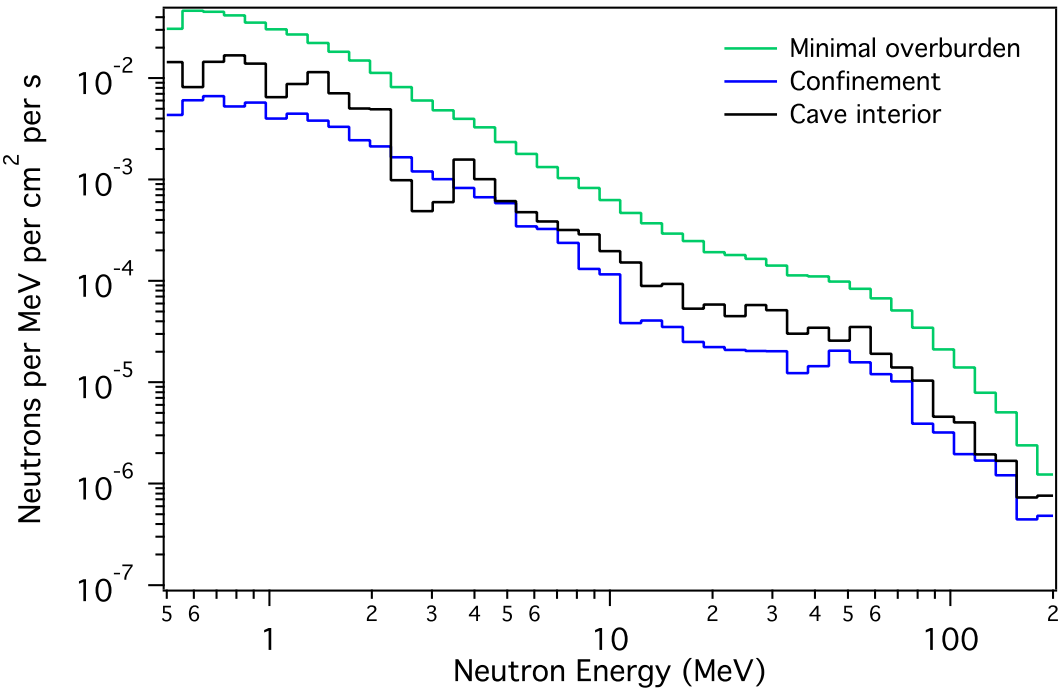

Figure 2.10: Measured fast neutron spectrum inside the Cave measured by FaNS-1 detector.

2.7.4 Thermal Neutrons: Radpack-GC

Additional neutron measurements were performed both inside and outside the shielding Cave with a Radpack-GC thermal neutron radiation detector (Sensor

Technology Engineering, Inc., Santa Barbara, CA). The Radpack-GC comprises seven ^{3}He proportional counters with active dimensions per counter of ⌀5.08 cm × 132 cm and fill pressures of 271 kPa. Measurements were carried out with the reactor both off and on. As in the FaNS measurements, an additional background measurement was performed at another location in the NCNR building with minimal overburden to gauge the effect of walls/ceiling of the NBSR confinement building on the cosmogenic neutron background rate. The measured count rate for each of these measurements are given in Table 2.3. Note that the thermal neutron count rate during reactor operations is reduced by a factor of approximately 4×10^{4} inside the shielding Cave compared to outside. However, it is also noteworthy that the count rate inside the Cave is approximately 4–5 times larger when the reactor is operating compared to when the reactor is off. This result may indicate that although the Cave greatly attenuates the thermal neutron flux as expected, there may be persistent neutron leakage though residual cracks. As mentioned previously, thermal neutrons are notorious for gas-like behavior.

Reactor State	Measurement Location	Acquisition Length (s)	Measured Rate (s^{-1})	Flux ($n/cm^2/s$)
Off	Outside Cave	1800	1.03 ± 0.02	$3.64 \pm 0.08 \times 10^{-3}$
Off	Inside Cave	3600	0.031 ± 0.003	$3.8 \pm 0.4 \times 10^{-5}$
Off	NCNR break area	1800	3.26 ± 0.04	$1.15 \pm 0.02 \times 10^{-2}$
On	Outside Cave	600	5870 ± 3	7.082 ± 0.004
On	Inside Cave	1845	0.13 ± 0.01	$1.6 \pm 0.1 \times 10^{-4}$
On	Inside Cave	3600	0.16 ± 0.01	$1.9 \pm 0.1 \times 10^{-4}$

Table 2.3: The measured count rates using the Radpack-GC thermal neutron detector and the calculated energy-integrated total fluxes.

To determine the total neutron flux for each measurement, detector response

coefficients for the Radpack-GC were simulated using MCNP 6.1.1 (*Goorley*, 2014). The response coefficients $R(E)$ are defined such that, given a flux distribution $\frac{d\phi}{dE}$, the differential count rate $\frac{dC}{dE}$ is given by the equation 2.2.

$$\frac{dC}{dE} = R(E) \cdot \frac{d\phi}{dE} \tag{2.2}$$

We divided the neutron energy spectrum into three bins: thermal ($E_N \leqslant 0.5$ eV), epithermal ($E_N = 0.5$ eV – 100 keV), and fast ($E_N \geqslant 100$ keV). For each energy bin, we assumed the following flux distributions:

$$\text{Thermal: } \frac{d\phi}{dE} \propto E \cdot e^{-E/0.0253} \ (\text{eV}^{-1}) \tag{2.3}$$

$$\text{Epithermal: } \frac{d\phi}{dE} \propto \frac{1}{E} \ (\text{eV}^{-1}) \tag{2.4}$$

$$\text{Fast: } \frac{d\phi}{dE} \propto \sqrt{E} \cdot \sinh\sqrt{2E} \cdot e^{-E} \ (\text{MeV}^{-1}) \tag{2.5}$$

We could then determine average response coefficients, $\langle R \rangle$, for each bin:

$$\langle R \rangle = \frac{\int_{E_1}^{E_2} R(E) \cdot \frac{d\phi}{dE} dE}{\int_{E_1}^{E_2} \frac{d\phi}{dE} dE} \tag{2.6}$$

For the thermal, epithermal, and fast neutron energy bins, the average response coefficients were $\langle R \rangle = 910.2$, 332.4, and 33.47 cm^2, respectively.

Finally, we estimated the total neutron flux as

$$\phi = \frac{C}{A_{Th} \cdot \langle R_{Th} \rangle + A_{Ep} \cdot \langle R_{Ep} \rangle + A_F \cdot \langle R_F \rangle} \tag{2.7}$$

where C is the total number of counts, $\langle R_{Th,Ep,F} \rangle$ are the average response coefficients for the thermal, epithermal, and fast energy bins, and $A_{Th,Ep,F}$ are the fractions of the total flux in each energy bins. For measurements outside the Cave when the reactor was off, we assumed flux fractions of 18%, 30%, and 52% for the thermal, epithermal, and fast bins, respectively. These percentages are based on the cosmogenic neutron spectrum given in *Gordon et al.* (2004a) up to neutron energies of 100 MeV, above which energy the detector response is virtually zero. When the reactor was operating, flux fractions of 90%/2%/8%, respectively, were assumed for measurements outside the Cave; these fractions were based on measurements performed at similar reactors (e.g., *Abrefah et al.* (2010)).

2.8 Conclusion

A shielding facility has been constructed at the NCNR to provide an environment with reduced reactor-related backgrounds for short-baseline reactor-neutrino detector development. We have reported the results of a detailed background measurement campaign and, where practical, reported unfolded spectra as well.

Gamma and fast neutron backgrounds are higher than expected and show unanticipated time-structure. This has been definitively traced to an adjacent neutron scattering instrument called MACS. To mitigate this, there are currently plans

to install additional shielding in the form of movable a steel curtain between MACS and the Cave. Nonetheless, though the spectrum is harder inside the Cave, integrated gamma fluxes within the inner cavity are less than a typical laboratory, and thermal neutron fluxes are effectively eliminated by the shielding it provides.

As of this writing, the Cave is available as a user facility. All experiment proposals should be submitted through the NCNR IMS system for consideration.

2.9 Acknowledgements

We would like to thank Peter Neubauer of Neubauer Engineering for engineering design consultation. We also gratefully acknowledge the funding for the mTC project, which contributed to the construction of the Cave, provided by National Geospatial-Intelligence Agency (NGA), the U.S. Department of Energy HEP, the National Science Foundation, and the University of Hawai'i.

We also acknowledge the support of the NIST, US Department of Commerce, in providing support for facilities used in this work during background measurements and detector testing. We also thank NIST personnel for assistance in completion of the Cave, and the UH Applied Research Laboratory for their administrative and technical support.

2.10 Output from this work:

- Li, V. A., R. Dorrill, M. J. Duvall, J. Koblanski, S. Negrashov, M. Sakai, S. A. Wipperfurth, K. Engel, G. R. Jocher, J. G. Learned, L. Macchiarulo, S. Mat-

suno, W. F. McDonough, H. P. Mumm, J. Murillo, K. Nishimura, M. Rosen, S. M. Usman, and G. S. Varner (2016), Invited Article: miniTimeCube, *Review of Scientific Instruments*, *87*(2), 021,301, doi:10.1063/1.4942243

- Li, V. A., J. Koblanski, R. Dorrill, M. J. Duvall, K. Engel, G. R. Jocher, J. G. Learned, S. Matsuno, W. F. McDonough, H. P. Mumm, S. Negrashov, K. Nishimura, M. Rosen, M. Sakai, S. M. Usman, G. S. Varner, and S. A. Wipperfurth (2018), Studies of MCP-PMTs in the miniTimeCube neutrino detector, *AIP Advances*, *8*(9), 095,003, doi:10.1063/1.5043308

- (in prep) Engel, K.L., Wipperfurth, S.A., Druetzler, A.T., Heimbach, C.R., Hutcheson, A.L., Jackson, E.G., Jocher, G.R., Langford, T.J., Learned, J.G., Li, V.A., McDonough, W.F., Nishimura, K.A., Phlips, B.F., Rasco, B.C., Woolf, R.S., and Mumm, H.P, The Cave: A Background Radiation Shielding Enclosure.

Chapter 3: Perceiving the Crust in 3-D: A Model Integrating Geological, Geochemical, and Geophysical Data

[1] V. Strati, F. Mantovani, and W.F. McDonough conceived and designed the work as it is. V. Strati and S.A. Wipperfurth carried out the sampling survey and together with M. Baldoncini performed the Th and U analyses with HPGe detectors. S. Wipperfurth carried out the ICPMS measurements. The 3-D geophysical model was constructed by V. Strati and F. Mantovani. All the authors participated in the data analysis and interpretation of the results, while V. Strati, M. Baldoncini, and F. Mantovani conducted the geoneutrino signal calculation. V. Strati, F. Mantovani took the lead in designing and composing the manuscript with the input from all the authors.

[2] This chapter has been published as:

Strati, V., S. A. Wipperfurth, M. Baldoncini, W. F. McDonough, and F. Mantovani (2017), Perceiving the Crust in 3-D: A Model Integrating Geological, Geochemical, and Geophysical Data, *Geochemistry, Geophysics, Geosystems*, *18*(12), 4326–4341, doi:10.1002/2017GC007067

3.1 Abstract

Regional characterization of the continental crust has classically been performed through either geologic mapping, geochemical sampling, or geophysical surveys. Rarely are these techniques fully integrated, due to limits of data coverage, quality, and/or incompatible data sets. We combine geologic observations, geochemical sampling, and geophysical surveys to create a coherent 3-D geologic model of a 50 $\times$ 50 km upper crustal region surrounding the SNOLAB underground physics laboratory in Canada, which includes the Southern Province, the Superior Province, the Sudbury Structure, and the Grenville Front Tectonic Zone. Nine representative aggregate units of exposed lithologies are geologically characterized, geophysically constrained, and probed with 109 rock samples supported by compiled geochemical databases. A detailed study of the lognormal distributions of U and Th abundances and of their correlation permits a bivariate analysis for a robust treatment of the uncertainties. A downloadable 3-D numerical model of U and Th distribution defines an average heat production of $1.5^{+1.4}_{-0.7}$ mW/m3, and predicts a contribution of $7.7^{+7.7}_{-3.0}$ TNU (a Terrestrial Neutrino Unit is one geoneutrino event per 10^{32} target protons per year) out of a crustal geoneutrino signal of $31.1^{+8.0}_{-4.5}$ TNU. The relatively high local crust geoneutrino signal together with its large variability strongly restrict the SNO+ capability of experimentally discriminating among BSE compositional models of the mantle. Future work to constrain the crustal heat production and the geoneutrino signal at SNO+ will be inefficient without more detailed geophysical characterization of the 3-D structure of the heterogeneous Huronian Supergroup,

which contributes the largest uncertainty to the calculation.

3.2 Introduction

Geoscientists map out and define the surface geology and from that predict 3D cross sections of regional terrains. Geological mapping in 3-D is a fundamental task for understanding the potential for economic resources and the geological evolution of a region. Infrequently are datasets from these surface campaigns fully integrated into a coherent depth projection using data from shallow geophysical surveys. Although geological data of various sorts have been collected almost everywhere on Earth, crustal data in most regions have vastly different resolution and data types that present challenges to integrate into a coherent 3-D picture that projects 10+ km into the crust. With the advent of advanced techniques of statistical analysis and extensive data collection with comparable uncertainties, it is now possible to integrate many different types of information into a single coherent model. The resultant models are useful in geophysical modeling (e.g., structural analysis, geodynamic simulations, seismic wave corrections, and heat flux), geologic interpretation (e.g., orogenic history, past environments, and crustal processes), and particle physics (e.g., geoneutrinos flux and muon tomography).

We report here a method of integrating available geological, geochemical, and geophysical data into a coherent 3-D model of the upper crust of the Sudbury region of Canada (see supporting information Dataset S1). Our efforts build on a previous study (*Huang et al.*, 2014), hereafter H14, that developed a 3-D model of

the thick LOcal Crust belonging to the 6°× 4°(∼440 km 460 km total area) region centered near Sudbury (hereafter defined as LOC) (Figure 3.1). H14 found that the Huronian Supergroup of the Southern Province was chemically and lithologically heterogeneous and revealed marked variations in its K, Th, and U contents. Consequently, predictions of the abundance and distribution of the heat producing elements in this unit came with considerable uncertainties, resulting in a large variability on estimates of the local radiogenic heat power and expected geoneutrino signal at the SNO+ detector located in Sudbury. Based on these findings, we performed additional geochemical sampling (112 new analyses) of the region and combined these data with the models published in H14 and in *Olaniyan et al.* (2015), to build a revised 3-D high-resolution model that describes the Close Upper Crust (CUC) corresponding to the 50 km × 50 km area around SNO+.

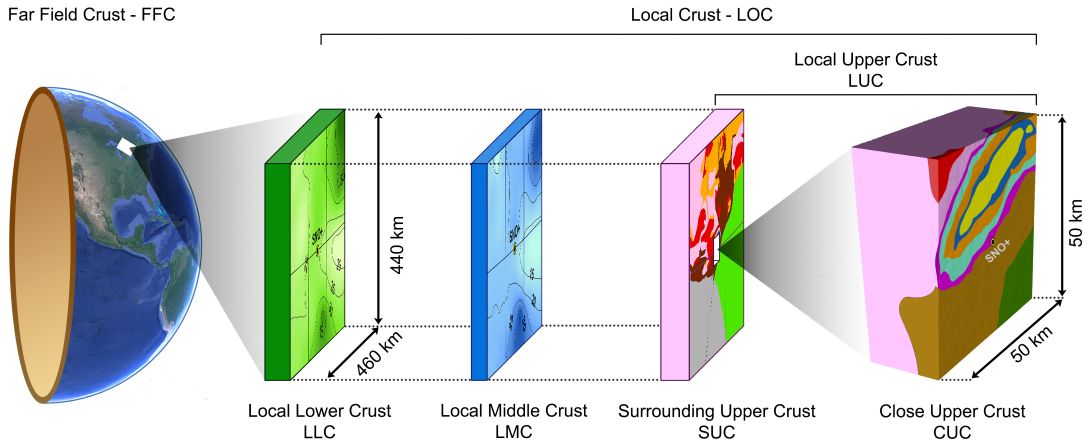

Figure 3.1: The crustal geoneutrino signal expected in SNO+ is calculated considering the Far Field Crust (FFC, the rest of the Earth's crust not included in the studied 6°× 4° region) and the LOcal Crust (LOC, the 6° × 4° regional area under study). Adopting the same structure of H14, the LOC is subdivided in Local Lower Crust (LLC), Local Middle Crust (LMC) and LUC (Local Upper Crust). The latter includes the Surrounding Upper Crust (SUC) and the Close Upper Crust (CUC), i.e. the closest 50 × 50 km region investigated in this study.

3.3 Motivation

Motivation of H14 and this study was to build a model that would then be used to calculate the expected geoneutrino signal at the SNO+ detector, which is a multi-purpose kilotonscale liquid scintillation detector located 2092 ($\pm$ 6) m underground at SNOLAB outside Sudbury (*Lozza*, 2016; *Sonley*, 2009). Integrating the 3-D geophysical (i.e. density and spatial distribution of units) and geochemical (i.e. K, Th, and U concentrations) data with the existing surface data yields a more coherent geological understanding of the regional crust surrounding Sudbury. Geoneutrinos are electron antineutrinos emitted in beta minus decays, with those occurring along the ^{238}U and ^{232}Th decay chains having sufficient energies to be detected (*Araki et al.*, 2005). One of the challenging goals that the SNO+ experiment wants to address in the geoneutrino field are the separation of ^{238}U and ^{232}Th geoneutrino spectral components together with the distinction between the mantle and the crustal contributions in a global analysis of the geoneutrino spectrum, comprising data coming from the ongoing KamLAND (*Gando et al.*, 2013) and Borexino (*Agostini et al.*, 2015) experiments. Insights into the mantle contribution to the geoneutrino signal at any individual detector can be pursued provided precise and accurate knowledge of the dominant geoneutrino background, mostly due to reactor antineutrinos, and a refined regional-scale model of the continental crust (*Baldoncini et al.*, 2015).

Understanding the power inside the Earth that drives plate tectonics, mantle convection, and the geodynamo are fundamental goals in our science. The emerging field of neutrino geoscience provides a new tool by which to define the abundance and

distribution of heat producing elements inside the Earth. At any given geoneutrino detector that is sited on continental crust, the mantle contribution is only 20% - 25% of the total signal (see Figure 2 in *Šrámek et al.* (2016)). Thus, to define the mantle contribution and power of the largely inaccessible Earth, it is crucial to understand the specific attributes of the local crustal contribution to the signal. Importantly, global geoneutrino models provide flux maps for the Earth (*Usman et al.*, 2015) which will be a reference for discriminating among distinct compositional paradigms of the bulk silicate Earth (*Dye*, 2010; *Fiorentini et al.*, 2007a; *Šrámek et al.*, 2016).

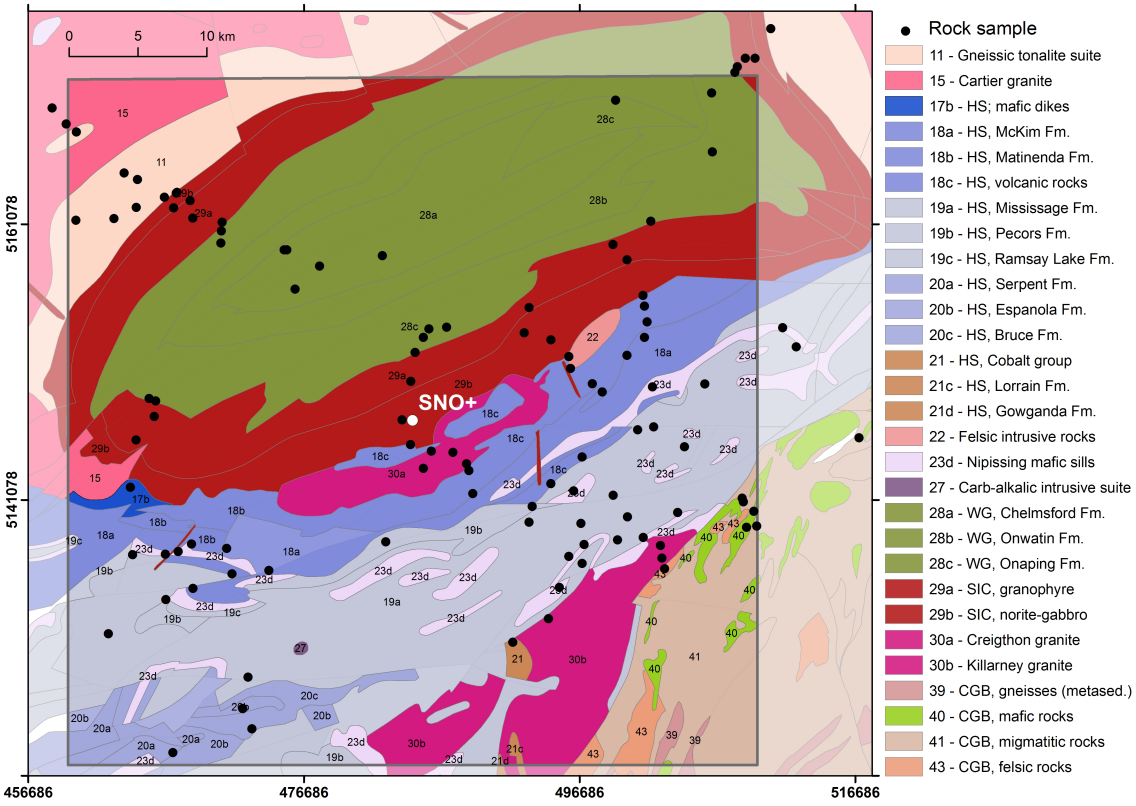

Figure 3.2: Location of the 112 rock samples. Rocks samples are collected in the CUC (inner box) and projected onto the Bedrock Geology of Ontario [Ontario Geological Survey, 2011] (HS = Huronian Supergroup, WG = Whitewater Group, SIC = Sudbury Igneous Complex, CGB = Central Gneiss Belt). (Cartographic reference system NAD1927 UTM Zone 17N).

3.4 Geologic Setting

The Close Upper Crust (CUC), i.e. the 50 × 50 km region centered at SNOLAB, is the target area of the 3D crustal model constructed for estimating the geoneutrino signal at SNO+. The study area is comprised mostly of the Southern Province and Sudbury Structure, and lesser areas of the Superior Province and the Grenville Front Tectonic Zone (GFTZ).

The Southern Province, covering much of the southwestern part of the study area, is primarily composed of Huronian Supergroup (HS), a well-exposed Paleoproterozoic succession deposited between 2.4 and 2.2 Ga as the result of a partial Wilson cycle with the rifting and development of a southward-facing passive margin (*Young et al.*, 2001). The HS can reach up to 12 km of thickness and it is composed of (from bottom to top) the Elliot Lake, Hough Lake, Quirke Lake, and Cobalt groups. A generalized stratigraphic column of the formations of HS is reported in Figure 5 of (*Young*, 2013). The different groups include variable lithologies, such as sandstones, mudstones, carbonates, conglomerates, and minor volcanic rocks (*Long*, 2004, 2009). In the study area, the HS is represented primarily by the Elliot Lake Group, a thick package of volcanic rocks and deep-water sediments, and the Hough Lake group, a basal diamictite that fines upward from mudstone to sandstone. The upper formation of the Hough Lake Group, the Mississage Fm., representing 18% of the total studied area, is made up of medium to coarse grained, arkosic to subarkosic sandstones. In the southwest area, carbonate rocks of the Quirke Lake group outcrop in a relative small portion of the study area, while the Cobalt Group is almost absent.

The supracrustal rocks of the HS are intruded by the mafic dikes and sills of the Nipssing Gabbro, which are less than 100 m thick, and by felsic intrusions, mainly the granitic rocks of the Creighton and Murray plutons (*Riller*, 2009). Following the HS deposition, a meteorite impact (1.85 Ga) (*Therriault et al.*, 2002) caused the formation of the Sudbury Igneous Complex (SIC) that intrudes the HS and that, together with the Whitewater group, constitutes the Sudbury Structure. The SIC is geographically divided into North, East, and South ranges and the main mass is composed of norite, quartz-gabbro, and granophyre. The basin of the impact crater was later filled by the Whitewater Group sediments, a 2900 m thick assemblage of breccias, hypabyssal intrusions, carbonaceous sediments, and turbidity sequences (*Rousell and Card*, 2009).

In the northwestern part of the studied region are the Archean crystalline rocks of the Superior Province, the Levack Gneiss Complex. These high-grade rocks (tonalite-granodiorite orthogneiss) form a collar, 0.5-5 km wide, around the North and East margin of the SIC. The complex is intruded by the felsic plutonic rocks of the Cartier Batholith (*Rousell and Card*, 2009).

In the southeast corner of the studied area are Grenville Province rocks in a crustal scale shear zone (GFTZ) that mark the northwest edge of the Grenville Orogeny. It is interpreted as a metamorphic transition comprising gneissic and migmatitic rocks originating from HS sedimentary rocks and Nipissing Gabbro that underwent deep metamorphic and granitization processes (*Davidson*, 1997; *Easton*, 2016).

3.5 Sampling Survey

Locations of the 112 collected rock samples are reported in Figure 3.2 (see supporting information Table S4) and are projected on the published 1:250,000 scale Bedrock Geology of Ontario (*Ontario Geologic Survey*, 2011) used as a guide for the survey. Sample GPS location and geological information (e.g. geological formation, lithology granulometry, recognized minerals) were recorded. Every sample was collected from fresh outcrops, representative of the geological formation, and placed in a polyethylene bag (Figure 3.3a). Later each sample was crushed, sealed in a polycarbonate container (Figure 3.3b) and left undisturbed for at least 5 weeks with the objective of establishing radioactive equilibrium between ^{226}Ra and ^{222}Rn (see Figure 2 of *Xhixha et al.* (2016)).

Figure 3.3: Rock sample of lapilli tuff (Geocode 28c, Onaping Fm.). (a) Each sample was collected from fresh outcrop and (b) then crushed and sealed in polycarbonate box of 180 cm^3 of volume

Provided the accessibility of the outcrops, the number of the samples collected for each cartographic unit was planned on the basis of the exposure area and the estimated volume, taking into account also the proximity to the detector. For each of the 22 cartographic units, identified by a Geocode, we report extent area, number of samples collected, and average U and Th abundances, with the average ratio between extent area and number of samples being ∼15 km^2/sample (Table 3.1). In the CUC area are also homogeneously distributed olivine diabase dikes emplaced along faults cutting across the Sudbury Structure having negligible volumes (*Tschirhart and Morris*, 2012). Although the reference geological map does not report the presence

of the dike swarm according to its spatial resolution, we chose to collect three samples in order to characterize these rocks. After checking that the U and Th abundances of these three samples (Table 3.1) are compatible with the average abundances of the CUC, we decided to exclude them for the geochemical modeling (see Section 3.7) performed with the remaining 109 samples out of the collected 112.

Unit	Geocode	Group and Formation	Area (km^2)	Area (%)	N	K ± σ (%)	U ± σ (µg/g)	Th ± σ (µg/g)
GT	11	Gneissic tonalite suite	91.5	3.7	9	1.21 ± 0.65	0.6 ± 0.9	2.8 ± 3.5
CT	15	Cartier granite	62.2	2.5	2	4.55 ± 0.28	1.8 ± 1.1	56.9 ± 27.3
HI	17b	HS; Mafic and ultramafic intrusive rocks and mafic dikes	8.2	0.3	1	0.32 ± 0.03	2.0 ± 0.2	3.2 ± 0.4
	18a	HS; Elliot Lake Group; McKim Fm.	121.9	4.9	7	1.94 ± 1.00	5.0 ± 3.0	16.2 ± 8.4
	18c	HS; Elliot Lake Group; volcanic rocks	125.3	5.0	6	3.30 ± 1.38	5.9 ± 3.2	23.2 ± 11.4
	19a	HS; Hough Lake Group; Mississage Fm.	442.4	17.7	18	$1.52^{+1.65}_{-0.79}$	$2.2^{+2.4}_{-1.2}$	$6.6^{+7.5}_{-3.5}$
	19b	HS; Hough Lake Group; Pecors Fm.	41.9	1.7	4	1.37 ± 1.49	2.9 ± 1.1	9.2 ± 4.3
	20a	HS; Quirke Lake Group; Serpent Fm.	15.5	0.6	1	2.45 ± 0.15	0.9 ± 0.1	4.2 ± 0.5
	20b	HS; Quirke Lake Group; Espanola Fm.	32.3	1.3	3	3.48 ± 0.86	3.7 ± 0.7	12.5 ± 2.1
	21	HS; Cobalt Group	4.6	0.2	1	1.59 ± 0.17	1.6 ± 0.2	3.1 ± 0.4
	23d	Mafic and related intrusive rocks and mafic dikes	88.0	3.5	6	0.70 ± 0.51	0.4 ± 0.3	1.7 ± 1.0
	30a	Felsic intrusive rocks	53.6	2.1	4	4.36 ± 0.25	5.9 ± 2.4	36.2 ± 6.4
	-	Sudbury Dyke Swarm; olivine diabase	-	-	3	0.48 ± 0.03	0.9 ± 0.5	4.0 ± 2.8
CM	28a	Whitewater Group; Chelmsford Fm.	153.1	6.1	4	1.29 ± 0.29	1.1 ± 0.1	5.1 ± 0.7
OW	28b	Whitewater Group; Onwatin Fm.	160.1	6.4	2	2.19 ± 0.35	1.1 ± 0.1	5.2 ± 1.4
OP	28c	Whitewater Group; Onaping Fm.	343.3	13.7	12	1.83 ± 0.95	3.1 ± 0.6	8.2 ± 1.0
GN	29a	SIC; granophyre	241.7	9.7	10	3.18 ± 0.40	3.4 ± 0.5	15.1 ± 2.4
NG	29b	SIC; norite-gabbro	157.9	6.3	9	1.21 ± 0.08	1.3 ± 0.8	6.8 ± 4.3
GF	30b	Felsic intrusive rocks	126.8	5.1	3	4.15 ± 0.24	6.8 ± 5.8	31.0 ± 17.5
	40	Mafic rocks	16.7	0.7	1	0.96 ± 0.06	1.3 ± 0.1	4.9 ± 0.5
	41	Migmatitic rocks and gneisses of undetermined protolith	124.0	5.0	5	2.41 ± 0.14	2.7 ± 2.3	13.0 ± 12.1
	43	Felsic igneous rocks	18.5	0.7	1	2.33 ± 0.14	2.9 ± 0.3	4.6 ± 0.5

Table 3.1: Summary of the Geocode units, aerial extent, number of sample (N), and average and uncertainties of element abundances. Geocodes of the reference geological map are reported for the corresponding unit abbreviation and the area of the exposed surface. For Geocodes with more than 10 samples the central value and the uncertainty for K, U, and Th abundances are derived from a normal or lognormal distribution fit inferred from the Kolmogorov-Smirnov test (see section 3.7); for the other Geocodes we report the mean and the standard deviation. For Geocodes with one sample the uncertainty corresponds to the statistical uncertainty of the HPGe measurement.

3.6 Analytical Method

The radioactive content of the collected samples was measured at the Department of Physics and Earth Sciences of the University of Ferrara, with a High Pure Germanium detector (HPGe) called MCA_Rad. Analytical details are given in (*Xhixha et al.*, 2013, 2016). The overall relative uncertainties on the K, eU and eTh (i.e. U and Th assumed in secular equilibrium) are of the order of 10%. In the analyzed dataset less than 4% of the samples have eU and eTh abundances below the Minimum Detectable Activity (MDA) defined in *Xhixha et al.* (2013) and corresponding to about 0.2 and 0.7 g/g, respectively (see supporting information Table S4).

Additional analyses of U and Th on 14 of the 112 samples, including those below MDA of MCA_Rad, were done at the Department of Geology at the University of Maryland using an ICPMS (Thermo-Finnigan Element 2) (see supporting information Table S1). These results are reported in supporting information, see Table S2. Aliquots of the samples used for gamma ray spectroscopy were powdered and analyzed for U and Th concentrations using a Standard Addition method detailed in *Gaschnig et al.* (2016). U and Th concentrations from Standard Addition have average relative uncertainty of 3.5%.

In addition, external calibration analyses using USGS rock standards were conducted for some 36 other elements including Th and U. The abundances of these elements were calculated by comparison to external standards that were dissolved alongside the samples. We calculated the counts-per-second/concentration

of the standard(s) using accepted concentrations from GeoReM (Queried 28 March, 2017). These ratios were compared to counts-per-second for each element within a sample to calculate a final concentration (see supporting information Table S5). U and Th results from this External Calibration method agree with the Standard Addition method. Uncertainties on the External Calibration analysis are 5% or better following *Gaschnig et al.* (2016).

The U and Th abundances of the five samples below the MDA of MCA_Rad are substituted by the values from ICPMS technique, which has a sensitivity better than HPGe investigation. Taking into account the experimental uncertainties for the remaining nine samples we observe an agreement at 2 sigma level and exclude any systematic effect. The dataset of 112 U and Th abundances is therefore composed by 98 and 14 values from the HPGe and ICPMS technique, respectively.

3.7 Construction of the Model

The geological units of the 3D model of the Close Upper Crust (CUC) (see supporting information Dataset S1) were defined considering the surface exposure described in the published 1:250,000 scale Bedrock Geology of Ontario [Ontario Geological Survey, 2011], which is conveniently simplified according to the spatial resolution of the available information about crustal structure. The upper crust is subdivided into nine units (Figure 3.4) on the basis of lithology, metamorphism, tectonic events, and evolutional history:

- 1. Chelmsford Fm., Whitewater Group (CM);

- 2. Onwatin Fm., Whitewater Group (OW);
- 3. Onaping Fm., Whitewater Group (OP);
- 4. Granophyre, Sudbury Igneous Complex (GN);
- 5. Norite-gabbro, Sudbury Igneous Complex (NG);
- 6. Cartier Granite (CT);
- 7. Huronian Supergroup and minor felsic and mafic Intrusions (HI);
- 8. Grenville Front Tectonic Zone rocks (GF) and 9. Gneissic Tonalite suite (GT).

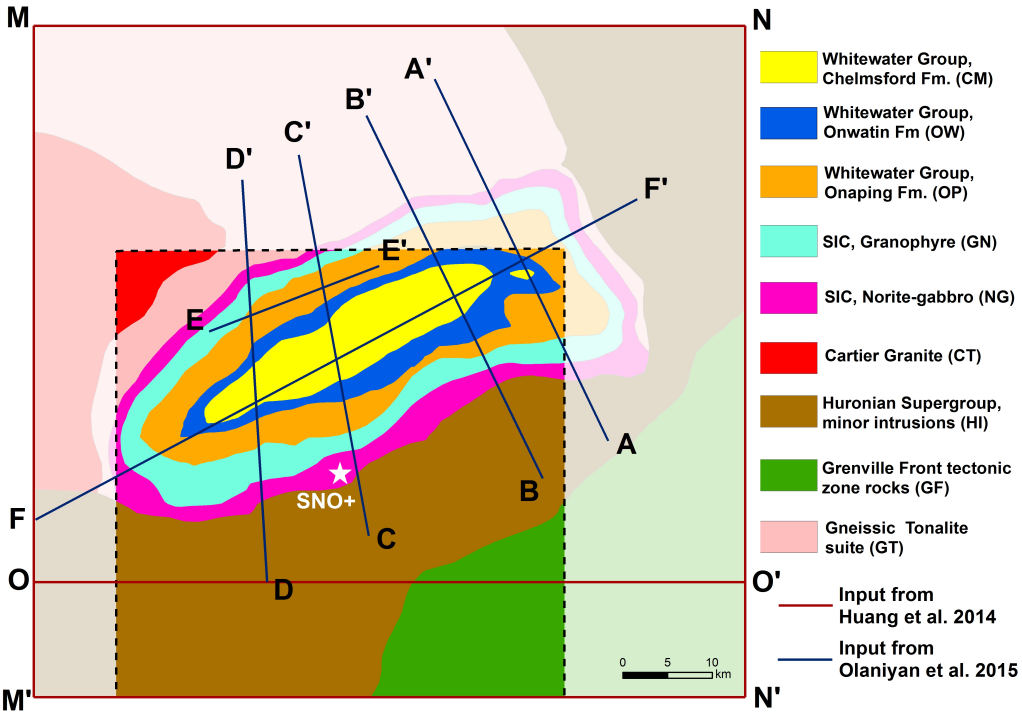

Figure 3.4: Geophysical inputs used for the construction of the 3D model. The six cross sections derived from *Olaniyan et al.* (2015) (AA', BB', CC', DD', EE', FF') and the five cross sections extracted from the H14 model (MM', M'N', NN', MN, OO') are projected on the simplified geological map. The inner box represents the CUC. (Cartographic reference system NAD1927 UTM Zone 17N). The CM, OW, and OP are, respectively the metagraywackes, the pelagic metasedimentary rocks and the breccias of the Whitewater Group that fills the Sudbury Basin while the main mass of the SIC is constituted by granophyre (GN) and norite-gabbro (NG). The HI, formally composed by the HS, includes also minor mafic (Nipissing mafic sills) and felsic intrusions (Creighton and Murray granite). The Gneissic Tonalite suite (GT), that is assumed to be representative of the rest of the upper crust, is an assemblage of high-grade gneissic rocks intruded on the Northwest area by the massive granitic rocks of the Cartier Batholith (CT). In the south-eastern portion of the CUC, the GF unit is characterized by the presence of migmatitic rocks, gneisses and felsic intrusions of the GFTZ. The Geocodes associated to each unit are detailed in Table 3.1.

3.7.1 Geophysical Modeling

The crustal structures of the nine units were defined by combination of multiple geological and geophysical inputs: (i) the contacts of the simplified geological map

(Figure 3.4), (ii) a published digital elevation model (*Jarvis et al.*, 2008), (iii) the map of depth of the top of the middle crust reported in H14, (iv) the 2.5D geological models along six profiles used for constructing the 3D model reported in *Olaniyan et al.* (2015) and (v) five virtual cross sections derived from the model developed in H14.

The surface topography for the CUC region uses the digital elevation model produced by the Shuttle Radar Topographic Mission (SRTM) (*Jarvis et al.*, 2008).

The bottom of the 3-D model has a 11 km resolution and is the surface of the top of the middle crust (Figure 3.1) determined in H14. The depth map of the top of the middle crust was obtained alongside the error estimation map by applying a geostatistical estimator (Ordinary Kriging) to 343 depth-controlling points. These points are derived from refraction surveys performed in the region surrounding Sudbury. The P-wave velocity of 6.6 km/s is adopted as a contour to identify the top of the middle crust in 18 refraction lines, two of which (XY and AB reported in [Winardhi and Mereu, 1997]) are within the CUC area. The top of the middle crust is a 2D input for the construction of the 3D model. The depth of the CUC varies between 16.4 and 20.4 km, with a mean of 18.4 km. The normalized estimation error of the map has an average value of 4.7%.

In *Olaniyan et al.* (2015) the 3D model was obtained by integrating a compilation of surface and subsurface geologic data with high-resolution airborne magnetic and gravity data. The authors evaluated qualitatively high resolution Bouguer gravity data with the computed field along with subsurface geologic data and created their cross section profiles. They observed a broad correlation between the mea-

sured and computed gravity field and found areas of misfit. The 2.5-D geological models reported in six profiles (AA', BB', CC', CC', EE' and FF' in Figure 3.4), are used as inputs for the modeling of the Sudbury Structure. Orientation data and boundary surfaces of the units of the Whitewater group (CM, OP, and OW units) and of the main mass of the SIC (GN and NG units) are modeled by extracting the depth-controlling points of the boundary surfaces from each profile.

For the remaining area of the CUC, the 3-D geometries of the units were developed in H14 on the basis of surface contacts between units and 16 interpreted crustal cross sections of the area, with the main inputs from *Easton* (2000) and *Adam et al.* (2000). In this perspective, five virtual cross sections (MM', NN', MN, M'N', and OO' in Figure 3.4) are extracted from H14 and used as input for inferring the structure of units not constrained by inputs from *Olaniyan et al.* (2015).

The geological interfaces of the 9 units are modeled using the interpolator method based on potential field theory (*Calcagno et al.*, 2008) and implemented in the software package GeoModeller. Using the available data from the geological reference map and that reported in *Olaniyan et al.* (2015) we reduced interpretational nonuniqueness of the potential field data by applying hard geological constraints, including (i) the stratigraphic succession of geological formations, (ii) geological contacts, (iii) structural data, and (iv) orientation data. Figure 3.5 provides 3D views of the determined geological model.

The adopted density values for each unit (Table 3.3) are from the model reported in *Olaniyan et al.* (2015) and the relative uncertainties from Table 5 in H14. Density of the HI unit is obtained from the weighted average of values of sediments

(2.70 g/cm^3) and mafic rocks (2.88 g/cm^3), assuming that their proportions are respectively 75% and 25% according to the exposure surface within the reference geologic map. The GT and GF units are assumed to have density equal to the Archean basement value (2.73 g/cm^3) reported in *Olaniyan et al.* (2015).

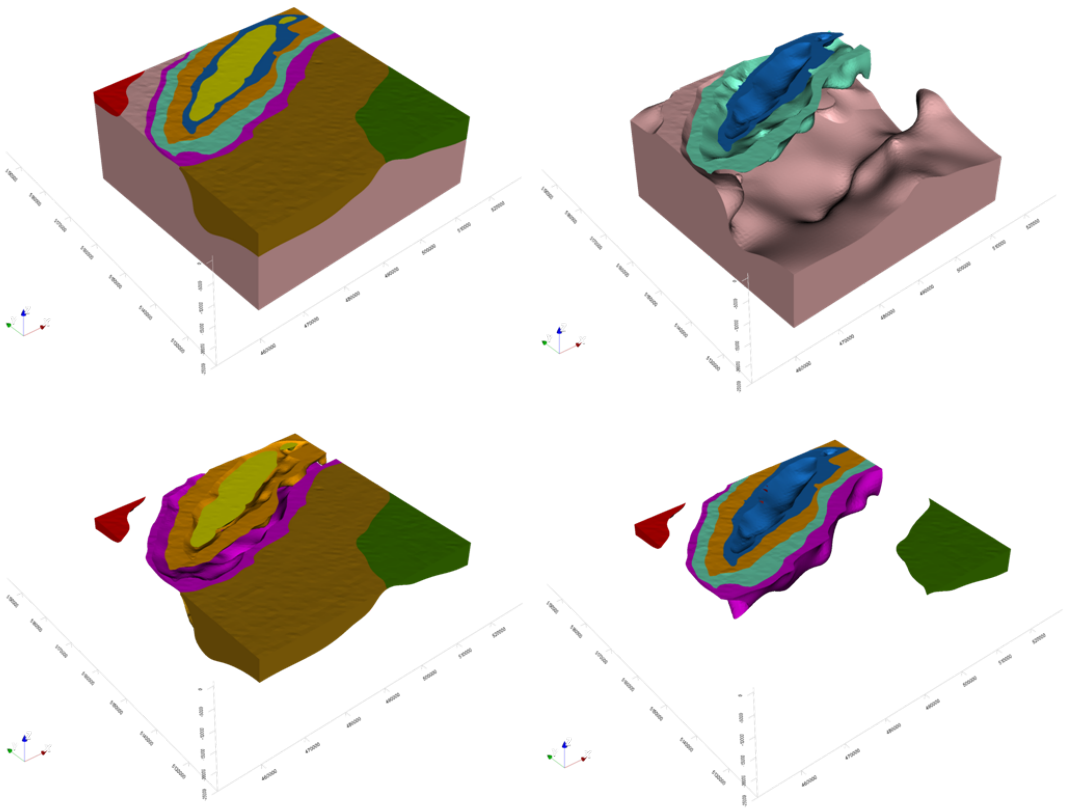

Figure 3.5: Views of the 3D model in GeoModeller. The 3D model takes into account contacts, structural data, and orientation data and follows the order of the stratigraphic succession of geologic units. Color of units is the same as in Figure 3.4. (Cartographic reference system NAD1927 UTM Zone 17N)

3.7.2 Geochemical Modeling

Based on the 109 representative outcrop samples we statistically evaluated the abundances of U and Th in the nine units. Analyses of the GT unit and the units representing the SIC were combined with data from the H14 model and from compiled geochemical databases.

For the six units with more than 10 samples (Table 3.3), the distribution function of U and Th concentrations is graphically evaluated using univariate statistics by means of frequency histograms. In order to discriminate the normal and log-normal distributions, the KolmogorovSmirnov (K-S) statistical test was applied, providing a p-value for rejecting the null hypothesis. The mean and standard deviation are calculated and used for the geochemical modeling of the other three units (CM, OW, and CT), characterized with less than five samples, corresponding approximately to 1% of the total volume of the CUC.

The first refinement in the geochemical modeling compared to H14 consisted in the use of collected rock samples to describe the chemical composition of the Whitewater Group, a sedimentary and volcanic sequence that fills the Sudbury Basin, as three different lithographic sequences with distinct volumes in the 3D geophysical model (CM, OW, and OP in Figure 3.4). In H14 the Whitewater Group was included with the Huronian Supergroup as a single unit with relatively high U ($4.2^{+2.9}_{-1.7}$ g/g) and Th ($11.1^{+9.2}_{-4.8}$ g/g) abundances. In this study, the turbidite wacke of the CM and the siltstone of OW, belonging to the same proximal turbiditic sequence, are characterized as a separate lithographic section with the same average U ($\sim$ 1

μg/g) and Th ($\sim$ 5 μg/g) abundances (Table 3.3), which are slightly lower than in other sedimentary units and this feature reflects their enrichment in carbonate. The breccia and igneous-textured rocks of the OP are enriched in U and Th with respect to the rest of the Whitewater group and show a normal distribution, with a relative low uncertainty (15%).

The geochemical inputs for modeling the main mass of the SIC come from a combined dataset that includes the samples reported in this study and the compiled database analyzed in H14, i.e. ICPMS compositional data reported in *Lightfoot et al.* (1997) (see supporting information Table S3 and Table S6). Table 3.2 reports the results of exploratory data analysis considering the two datasets separately and all the data together. The central values of U and Th abundances agree at 1 sigma level with the values reported in *Mareschal et al.* (2017). Although the previous and the new data are characterized by different sources, measurement methodology, and sampling strategies, our analysis demonstrate that the two datasets belong to the same population and can be treated as a single distribution. In the Surrounding Upper Crust (SUC) (see Figure 3.4), the U ($2.0^{+0.4}_{-0.2}$ μg/g) and Th ($10.5^{+1.3}_{-1.1}$ μg/g) abundances associated to the "Sudbury Igneous Complex" unit are obtained by equally weighting the values of the GN and NG units , in agreement with the mixing reported in H14.

Dataset	Sudbury Igneous Complex					
	Granophyre (GN)			Norite-gabbro (NG)		
	Number of samples	U ± σ [μg/g]	Th ± σ [μg/g]	Number of samples	U ± σ [μg/g]	Th ± σ [μg/g]
H14	25	3.3 ± 0.2	14.9 ± 1.0	99	1.3 ± 0.4	$5.9^{+1.9}_{-1.5}$
This study	10	3.4 ± 0.5	15.1 ± 2.4	9	1.3 ± 0.8	6.8 ± 4.2
All data	35	3.3 ± 0.3	15.0 ± 1.5	108	$1.2^{+0.6}_{-0.4}$	$5.9^{+2.1}_{-1.5}$

Table 3.2: Exploratory data analysis results for U and Th abundance of the GN and NG units which compose the main mass of the SIC (Figure 3.4).

The dataset adopted for the geochemical characterization of the Huronian Supergroup and minor felsic and mafic Intrusions unit (HI in Figure 3.4) includes 41 samples belonging to the Huronian Supergroup (Geocode 17b, 18a, 18c, 19a, 19b, 20a, 20b, 21) and the 10 rock samples representative of the minor mafic (Geocode 23d, Nipissing mafic sills) and felsic intrusions (Geocode 30a, Creighton and Murray granite). The frequency histograms and K-S test (Figure 3.6) indicate that the U and Th concentrations in the HI unit are positively skewed and fit a lognormal distribution. The parameters, μ and σ, obtained from the lognormal probability density function (Figure 3.6) give the central tendency and the asymmetrical uncertainties of U and Th abundances (Table 3.3). The U and Th abundances of the HI unit in the CUC are $2.3^{+4.0}_{-1.5}$ μg/g and $8.0^{+15.3}_{-5.3}$ μg/g, respectively. This lower, revised estimate for the Huronian Supergroup, as compared to that reported in H14, results from a targeted and refined collection of samples specifically aimed at the geochemical characterization of the unit. In H14 Huronian Supergroup samples had an anomalous geographical distribution since they were collected only in the western portion of the study area. At the same time, there was an additional lithographic

bias as the extensive amount of arkose and quartz arenites in the Mississage Fm. close to SNO+ was not characterized with a proportionate number of samples.

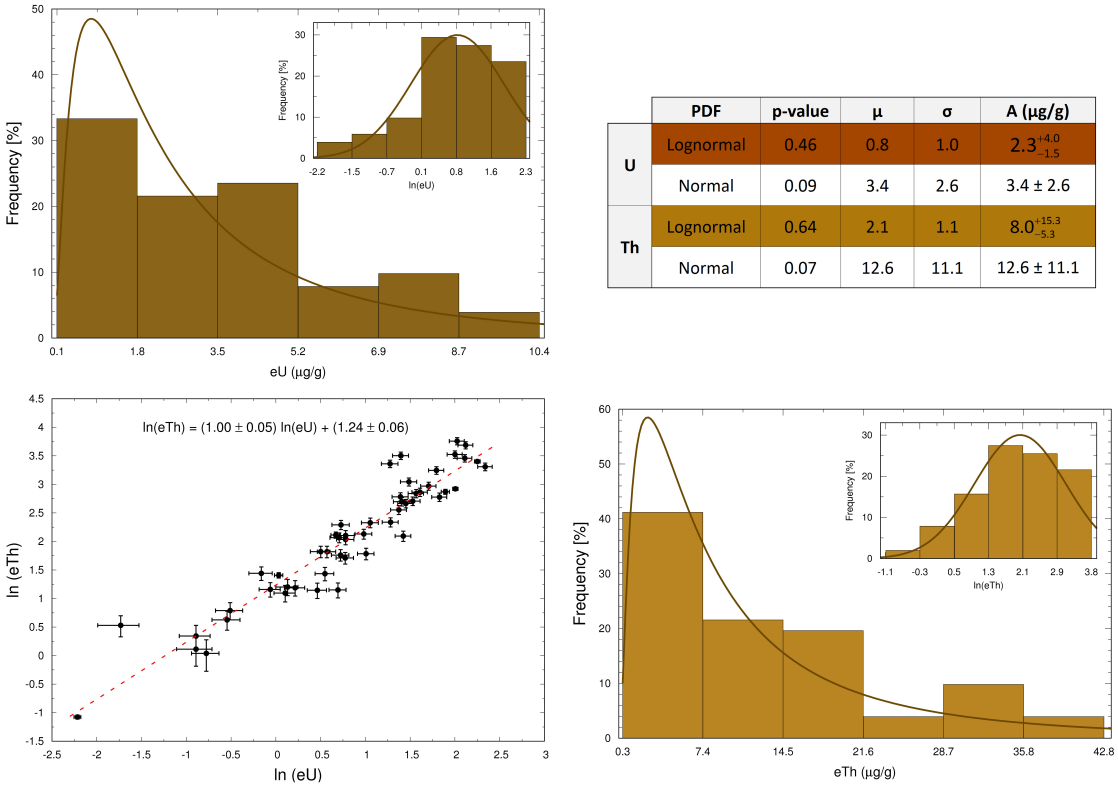

	PDF	p-value	µ	σ	A (µg/g)
U	Lognormal	0.46	0.8	1.0	$2.3^{+4.0}_{-1.5}$
	Normal	0.09	3.4	2.6	3.4 ± 2.6
Th	Lognormal	0.64	2.1	1.1	$8.0^{+15.3}_{-5.3}$
	Normal	0.07	12.6	11.1	12.6 ± 11.1

Figure 3.6: Frequency histograms for (top left) U and (bottom right) Th measurements of HI fitted with a lognormal distribution and for the logarithm abundances fitted with a normal distribution. The p-value obtained from the K-S test and the parameters of the fit (μ and σ), considering a lognormal or a normal distribution, are reported in the table on the top right plot together with the result in terms of abundances and uncertainties (A). The plot of the correlation of U and Th abundances and the result of the fit are reported in the bottom left plot, where the error bars refer to experimental uncertainty during measurement.

Although the Gneissic Tonalite suite unit (GT in Figure 3.4), constituted by tonalitic gneiss and minor paragneiss, is only the 4% of the area of the CUC, it is supposed to be representative of the high-grade gneissic rock of the rest of the upper crust (*Huang et al.*, 2014). The GT unit has limited exposure (Table 3.1) in the northwest, but comprises 63.7% of the volume of the CUC (Table 3.3). Due to its

relevance for estimating the geoneutrino signal, data from the 9 collected samples were integrated with 37 other samples (supporting information Table S7) extracted from compiled databases (*Ayer et al.*, 2010; *Beakhouse*, 2011; *Berger*, 2012) on the base of both lithologic and geographic criteria. The final dataset includes the tonalite gneiss samples, attributed to Geocode 11 (gneissic tonalite suite) and Geocode 12 (foliated tonalite suite) of the reference map. The same statistical analysis adopted for the HI unit was applied to the updated GT unit, which shows a lognormal distribution for U and Th concentrations (Figure 3.7) and agree with the values adopted for the modeling of the "Tonalite/tonalite gneiss" unit in H14 ($0.7^{+0.5}_{-0.3}$ μg/g for U and $3.1^{+2.3}_{-1.3}$ μg/g for Th).

Unit	Volume $[10^3 km^3]$	Volume [%]	Density $[g/cm^3]$	Mass $[10^{15} kg]$	Number of samples	U ± σ [μg/g]	Th ± σ [μg/g]	r
GT	29.69 ± 1.40	63.7	2.73± 0.08	81.05± 5.01	46	$0.7^{+1.0}_{-0.4}$	$2.7^{+6.0}_{-1.9}$	0.81
HI	10.52 ± 0.49	22.6	2.75± 0.04	28.93± 1.79	51	$2.3^{+4.0}_{-1.5}$	$8.0^{+15.3}_{-5.3}$	0.95
NG	2.64 ± 0.12	5.7	2.83 ± 0.10	7.47± 0.46	108	$1.2^{+0.6}_{-0.4}$	$5.9^{+2.1}_{-1.6}$	0.84
GN	1.43 ± 0.07	3.1	2.70± 0.10	3.86 ± 0.32	35	3.3 ± 0.3	15.0 ± 1.5	0.58
OP	0.94 ± 0.04	2.0	2.77± 0.04	2.60± 0.22	12	3.1 ± 0.6	8.2 ± 1.0	-0.15
GF	0.83 ± 0.04	1.8	2.73± 0.08	2.27± 0.12	10	$2.7^{+3.4}_{-1.5}$	$10.9^{+17.3}_{-6.7}$	0.89
OW	0.30 ± 0.01	0.6	2.68± 0.04	0.80± 0.05	2	1.1 ± 0.01	5.2 ± 1.5	-
CM	0.23± 0.01	0.5	2.75 ± 0.04	0.62 ± 0.05	4	1.1 ± 0.1	5.1 ± 0.7	-
CT	0.04 ± 0.002	0.1	2.65± 0.02	0.11± 0.01	2	1.8 ± 1.1	56.9 ± 27.3	-

Table 3.3: For each modeled unit the geophysical properties (volume, density and mass) and the U and Th abundances are reported together with the number of samples used for their characterization. The mass uncertainty is obtained by summing the volume uncertainty from the estimation errors of the depth to the top of the middle crust, i.e. 4.7%, and the density uncertainty derived from H14. The correlation coefficient r, with the exception of GN and OP units, is calculated assuming logarithmic distribution of the U and Th abundances.

The composition of the Cartier Granite unit, (CT in Figure 3.4) which is characterized by a poor exposure (Table 3.1) and a relatively small volume in the CUC (Table 3.3), is inferred from the analysis of two samples. The U and Th abundances measured are in agreement with the range reported in Table 1 of *Meldrum et al.* (1997) and that for the "Felsic intrusion" unit of H14. These rocks have an anomalous high average Th/U ratio of 32 compared to average continental crust Th/U = 4.3 (*Rudnick and Gao*, 2003). The 10 samples from the Grenville Front Tectonic Zone unit (GF in Figure 3.4), occupying the southeast portion of the CUC and corresponding to 1.8% of the total volume, have significant compositional variability (Table 3.1) linked to the different lithologies (gneisses, felsic, mafic, and migmatitic rocks). Results of K-S statistical tests reveal their U and Th abundances and uncertainties are lognormally distributed (Table 3.3).

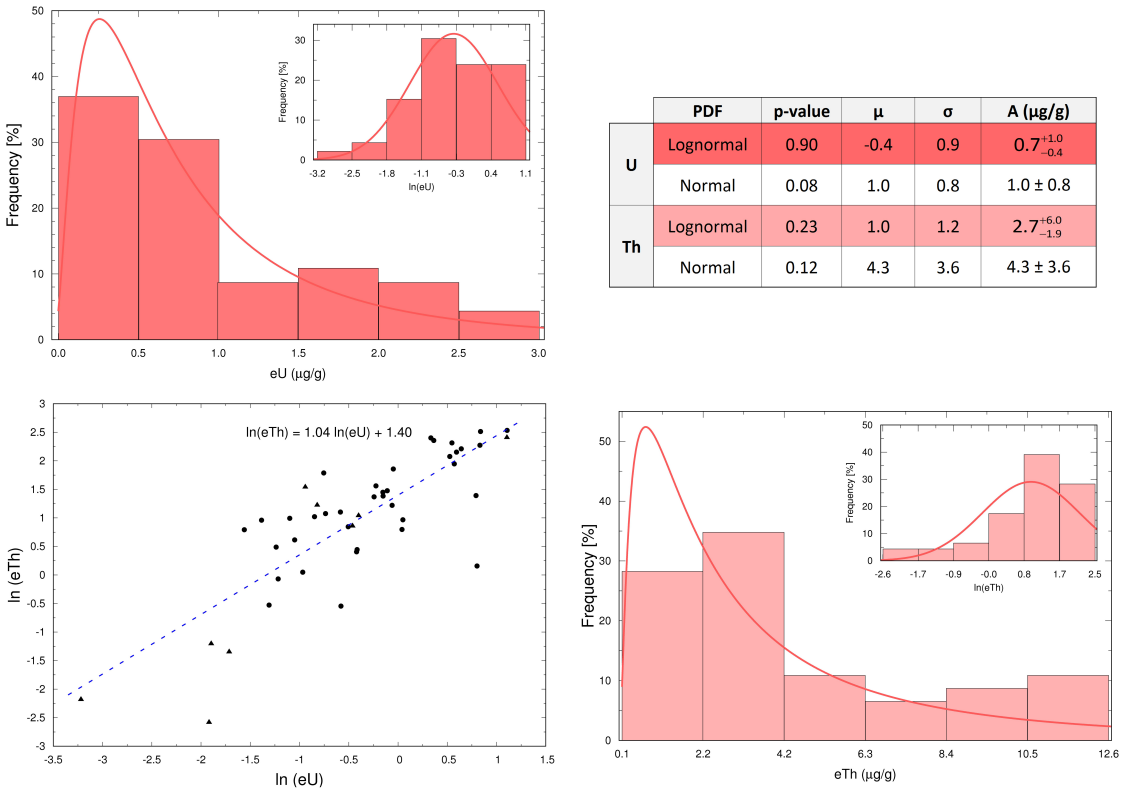

	PDF	p-value	μ	σ	A (µg/g)
U	Lognormal	0.90	-0.4	0.9	$0.7^{+1.0}_{-0.4}$
	Normal	0.08	1.0	0.8	1.0 ± 0.8
Th	Lognormal	0.23	1.0	1.2	$2.7^{+6.0}_{-1.9}$
	Normal	0.12	4.3	3.6	4.3 ± 3.6

Figure 3.7: Frequency histograms for (top left) U and (bottom right) Th measurements of GT fitted with a lognormal distribution and for the logarithm abundances fitted with a normal distribution. The p-value obtained for the K-S test and the parameters of the fit (μ and σ), considering a lognormal or a normal distribution, are reported in the table on the upper-left panel together with the result in term of abundances (A) and uncertainties. The plot of the correlation of U and Th abundances and the result of the fit are reported in the bottom left plot (triangles refer to samples collected in this study; dots refer to data from compiled databases)

3.8 Geoneutrino Signal Calculation

Predicting a geoneutrino signal at a detector depends upon: (1) the abundance and distribution of Th and U, (2) propagation of the electron antineutrino from the decay point to the detector, and (3) detection of the particle via the Inverse Beta Decay (IBD) reaction within the detector. The final 3D crustal model for the CUC was divided into cells of 0.1 km × 0.1 km × 0.1 km dimensions, for a

total of about 5 × 107 voxels (see supporting information Dataset S1). Spatial, geophysical, and geochemical attributes were assigned to each voxel. The activity of the individual isotopes (i.e., the average number of decays occurring per unit time) for each voxel was computed by dividing the number of radioactive nuclei by the corresponding radioisotope mean lifetime, the former estimated on the base of the radioisotope abundance and the volumetric density defined by the 3D model. The geoneutrino flux reaching SNO+ is then calculated by applying the isotropic $1/4\pi r^2$ spherical scaling factor, weighted for the corresponding geoneutrino spectrum (normalized to the number of geoneutrinos emitted per decay) (*Fiorentini et al.*, 2007a), and oscillated by the electron antineutrino three-flavor survival probability (*Capozzi et al.*, 2017) calculated with $\sin^2\Theta_{12}$= 2.97×10−1, $\sin^2\Theta_{13} = 2.15\times10^{-2}$, $\delta m^2 = 7.37\times10^{-5}$ eV2, $\Delta m^2 = 2.25 \times 10^{-3}$ eV^2 (*Capozzi et al.*, 2017). Finally, the geoneutrino signal (in TNU) and spectra (Figure 3.9) originating from each cell are calculated combining U and Th oscillated geoneutrino fluxes with IBD cross section. The predicted geoneutrino signals originating by U and Th in the nine units of the CUC are reported in (Table 3.4). The geophysical and geochemical uncertainties associated to each unit are propagated to obtain the geoneutrino signal uncertainties.

Unit	$G_U \pm \sigma$	$G_{Th} \pm \sigma$	$S_U \pm \sigma$	$S_{Th} \pm \sigma$	$S_{TOT} \pm \sigma$
GT	0.70 ± 0.05	0.041 ± 0.003	$0.5^{+0.7}_{-0.3}$	$0.11^{+0.24}_{-0.07}$	$0.6^{+0.9}_{-0.4}$
HI	1.51 ± 0.09	0.101 ± 0.006	$3.5^{+6.1}_{-2.2}$	$0.8^{+1.5}_{-0.5}$	$4.3^{+7.6}_{-2.7}$
NG	0.72 ± 0.05	0.049 ± 0.003	$0.9^{+0.4}_{-0.2}$	$0.29^{+0.09}_{-0.07}$	$1.2^{+0.4}_{-0.3}$
GN	0.19 ± 0.01	$[1.25 \pm 0.10] \times 10^{-2}$	$0.62^{+0.09}_{-0.07}$	0.19 ± 0.02	0.80 ± 0.08
OP	$[6.5 \pm 0.4] \times 10^{-2}$	$[4.2 \pm 0.3] \times 10^{-3}$	0.20 ± 0.04	$[3.50 \pm 0.40] \times 10^{-2}$	0.24 ± 0.04
GF	$[1.4 \pm 0.1] \times 10^{-2}$	$[7.9 \pm 0.6] \times 10^{-4}$	$\left[2.6^{+3.5}_{-1.5}\right] \times 10^{-2}$	$\left[0.9^{+1.4}_{-0.5}\right] \times 10^{-2}$	$\left[3.6^{+4.5}_{-2.1}\right] \times 10^{-2}$
OW	$[1.55 \pm 0.10] \times 10^{-2}$	$[9.8 \pm 0.6] \times 10^{-4}$	$[1.70 \pm 0.02] \times 10^{-2}$	$[0.51 \pm 0.15] \times 10^{-2}$	$[2.2 \pm 0.2] \times 10^{-2}$
CM	$[1.24 \pm 0.08] \times 10^{-2}$	$[7.8 \pm 0.5] \times 10^{-4}$	$[1.37 \pm 0.15] \times 10^{-2}$	$[0.40 \pm 0.06] \times 10^{-2}$	$[1.8 \pm 0.2] \times 10^{-2}$
CT	$[2.03 \pm 0.12] \times 10^{-4}$	$[1.05 \pm 0.06] \times 10^{-5}$	$[0.4 \pm 0.2] \times 10^{-3}$	$[0.6 \pm 0.3] \times 10^{-3}$	$[1.0 \pm 0.4] \times 10^{-4}$

Table 3.4: Geoneutrino signals and uncertainties (σ) in TNU for uranium (S_U), thorium (S_{Th}) and total signals (S_{TOT}) for the nine units of the CUC. In the first two columns are reported the geoneutrino signals from U (G_U) and Th (G_{Th}) calculated with unitary abundances.

Geochemical uncertainties on the geoneutrino signal were estimated taking into account correlations between U and Th abundances (Table 3.3) and their distributions as follows.

1. For the GT, HI, NG and GF units a bivariate normal distribution describing the joint (ln(U), ln(Th)) Probability Density Function (PDF) was built. For each unit the adopted statistical parameters are the logarithmic U and Th mean and sigma values calculated from the abundances reported in Table 3.3, and the logarithmic U and Th covariance coefficient determined from U and Th concentrations of individual samples.

2. For the GN unit a bivariate normal distribution characterizing the joint (U, Th) PDF was modeled. The statistical parameters are the mean and sigma values reported in Table 3.3 for U and Th and the covariance coefficient determined from U and Th concentrations of individual samples.

3. For the OP unit the r = -0.15 correlation coefficient indicates a non evident correlation among U and Th abundances (Table 3.3): the U and Th geochemical distributions are separately modeled as individual normal PDFs having as U and Th mean and sigma the values reported in Table 3.3.

4. For the OW, CM and CT units the number of collected samples is not sufficient for establishing a correlation between U and Th concentrations. For each unit the U and Th geochemical distributions are built as distinct normal PDFs having as U and Th mean and sigma the values reported in Table 3.3.

The mentioned geochemical PDFs together with the geophysical uncertainties are the input ingredients of a Monte Carlo uncertainty propagation procedure: by performing 104 Monte Carlo iterations, the U, Th, and total geoneutrino signal distributions have been built, which are characterized by the median $\pm$ 1σ values reported in Table 3.4. We used the same approach for predicting the geoneutrino signals and their uncertainties for the SUC (Figure 3.1), the Local Middle Crust (LMC), and the Local Lower Crust (LLC) (Table 3.5) which takes into account the geophysical and geochemical inputs reported in Table 4 of H14. The only exception is that of "Sudbury Igneous Complex", which we assigned U and Th abundances on the base of the geochemical considerations described in Section 3.7.

		$S_U \pm \sigma$	$S_{Th} \pm \sigma$	$S_{TOT} \pm \sigma$
LUC	CUC	$6.1^{+6.2}_{-2.4}$	$1.6^{+1.7}_{-0.6}$	$7.7^{+7.7}_{-3.0}$
	SUC	$4.1^{+1.0}_{-0.7}$	$1.0^{+0.4}_{-0.3}$	$5.2^{+1.1}_{-0.8}$
LMC		$0.9^{+0.5}_{-0.3}$	$0.3^{+0.2}_{-0.1}$	$1.2^{+0.6}_{-0.4}$
LLC		$0.4^{+0.3}_{-0.2}$	$0.2^{+0.2}_{-0.1}$	$0.6^{+0.4}_{-0.2}$
Total		$12.0^{+6.2}_{-2.7}$	$3.3^{+1.8}_{-0.9}$	$15.3^{+7.7}_{-3.3}$

Table 3.5: Summary of geoneutrino signals and uncertainties (σ) in TNU from uranium (S_U), thorium (S_{Th}), and total signals (S_{TOT}) for different components of the LOcal Crust (LOC). Local Upper Crust (LUC), Close Upper Crust (CUC), Surrounding Upper Crust (SUC), Local Middle Crust (LMC), and Local Lower Crust (LLC) are the building blocks defined in Figure 3.1 and used for modeling the crust surrounding SNO+.

The calculation of the geoneutrino signal of the Far Field Crust (FFC; Figure 3.1) and Continental Lithospheric Mantle (CLM) (Table 3.6) is described in *Huang et al.* (2013) and updated with oscillation parameters from *Capozzi et al.* (2017).

	$S_{TOT} \pm \sigma$
LOC	$15.3^{+7.7}_{-3.3}$
FFC	$15.2^{+2.7}_{-2.4}$
Bulk Crust	$31.1^{+8.0}_{-4.5}$
CLM	$2.1^{+3.0}_{-1.3}$
Lithosphere	$34.2^{+9.2}_{-5.3}$

Table 3.6: Summary of the total geoneutrino signal (S_{TOT}) and uncertainties (σ) in TNU from the different components of the lithosphere.

3.9 Heat Production

According to *Mareschal et al.* (2017) the CUC is located in a geothermally anomalous region, the Sudbury Structure, with a mean heat flux of 50 $\pm$ 7 mW/m^2; this flux is larger than the flux typical of the Superior Province of 40 $\pm$ 8 mW/m^2. The bulk crustal radioactivity has been estimated through inversion of heat flux measurements (*Perry et al.*, 2009), however this approach yields a nonunique constraint for modeling the geoneutrino flux. The energy released by K, Th, and U decay chains provides the crustal radiogenic power, whereas the current geoneutrino detection method (i.e., Inverse Beta Decay reaction) only measures geoneutrinos produced by U and Th decay chains. Estimating the geoneutrino signal from heat flux data requires, among others, the following inputs: (i) the Moho heat flow, (ii) the amount of heat producing elements in the crust, (iii) heat flux data from deep boreholes, and (iv) models that constrain horizontal and vertical heat transport.

Given the U, Th, and K abundances and lithologic densities, one can calculate the corresponding heat production per unit volume, H:

$$H\ (\ \mu Wm^3\ ) = \rho \times (\ 0.0985[U\ ] + 0.0263[Th\ ] + 0.0333[\ K\ ])$$

where concentrations of [U] and [Th] are in μg/g, and [K] is in %, and ρ is density in g/cm^3. Adopting the element specific heat generation in μW/g from *Dye* (2012), the geochemical abundances in Table 3.1 and the densities in Table 3.3, we calculated the H values for each Geocode of the geological reference map in the CUC (Figure 3.2).

A heat flux map does not discriminate heat production contributions of U and Th (HU+Th) from K (HK) and such maps have an inherent problem with accurately predicting a geoneutrino signal. In typical crustal rocks, contributions to surface heat flux from K heat production can represent up to 30% of the total signal. Uncertainty estimates from HK/H can vary significantly among different lithologies. The Mississage Fm. of the Huronian Supergroup and the Onaping Formation of the Whitewater Group, which together cover more than 30% of the CUC area (Table 3.1), have HK/H 10%, whereas the GT unit, which occupies 63.7% by volume of the Close Upper Crust, has a HK/H $\sim$ 22%. Mafic and ultramafic intrusive rocks of HS and sandstones of Serpent Fm. have HK/H $\sim$ 4 % and HK/H $\sim$ 29 % respectively.

Our distribution of H values (Figure 3.8) is comparable with that reported in Figure 4 of *Phaneuf and Mareschal* (2014). Even though the study area in *Phaneuf and Mareschal* (2014) is wider than the CUC, the histograms of spatial frequency of H show comparable lognormal distributions (Figure 3.8) with central values that are compatible at the 1σ level.

Heat production for the Granophyre and Norite Gabbro subunits of the SIC are 2.3 $\pm$ 0.3 and 1.0 $\pm$ 0.5 μWm^{-3}, respectively (Table 3.1), in agreement with that reported in Table 5 of *Mareschal et al.* (2017). The predicted mean heat production

of the SIC is 1.6 ± 0.6 μWm^{-3}, consistent with it being a melt sheet of upper crustal (high heat production) (*Darling et al.*, 2010) and lower crustal (low heat production) (*Mungall et al.*, 2004) lithologies. The average heat production in the CUC, weighted according to our 3-D model, is $1.0^{+0.8}_{-0.3}$ μWm^{-3}. Adding contributions from the Middle and Lower crust yields a total heat production above the Moho of $0.7^{+0.4}_{-0.2}$ μWm^{-3}.

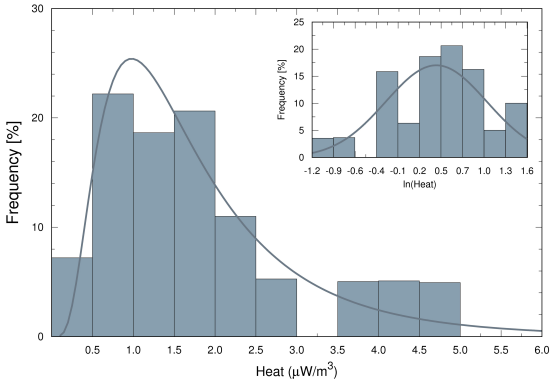

	PDF	μ	σ	H (μW/m^3)
This study	Lognormal	0.4	0.7	$1.5^{+1.4}_{-0.7}$
	Normal	1.8	1.2	1.8 ± 1.2
P14	Lognormal	0.02	0.6	$1.0^{+0.8}_{-0.4}$
	Normal	1.2	0.9	1.2 ± 0.9

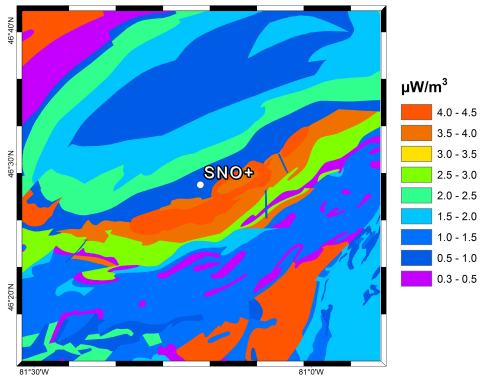

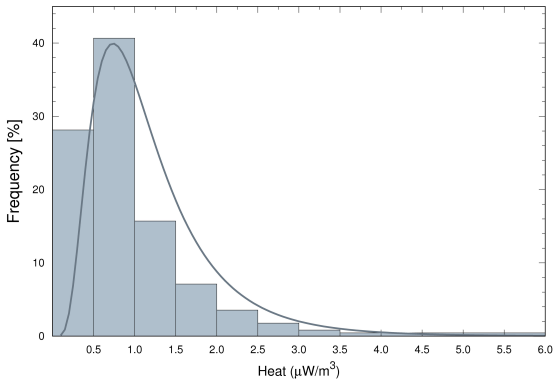

Figure 3.8: Spatial distribution of H values in the CUC is reported in the bottom left plot. In the table are reported the parameters (μ and σ) of the fit considering a lognormal or a normal distribution of the spatial frequencies obtained in this study (top left plot) and in *Phaneuf and Mareschal* (2014) (bottom right plot) together with the results in term of H and its uncertainties.

3.10 Discussion

With the aim of improving our model ofthe geoneutrino flux originating from units surrounding SNO+, we initiated a strategy of dense sampling. The strength of the adopted approach is to prevent a potential bias introduced by compiled literature data (*Huang et al.*, 2014; *Phaneuf and Mareschal*, 2014) that are often motivated by other sampling strategies (e.g. mineral exploration). The Bedrock Geology of Ontario map (*Ontario Geologic Survey*, 2011) provided a functional spatial scale for geoneutrino studies in the CUC. This map guided our statistical sampling of units, set the rationale for identifying the independent units , and guided us in establishing the building blocks of the presented model. The sampling resolution (i.e. one sample for 15 km2) was proportional to the surface extent of each cartographic unit.

In H14 the unit including the Huronian Supergroup was predicted to be the dominant near-field, crustal source of the geoneutrino signal at SNO+ and thus it was systematically studied and sampled to improve our knowledge of its composition. The results of the current study highlight the intrinsic heterogeneity of this unit, and the lognormal distribution of U and Th abundances ($2.3^{+4.0}_{-1.5}$ and $8.0^{+15.3}_{-5.3}$ μg/g respectively) and its excellent U-Th correlation (r = 0.95). Any further modeling of the geoneutrino signal at SNO+, following the methodology of this study and H14, will be ineffective without further geophysical characterization of the geochemically heterogeneous Huronian Supergroup. It is a complex mixture of different lithologies that records cyclic deposition during its 200 Ma development toward becoming a passive margin. Glacial events, metamorphic processes, and cross-cutting

volcanic fissure-type eruptions have allover-printed this stratigraphic sequence leaving a challenging riddle for the geological community.

In geochemical and environmental surveys, highly incompatible trace elements, such as U and Th, generally follow right skewed distributions: this observation triggered a scientific debate on the a priori adoption of lognormal tendency to describe a statistical population (*Ahrens*, 1954; *Reimann and Filzmoser*, 2000). The deviation from normality has serious consequences for the statistical treatment of geochemical data since the widespread practice of using the mean and the standard deviation presupposes that data have a Gaussian distribution. In this study, we applied Kolmogorov-Smirnov statistical tests revealing lognormal tendencies of U and Th for the majority of the modeled units (Table 3.3). Where a strong correlation between logarithmic U and Th was observed, a bivariate analysis for the calculation of geoneutrino signal was performed (*Fogli et al.*, 2007), leading to a refinement of the signal uncertainty estimation.

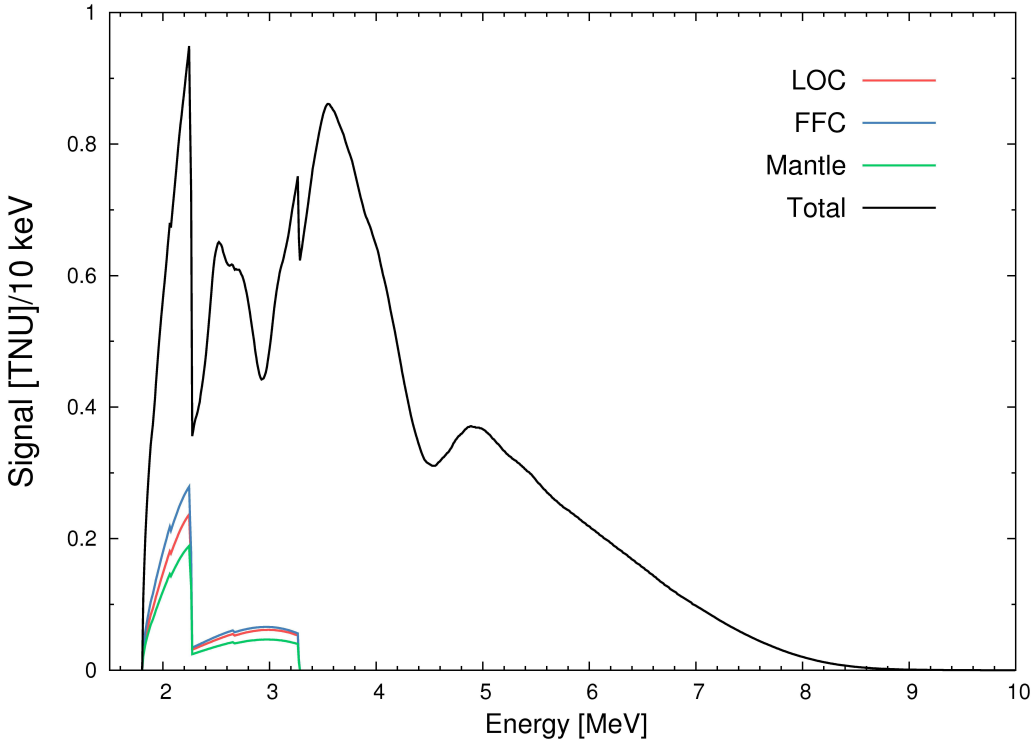

Figure 3.9: Antineutrino spectra expected at SNO+. The geoneutrino spectra are subdivided into the components of LOC (red), FFC (blue), and mantle (green) which includes CLM. The reactor antineutrino spectrum is modeled according to *Baldoncini et al.* (2016) and summed to the geoneutrino components to obtain the total antineutrino spectrum (black).

The bulk crust geoneutrino signal expected at SNO+, corresponding to $31.1^{+8.0}_{-4.5}$ TNU, can be expressed as the sum of two comparable and independent contributions, the signal from the 6°× 4°crust surrounding SNO+ (LOC) ($15.3^{+7.7}_{-3.3}$ TNU) and the signal from the rest of global crust (FFC) ($15.2^{+2.7}_{-2.4}$ TNU) (Table 3.6). U and Th in the CUC contributes 51% of the signal (Table 3.5) of the LOC. The signal from the Continental Lithospheric Mantle (CLM) beneath the Mohorovii discontinuity is calculated according to the model described in *Huang et al.* (2013) (Table 3.6).

The overall antineutrino spectrum includes the geoneutrino and the reactor

antineutrino components (Figure 3.9), which are modeled according to the predictions discussed in *Baldoncini et al.* (2016). The different portions of geoneutrino spectra contributed by LOC and FFC, particularly in the energy region [1.81 - 2.25 MeV] highlight how differences in Th/U of these two crustal components affect the geoneutrino spectrum expected at SNO+.

The mantle geoneutrino spectrum (Figure 3.9) was built according to a Bulk Silicate Earth (BSE) model constrained by the relative abundances of the refractory lithophile elements in chondritic meteorites (*McDonough and Sun*, 1995), producing a mantle signal of $6.9^{+2.7}_{-2.5}$ TNU.

Competing compositional models for the BSE estimate markedly dissimilar radiogenic power (Q) due to differences in amount of Th and U predicted in the Earth. These estimates were classified (*Dye et al.*, 2015; *Šrámek et al.*, 2013) as low Q, e.g. *Javoy et al.* (2010); *O'Neill and Palme* (2008) (8 ± 2 TW), medium Q, e.g. *McDonough and Sun* (1995) (16.6 ± 3.0 TW), and high Q, e.g. *Turcotte and Schubert* (2014) (26 ± 3 TW) models. The estimated mantle geoneutrino signal for low-Q and high-Q models at SNO+ are 3.0 ± 0.7 TNU and $13.5^{+2.6}_{-2.3}$ TNU, respectively. The 1σ uncertainty of geoneutrino signal predicted by LOC encompasses both low and high Q mantle signals, restricting the potential of SNO+ to discriminate between BSE compositional models on the basis of experimental results. On the other hand, by integrating mantle compositional data from Borexino (*Agostini et al.*, 2015) and KamLAND [(*Šrámek et al.*, 2016), the results from SNO+ can most usefully be used to resolve U and Th composition of local upper crust belonging to the Southern Province.

Acknowledgements

This work was partially funded by the National Institute of Nuclear Physics (INFN) through the ITALian RADioactivity project (ITALRAD) and by the Theoretical Astroparticle Physics (TAsP) research network. The coauthors acknowledge the support of the Geological and Seismic Survey of the Umbria Region (UMBRIARAD), the University of Ferrara (Fondo di Ateneo per la Ricerca scientifica FAR 2016), the Project Agroalimentare Idrointelligente CUP D92I16000030009 and the MIUR (Ministero dell'Istruzione, dell'Universit e della Ricerca) under MIUR-PRIN-2012 project. S.A.Wipperfurth gratefully acknowledges support from the support of DOE-INFN exchange program (2016) and the UMD GS Summer Research Fellowship. W.F. McDonough gratefully acknowledges support from NSF EAR 1067983, the University of Maryland, and Tohoku University.

The authors thank Ivan Callegari, Kassandra Raptis, Matteo Albri, Giovanni Fiorentini, Barbara Ricci, Gerti Xhixha, Enrico Chiarelli, and Carlo Bottardi for useful discussions. Richard Ash for help with the ICPMS analyses. The authors are grateful to Oladele Olaniyan and Richard Smith for providing help and sharing data of the 3D model published in *Olaniyan et al.* (2015). The authors appreciate the essential support and valuable insights from Mike Easton, Mark Chen, Nigel Smith, Eligio Lisi and Pedro Jugo. Finally, we appreciate and thank the careful reviews from J. C. Mareschal and an anonymous reviewer, and insights from and editorial efforts of Uli Faul.

Readers can find detailed geochemistry data and the 3D numerical model in

Supporting Information.

3.11 Output from this work:

- Strati, V., S. A. Wipperfurth, M. Baldoncini, W. F. McDonough, and F. Mantovani (2017), Perceiving the Crust in 3-D: A Model Integrating Geological, Geochemical, and Geophysical Data, *Geochemistry, Geophysics, Geosystems*, *18*(12), 4326–4341, doi:10.1002/2017GC007067

- Baldoncini, M., V. Strati, S. Wipperfurth, G. Bellini, F. Mantovani, W. McDonough, and B. Ricci (2016), Geoneutrinos and reactor antineutrinos at SNO+, *Journal of Physics: Conference Series*, *718*, 062,003, doi:10.1088/1742-6596/718/6/062003

- Strati, V., S. A. Wipperfurth, M. Baldoncini, W. F. McDonough, S. Gizzi, and F. Mantovani (2018), Geoneutrinos from the rock overburden at SNO+, *arXiv:1808.03199 [physics]*

Chapter 4: Upper Crust and Bulk-Crust Heat Production Inferred from Heat Flux Studies

[1] S.A. Wipperfurth created/wrote all of the material in this chapter with insight from W.F. McDonough and V. Lekic (University of Maryland Professor of geology).

4.1 Introduction

The HPE abundance in the continental crust decreases with depth. Estimates of the HPE concentration within the crust are commonly derived from data compilations from representative crustal lithologies (e.g. *Rudnick and Gao* (2014)). *Huang et al.* (2013) calculated the abundance of HPE within the middle and lower crust on a 2x2 degree grid (16,200 cells). They calculated HPE concentrations from a global seismic compressional velocity (Vp) model (CRUST2.0; *Bassin et al.* (2000)) and an inverse correlation between Vp and composition obtained from compilations of laboratory measurements of amphibolite and granulite (assumed middle and lower crust, respectively) rock types. Assumptions of amphibolite and granulite for the middle and lower crust are from exposed crustal cross sections and xenoliths (*Rudnick and Gao*, 2014). For the upper crust, *Huang et al.* (2013) adopted HPE abundance val-

ues derived from shales which are thought to be derived from large portions of the upper crust (*Rudnick and Gao*, 2014). Their global reference model therefore contained homogeneous HPE concentrations within the upper crust but heterogeneous and spatially variable concentrations within the middle and lower crust, a first for geoneutrino studies.

The surface heat flux on continents is primarily a result of heat production within the crust, with subordinate contributions from the mantle (*Jaupart and Mareschal*, 2015). *Davies* (2013) reported the surface heat flux on a 2×2 degree grid. When available, they calculated average heat flux of each cell directly from bore-hole measurements from a global compilation. In areas with few or no measurements, they extrapolated the surface heat flux from regions having similar geologic evolutionary histories.

4.2 Calculating Surface Heat flux

To further our understanding of the global surface heat flux and the impact from the continental crust, we created a global reference Earth model based on the methods of *Huang et al.* (2013) using an updated 1×1 degree geophysical model (CRUST1.0; *Laske et al.* (2013)). This combined geophysical and geochemical model contains information on density, HPE abundance, and layer thickness for a sedimentary layer and the upper, middle, and lower crust. This global reference model includes input uncertainties in p-wave velocity (3%), layer thickness (10%), and HPE abundances (variable uncertainty) (*Huang et al.*, 2013). Calculated abundances in

the middle and lower crust yield HPE concentrations between that of *Huang et al.* (2013) (low) and *Rudnick and Gao* (2014) (high) for the middle and lower crust, with the upper crust abundances from *Rudnick and Gao* (2014).

The heat production was calculated in each 1×1 degree voxel (3D pixel) using decay energies from *Dye* (2012), the abundance of HPE's, and the mass of the voxel. The heat production within each voxel was combined vertically and divided by the 1×1 degree surface area to calculate the expected heat flux from radioactive decay in the continental crust by assuming steady state 1-D heat conduction in the upward direction (Equation 4.1). Heat flux out the top of a layer is calculated as:

$$Q = \sum \frac{H_k}{area} = \sum \frac{a_i A_i V_k \rho_k}{area} \tag{4.1}$$

where Q is heat flux (mW/m^2), H is heat production within each layer voxel (mW), a is the abundance of HPE (kg/kg), A is heat production per mass of element (mW/kg of element), V is the volume of each layer voxel (m^3), ρ is the density of each layer voxel (kg/m^3), *area* is the top surface area of each 1×1 degree cell (m^2), subscript i refers to U, Th, or K, and subscript k refers to the layer (sediment, upper, middle, or lower crust). The surface heat flux is a combination of the flux from the continental crust and that which crosses the crust-mantle boundary (Moho) from the mantle. Moho heat flux is a result of any heat production or latent heat within the mantle and core below each 1×1 degree cell. Studies have estimated the Moho heat flux to be between 12 and 35 mW/m^2 by fitting crustal geotherms to pressure-temperature arrays derived from lower crustal xenoliths or by

fitting geotherms to geophysical parameters (e.g. seismic wave speed, gravity, borehole temperature, and/or surface heat flux)(*Jaupart and Mareschal*, 2015). Values calculated for the Archean Superior Province, a region heavily studied for mantle heat flux, are predicted to be 15 ± 3 mW/m^2 (*Jaupart and Mareschal*, 2015).

4.3 Comparison of Model and Observations

There is a misfit between modeled heat flux from our global reference model (with assumed Moho heat flux of 15 mW/m^2) and that reported by *Davies* (2013) on a 2×2 grid (Figure 4.1). A negative difference shows that our modeled surface heat flux is greater than that observed. This misfit could be caused by the assumption of homogeneous concentrations of HPE within the upper crust, relative to the heterogeneous abundances in the middle and lower crust (*Huang et al.*, 2013), incorrect assumption of Moho heat flux, or a combination of both. Because there exist a significant amount of negative differences in figure 4.1 when using a Q_{Moho} near the minimum realistic value (i.e. 15 mW/m^2) we hypothesized that the misfit is caused by homogeneous upper crust abundances, as a larger Moho flux would drive upper crustal abundances even more negative. The simplifying assumption of a homogeneous upper crust is especially problematic as this layer is expected to produce ∼1/2 of the heat production of the entire crust due to enrichment in HPE abundance (*Huang et al.*, 2013). Furthermore, this assumption results in high heat production where the crust is thickest — such as in the Himilayas — which is not supported by the measured heat flux (Figure 4.1). To overcome the assumption of

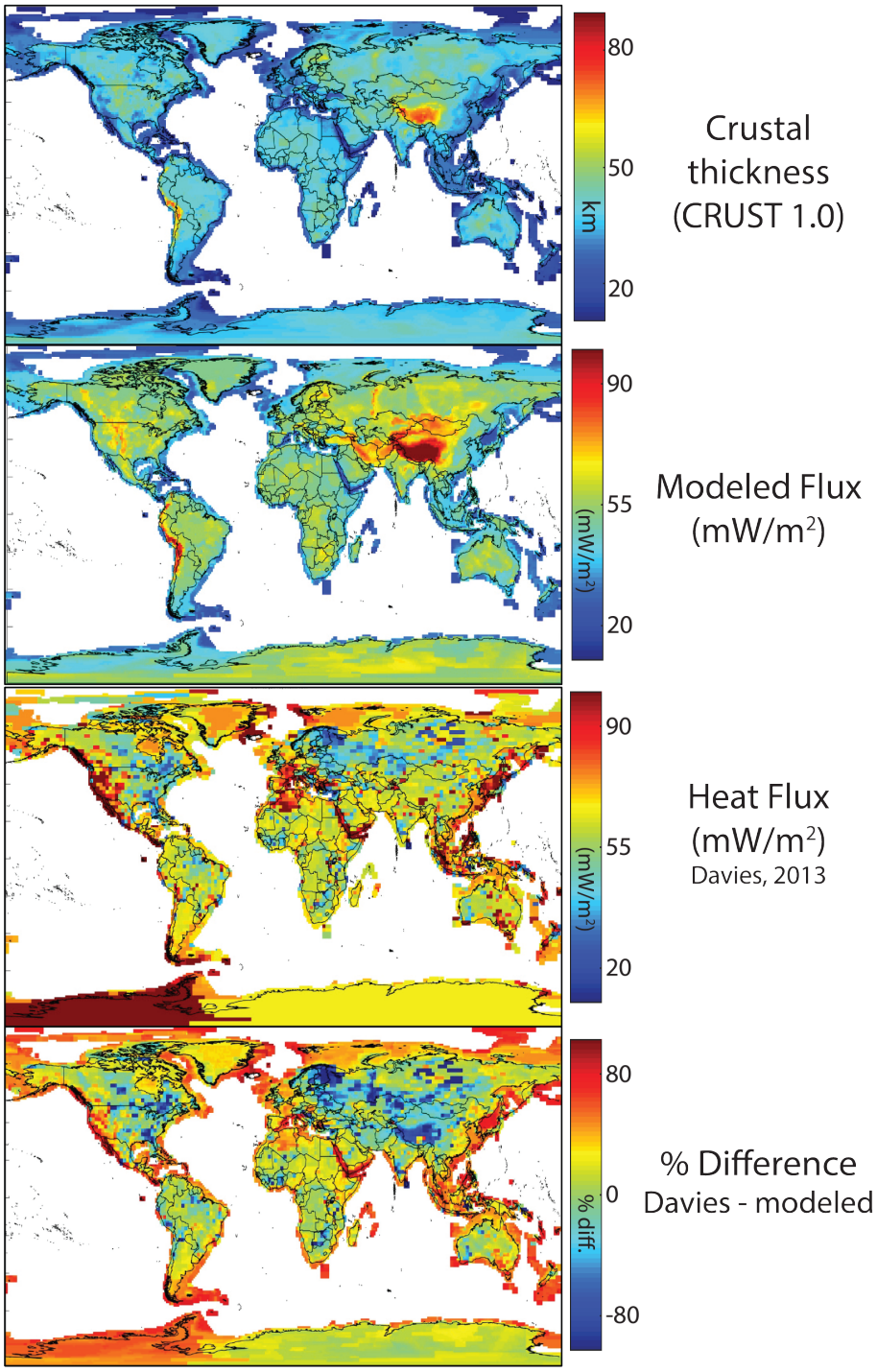

Figure 4.1: CRUST1.0 crustal thickness (km), modeled surface heat flux (mW/m^2) with $Q_{Moho} = 15$ mW/m^2, *Davies* (2013) surface heat flux (mW/m^2), and % difference between *Davies* (2013) and modeled heat flux.

homogeneity we calculated the expected heat flux from the upper crust to fit the observed. Following equation 4.2:

$$Q_{UC} = Q_{Surface} - Q_{MC+LC} - Q_{Moho} \tag{4.2}$$

where Q_{UC} is the upper crust heat flux, $Q_{Surface}$ is the observed heat flux, Q_{MC+LC} is the calculated heat flux from the middle and lower crust voxels, and Q_{Moho} is the heat flux across the Moho. We assumed Th/U and K/U of 4.25 and 12,300, respectively, based on analysis of glacial diamictites, which are thought to provide a comprehensive sampling of the crust (*Gaschnig et al.*, 2016). By combining calculated Q_{UC} and known Th/U and K/U ratios of the upper continental crust we calculated the abundance of HPE within the upper crust. We applied a conservative 25% uncertainty to the surface heat flux measurements from *Davies* (2013).

Hydrothermal systems effects heat flux and produce abnormal heat patterns in actively or recently deforming regions. Therefore, interpretation of our model output was limited to stable crust, defined simply as Proterozoic and Archean age crust following the crust type scheme of CRUST1.0. Coastal regions should be ignored as there is a discrepancy in the definition of oceanic crust between *Davies* (2013) and CRUST1.0, where *Davies* (2013) applied a half-space cooling model to oceanic crust which is not applicable to continental crust. This results in unreasonably high U abundances (>6 ppm) in coastal areas. We find that for stable regions with assumed low Moho heat flux (15 mW/m^2)(Figure 4.2 left column), the model overestimates average upper crust HPE abundance relative to similar models (e.g.

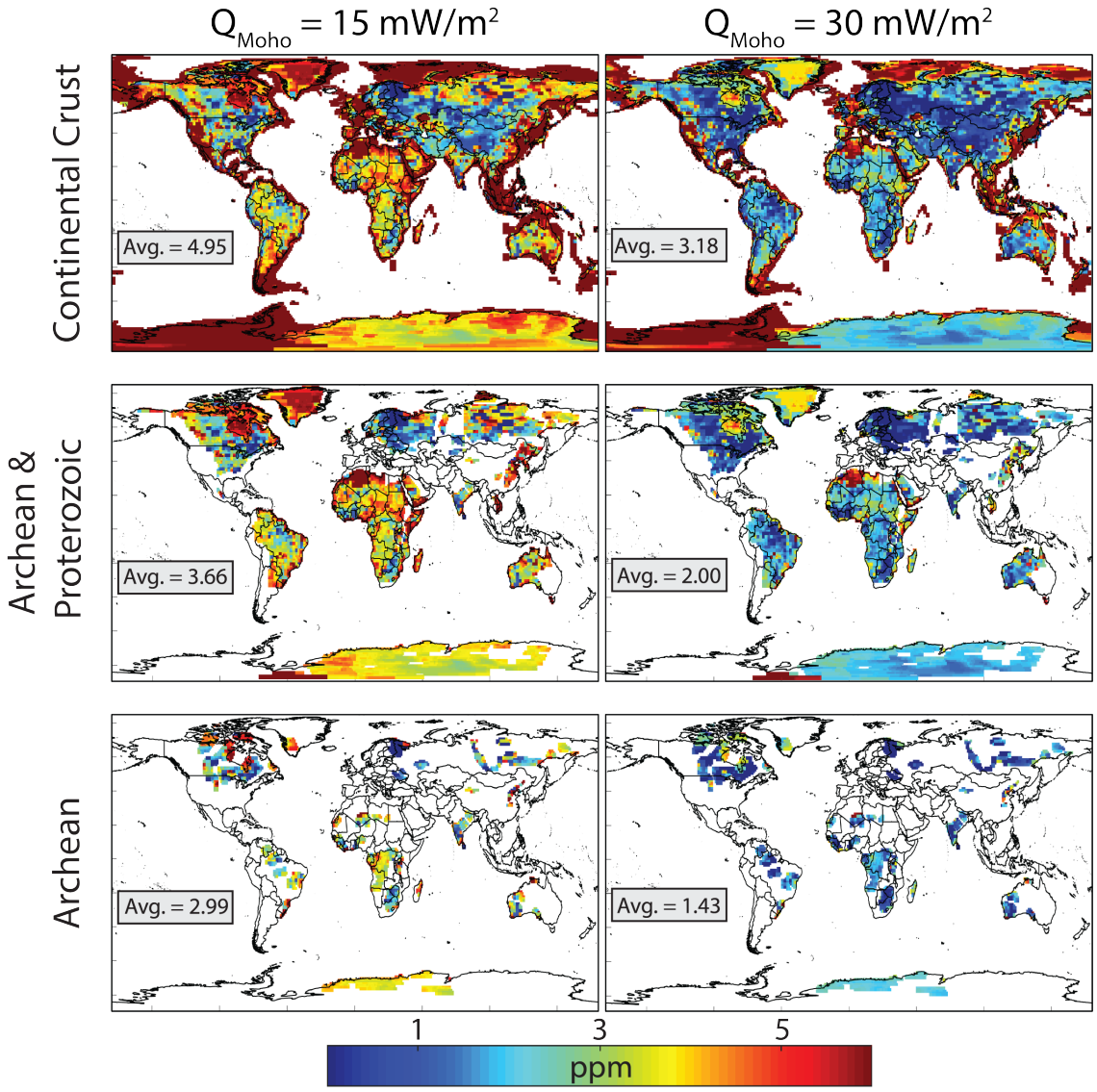

Figure 4.2: Calculated U concentration (part per million (ppm)) with Moho heat flux of 15 mW/m^2 (left panels) and 30 mW/m^2 (right panels), for the entire continental crust (top), only stable crust (Archean + Proterozoic)(middle), and Archean crust (bottom). Cells with abundances equal to or greater than six ppm U are the same color (deep red). Cells are defined on 1x1 degree basis, although patterns will be visible at 2×2 degree due to grid definition from *Davies* (2013). Average uranium concentrations reported in boxes to the west of South America represent mass weighted average uranium abundance (ppm) within the modelled regions.

Rudnick and Gao (2014)). For Archean crust, often observed to have low surface heat flux (*Nyblade and Pollack*, 1993; *Mareschal et al.*, 2017), HPE estimates when Moho heat flux is assumed low are consistent with previous estimates (Figure 4.2). High Moho heat flux (30 mW/m^2) yields low abundance estimates in both stable and Archean regions due to the tradeoff between upper crust HPE abundance and Moho heat flux (Figure 4.2 right column). For Moho heat flux values of either 15 or 30 mW/m^2, there is significant concentration heterogeneity, with areas of both very high and very low HPE concentration within Archean and Proterozoic crust. These results are inconsistent with the conclusion of *Gaschnig et al.* (2016), who found no significant difference between Archean and post-Archean crust. Similarly, the magnitude of lateral heat production heterogeneity is inconsistent with regional studies (*Jaupart and Mareschal*, 2014). Therefore the heterogeneity observed in Figure 4.2 is not expected, and this work highlights the necessity to better understand the relationship between surface and Moho heat flux, and abundances of HPE within the crust.

4.4 Constraining Moho Heat Flux

In the previous section heat production and HPE abundances in the upper crust were constrained by assuming a constant laterally homogenous Moho heat flux and middle and lower crust heat production. This section approaches crustal HPE abundances from a different direction by instead comparing a calculatd expected Moho heat flux to surface heat flux. The past decade has seen advance-

ments in the mapping of global seismic shear-wave velocity (Vs) variations (*French et al.*, 2013). Variations in Vs are more sensitive to temperature variation than Vp (compressional velocity)(*Cammarano et al.*, 2003). *Cammarano and Guerri* (2017) calculated the temperatures within the lithosphere from comparison of a global Vs model and a temperature-composition database created using the thermodynamic modeling package Perple_X (*Connolly*, 2005). They assumed a pyrolite composition, allowing calculation of the temperature necessary to cause the observed Vs in pyrolite. Temperatures were calculated at 60, 100, 140, and 180 km depth. Uncertainty was reported for these temperatures, average of $\pm$ 100 K, and is primarily a result of uncertainties associated with properties of mineral phases and less to do with the assumed mineral composition of the lithospheric mantle.

Cammarano and Guerri (2017) assumed no radiogenic heat production in the lithosphere, assumed thermal conductivities for the crust and lithospheric mantle, and using temperatures calculated at 180 km depth they derived estimated mantle heat fluxes ($\sim$ comparable to Moho heat flux) of 16-20 mW/m^2 in stable cratons, consistent with previous predictions for Moho heat flux under stable crust *Jaupart and Mareschal* (2015). The assumption of no heat production in the lithosphere means that any heat flux must be from the temperature at 180km depth. Finally, they calculated the crustal heat production in 2x2 degree cells by comparison of their calculated Moho heat flux and surface heat flux from *Davies* (2013). Their method is similar to equation 4.2 except they did not differentiate between crustal layers.

Temperatures from *Cammarano and Guerri* (2017) were used in conjunction

with the geophysical model LITHO1.0 (*Pasyanos et al.*, 2014) to calculate crustal heat production. LITHO1.0 is similar to CRUST1.0 but defines lithosphere asthenosphere boundary (LAB) depths. We adopt Vs derived lithospheric mantle temperatures from *Cammarano and Guerri* (2017) closest to the LAB as possible but at least 10km above the boundary in order to avoid any seismic noise created by the LAB boundary. Locations for which *Cammarano and Guerri* (2017) did not calculate data within the lithosphere as defined by LITHO1.0 were excluded (i.e. LAB depth < 60 km). Assuming a lithospheric mantle heat production from *McDonough* (1990), no heat production in the crust, a lithospheric mantle thermal conductivity (*Pasquale et al.*, 2015), and a crustal thermal conductivity (*Miao et al.*, 2014), we calculated a Q_{Moho} of 16 ± 4 mW/m^2. We assumed uncertainty on surface heat flux from *Davies* (2013) of 25%, and uncertainty on the thermal conductivity's of 15% to accommodate different lithologies in the crust (*Chapman*, 1986). Our calculated Moho heat fluxes are consistent with calculations from *Cammarano and Guerri* (2017) and *Jaupart and Mareschal* (2015).

The bulk heat production of the continental crust was calculated using three separate methods: 1) summation of all continental crust cells, 2) extrapolation of the heat production from Archean + Proterozoic crust, and 3) extrapolation using only Archean crust. Extrapolation involved characterizing the probability density function of heat production in stable or Archean regions, then applying that distribution to the bulk crust. Heat production in the continental crust is reported as μW/m^3 (Table 4.1) and terra-watt (TW) (Table 4.2) along with the estimates from *Huang et al.* (2013) and *Cammarano and Guerri* (2017).

	All CC (μW/m^3)	Archean + Proterozoic	Archean
This study[a]	1.05 ± 60%	0.95 ± 40%	0.91 ± 50%
Huang et al. (2013)[b]	0.97 ± 20%		
Cammarano and Guerri (2017)	1.2		

Table 4.1: Calculated bulk continental crustal heat production (in μW/m^3) from this study and others. Values from this study were calculated for the entire continental crust, Archean + Proterozoic crust, and only Archean crust.
[a]: Mass weighted values.
[b]: Calculated using mass of LITHO1.0 and *Huang et al.* (2013) values.

	Continental Crustal Heat Production (TW)
This Study[a]	6.95 ± 50%
Huang et al. (2013)[b]	7.5 ± 15%
Cammarano and Guerri (2017)[c]	9.3

Table 4.2: Bulk continental crust heat production (in TW).
[a]: Assumes heat production per volume μW/m^3 from Archean crust.
[b]: Calculated using mass of LITHO1.0 and *Huang et al.* (2013) values.
[c]: Calculated using mass of LITHO1.0 and *Cammarano and Guerri* (2017) values.

4.5 Discussion

Global models for the heat production in the continental crust predict high surface heat flux in regions with thick crust, and low surface heat flux in regions with thin crust. Consequently, modeled surface heat flux misfits with observed surface heat flux. This misfit is likely due to assumptions related to the upper crust which produces ~60% of the heat production of the continental crust. Our modeled heat flux in Archean regions often over predicts observed heat flux values by upwards of 100%. Inversion of the surface heat flux for upper crust HPE abundances yields anomalously high abundances with wide spatial variability. Constraining the

modeling to stable Archean + Proterozoic or only Archean crust still yields high abundances with large spatial variability. This variability conflicts with observed similarity between the heat producing element abundances of Archean and Proterozoic rocks, with no obvious spatial heterogeneity on scales observed in our modeling (*Gaschnig et al.*, 2016).

Bulk-continental crust heat production is lower than that calculated by *Cammarano and Guerri* (2017), especially when extrapolating average values from Archean crust to the bulk-continental crust (Table 4.1). Depths of temperatures in this study chosen at depths close to the LAB, while *Cammarano and Guerri* (2017) used temperatures from the same depth regardless if that depth was actually within the lithosphere. It is unclear why the central value of the bulk-heat production of the continental crust from *Cammarano and Guerri* (2017) is ∼20% larger than this study. Bulk-heat productions from this study more closely resemble those calculated from *Huang et al.* (2013), although they are in agreement with *Huang et al.* (2013) and *Cammarano and Guerri* (2017) when including uncertainty. Uncertainty from this study is much larger than these previous studies as uncertainty on thermal conductivities (15%) and surface heat flux (25%) were included. The abundance of HPE within the upper crust using Moho heat fluxes calculated from the *Cammarano and Guerri* (2017) data was not calculated, although the result should be similar to the result in section 4.3 because the average calculated Q_{Moho} is similar to what we assumed in that calculation.

4.6 Future Prospects

A more detailed analysis of the misfit between models of crustal heat production and surface heat flux is needed. For example, a spatial analysis of continental crust cells which do not agree with observed surface heat flux within 1σ uncertainty could be useful in targeting regions for modeling improvement. Furthermore, the proportion of cells which misfit surface heat flux would provide a very basic test of the accuracy of the global model assuming, although interpretation of this proportion would be dependent on the assumptions of a Q_{Moho} and that the surface heat flux is only impacted by mantle heat flux and internal heat production.

The calculations detailed in this study have focused on changing the abundance of HPE within the upper or bulk crust. Alternatively, the HPE abundances could be held constant and the thickness of the upper crust could vary to fit surface heat flux. Moho depths (= crustal thickness) represent seismic discontinuities while the depths to upper, middle, and lower crust boundaries do not. In fact, geophysical models such as CRUST2.0, CRUST1.0, and LITHO1.0 attribute $\sim$1/3 of the crustal thickness as the upper crust. Figure 4.1 shows regions of thick crust do not show anomalously high surface heat flux — unlike the modeled flux.

Future studies involving the global surface heat flux should explore the thickness of the upper crust as a proxy for observed surface heat flux variation. This direction of modeling is similar to the classic comparison of average heat production vs average heat flux for cratonic scale regions, where the slope of the best fit line is equivalent to the thickness of a high-heat producing layer — often assumed to be

equivalent to the upper crust (*Jaupart and Mareschal*, 2014). Normally, these calculations are performed for a specific craton. The suggestion here would constrain the average heat production to that of *Rudnick and Gao* (2014) globally rather than use sparse region specific values and calculate the thickness of upper crust. Modified upper crust thicknesses would significantly effect the prediction of the geoneutrino signals due to the reliance of upper crust thickness on calculated signals.

Chapter 5: Reference Models for Earth's Geoneutrino Flux

[1] S.A. Wipperfurth wrote all of the material in this chapter with input on model creation and analysis from O. Šrámek and W.F. McDonough.

[2] This chapter is a paper to be submitted as:

Scott A. Wipperfurth, Ondřej Šrámek, and William F. McDonough. Reference Models for Earth's Geoneutrino Flux, 2019.

5.1 Abstract

Debate continues on the amount and distribution of radioactive heat producing elements (i.e., U, Th, and K) in the Earth, with estimates for mantle heat production varying by a factor of 30. Constraints on the bulk-silicate Earth's (BSE) radiogenic power also places constraints on the BSE composition. Geoneutrino detection is a direct measure of the Earth's decay rate of Th and U. The geoneutrino signal has contributions from the local (∼40%) and global (∼35%) continental lithosphere and the underlying inaccessible mantle (∼25%). Geophysical models are combined with geochemical datasets to predict the geoneutrino signal at current and future geoneutrino detectors. We propagated uncertainties, both chemical and physical, through Monte Carlo methods. Estimated total signal uncertainties

are on the order of ∼20%, proportionally with geophysical and geochemical inputs contributing ∼30% and ∼70%, respectively. We find that estimated signals, calculated using CRUST2.0, CRUST1.0, and LITHO1.0, are within physical uncertainty of each other, suggesting that the choice of underlying geophysical model will not change results significantly, but will shift the central value up to ∼15%, depending on the crustal model and detector location. Similarly, we see no significant difference between layer abundances and bulk-crustal heat production when using these geophysical models. The bulk crustal heat production is calculated as $\sim 7 \pm 2$ (1σ) terra-watts, which includes an increase of 1 TW in uncertainty relative to previous studies.

5.2 Introduction

There are two major sources of Earth's heat, estimated at 47 ± 2 terra-watts (TW) (*Davies and Davies*, 2010): primordial heat remaining from planetary assembly and core formation, and radiogenic heat produced during radioactive decay of the heat-producing elements (HPEs) uranium (U), thorium (Th), and potassium (K). Estimates of the amount of radioactive heat produced in the bulk-silicate Earth (BSE) fall into three categories: low, medium, and high heat production. These models include: [LOW] early Earth collisonal erosion of an HPE enriched crust (*O'Neill and Palme*, 2008) or assuming the BSE = enstatite chondrites (*Javoy*, 1999; *Javoy et al.*, 2010); [MEDIUM] combining observation from chondrites and mantle melting trends of terrestrial samples (*McDonough and Sun*, 1995; *Palme*

and O'Neill, 2014); and [HIGH] simple parameterized mantle convection models (*Turcotte and Schubert*, 2014). These models differ in BSE heat production by a factor of three (11 to 33 TW). Removal of the crustal signature and considering the 1-sigma bounds leads to a factor of thirty in estimates of the radiogenic power of the modern mantle (*Šrámek et al.*, 2013). Figure 5.1 shows the relative radiogenic heat proportion of the crust and mantle for each BSE compositional model as well as the expected geoneutrino signal at the SNO+ detector in Canada ($\sim$ average crust). The geoneutrino prediction in Figure 5.1 uses the model described in this paper. Characterization of the amount and distribution of the BSE radiogenic heat source would improve understanding of the power available for mantle convection, plate tectonics, and the geodynamo. Furthermore, constraining the amount of U and Th also constrains the relative amount of other refractory elements in the Earth (*Bellini et al.*, 2013; *McDonough and Sun*, 1995).

Over the last decade particle physicists have detected and analyzed the Earth's geo-neutrino flux, electron anti-neutrinos of terrestrial origin produced during $\beta-$ decay ($n \rightarrow p + e^{-} + \bar{\nu_e}$). The intensity of this flux is proportional to the concentration and distribution of U, Th, and K inside the Earth. However, these elusive particles are exceedingly difficult to detect as they are charge-less leptons with negligible interaction cross sections ($\approx 10^{-43} cm^2$)(*Dye*, 2012). The geo-neutrino flux is measured in large, underground, liquid scintillation detectors using the inverse beta decay (IBD) process ($\bar{\nu_e} + p \rightarrow e^{+} + n$). The IBD reaction creates two flashes of light, separated in time ($\sim$200 μ) and space ($\sim$30 cm), which allows for constraint of

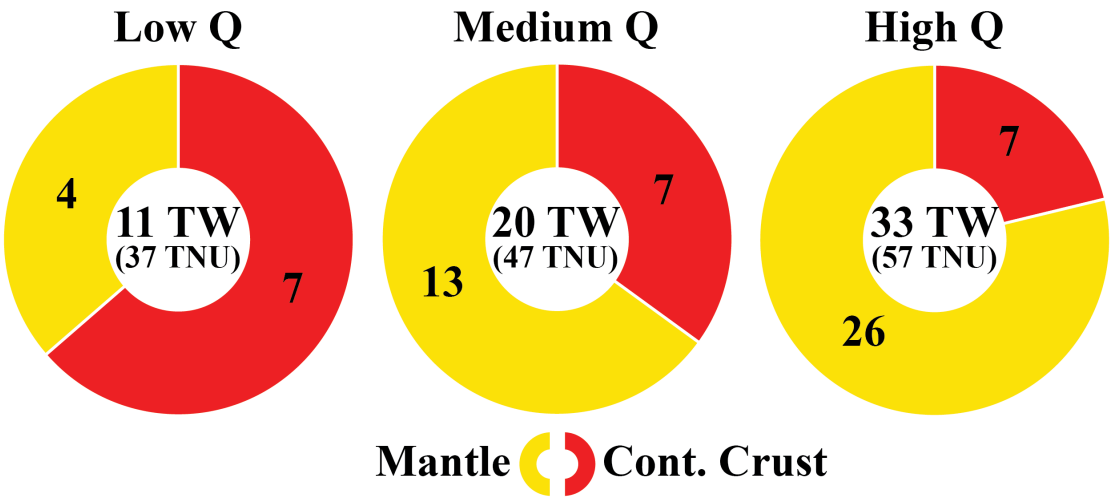

Figure 5.1: Relative proportion of heat production in the modern mantle (yellow) and average continental crust (red) for three groups of BSE models: Low Q (*Javoy*, 1999; *Javoy et al.*, 2010; *O'Neill and Palme*, 2008), medium Q (*McDonough and Sun*, 1995), and high Q models (*Turcotte and Schubert*, 2014). The total radiogenic heat production predicted by each model is shown in the center of each pie-diagram with the predicted signal at the SNO+ detector (Canada: ~ average crust) below in parentheses. Signals are reported in terrestrial neutrino unit (TNU), where one TNU = one detection in one year exposure of a 1 kton detector with 100% detection efficiency.

the geo-neutrino energy and direction (*Bellini et al.*, 2013). Geo-neutrino detectors are presently counting at the Kamioka Liquid-Scintillator Anti-Neutrino Detector (KamLAND; 1 kt; Japan) and the Borexino Detector (0.3 kt; Gran Sasso, Italy), with the SNO+ Detector (1 kt; Sudbury, Canada) scheduled to begin measurements in 2019, the JUNO detector to complete construction by 2021 (20 kt; China)(*Adam et al.*, 2015), and the Jinping detector beginning construction soon (*Beacom et al.*, 2016).

To understand the geoneutrino flux and heat production from the inaccessible mantle, models of the distribution and amount of U, Th, and K in the accessible crust have been created. These models combine geochemical and geophysical information

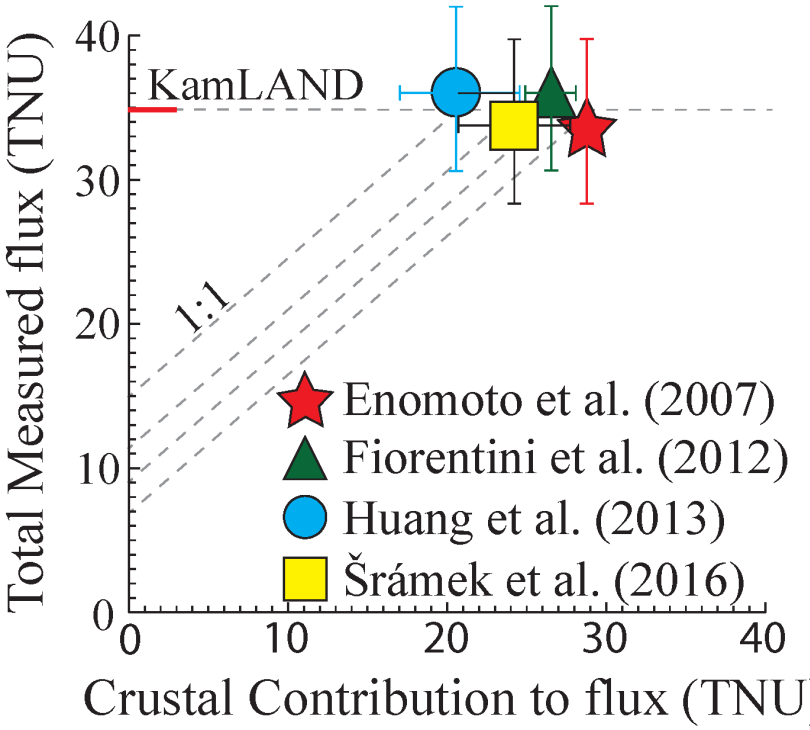

Figure 5.2: Model predictions of geoneutrino signal at KamLAND from *Enomoto et al.* (2007)(28.2 TNU), *Fiorentini et al.* (2012)(26.5 $\pm$1.52 TNU), *Huang et al.* (2013)(20.6$^{+4.0}_{-3.5}$ TNU), and *Šrámek et al.* (2016)(24.2 $\pm$3.5 TNU). Values share the same measured flux (y-axis) from *Watanabe* (2016) (34.9$^{+6.0}_{-5.4}$ TNU) but are offset for visibility. The y-intercept (from a slope 1 line) represents the signal from the mantle after removal of the crustal contribution.

to calculate a global crustal flux — with uncertainty — at each detector. Because the geoneutrino signal is dependent on distance from the detector ($1/r^2$ relationship), high-resolution regional models are often coupled with the global model to more accurately predict the flux and uncertainty. A meta-analysis of previously published estimates reveal discrepancies in the predicted flux. For example, estimated fluxes at KamLAND can vary by as much as 40%, with particular distinction between models produced respectively by the geoscience and physics communities (Figure 5.2). Differences between estimates is largely a function of global geophysical model chosen or the geochemical modeling methodology in the region surrounding the detector (e.g. including local geologic information).

The creation of a geoneutrino model for the crust, including [U,Th,K] abundances, heat production, and geoneutrino flux from each crustal layer is reported. The geochemical model we adopt is appended to three different geophysical models to test the dependence of the final signal on the chosen input model. Crustal masses, geochemical abundances, and geoneutrino fluxes at six detector locations is calculated and results compared for different geophysical inputs. Uncertainties are correlated and propagated using Monte Carlo methods.

5.3 Geophysical Model

The lithosphere is the outer rigid silicate shell of the Earth and is composed of the thick mafic lithospheric mantle and the relatively thinner more felsic crust. In the past few decades authors moved from characterizing the vertical profile of

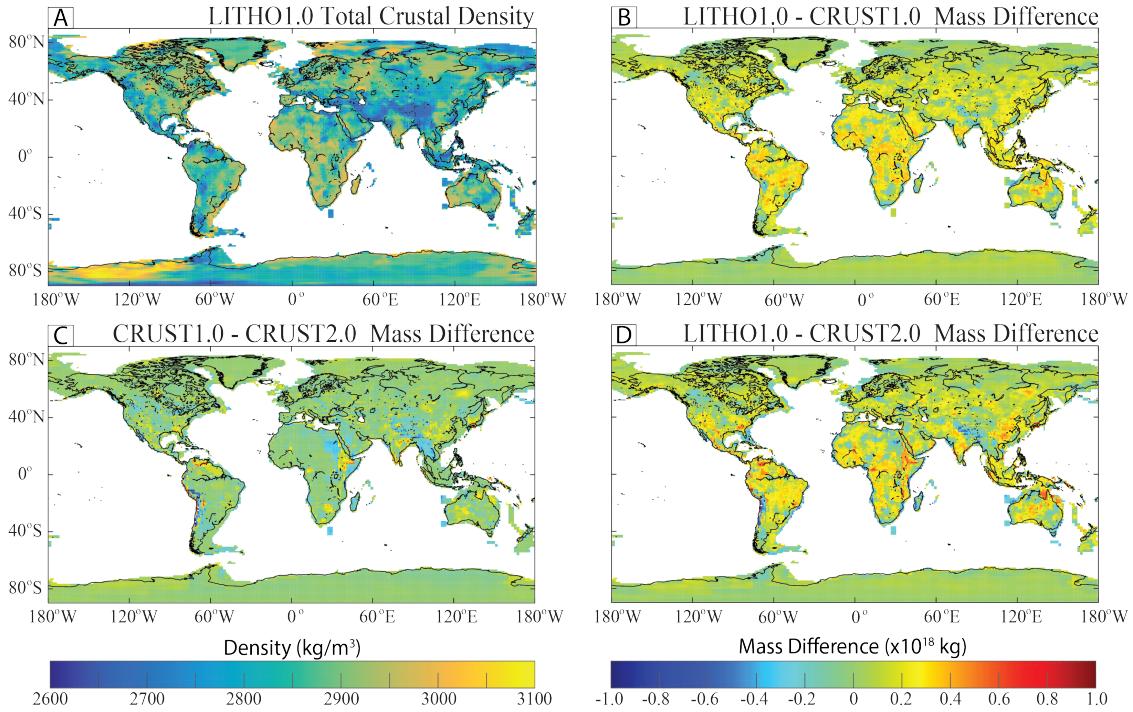

Figure 5.3: A) Density of LITHO1.0 model (left colorbar). B,C,D) Differences in crustal cell mass (1° × 1° resolution; right colorbar) between LITHO1.0 - CRUST1.0, CRUST1.0 - CRUST2.0, and LITHO1.0 and CRUST2.0. For reference, the average mass of a 1×1 degree crustal column is approximately equal to 10^{18} kg. Densities vary from 2600 to 3100 kg/m^3, with granite like densities (~2700 kg/m^2) appearing under the Himalayas. CRUST1.0-CRUST2.0 show the least variability in mass differences, while LITHO1.0 appears most variable compared to CRUST1.0 and CRUST2.0.

the crust as a single bulk layer to a combination of an upper crust and lower crust (e.g. *Hacker et al.* (2015)), an upper crust, middle crust, and lower crust (e.g. CRUST5.1 (*Mooney et al.*, 1998)), or as a continuously changing density structure (e.g. GEMMA1.0 (*Reguzzoni and Sampietro*, 2015) or *Szwillus et al.* (2019)). Furthermore, authors have begun to laterally characterize the crust as a assemblage of different groups with similar seismic structure, something that has previously been performed (e.g. *Pakiser and Robinson* (1966)) but rarely with regard to 3D models. Modern global physical models are constructed using global and local seismic studies, gravity surveys, or a combination of both. The primary purpose of geophysical

models has been the need for crustal corrections in mantle tomography (*Mooney et al.*, 1998).

CRUST5.1 provided a global model by providing seismic compressional (Vp) and shear wave (Vs) velocity averages for regions with similar crustal structure in order to extrapolate to regions where there was limited or no data (*Mooney et al.*, 1998). This model defined the crust as three layers (upper, middle, and lower) with a sediment layer on top. The subsequent family of geophysical models built on CRUST5.1 have a generational increase in input data, resulting in resolution changes from CRUST5.1 (5° × 5°) → CRUST2.0 (2° × 2°; *Bassin et al.* (2000)) → CRUST1.0 (1° × 1°; *Laske et al.* (2013)). Of note, CRUST2.0 and CRUST1.0 provide limited description of the model inputs or methodology aside from an AGU and EGU abstract, respectively. The most recent iteration of the "CRUST" family of models, LITHO1.0 (∼1° × 1°) (*Pasyanos et al.*, 2014), perturbed CRUST1.0 parameters (density, Vp, Vs, layer thickness) to fit a global surface wave dataset and for the first time included lithosphere-asthenosphere boundary (LAB) depths. LITHO1.0 reports Vp and Vs within the model with a continuous probability distribution, while CRUST2.0 and CRUST1.0 report a few discrete velocities within each layer. In comparison to other studies, LITHO1.0 shows a smaller misfit to high-resolution seismic studies compared to CRUST1.0 (*Olugboji et al.*, 2017). CRUST2.0, CRUST1.0, and LITHO1.0 are adopted as the physical basis in the model in order to test their effect on modeled outputs. Importantly, these models do not provide an estimate of uncertainty on model parameters. A comparison of the mass and thickness of layers within these models is shown in Table 5.1, while a comparison of crustal

geoneutrino fluxes from each model in Table 5.4. These geophysical models are not combined with the more recent gravity based GEMMA1.0 (as was done by *Huang et al.* (2013)) due to ambiguity regarding GEMMA1.0's dependence on the adopted density structure of the crust in their interpretation of the gravity signal. However, this also means that we do not have a measure of uncertainty on crustal thickness and must rely on estimates from previous studies (see Section 5.5).

Previous geoneutrino reference models were generally built upon the most recent model available. The first model post the start of geoneutrino measurements at KamLAND was that of *Mantovani et al.* (2004) built using the Preliminary Reference Earth Model (PREM)(*Dziewonski and Anderson*, 1981), followed by the models of *Enomoto et al.* (2007) and *Fiorentini et al.* (2012) for the geoneutrino flux at KamLAND and Borexino (built on the geophysical model CRUST2.0). *Huang et al.* (2013) is built on a combination of the physical models CRUST2.0, CUB2.0 (*Shapiro and Ritzwoller*, 2002), and GEMMA1.0 and has been used in the prediction of fluxes at SNO+ (*Huang et al.*, 2014; *Strati et al.*, 2017) and JUNO (*Strati et al.*, 2015), among others. Finally, *Šrámek et al.* (2016) calculated the flux at Jinping with a model built upon CRUST1.0 (*Laske et al.*, 2013).

LITHO1.0 is re-meshed from its initial tesselation (level 7; $\sim 1^\circ \times 1^\circ$) form in to a $1^\circ \times 1^\circ$ grid. Similarly, CRUST2.0 is re-meshed into a $1^\circ \times 1^\circ$ grid from its previous $2^\circ \times 2^\circ$ grid. Re-meshing was necessary to more easily compare modeled outputs. We split the LITHO1.0 and CRUST1.0 cells into continental and oceanic crust using the crust type characterization from CRUST1.0 and split CRUST2.0 by its own classification. For CRUST1.0 and CRUST2.0, oceanic crust is defined as

types A0, A1, B-, V1, Y3 or all A and B types, respectively; these correspond to crustal types labeled "oceanic". The final models contain sediment layers (two for CRUST2.0 and 3 for CRUST1.0 and LITHO1.0), upper, middle, and lower crust, and lithospheric mantle. Sedimentary thickness within the "CRUST" family are from a digitization of energy industry datasets (*Laske and Masters*, 1997).

Continental lithospheric mantle LAB depths are provided by LITHO1.0 or for CRUST2.0 and CRUST1.0 the LAB is set to 175 $\pm$ 75 km depth following *Huang et al.* (2013). Although this study focuses on the lithosphere and continental crust, we include a convecting mantle in order to provide an estimate of the total geoneutrino signal expected at a detector. For the convecting mantle we define the lower 750 km as the Enriched Mantle, which equals $\sim$19% of the mantle by mass (*Arevalo et al.*, 2013; *Dziewonski and Anderson*, 1981). PREM densities are adopted for the mantle (*Dziewonski and Anderson*, 1981). The mass of the BSE reported in table 5.1 is a combination of PREM for the mantle and either CRUST2.0, CRUST1.0, or LITHO1.0 for the lithosphere.

			CRUST2.0		CRUST1.0		LITHO1.0	
	Layer	$\sim \rho$ (g/cm^3)	d (km)	M (10^{21} kg)	d (km)	M (10^{21} kg)	d (km)	M (10^{21} kg)
CC	Sed	2.2	2.02 ±2.1	0.8 ±0.1	1.64 ±2.2	0.7 ±0.1	1.54 ±2.0	0.7 ±0.1
	UC	2.75	11.60 ±3.9	7.0 ±0.9	11.71 ±4.0	6.3 ±0.8	12.79 ±4.1	6.9 ±0.8
	MC	2.84	11.18 ±3.4	7.2 ±0.9	11.57 ±3.0	6.4 ±0.8	13.06 ±3.8	7.3 ±0.9
	LC	3.02	9.93 ±2.9	6.7 ±0.8	10.73 ±2.7	6.2 ±0.8	12.22 ±3.6	7.2 ±0.9
	Bulk CC	2.9	34.25 ±8.8	21.8 ±2.6	35.53 ±7.6	19.6 ±2.4	39.60 ±9.1	22.2 ±2.6
OC	Sed	1.9	1.86 ±0.2	0.3 ±0.0	1.90 ±0.1	0.4 ±0.1	1.90 ±0.1	0.4 ±0.1
	C	2.9	6.80 ±1.5	5.6 ±0.7	7.82 ±2.9	7.1 ±0.9	10.46 ±4.3	9.2 ±1.1
Mantle	LM	3.34	139.90 ±8.4	102.8 ±12.4	139.47 ±7.6	87.7 ±10.6	114.31 ±82.2	62.9 ±7.5
	DM	4.4	1966 ±0	3149.9 ±0.0	1966 ±0	3168.5 ±0.0	1987 ±84	3187.3 ±0.0
	EM	5.4	750	754.3 ±0.0	750	754.2 ±0.0	750	754.3 ±0.0
	BSE	4.45	2891	4034.7 ±15.7	2891	4037.6 ±13.8	2891	4036.3 ±11.2

Table 5.1: Physical properties of the layers of the Bulk-Silicate Earth (BSE) modeled using the geophysical models CRUST2.0, CRUST1.0, and LITHO1.0. The density reported is the mean between the three models with variation between model layers of <2.5% (except 10.5% variation for lower crust). BSE mass is from a combination of PREM (*Dziewonski and Anderson*, 1981) derived mass of the DM and EM combined with the lithosphere mass.

5.4 Geochemical Model

The Earth's crust is composed of mafic oceanic crust (avg. $\sim$ 7 km thick) and relatively more felsic continental crust (avg. $\sim$ 35 km thick). The geochemistry of the continental crust has been explored extensively over the past decades, particularly the accessible upper crust. Generally the crust is thought to decrease in SiO_2 with depth from 67% in the upper crust to 53% in the lower crust (*Rudnick and Gao*, 2014). These observations are from surface exposures of the upper, middle, and lower crust as well as xenolith samples. Furthermore, it has long been observed that increasing metamorphic grade cannot account for the increase in the observed Vp with depth, rather requiring a compositional increase in maficity (*Christensen and Mooney*, 1995). The relationship between seismic velocity and chemical composition has been observed empirically, due to the chemical effect on the shear and bulk modulus of which Vp relies (*Pakiser and Robinson*, 1966; *Christensen*, 1965; *Christensen and Mooney*, 1995). However, observed Vp of different lithologies are non-unique, requiring further assumption to have any meaningful result when inverting Vp for composition. The methodology of *Huang et al.* (2013) is adopted, which assumes the continental middle crust is composed of amphibolite and the continental lower crust of granulite metamorphic rocks. These assumptions are based on surface exposed crustal crossections and xenolith data (*Rudnick and Gao*, 2014). *Huang et al.* (2013) correlated Vp and SiO_2 and SiO_2 and [U, Th, K] of amphibolite and granulite by a linear relationship between mafic and felsic endmembers. This correlation is characterized by a simple mass-balance defined by the following

equations:

$$V_{model} = V_f f + V_m m \tag{5.1}$$

$$1 = f + m \tag{5.2}$$

$$a_{output} = a_f f + a_m m \tag{5.3}$$

where V_f,V_m, a_f, and a_m are the Vp and abundance of the felsic and mafic endmembers of amphibolite (middle crust) and granulite (lower crust), V_{model} is the Vp provided by the geophysical model, and f and m are the mass proportions of felsic and mafic endmembers. The velocities of the amphibolite and granulite datasets are derived from laboratory measurements at room temperature and 600 MPa (*Huang et al.*, 2014). These measurements are temperature corrected (-4×10^{-4} km/s/°C) following a mid-range geotherm (q_s = 60 mW/m^2) (*Turcotte and Schubert*, 2014; *Pollack and Chapman*, 1977)) and pressure corrected (2×10^{-4} km/s/MPa) from pressures calculated from the parameters provided by the geophysical model (P = ρgh) (*Huang et al.*, 2013). Temperature and pressure corrections are from empirical studies (*Rudnick and Fountain*, 1995; *Christensen and Mooney*, 1995). In cases where the Vp from the geophysical model is larger than the mafic endmember or smaller than the felsic endmember, we set f to be 0 or 1, respectively. In LITHO1.0, this occurs in ∼11% (36% f=0 and 84% f=1, proportionally) of middle crustal and ∼42% (98% f=0 and 2% f=1, proportionally) of lower crustal continental tiles. Model Vp outside the range of endmembers also occurs in CRUST2.0

and CRUST1.0, with the middle (lower) crust having 11% (23%) and 0% (64%), respectively. This method is especially problematic for the lower crust, but for the purposes of this study the impact has a negligible effect on the geoneutrino signal as the lower crust is generally depleted in [U,Th,K] relative and is farther from the geoneutrino detectors than the upper or middle crust (see Section 5.6).

HPE abundance for the upper crust is not calculated from a Vp and composition correlation because near surface processes strongly effect observed Vp and because we cannot simplify the upper crust as a single metamorphic grade (as we do for the middle and lower crust). Without the simplifying assumption of a single metamorphic grade there are too many non-unique lithologies that could be present. Instead values calculated from a meta-analysis of previously published upper crust estimates is adopted (*Rudnick and Gao*, 2014), which equates to a central value (mean) and uncertainty on that value rather than a standard deviation. Although this uncertainty is not consistent with our overall adoption of 1-sigma uncertainties in this study the analysis of *Rudnick and Gao* (2014) currently provides the best estimate of upper crust composition.

Sediment compositions are from the GLOSSII model of subducted sediments, as these material would be the remnants of continental weathering and marine activity (*Plank*, 2014). This assumption is acceptable as the location of sedimentary basins in the geophysical model is generally along coastlines. The continental lithospheric mantle is characterized by a suite of xenoliths compiled by *Huang et al.* (2013). For the oceanic crust we adopt the bulk oceanic crust composition from *White and Klein* (2014). The lithospheric mantle below oceanic crust is assumed to

have the same composition as the upper mantle.

The BSE composition is calculated from the U abundance given by *McDonough and Sun* (1995), whereas Th and K are calculated from observed Th/U and K/U (*Wipperfurth et al.*, 2018; *Arevalo et al.*, 2009). Similarly, a conservative upper mantle (LAB to 750 km above CMB) U abundance based is assumed based on the compilation from *Arevalo et al.* (2013) and the Th and K abundance is calculated from observed Th/U and K/U values from mid-ocean ridge basalt samples (*Wipperfurth et al.*, 2018; *Arevalo et al.*, 2009). The abundances within the enriched mantle are the remainder from subtraction of the lithosphere and upper mantle from the BSE composition (Table 5.2). Iterations where the enriched mantle is more depleted than the depleted mantle, which occurs in ∼25% of iterations, are discarded. This avoids conflicts with observed OIB samples with enriched HPE abundances compared to MORB samples (*Arevalo et al.*, 2013).

5.5 Uncertainties and Correlation

The attribution of uncertainty is the most difficult and time consuming part of numerical modeling. When available, uncertainties directly reported by the data source are adopted. When not available, relative uncertainties in agreement with literature estimates are adopted and always correspond to 1σ except for abundances in the upper crust. [U,Th,K] abundances display log-normal distributions, a trait shared with other incompatible elements (*Ahrens*, 1954; *McDonough*, 1990; *Wipperfurth et al.*, 2018). Model outputs which depend on asymmetrical abundance

		CRUST2.0	CRUST1.0	LITHO1.0
Upper Crust [a]	U (μg/g)		2.7 $\pm$0.60	
	Th (μg/g)		10.5$\pm$1.0	
	K (wt%)		2.32$\pm$0.19	
	P (TW)	$4.2^{+0.9}_{-0.8}$	$3.8^{+0.8}_{-0.7}$	$4.1^{+0.9}_{-0.7}$
Middle Crust [b]	U	$0.82^{+0.87}_{-0.42}$	$0.94^{+0.95}_{-0.47}$	$0.84^{+0.87}_{-0.43}$
	Th	$3.64^{+6.27}_{-2.30}$	$4.62^{+7.11}_{-2.80}$	$3.88^{+6.03}_{-2.36}$
	K	$1.42^{+1.52}_{-0.73}$	$1.69^{+1.66}_{-0.84}$	$1.47^{+1.47}_{-0.74}$
	P	$1.4^{+1.8}_{-0.8}$	$1.5^{+1.7}_{-0.8}$	$1.5^{+1.7}_{-0.8}$
Lower Crust [c]	U	$0.15^{+0.22}_{-0.09}$	$0.19^{+0.27}_{-0.11}$	$0.17^{+0.24}_{-0.10}$
	Th	$0.81^{+1.94}_{-0.57}$	$1.14^{+2.89}_{-0.82}$	$0.95^{+2.27}_{-0.67}$
	K	$0.70^{+0.80}_{-0.37}$	$0.91^{+1.12}_{-0.50}$	$0.78^{+0.90}_{-0.42}$
	P	$0.4^{+0.6}_{-0.2}$	$0.5^{+0.8}_{-0.3}$	$0.5^{+0.7}_{-0.3}$
Bulk Continental Crust [d]	U	$1.31^{+0.35}_{-0.28}$	$1.35^{+0.36}_{-0.29}$	$1.29^{+0.35}_{-0.27}$
	Th	$5.81^{+1.96}_{-1.47}$	$6.25^{+2.26}_{-1.66}$	$5.77^{+1.99}_{-1.48}$
	K	$1.81^{+0.51}_{-0.39}$	$1.96^{+0.57}_{-0.44}$	$1.81^{+0.52}_{-0.40}$
	K/U	$11{,}500^{+1{,}800}_{-1{,}600}$	$12{,}100^{+2{,}000}_{-1{,}700}$	$11{,}800^{+2{,}000}_{+1{,}700}$
	Th/U	$4.4^{+0.7}_{-0.6}$	$4.6^{+0.8}_{-0.7}$	$4.5^{+0.8}_{-0.7}$
	P	$7.0^{+2.1}_{-1.6}$	$6.6^{+2.0}_{-1.6}$	$7.0^{+2.1}_{-1.6}$

Table 5.2: Calculated abundances, element ratios, and power for the upper crust, middle crust, lower crust, and bulk-continental crust. Upper crust abundances are same in all models, but power varies as mass of crust varies. Reported uncertainties are 1σ. Bulk continental crust values are weighted by mass of each layer and include the sediment contribution (see Supplementary Information for sediment values). K/U and Th/U are mass ratios.
a = Values from *Rudnick and Gao* (2014).
b = Calculated from Vp-(U,Th,K) correlation of amphibolites.
c = Calculated from Vp-(U,Th,K) correlation of granulites.
d = Mass-weighted values for bulk continental crust.

distributions are reported as geometric mean $\pm$ 1σ uncertainties. 5% uncertainty is ascribed to Vp, which is primarily based on the recent comparison of a high-

resolution surface wave model of the US with CRUST1.0 and LITHO1.0 (*Olugboji et al.*, 2017), although is in agreement with earlier estimates (*Mooney et al.*, 1998). Because density is derived from Vp in the "CRUST" family of models, 5% uncertainty is also applied to density. 12% uncertainty is ascribed to crustal thickness based on the comparison of CRUST2.0, CUB2.0 (*Shapiro and Ritzwoller*, 2002), and GEMMA1.0 by *Huang et al.* (2013).

The correlation of uncertainties is equally as important as absolute uncertainty attribution and largely dictates the relative magnitude of the uncertainty on the modeling output. For example, no correlation in thickness of layers, and thereby no correlation of the mass, results in negligible uncertainty on the estimated mass of the crust ($\ll$1%). This result is unrealistic as we do not know the crustal mass to such precision. Thickness is correlated across all layers; in this way the crust is modeled when it is most massive (all layers as thick as possible) and least massive (all layers as thin as possible). A partial uncertainty would be ideal but is impossible without in-depth knowledge of the correlation of input data used to construct the geophysical model (e.g. the foundational data of LITHO1.0 and their correlations). Vp and density are not correlated between the middle and lower crust as it is unclear how Vp and density would shift given a change in one of the layers. Abundances are correlated within each layer as there is a longstanding observation of a general correlation between [U,Th,K] due to their similar incompatibilities during mantle and crustal melting. This correlation also applies to the endmember abundances for amphibolite and granulite. However, abundances are not correlated between layers because the samples used to estimate the abundances of the upper, middle, and

lower crust are not the same samples and therefore variability within each dataset is independent of the others. There is, however, an inherent correlation between the middle and lower crust in our model because of the correlation of Vp within these layers from the geophysical model coupled with our geochemical methods. All correlations described above assume 100% correlation between parameters.

5.6 Numerical Model and Geoneutrino Flux

The geophysical and geochemical information are combined into a coherent model, with attributes assigned for each $1^\circ \times 1^\circ$ cell for each layer. A Monte Carlo simulation with 3×10^4 iterations is used to propagate uncertainty. In each iteration the input variable's probability density function is randomly sampled. This method allows for combination of normal and log-normal distributions. The code is written for parallel computing in MATLAB using either LITHO1.0, CRUST1.0, or CRUST2.0, taking ~8 hours on an 4 core (8 thread) Intel CPU for 3×10^4 iterations of the Monte Carlo. In this way we have provided an environment to use and test these different geophysical models within a self-consistent framework. The effect of the number of iterations on the final flux was tested by performing 10 repeated calculations with 20×10^4 iterations each, with relative variation in the central value and 1-sigma uncertainties of 0.1% and 0.5%, respectively.

For each voxel (3D pixel) within a layer, the mass was calculated from the the density and thicknesses provide by the geophysical model. Multiplication of the mass by HPE abundance yields the mass of HPE within each voxel. The heat

production within each voxel is calculated using updated decay and heat ouput parameters from *Ruedas* (2017). Finally, the geoneutrino flux can be calculated for U and Th.

5.6.1 Calculating Flux

We calculate the geoneutrino flux at detector locations defined by latitude, longitude, and depth below surface (see Table A2.1). The number of antineutrinos detected at a detector is defined by *Dye* (2012) as

$$\frac{dN(E_{\bar{\nu}_e})}{dE_{\bar{\nu}_e}} = \epsilon \frac{N_A \lambda}{\mu} \sigma_P(E_{\bar{\nu}_e}) \frac{dn(E_{\bar{\nu}_e})}{dE_{\bar{\nu}_e}} \int_{\oplus} P_{ee}(E_{\bar{\nu}_e}) dV \frac{a(\vec{r}\prime)\rho(\vec{r}\prime)}{4\pi|\vec{r} - \vec{r}\prime|^2} \tag{5.4}$$

where the units are as follows:

Symbol	Description	Units
$\frac{dN(E_{\bar{\nu}_e})}{dE_{\bar{\nu}_e}}$	$\#\bar{\nu}_e$ detected per energy	$\bar{\nu}_e$
ϵ	10^{32} proton $\times$ 3.154$\times 10^7$ s $\times$ 100%	proton$\times$s
N_A	Avagodro Constant	$\frac{atom}{mol}$
λ	Decay constant	$\frac{decay}{s \times atom}$
μ	Atomic mass in kg	$\frac{kg}{mol}$
σ_P	$\bar{\nu}_e$ Cross-section in m^2 (function of $E_{\bar{\nu}_e}$)	$\frac{m^2}{proton}$
$\frac{dn(E_{\bar{\nu}_e})}{dE_{\bar{\nu}_e}}$	$\#\bar{\nu}_e$ emitted per energy	$\frac{\bar{\nu}_e}{decay}$
P_{ee}	Oscillation probability (function of $E_{\bar{\nu}_e}$)	unit-less
$a(\vec{r}\prime)$	Abundance of radionuclide in cell	$\frac{kg}{kg}$
$\rho(\vec{r}\prime)$	Density of rock in cell	$\frac{kg}{m^3}$
$\vec{r} - \vec{r}\prime$	Distance from cell to detector	m

Table 5.3: Variables used in the calculation and propagation of the geoneutrino flux.

This equation accounts for the number of decays of each isotope, the emitted neutrino energy spectrum, the distance the isotope is from the detector, and the probability of a neutrino oscillation over that distance. Oscillation parameters (P_{ee} and σ_P) are calculated from the most recent values from *Capozzi et al.* (2017). The flux is calculated and propagated for every 75 KeV across the geoneutrino energy spectrum (∼1800 KeV - 3300 KeV) calculated by *Enomoto* (2006a). The output from equation 5.4 is in terrestrial neutrino unit (TNU), which is the number of neutrinos detected per 10^{32} protons (≈one kton liquid scintillator) per one year with 100% detector efficiency (see ϵ in Table 5.3). Adoption of TNU allows for simple comparison of signals between detectors of different sizes and efficiencies.

As the geoneutrino signal is dependent on the distance from the detector ($\vec{r}-\vec{r}\prime$)

it is necessary to increase the mesh resolution for cells near the detector, otherwise the flux would be calculated at the center of each $1^\circ \times 1^\circ$ voxel. The mesh resolution is increased until the final flux reaches stability. This results in cell sizes increasing from $\sim$ 100 m^3 next to the detector, 10 km^3 at 500 km distance, and the initial cell size after 1000 km. The re-meshing is a necessary step in the calculation of the geoneutrino signal but is computationally intensive, increasing computation time by 40%.

5.7 Results and Discussion

This study provides an updated reference model to *Huang et al.* (2013) for the abundance of heat producing elements in the lithosphere, their heat production, the geoneutrino flux at current and future detectors, and a comparison of these outputs from three commonly used geophysical models. The crustal abundances and geoneutrino flux are a result of the complex amalgamation of laterally and vertically variable seismic velocity, layer thickness, layer density, and [U,Th,K] abundance. These parameters change from cell to cell in a convoluted way, making analysis of the specific cause of differences in the geoneutrino flux and crustal abundances between geophysical models difficult. For these reasons the following section will attempt to convey some of the major differences when using different geophysical models rather. A broad overview of different lithospheric thickness models is provided by *Steinberger and Becker* (2016), which compliments this study.

The geoneutrino flux results at six detectors are shown in Table 5.4, which

includes flux from the bulk continental crust and total expected flux. A full breakdown of each flux is included in appendix A2. To illustrate the similarity between fluxes when using CRUST2.0, CRUST1.0, and LITHO1.0, the maximum difference in the central value as well as the Overlapping Coefficient (OVL), which measures the degree with which the distributions overlap (*Inman and Bradley Jr.*, 1989), is included. The results of this study show that the choice of global physical model has only a small effect on the predicted crustal geoneutrino signal (Table 5.4). Estimates for the crustal geoneutrino flux at KamLAND, SNO+, and Jinping show larger variation between predictions than the other models (15% maximum variation in the central value) although still within 1-sigma uncertainty. OVL values are always greater than 70% overlap, with average overlap greater than 90%. Considering only the central value or the OVL suggests more similarity between LITHO1.0 and CRUST1.0 compared to CRUST2.0. This is in contrast to the apparent similarity in regional masses between CRUST2.0 and CRUST1.0 observed in Figure 5.3.

		Geoneutrino Flux (TNU)				Overlapping Coefficient		
Detector		**CRUST2**	**CRUST1**	**LITHO1**	**| Δ |**	**L1,C1**	**L1,C2**	**C1,C2**
KamLAND	Bulk CC	$22.7^{+5.9}_{-4.7}$	$24.2^{+6.7}_{-5.2}$	$26.4^{+7.1}_{-5.6}$	15	85	74	89
	Total	$34.7^{+5.8}_{-5.0}$	$36.6^{+6.5}_{-5.5}$	$37.9^{+6.6}_{-5.6}$	9	92	78	87
Borexino		$30.5^{+8.1}_{-6.4}$	$29.9^{+8.0}_{-6.3}$	$30.5^{+7.7}_{-6.2}$	2	96	98	96
		$43.2^{+8.0}_{-6.7}$	$42.9^{+7.9}_{-6.6}$	$42.1^{+7.3}_{-6.2}$	1	95	94	98
SNO+		$37.3^{+10.2}_{-8.0}$	$32.9^{+9.6}_{-7.4}$	$33.8^{+9.6}_{-7.5}$	13	95	84	80
		$49.8^{+9.7}_{-8.1}$	$45.7^{+9.3}_{-7.7}$	$46.8^{+9.4}_{-7.8}$	8	95	86	82
JUNO		$28.1^{+7.5}_{-5.9}$	$28^{+7.7}_{-6.1}$	$29.2^{+8.0}_{-6.3}$	4	93	93	99
		$40.5^{+7.4}_{-6.3}$	$40.7^{+7.6}_{-6.4}$	$40.4^{+7.4}_{-6.3}$	1	98	99	99
Jinping		$42.5^{+11.5}_{-9.1}$	$47.2^{+12.7}_{-10.0}$	$48.5^{+13.1}_{-10.3}$	13	96	78	83
		$55^{+10.9}_{-9.1}$	$59.9^{+12.1}_{-10.1}$	$59.9^{+12.2}_{-10.1}$	9	100	81	81
Hawaii		$2.3^{+0.7}_{-0.5}$	$2.1^{+0.6}_{-0.5}$	$2.3^{+0.7}_{-0.5}$	6	90	93	83
		$12.9^{+2.8}_{-2.3}$	$12.9^{+2.8}_{-2.3}$	$12.8^{+2.7}_{-2.3}$	1	98	99	99

Table 5.4: Continental crust (top row) and total flux (bottom row) (in TNU) for each detector location from each geophysical model. The second column is the latitude and longitude of the detector, with latitude from -90 to 90 and longitude from -180 to 180 degrees. | Δ | reports the maximum difference between the largest and smallest flux central value estimated at each detector, with | Δ | = |(x-y)/((x+y)/2)| ×100. The overlapping coefficient refers to the degree of overlap of the two distributions listed at the head of each column (from 0 to 100% overlap), with L1 = LITHO1.0, C1 = CRUST1.0, and C2 = CRUST2.0.

Abundances in the all layers are comparable (within 1σ) to both *Rudnick and Gao* (2014) and *Huang et al.* (2013). Uncertainties reported in the middle and lower crust are larger than those reported by *Huang et al.* (2013). K/U and Th/U of the bulk crust are also in agreement at 1σ with previous estimates (*Huang et al.*, 2013; *Wipperfurth et al.*, 2018).

The bulk-continental crust heat production is negligibly different between the geophysical models (Table 5.2) and following a similarity of abundance is consistent with previous estimates (*Huang et al.*, 2014; *Rudnick and Gao*, 2014; *Mareschal and Jaupart*, 2013). Furthermore, an estimate of bulk continental heat production of $7.0^{+2.1}_{-1.6}$ TW (using LITHO1.0) encompasses average heat production in stable Precambrian (5.9 $\pm$0.6 TW) and Phanerozoic (8.3 $\pm$1.0 TW) crust estimated from heat flow studies (*Mareschal and Jaupart*, 2013). The similarity of continental crust heat production when using CRUST2.0 and LITHO1.0 is again in contrast with the crustal flux similarity of CRUST1.0 and LITHO1.0 or the crustal mass similarity of CRUST2.0 and CRUST1.0. The similarity in crustal heat production of CRUST2.0 and LITHO1.0 is a reflection of their similar bulk crustal mass compared to the lower mass from CRUST1.0 (Table 5.1).

Reported uncertainties are larger than *Huang et al.* (2013) primarily as a result of increased correlation of abundance and geophysical uncertainties. Increased correlation causes an inverse effect on uncertainty for the bulk crustal K/U and Th/U, resulting in less uncertainty than described by *Huang et al.* (2013). Some previous geoneutrino flux predictions did not include uncertainty on geophysical inputs, including crust thickness (e.g. *Šrámek et al.* (2016); *Fiorentini et al.* (2012); *Enomoto*

et al. (2007)), meaning these studies report smaller uncertainty on fluxes. Similar to flux, the uncertainty on continental crustal heat production is ~50% larger than that estimated by *Huang et al.* (2013)($6.8^{+1.4}_{-1.1}$ TW). In general, geophysical uncertainties (on thickness, density, and Vp) account for ~30% of the flux uncertainty, with the remaining proportion (~70%) from the geochemical inputs. When only considering the geophysical uncertainty, as the same geochemical method was applied to each geophysical model, the calculated crustal flux's are still negligibly different.

5.8 Suggested Modeling Improvements

The discernment of BSE compositional models (i.e. low, medium, or high Q) will negligibly be affected by which geophysical model is adopted, as the fluxes are too similar (see Figure 5.1 for comparison). Regardless, we suggest future studies adopt LITHO1.0 over CRUST2.0 or CRUST1.0. LITHO1.0 includes estimates of lithosphere-asthenosphere boundary (LAB) depths which are consistent with other estimates, while CRUST2.0 and CRUST1.0 do not include LAB depth (*Steinberger and Becker*, 2016). LITHO1.0 contains continuous distributions for Vp and density due to the perturbation of CRUST1.0 to fit surface wave data, while CRUST2.0 and CRUST1.0 provide a few discrete values. Finally, available information for the methodology and data incorporated into LITHO1.0 (*Pasyanos et al.*, 2014) is greater than for CRUST2.0 (AGU abstract; *Bassin et al.* (2000)) or CRUST1.0 (EGU abstract; *Laske et al.* (2013)). Recent modeling by *Szwillus et al.* (2019) is even more transparent in methodology and input data than LITHO1.0 and provides

uncertainty estimates, although the relatively recent publication time of *Szwillus et al.* (2019) has limited its use in this study.

Future studies with the goal to update LITHO1.0 should aim to better understand the density and seismic structure beneath the Himalayas and Andes regions. The 'CRUST' family of models predicts felsic-like densities in the entire crustal column in these regions (including the expected mafic lower crust)(Figure 5.3). This prediction is in conflict with some regional studies (e.g. *Monsalve et al.* (2008); *Bai et al.* (2013)) although agreement with other global studies (e.g. *Hacker et al.* (2015)) as and regional seismic models (*Gilligan and Priestley*, 2018; *Agius and Lebedev*, 2017). Additionally, LITHO1.0 perturbed CRUST1.0 parameters up to 5% to fit observed surface waves, which a comparison of CRUST1.0 and LITHO1.0 Vp in the Himilayas shows that this perturbation reached saturation (i.e. 5% change between LITHO1.0 and CRUST1.0). If the model was not limited to 5% change the output would be more mafic than current. Because of the saturation of the method used by *Pasyanos et al.* (2014), LITHO1.0 in its current state may not be in agreement with observed regional data and should be revisited. Similar phenomena are observed under the Andes Mountains in South America (e.g. *Lucassen et al.* (2001)). The Himilayas are particularly relevant for the geoneutrino prediction signal at Jinping and to a lesser extent, JUNO, while the Andes will be relevant to the future ANDES underground laboratory (*Bertou*, 2012).

The geochemical method of conversion of Vp to [U,Th,K] does not work well in the lower crust (and to some degree in the middle crust) as the model often surpasses the endmember condition. This is a problem due to simplifying assumptions (i.e.

assuming endmembers) indicating a need for a more sophisticated modeling space. A joint probability analysis of the available amphibolite or granulite samples with measured Vp could avoid this problem (see Appendix A2 for details). This analysis would not assume any specific relationship between Vp and SiO_2(unlike the linear relationship we assumed in this study) but instead would use the joint probability of Vp and SiO_2 from the dataset. Currently there are too few samples (∼100-150) with experimentally measured Vp to create a robust analysis. Incorporation of a thermodynamic modeling software (such as Perple_X (*Connolly*, 2005)) would allow for the calculation of seismic wavespeed for 500 samples, which would significantly increase the robustness of a joint probability analysis. Calculated Vp using Perple_X for samples used in *Huang et al.* (2013) by *Hacker et al.* (2015) closely resemble laboratory measurements, indicating the viability of thermodynamically calculated Vp.

The attribution of uncertainty on the concentration of heat producing elements in the upper crust is not consistent with uncertainty on other parameters, including abundances in other layers. Often cited studies on the upper crust composition report sigma-mean (*Rudnick and Gao*, 2014) or Median Absolute Deviation (MAD)(*Gaschnig et al.*, 2016), both of which report smaller error estimates than the standard deviation. Any regional or global geoneutrino modeling should adopt consistent error estimators, be it standard deviation or MAD, or justify the treatment of the upper crust separately from other portions of the crust. Upper crust U abundance used in this study is *Rudnick and Gao* (2014) 2.7 ± 0.6 $\mu g/g$ (sigma-mean), contrasting with that from *Gaschnig et al.* (2016) of 2.66 ± 0.87 $\mu g/g$. The

standard deviation of the glacial diamictite data (assumed to sample large portions of the upper crust) from *Gaschnig et al.* (2016) is 150% of the MAD. Because the upper crust is the dominant heat and geoneutrino emitter, consistent uncertainty estimates on abundances could significantly increase uncertainties on the predicted crustal geoneutrino flux. Moreover, log-normal fitting of the data from *Gaschnig et al.* (2016) provides a better fit to the data than a normal distribution and is consistent with the expected log-normal distribution of incompatible elements.

Underestimation of the upper crust uncertainty or problems associated with middle/lower crust abundance calculations have a mitigated effect on predicted fluxes if a high-resolution regional geoneutrino model is combined with the global model (e.g. (*Huang et al.*, 2014; *Strati et al.*, 2017; *Enomoto et al.*, 2007; *Coltorti et al.*, 2011)). Because of the distance dependence of the geoneutrino flux (see 5.4) the regional area provides ∼40% of the geoneutrino signal at a detector. High-resolution seismic and geochemical studies of the region largely negate the negative effects outlined in this study and provide the most robust estimate of the flux at any detector location. This is exemplified in the studies of *Huang et al.* (2014) and *Strati et al.* (2017), who calculated larger uncertainties on the geoneutrino flux at SNO+ when they included a regional model compared to only using a global model. Although the uncertainty is larger than that estimated from the global model, their estimate includes more local information and is therefore likely to be a more accurate estimate of uncertainty.

5.9 Acknowledgments

Support for this study was provided by the NSF EAPSI program Award #1713230 (to S.A.W), NSF grant EAR1650365 (to W.F.M.), and the Czech Science Foundation grant GAČR 17-01464S (to O.Š.). There are no financial or interest conflicts with this work. We would like to thank Fabio Mantovani, Bedřich Roskovec, and Steve Dye for insightful comments and discussion.

Chapter 6: Earth's chondritic Th/U: Negligible fractionation during accretion, core formation, and crust-mantle differentiation

[1] W.F. McDonough initiated the project with study direction from M. Guo and S.A. Wipperfurth. M. Guo prepared and analyzed the input data. S.A. Wipperfurth and O. Šrámek designed the Monte Carlo model with S.A. Wipperfurth coding and performing the modeling. Analysis of data was performed by all authors. W.F. McDonough took the lead in writing the manuscript with input from all the authors.

[2] This chapter has been published as:

Wipperfurth, S. A., M. Guo, O. Šrámek, and W. F. McDonough (2018), Earth's chondritic Th/U: Negligible fractionation during accretion, core formation, and crust–mantle differentiation, *Earth and Planetary Science Letters*, *498*, 196–202, doi:10.1016/j.epsl.2018.06.029

6.1 Abstract

Radioactive decay of potassium (K), thorium (Th), and uranium (U) power the Earth's engine, with variations in 232Th/238U recording planetary differentiation, atmospheric oxidation, and biologically mediated processes. We report several thousand $^{232}Th/^{238}U$ (κ) and time-integrated Pb isotopic (κ_{Pb}) values and assess their ratios for the Earth, core, and silicate Earth. Complementary bulk silicate Earth domains (i.e., continental crust $\kappa_{Pb}^{CC} = 3.95\ ^{+0.19}_{-0.13}$ and modern mantle $\kappa_{Pb}^{MM} = 3.87\ ^{+0.15}_{-0.07}$) tightly bracket the solar system initial $\kappa_{Pb}^{SS} = 3.890 \pm 0.015$. These findings reveal the bulk silicate Earth's κ_{Pb}^{BSE} is $3.90\ ^{+0.13}_{-0.08}$ (or Th/U = 3.77 for the mass ratio), which resolves a long-standing debate regarding the Earth's Th/U value. We performed a Monte Carlo simulation to calculate the κ_{Pb} of the BSE and bulk Earth for a range of U concentrations in the core (from 0 to 10 ng/g). Comparison of our results with κ_{Pb}^{SS} constrains the available U and Th budget in the core. Negligible Th/U fractionation accompanied accretion, core formation, and crust - mantle differentiation, and trivial amounts of these elements (<0.2 ng/g U) were added to the core and do not significantly power (~0.03 TW) the geodynamo.

6.2 Introduction

The Earth's engine is powered by an unknown proportion of primordial and radiogenic power (*Šrámek et al.*, 2013; *Jellinek and Jackson*, 2015). Hence, we lack a gauge informing us as to how much and what proportion of fuel from either source

remains in the Earth and what fraction is stored in the continental crust, mantle, and/or the core (*Wohlers and Wood*, 2015). This fuel powers volcanoes to erupt, the mantle to convect, tectonic plates to separate, and contributes to the generation of the protective magnetosphere that shields Earth's life from harmful cosmic rays.

Radioactive decay of K, Th, and U produces heat and contributes more than 99% of the non-primordial power to the Earth (*Arevalo et al.*, 2013; *Ruedas*, 2017). The planet's primordial power comes from the accretion energy derived from assembling a uniform Earth and the gravitational energy release accompanying core formation. Given the Earth's size and mass, the accretion energy is of the order 10^{32} joules (or an equivalent temperature increase of the planet of tens of thousands of degrees), whereas the energy released by core–mantle differentiation is an order of magnitude smaller (*Flasar and Birch*, 1973; *Šrámek et al.*, 2010).

Defining the amount and distribution of the radioactive elements inside the Earth will exclude competing models of the meteoritic building blocks of planet construction, which resulted in its unique composition (*Šrámek et al.*, 2013; *Javoy and Kaminski*, 2014; *Wohlers and Wood*, 2015; *Jellinek and Jackson*, 2015; *Wohlers and Wood*, 2017). It has been speculated that under certain conditions of planet formation a minor to significant fraction of these heat producing elements may have been sequestered into the Earth's core (*Wohlers and Wood*, 2015; *Chidester et al.*, 2017; *Blanchard et al.*, 2017). In addition, speculations abound on the existence of deep Earth reservoirs, which remain poorly sampled and mostly unaccounted for in the chemical descriptions of the Earth (*Rizo et al.*, 2016; *Jackson et al.*, 2017).

Here we present a global assessment of the relative abundance of Th and U

in the Earth and its distribution — specifically between the crust, mantle, and core — and examine the degree to which fractionation of these elements has deviated from the primordial Th/U value seen in primitive meteorites (i.e., troilites from iron meteorites and chondrites). Our findings place into perspective this ratio and its importance in constraining chemical and biological processes that have occurred in the past.

Importantly, Th and U are refractory elements, those that condensed from the nebula at high temperatures (>1350 K), and are assumed to be accreted in chondritic proportions, with limited variability (circa $\leqslant \pm 10\%$) in their ratio. Both Th and U decay to separate isotopes of lead (^{232}Th to ^{208}Pb and ^{238}U to ^{206}Pb) and thus one can evaluate the Earth's Th/U ratio using both the measured molar ^{232}Th/^{238}U values (κ) and their time-integrated Pb isotopic values (κ_{Pb}; see supplementary information for details)(*Tatsumoto et al.*, 1973; *Tatsumoto*, 1978; *Galer and O'Nions*, 1985). The κ_{Pb} ratio of the bulk silicate Earth's (BSE) reservoirs is derived by calculating the ^{208*}Pb/^{206*}Pb ratio after subtraction of the BSE initial ^{208}Pb/^{206}Pb value and time integrating the contributions from the two decay chains.

Recent estimates for the chondritic/solar system value of Th/U were reported from a Pb-Pb isotope array using troilites from iron meteorites (κ^{ss}_{Pb}= 3.890 $\pm$ 0.015 (*Blichert-Toft et al.*, 2010) and from seven dissolutions of the carbonaceous chondrite, Allende (Th/U$_{(mass\ ratio)}$ 3.77 $\pm$ 0.07 (*Pourmand and Dauphas*, 2010)). We recalculated the κ^{ss}_{Pb} value reported in *Blichert-Toft et al.* (2010) using their reported initial ^{208}Pb*/^{206}Pb* value of 0.9572 $\pm$ 0.0038 and the following inputs: age of the Earth (4.568 x 10^9 years), and the decay constants, λ_{238U} = 1.5514 x

10^{-10} ($t_{1/2}$ = 4.468 x 10^9 yr) and λ_{232Th} = 4.9511 x 10^{-10} ($t_{1/2}$ = 14.0 x 10^9 yr). Using these inputs and the ^{238}U natural molar isotopic fraction of 0.992742, we calculate a $Th/U_{(molar)} = 3.861 \pm 0.016$ and a $Th/U_{(mass)} = 3.764 \pm 0.016$ for this troilite dataset. Thus, the troilite and chondritic results are in full agreement and establish Earth's $Th/U_{(mass)}$ value, assuming chondritic proportions of refractory lithophile elements (*McDonough and Sun*, 1995).

We report a new global compilation of κ and κ_{Pb} values for oceanic and continental rocks, with the former samples serving as a proxy for the modern mantle (MM) and the latter for the bulk of the continental crust (CC). Following this we use the solar system/chondritic value of κ_{Pb} and the data for the BSE to draw conclusions about the negligible contribution of the Earth's core in these heat producing elements' balance.

6.3 Methods

The continental crust and the modern mantle are understood as complementary reservoirs of the BSE. Their κ and κ_{Pb} values have been previously examined (*Galer and O'Nions*, 1985; *Elliott et al.*, 1999; *Paul et al.*, 2003; *Andersen et al.*, 2015; *Castillo*, 2016; *Kumari et al.*, 2016). In combination, the reservoirs' κ ratios combine to the BSE κ following these mass balance relationships:

$$M^{BSE} = M^{MM} + M^{CC} \tag{6.1}$$

$$M^{BSE}a_{Th}^{BSE} = M^{MM}a_{Th}^{MM} + M^{CC}a_{Th}^{CC} \tag{6.2}$$

$$M^{BSE}a_{U}^{BSE} = M^{MM}a_{U}^{MM} + M^{CC}a_{U}^{CC} \tag{6.3}$$

where equations (6.2) and (6.3) can be combined into

$$\frac{a_{Th}}{a_U})^{BSE} = \frac{M^{MM}a_{Th}^{MM} + M^{CC}a_{Th}^{CC}}{M^{BSE}a_{U}^{BSE}} = (\frac{a_{Th}}{a_U})^{MM}\frac{M^{MM}a_{U}^{MM}}{M^{BSE}a_{U}^{BSE}} + (\frac{a_{Th}}{a_U})^{CC}\frac{M^{CC}a_{U}^{CC}}{M^{BSE}a_{U}^{BSE}} \tag{6.4}$$

$$= (\frac{a_{Th}}{a_U})^{MM}\frac{m_{U}^{MM}}{m_{U}^{BSE}} + (\frac{a_{Th}}{a_U})^{CC}\frac{m_{U}^{CC}}{m_{U}^{BSE}}$$

and where M, m_U, and m_{Th} represent the mass of rock, U, and Th in the reservoir of interest, a = the abundance of U or Th (mass fraction), MM = modern mantle, and CC = continental crust. Multiplication of the above equations by the ratio in atomic masses of Th and U and by the molar fraction of ^{238}U relative to U will yield κ. Thus, calculation of the κ and κ_{Pb} of the BSE requires weighting the κ and κ_{Pb} of the modern mantle or continental crust by only the U mass within each reservoir.

6.4 Data

		κ					κ_{Pb}			
Reservoir	# of data	Mean	Geometric mean	Median	SiO_2 at 60 wt%	# of data	Mean	Geometric mean	Median	SiO_2 at 60 wt%
				Modern Mantle						
MORB	2,558	3.14	3.05	$3.12^{+0.72}_{-0.71}$		936	3.84	3.84	$3.84^{+0.09}_{-0.09}$	
OIB	10,599	4.07	3.66	$3.67^{+0.99}_{-0.63}$		6,576	3.91	3.90	$3.87^{+0.16}_{-0.07}$	
				Continental Crust						
igneous	120,836	4.73	3.42	$3.56^{+1.60}_{-1.29}$	$3.61^{+1.0}_{-0.6}$	22,318	3.99	3.97	$3.95^{+0.19}_{-0.11}$	$3.95^{+0.07}_{-0.06}$
metamorphic	8,287	5.37	3.10	$3.61^{+3.26}_{-2.00}$	$3.57^{+1.8}_{-1.2}$	664	4.12	4.05	$3.99^{+0.40}_{-0.28}$	$3.99^{+0.3}_{-0.2}$
sedimentary	11,682	3.09	1.52	$2.61^{+1.87}_{-2.16}$	$2.60^{+0.9}_{-0.7}$	169	3.99	3.97	$4.00^{+0.11}_{-0.10}$	$4.00^{+0.08}_{-0.05}$

Table 6.1: Summary of κ and κ_{Pb} for MORB, OIB, and continental crust (igneous, metamorphic, and sedimentary datasets). 68% confidence limits are reported alongside the median value for each dataset and method. Weighting by SiO2 at 60 wt% is also reported for the continental crust (see text and supplementary materials for details).

Some 150,000 measurements acquired through the *EarthChem* (www.earthchem.org) repository were statistically assessed and are provided as an electronic supplement. Select measures, including the arithmetic mean, geometric mean, and median are reported in Table 6.1 for oceanic basalts and continental igneous, sedimentary, and metamorphic rocks. Moreover, this analysis provides the full assessment of the data distribution and uncertainties (Table 6.1 and Supplementary Information). The central value $\pm$ uncertainty reported hereafter refers to the median $\pm$ 68% confidence limit unless otherwise stated. This statistical approach addresses the influence of outliers on the central value and describes the spread of data without assuming a distribution shape, such as gaussian.

Sample location maps and histograms of κ and κ_{Pb} are provided in Figures 6.1, 6.2 and 6.3. Data trends versus SiO_2, along with regression analyses are reported for continental rocks in Table 6.1 and Figure S1. The electronic supplement contains the following: (i) detail the κ and κ_{Pb} definitions and analysis; (ii) description of the κ versus SiO_2 regression for continental rocks; (iii) a description of the method of assessing the crustal composition using crustal types; (iv) details of the mathematical formulation; (v) additional figures and tables; (vi) all chemical data used; (vii) the MATLAB code; and (viii) the results of the Monte Carlo analysis.

Significant analytical advances over the last few decades allow for a reassessment of the κ value for fresh, unaltered mid-ocean ridge basalt (MORB). Table 6.1 reports the arithmetic mean, median, and geometric mean for 2,558 high precision κ values for MORB, many of which have been recently determined by laser ablation measurements (*Arevalo and McDonough*, 2010; *Gale et al.*, 2013). The present

survey provides an improved estimate of the central value and 68% confidence limits for κ and κ_{Pb} of MORB (Figure 6.1 and 6.3). The similarity of the arithmetic mean, median, and geometric mean for κ^{MORB} of $\sim$3.1 $\pm$ 0.7 are consistent with a gaussian data distribution. This value and its uncertainty is comparable, at the low end of the limit, to earlier estimates of $\sim$2.5 (*Galer and O'Nions*, 1985; *Elliott et al.*, 1999; *Paul et al.*, 2003). The κ_{Pb}^{MORB} of 3.84 $\pm$ 0.09 for MORB is identical to earlier estimates and overlaps with that of the solar system initial (3.890 $\pm$ 0.015). The homogeneity of the MORB κ_{Pb} stands in contrast to the greater variability seen in κ (Figure 6.3).

Similarly, the statistics for κ and κ_{Pb} of ocean island basalts (OIB) have been enhanced based on many thousand measurements and improved data quality. The κ^{OIB} value ($3.67\ ^{+0.99}_{-0.63}$) is more variable than that for MORB, whereas the κ_{Pb}^{OIB} value ($3.87\ ^{+0.16}_{-0.07}$) is comparable to that for MORB and again overlaps with that of the solar system value (3.890 $\pm$ 0.015). We treat OIB and MORB samples collectively as representing the Modern Mantle (MM), with the former sampling a dominantly incompatible element enriched source and the latter an incompatible element depleted source. The relative mass fractions of these two mantle domains and their concentrations are not well constrained, but estimates place the OIB source as representing about 20% the mass of the Modern Mantle (*Arevalo et al.*, 2013). In any case, thanks to the similarity of the κ_{Pb} values for MORB and OIB, our subsequent analysis is largely independent of the reservoirs' relative sizes. Simple combining of the OIB and MORB datasets yield a modern mantle κ^{MM}= $3.54\ ^{+0.96}_{-0.69}$ and κ_{Pb}^{MM}= $3.87\ ^{+0.15}_{-0.07}$. Alternatively, assuming mantle mass fractions and concen-

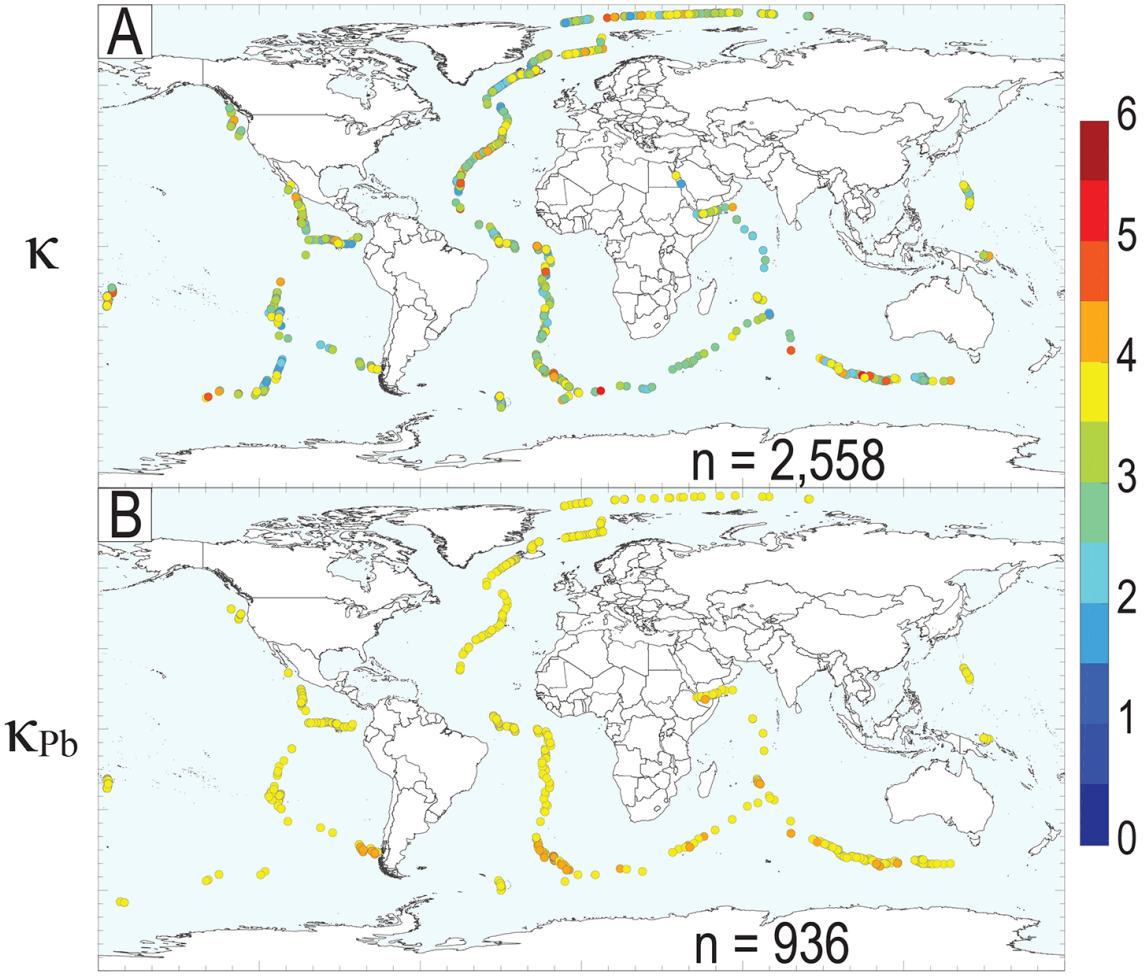

Figure 6.1: Distribution of samples used in the calculation of κ (A) and κ_{Pb} (B) for MORB. Circle colors indicate κ and κ_{Pb} value. The number of samples comprising each dataset are reported on the bottom right of each map.

trations of OIB and MORB from Arevalo et al. (2013) yields a ${}^{weighted}\kappa^{MM} = 3.46\,{}^{+0.72}_{-0.57}$ and ${}^{weighted}\kappa^{MM}_{Pb} = 3.86^{+0.09}_{-0.06}$. The similarity of the weighted and unweighted κ^{MM}_{Pb} is a result of the enrichment in U and Th of the OIB source relative to the MORB source. We use the unweighted values in later calculations.

The continental crust is the remaining known BSE reservoir for Th and U and its contribution is estimated to contain some ~30% to 50% of the inventory of these heat producing elements (*Huang et al.*, 2013; *Rudnick and Gao*, 2014). Assessing

the κ and κ_{Pb} values for the bulk of the continental crust presents a challenge, given different rock types from which to select, sampling biases, and weighting fractions for the values for the upper, middle, and lower crust. Therefore, to evaluate κ values in igneous, metamorphic, and sedimentary rocks we used a best fit line between κ and SiO_2 to calculate the average κ value at 60 wt.% SiO_2 (Table 6.1 and Figure S1). Results of these and an additional method agree with statistical measures for the unweighted datasets, particularly for κ_{Pb} (Table 6.1 and Table S3). We use the unweighted values in later calculations.

Marked differences are found between the gaussian fit (arithmetic mean and standard deviation), log-normal fit (geometric mean and corresponding asymmetrical uncertainty), and the median with 68% confidence limits, for κ and Th and U abundances for igneous, sedimentary, and metamorphic rocks (Table 6.1 and Table S3), whereas κ_{Pb} values are nearly identical in these different datasets (Table 6.1). The uniformly lower κ values in sedimentary rocks (Figure 6.3, including the peak for U rich sediments with low Th/U values), reflect the mobility of U presently at oxidized surface conditions; these samples likely add a small contribution ($\sim$10%) to the overall continental crustal signal (*Wilkinson et al.*, 2009). The median, geometric mean, and 60 wt.% SiO_2 estimates of κ values ($\sim$3.6) for igneous and metamorphic rocks are low when compared to conventional estimates (i.e., Th/U $> \sim$4 for the continental crust), but their wide confidence limits at 68% and markedly asymmetric distribution indicate a positively skewed population (Table 6.1 and Figure 6.3). The median and geometric mean κ values of mantle and crustal datasets are not complimentary relative to the chondritic reference frame, albeit are within uncertainty.

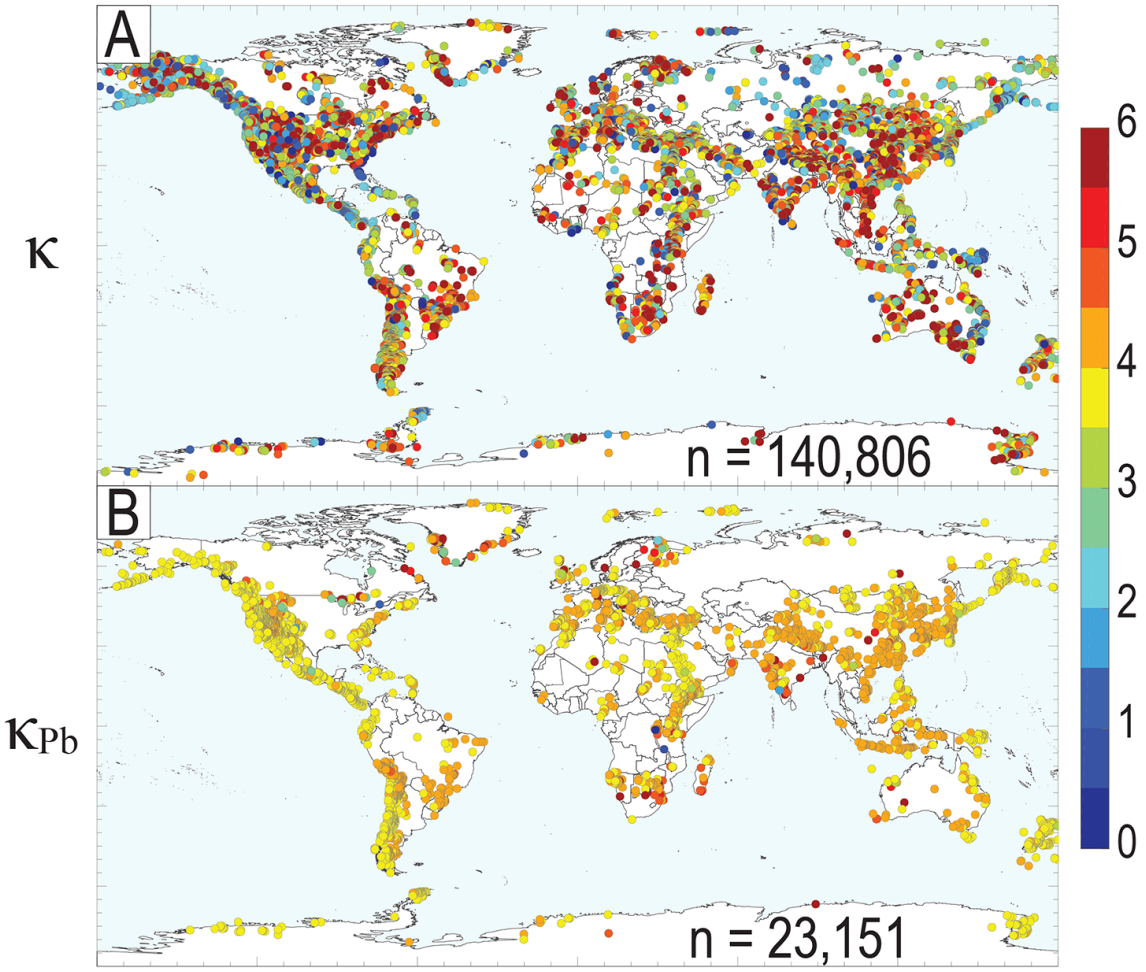

Figure 6.2: Distribution of samples used in the calculation of κ (A) and κ_{Pb} (B) for continental crust (igneous, sedimentary, and metamorphic datasets). Circle colors indicate κ and κ_{Pb} value. The number of samples comprising each dataset are reported on the bottom right of each map.

The arithmetic mean, geometric mean, and median of κ_{Pb} for continental igneous and metamorphic rocks overlap and are slightly super-chondritic. The median κ_{Pb} values show a complementary relationship with the OIB and MORB values (Table 6.1).

The continental crust κ_{Pb}^{CC} of $3.95\ ^{+0.19}_{-0.13}$ (combined igneous and metamorphic data) overlaps with previously reported values calculated from Pb isotopic compositions for the continents (*Rudnick and Goldstein*, 1990), although some of these higher model estimates (*Zartman and Doe*, 1981) only marginally overlap with the data presented here. Also, the κ_{Pb}^{sed} value of $4.00\ ^{+0.11}_{-0.14}$ for sedimentary rocks agrees with the estimate of 4.04 based on the Pb isotopic composition of the upper crust (*Millot et al.*, 2004).

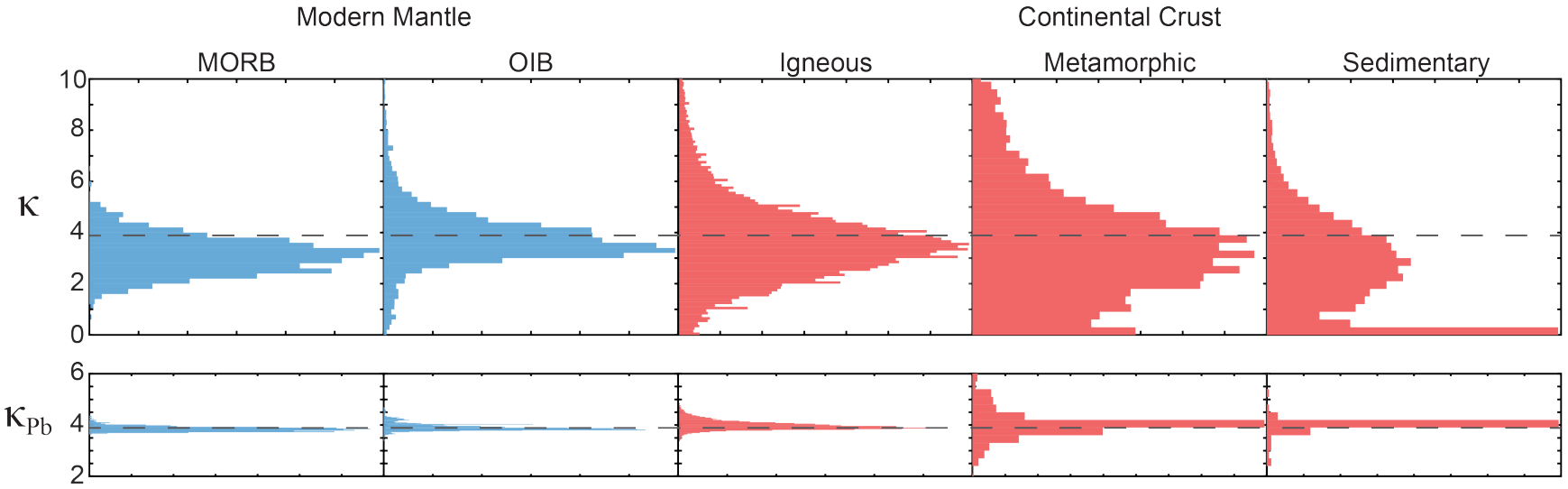

Figure 6.3: Histograms of κ and κ_{Pb} for MORB, OIB, and continental igneous, metamorphic, and sedimentary rocks used in this study. The y-axis shows κ and κ_{Pb} values at the same scale and the x-axis shows frequency of sample per bin normalized to total number of samples. The dashed dark-grayhorizontal line in each plot is the solar system initial value (adapted from *Blichert-Toft et al.* (2010).

Concentration data for Th and U in rocks from the continental crust and modern mantle are provided in Table S1. In all cases the estimated concentrations based on the arithmetic mean, geometric mean, and median reveal that the latter two are comparable and lower than the arithmetic mean, indicating a non-gaussian, positively skewed data distribution in all geological settings. The arithmetic mean of Th and U abundances for MORB are comparable to earlier estimates (*Arevalo and McDonough*, 2010; *Gale et al.*, 2013). Estimates of Th and U abundance in the continental crust, based on arithmetic mean, are higher than existing estimates for the upper crust and reflect a strong biasing of the data by outliers with high concentrations. The median and log-normal estimates of Th and U abundances in igneous and metamorphic rocks are comparable with global estimates for the bulk continental crust (*Rudnick and Gao*, 2014); based only on the median abundances the Th/U is ~3.6 to 3.8, comparable to the weighted median κ value for these rocks.

6.5 Calculating the Earth's core contribution

We also examine the role of the Earth's core in establishing the budget of these elements. To date, experimental studies conducted at conditions ranging from low to high pressure and high temperature have examined the partitioning of Th and U between metal (and metal-sulfide) and silicate and document a marked difference in the behavior of these two elements, with U, and not Th, being weakly partitioned into the metal (*Chidester et al.*, 2017; *Blanchard et al.*, 2017). These same studies either did not include Th in their experiments or report D_U partition coefficients and

below limits of detection values for D_{Th} (*Chidester et al.*, 2017). The Earth's core is recognized as having a mix of light elements that account for its density deficit relative to iron, with a limited contribution from the volatile element sulfur (*McDonough*, 2017). In a sulfur saturated, non-peridotitic set of experiments, D_{Th} was found to be $\sim 0.1 D_U$ (*Wohlers and Wood*, 2017).

The mass balance of the bulk Earth ($\oplus$) is:

$$m_U^{\oplus} = m_U^{CC} + m_U^{MM} + m_U^{core} [5]$$

The core/mantle (i.e., metal/silicate) partition coefficient is defined as $D_{Th} \equiv a_{Th}^{core}/a_{Th}^{BSE}$. We further define

$$D_\kappa \equiv \frac{D_{Th}}{D_U} = (\frac{Th}{U})^{Core} \ (\frac{U}{Th})^{BSE} = \frac{\kappa^{core}}{\kappa^{BSE}} [6]$$

to express

$$\kappa_{Pb}^{core} = D_\kappa \kappa_{Pb}^{BSE} = D_\kappa (\kappa_{Pb}^{CC} \frac{m_U^{CC}}{m_U^{BSE}} + \kappa_{Pb}^{MM} \frac{m_U^{MM}}{m_U^{BSE}}) [7]$$

As U is removed from the BSE (specifically the mantle) and added to the core, the mass balance between the mantle and crust (equation [8]) changes, as does κ_{Pb}^{BSE} and κ_{Pb}^{core} (equation [7]). We use $D_\kappa = 0.1$ as an upper limit during metal-silicate segregation (Wohlers and Wood, 2017). Finally, the bulk Earth $\kappa_{Pb}^{\oplus}$is calculated as

$$\kappa_{Pb}^{\oplus} = \kappa_{Pb}^{CC} \frac{m_U^{CC}}{m_U^{\oplus}} + \kappa_{Pb}^{MM} \frac{m_U^{MM}}{m_U^{\oplus}} + \kappa_{Pb}^{core} \frac{m_U^{core}}{m_U^{\oplus}} [8]$$

Using the data (Table 6.1 and S1) and its distribution (Figure 6.3), we performed a Monte Carlo simulation to calculate the κ_{Pb} of the BSE and bulk Earth for a range of U concentrations in the core (from 0 to 10 ng/g) and a bulk Earth U mass from *McDonough and Sun* (1995). The lower limit assumption of $m_U^{core} = 0$ puts all the U in the BSE (equation [5]). As U is added to the core it is removed from the mantle U mass budget. We adopt weights based on the U mass fraction in the continental crust and mantle (equation [4]). κ and κ_{Pb} were randomly sampled 500,000 times from the available data for each reservoir, avoiding assumptions on distribution shape. We re-sample the distributions in cases where the mass of U in the combined crust and core reservoirs result in a larger U mass than permitted by the assumed bulk Earth model. This re-sampling removed a subset of crustal data with high U abundances, and resulted in a $\kappa^{\mathrm{CC}} = 3.78^{+1.75}_{-1.30}$, similar to results reported in Table 6.1. We also observe a lack of correlation between U or Th abundance, and κ.

Based on an assumption of $\mathrm{U}^{core} = 0$ ng/g, the $\kappa_{Pb}^{BSE} = 3.903\ ^{+0.127}_{-0.078}$ (equivalent to $\mathrm{Th/U}_{BSE}$ (mass ratio) $= 3.776\ ^{+0.122}_{-0.075}$). Figure 6.4 shows the modeled results. The intersection of the median, 68%, and 95% confidence limits (c.l.) of $\kappa_{Pb}^{\oplus}$ with the respective parameters for κ_{Pb}^{SS} yields a U abundance in the core of 0.16 ng/g, 1.9 ng/g, and 4.6 ng/g, respectively (Figure 6.4 and S3). The heat production in the core from U and Th (calculated using κ_{Pb}^{core}) is 0.033 TW, 0.41 TW, and 1.0 TW, respectively for the median, 68% c.l., and 95% c.l. intercepts.

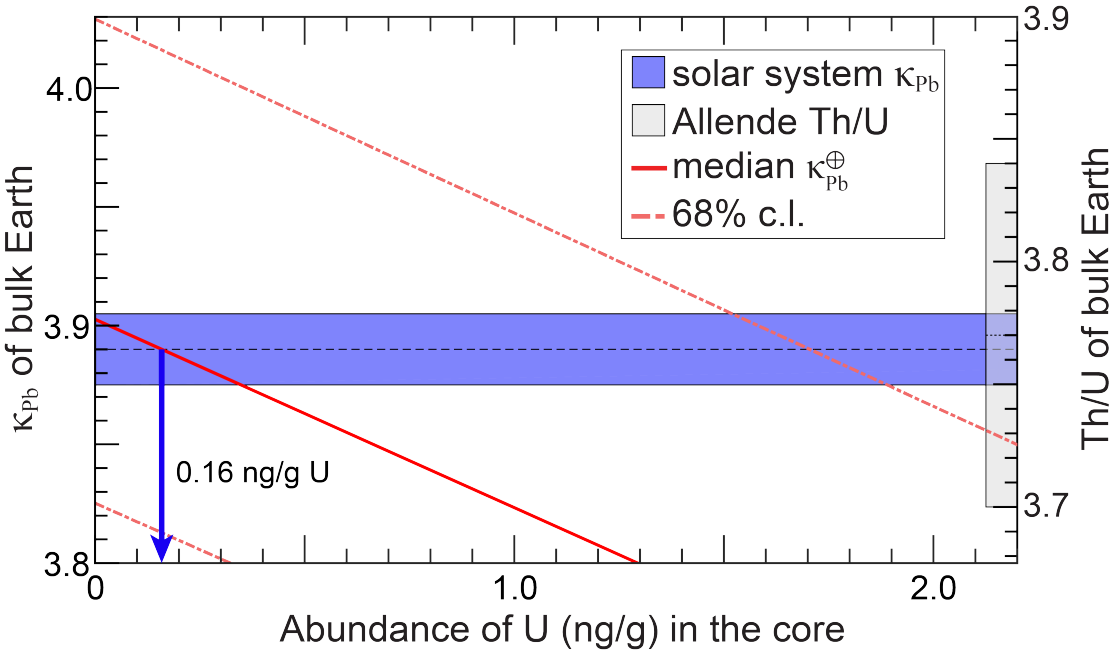

Figure 6.4: Modeled U abundance (in ng/g) in the core vs. κ_{Pb} of the bulk Earth (left y-axis) and Th/U (mass ratio) of the bulk Earth (right y-axis). The median (red solid) and 68% confidence limit (red dashed) are plotted against the solar-system κ_{Pb} (blue shaded horizontal region with 1-sigma bounds; adapted from *Blichert-Toft et al.* (2010)) and Allende meteorite (grayshaded region along right y-axis with 1-sigma bounds and arbitrary x-axis size; *Pourmand and Dauphas* (2010)). The intersection of the median κ_{Pb} of the bulk Earth and solar system is marked by a solid vertical blue arrow (corresponding to 0.16 ng/g).

6.6 Discussion

The results of this study find that the $\kappa_{Pb}^{MM} = 3.87\ ^{+0.15}_{-0.07}$ and $\kappa_{Pb}^{CC} = 3.95\ ^{+0.19}_{-0.13}$ are statistically indistinguishable, $\kappa_{Pb}^{MM} \approx \kappa_{Pb}^{CC}$, and therefore a mass weighted estimate for the $\kappa_{Pb}^{BSE} = 3.90\ ^{+0.13}_{-0.08}$ is comparable to the solar system/chondritic value (*Pourmand and Dauphas*, 2010; *Blichert-Toft et al.*, 2010). These findings resolve a long-standing debate on the BSE estimate of its Th/U value, which has previously been estimated using chondritic assumptions or limited sample sets (*Allègre et al.*, 1986, 1988; *Rocholl and Jochum*, 1993; *Javoy and Kaminski*, 2014).

Second, negligible Th/U fractionation accompanied crust - mantle differentiation. The 1.0% difference between the median κ_{Pb}^{CC} and κ_{Pb}^{MM} reveals that U^{6+} recycling back into the mantle has either been a relatively recent process or that limited recycling followed atmospheric oxygenation at 2.4 Ga and evolved slowly with time. These finding are strikingly inconsistent with claims of widespread pollution of the upper mantle with recycled uranium (*Andersen et al.*, 2015) and claims of biologically driven fractionation leaving its imprint on the mantle (*Sleep et al.*, 2013).

Third, negligible Th/U fractionation accompanied accretion and core formation, and therefore trivial amounts of U (<4.6 ng/g at 95% c.l., Figure 6.4 and S3) and proportionally miniscule amounts of Th have been sequestered into the Earth's core, and thus U and Th play little to no role in powering the geodynamo (*Nimmo*, 2015). A maximum of 1.0 TW is available from U and Th in the core at 95%

confidence limits. Likewise, this finding falsifies the hypothesis of a natural nuclear reactor in the Earth's core (*Hollenbach and Herndon*, 2001).

Using the findings reported here, we recommend that the uncertainty analyses reported in *McDonough and Sun* (1995) be updated to ±10% for the abundances of Th and U (following the uncertainty of κ_{Pb}^{BSE}). This update sets the uncertainty values for these elements as being equal to that for the rest of the refractory lithophile elements.

The precision reported here for the global Th/U value validates and updates the assumed fixed ratio to Th/U (mass ratio) = 3.8 for use in geoneutrino detection studies (*Gando et al.*, 2013; *Agostini et al.*, 2015), particularly given the crust and mantle domains share similar values. That said, however, differences in this ratio may be found in crustal regions beneath individual detectors. An independent measure of this value by particle physicists is welcomed and will be a critical test of our global interpretation.

There remains debate regarding the absolute abundances of U and Th in the BSE, with estimates varying by a factor of three (*Šrámek et al.*, 2013). The agreement of κ_{Pb}^{CC} and κ_{Pb}^{MM} and the results for the abundances of U and Th in the continental crust are combined with an assumption of a BSE model (*McDonough and Sun*, 1995) to show that the power balance for these elements is 65% (13 TW) in the mantle and 35% (7 TW) in the crust, a conclusion consistent with geoneutrino results (*Gando et al.*, 2013; *Agostini et al.*, 2015). These results highlight the significance of the 13 TW of power driving mantle convection. Our conclusions, nonetheless, are independent of chosen BSE model or reservoir weights (including

weighting of MORB and OIB samples for MM), given the near equivalence of $\kappa_{Pb}$for BSE reservoirs. Moreover, our findings emphasize the need for further understanding the energy budget of the core.

6.7 Output from this work:

- Wipperfurth, S. A., M. Guo, O. Šrámek, and W. F. McDonough (2018), Earth's chondritic Th/U: Negligible fractionation during accretion, core formation, and crust–mantle differentiation, *Earth and Planetary Science Letters*, *498*, 196–202, doi:10.1016/j.epsl.2018.06.029

Chapter 7: Radiogenic power and luminosity of the Earth and other terrestrial bodies through time

[1] S.A. Wipperfurth, W.F. McDonough, and O. Šrámek proposed and conceived of various portions of this study and also independently conducted heat production and luminosity calculations. O .Šrámek calculated the β decay spectra for the SLR and ^{40}K. All authors contributed to the interpretation of the results. The manuscript was written by WFM, with edits and additions from O˘Šrámek and S.A. Wipperfurth.

[2] This chapter is in preparation to be submitted as:
William F. McDonough, Ondřej Šrámek, and Scott A. Wipperfurth, Radiogenic power and luminosity of the Earth and other terrestrial bodies through time, 2019.

7.1 Abstract

We report the Earth's rate of radiogenic heat production and (anti)neutrino luminosity from geologically relevant short-lived radionuclides (SLR) and long-lived radionuclides (LLR) using decay constants from the geological community, updated nuclear physics parameters, and calculations of the β spectra. We carefully account for all branches in ^{40}K decay using the updated β^- energy spectrum from physics

and an updated branching ratio from geological studies. We track the time evolution of the radiogenic power and luminosity of the Earth over the last 4.57 billion years, assuming an absolute abundance for the refractory elements in the silicate Earth and key volatile/refractory element ratios (e.g., Fe/Al, K/U, and Rb/Sr) to set the abundance levels for the moderately volatile elements. The relevant decays for the present-day heat production in the Earth are from ^{40}K, ^{87}Rb, ^{147}Sm, ^{232}Th, ^{235}U, and ^{238}U.

The radiogenic heating rate of Earth-like material at Solar System formation was some 3000 times greater than present-day value, largely due to decay of ^{26}Al in the silicate fraction which was the dominant radiogenic heat source for the first $\sim$ 10 My. Decay of ^{60}Fe contributed a non-negligible amount of heating during the first $\sim$ 15 My after CAI (Calcium Aluminum Inclusion) formation, interestingly within the time frame of core–mantle segregation. Using factors and equations presented here, one can readily calculate the first-order thermal history of various size bodies in the solar system and exoplanets.

7.2 Introduction

Radioactive decay inside the Earth produces heat, which in turn contributes power to driving the Earth's dynamic processes (i.e., mantle convection, volcanism, plate tectonics, and potentially the geodynamo). The physics community, using the latest numbers from nuclear physics databases, provide estimates of the heat production and geoneutrino luminosity of the Earth (*Dye*, 2012; *Ruedas*, 2017; *Us-*

man et al., 2015; *Enomoto*, 2006b; *Fiorentini et al.*, 2007b). These studies include comprehensive reviews of the fundamental physics of these decay schemes, covering both the energy added to the Earth and that removed by the emitted geoneutrino. This note draws attention to differences in decay constants as reported in the geological and physics literature and recommends the former as being more accurate and precise. The absolute accuracy of geological studies is underpinned by the ^{238}U decay constant (*Jaffey et al.*, 1971) and their relative accuracies are based on multiple cross-calibrations for different decay systems on the same rocks and mineral suites. Improvements in measurement precision comes from repeated chronological experiments.

There are a number of naturally occurring short-lived (referred to the Earth's age; half-lives $t_{1/2} < 10^8$ years) and long-lived ($t_{1/2} > 10^9$ years) radionuclides; those discussed here have half-lives between 10^5 and 10^{11} years. The long-lived decay constants are listed in Table 7.1 along with their decay modes and decay energies. The decay modes include alpha (α), beta-minus (β^-), and electron capture (EC). The beta-plus (β^+) decay mode is less common, but is seen in the ^{26}Al system, as well as a few minor branches in the Th and U decay chains and also likely in the ^{40}K chain. Geoneutrinos are naturally occurring electron antineutrinos ($\bar{\nu_e}$) produced during β^- decay and electron neutrinos (ν_e) produced during ε (i.e., β^+ and EC) decays. The generic versions of these decay schemes are:

$$
\begin{aligned}
\text{Alpha} \quad (\alpha) \qquad & {}^{A}_{Z}X \rightarrow {}^{A-4}_{Z-2}X' + \alpha + Q, \\
\text{Beta Minus} \quad (\beta^-) \qquad & {}^{A}_{Z}X \rightarrow {}^{A}_{Z+1}X' + e^- + \bar{\nu_e} + Q, \\
\text{Electron Capture} \quad (\text{EC}) \qquad & {}^{A}_{Z}X + e^- \rightarrow {}^{A}_{Z-1}X' + \nu_e + Q, \\
\text{Beta Plus} \quad (\beta^+) \qquad & {}^{A}_{Z}X \rightarrow {}^{A}_{Z-1}X' + e^+ + \nu_e + Q, \\
\varepsilon \qquad & \text{refers to the combination of EC and } \beta^+
\end{aligned}
\tag{7.1}
$$

with parent element X, daughter element X', mass number A, atomic number Z, energy of reaction Q, electron e^-, positron e^+, and alpha particle α (${}^{4}_{2}$He nucleus).

Table 7.1: Extant long-lived radioactive decay systems.

Decay system	Mole frac. (%)	Decay mode	λ (yr^{-1})	Q (MeV)
$^{40}\mathrm{K} \rightarrow {}^{40}\mathrm{Ar}$	0.01167	ε (10.56%)	5.810×10^{-11}	1.504
$^{40}\mathrm{K} \rightarrow {}^{40}\mathrm{Ca}$	0.01167	β^- (89.44%)	4.910×10^{-10}	1.311
			5.491×10^{-10}	(total) 1.331
$^{87}\mathrm{Rb} \rightarrow {}^{87}\mathrm{Sr}$	27.83	β^-	1.397×10^{-11}	0.2823
$^{138}\mathrm{La} \rightarrow {}^{138}\mathrm{Ce}$	0.0888	β^- (34.8%)	2.34×10^{-12}	1.052
$^{138}\mathrm{La} \rightarrow {}^{138}\mathrm{Ba}$	0.0888	EC (65.2%)	4.39×10^{-12}	1.742
			6.73×10^{-12}	(total) 1.504
$^{147}\mathrm{Sm} \rightarrow {}^{143}\mathrm{Nd}$	14.993	α	6.539×10^{-12}	2.311
$^{176}\mathrm{Lu} \rightarrow {}^{176}\mathrm{Hf}$	2.598	β^-	1.867×10^{-11}	1.194
$^{187}\mathrm{Re} \rightarrow {}^{187}\mathrm{Os}$	62.60	β^-	1.666×10^{-11}	0.0025
$^{190}\mathrm{Pt} \rightarrow {}^{186}\mathrm{Os}$	0.0136	α	1.415×10^{-12}	3.269
$^{232}\mathrm{Th} \rightarrow {}^{208}\mathrm{Pb}$	100	6α and $4\beta^-$	4.916×10^{-11}	(total) 42.646
$^{235}\mathrm{U} \rightarrow {}^{207}\mathrm{Pb}$	0.72033	7α and $4\beta^-$	9.8531×10^{-10}	(total) 46.397
$^{238}\mathrm{U} \rightarrow {}^{206}\mathrm{Pb}$	99.274	8α and $6\beta^-$	1.5513×10^{-10}	(total) 51.694

Decay energy Q calculated from mass differences between parent and final daughter nuclide mass data from (*Wang et al.*, 2017); see Table 7.2 for details on decay constant λ. Mole fraction of U isotopes calculated from U = ^{238}U + ^{235}U + ^{234}U; $^{238}\mathrm{U}/^{235}\mathrm{U} = 137.818 \pm 0.045$ (*Hiess et al.*, 2012); $^{234}\mathrm{U/U} = (5.5 \pm 0.1) \times 10^{-5}$ (*Villa et al.*, 2016).

We report here radiogenic heat production and (anti)neutrino luminosity from geologically relevant short-lived radionuclides (SLR) and long-lived radionuclides (LLR). For the LLR we compare half-lives used in the geological and nuclear physics communities and recommend use of the former. We calculate the heat added to the Earth by these nuclear decays, as well as that removed by the (anti)neutrino that leaves the Earth. We calculate estimates of the embedded and removed energy of decay, particularly for the SLR, from β decay spectra calculated using Fermi theory and shape factor corrections. We conclude by presenting models for the Earth's radiogenic heat production and geoneutrino luminosity for the last 4568 million years, along with simple rules for extrapolating these results to other terrestrial bodies and exoplanets.

7.3 Contrasting methodologies

In compiling the data needed to calculate all of the observables, we found differences between the decay constants ($\lambda = \ln 2/t_{1/2}$) reported by the geological and nuclear physics communities. Values for extant systems are provided in a side-by side comparison in Table 7.2. The rightmost column reports the relative difference, in percent, between the decay constants from these communities and for some, the difference can be considerable (more than 30%). An updated physics number for the half-life of ^{190}Pt reported in *Braun et al.* (2017) agrees with the numbers obtained by *Cook et al.* (2004), who presented a detailed study of a suite of well behaved (closed system evolution), 4.5 billion year old, iron meteorites (i.e., group IIAB and

IIIAB).

There is a 1.1% difference in the decay constant for ^{40}K between literature sources, which is a nuclide that provides ∼20% of the planet's present-day radiogenic heat and ∼70% of its geoneutrino luminosity (see Table 7.3). This difference is outside of the uncertainty limits on the half-life of ^{40}K, recently established by geochronologists (*Renne et al.*, 2011).

Table 7.2: Comparison of half-life values ($t_{1/2}$, in years) of long-lived radionuclides.

	NNDC	**Geochronology**			
Nuclide	$t_{1/2}$ (±)	$t_{1/2}$ (±)	%±	Ref.	%Δ (NNDC vs. Geo)
^{40}K	$1.248(3) \times 10^{9}$	$1.262(2) \times 10^{9}$	0.2	N'18	-1.1
^{87}Rb	$4.81(9) \times 10^{10}$	$4.961(16) \times 10^{10}$	0.3	V'15	-3.0
^{138}La	$1.03(1) \times 10^{11}$	$1.03(2) \times 10^{11}$	1.9	SH'81	0
^{147}Sm	$1.07(1) \times 10^{11}$	$1.06(1) \times 10^{11}$	0.9	B'01	0
^{176}Lu	$3.76(7) \times 10^{10}$	$3.713(16) \times 10^{10}$	4.3	S'04	1.3
^{187}Re	$4.33(7) \times 10^{10}$	$4.16(4) \times 10^{10}$	1.0	B'01	4.1
^{190}Pt	$6.5(3) \times 10^{11}$	$4.899(44) \times 10^{11}$	0.9	C'04	33
^{232}Th	$1.40(1) \times 10^{10}$	$1.41(1) \times 10^{10}$	1.0	F'60	-0.7
^{235}U	$7.038(5) \times 10^{8}$	$7.0348(20) \times 10^{8}$	0.03	H'12	0.05
^{238}U	$4.4683(24) \times 10^{9}$	$4.4683(96) \times 10^{9}$	0.2	V'16	0

(±) for $t_{1/2}$ values in the parentheses represent uncertainty in the last reported significant figure. %± is the relative uncertainty, %Δ is the relative difference [(X/Y)-1] between NNDC (National Nuclear Data Center) and Geochronology. Data source for the NNDC is www.nndc.bnl.gov. Sources in the table are as follows: N'18 (*Naumenko-Dèzes et al.*, 2018), V'15 (*Villa et al.*, 2015), SH'81 (*Sato and Hirose*, 1981; *Tanimizu*, 2000), B'01 (*Begemann et al.*, 2001), S'04 (*Söderlund et al.*, 2004), C'04 (*Cook et al.*, 2004), F'60 (*Farley*, 1960), H'12 (*Hiess et al.*, 2012), V'16 (*Villa et al.*, 2016).

Differences in decay constants reported by the geological and nuclear physics communities come from the methods used to establish the absolute and relative half-lives. Physics experiments typically determine a half-life value by measuring the activity $A = -dN/dt = \lambda N$ (N is the number of atoms) of a nuclide over time, whereas geochronology studies empirically compare multiple decay systems for a rock or suite of rocks that demonstrate close system behavior (show no evidence of loss of parent or daughter nuclide). The number of atoms N of parent nuclide evolves according to $N = N_0 e^{-\lambda t}$, therefore $\ln N = \ln N_0 - \lambda t$. A plot of $\ln N$ (ordinate) vs. t (abscissa) gives a line of slope $-\lambda$ with y-intercept equal to $\ln N_0$.

Direct counting experiments generally involve the isolation of a pure mass of the parent nuclide of interest, knowing exactly the number of parent atoms at the start of the experiment, and then determining the ingrowth of daughter atoms produced at one or more times later (*Begemann et al.*, 2001). Geochronological experiments compare multiple chronometric methods (e.g., U–Pb and K–Ar systems (*Renne et al.*, 2011)) and develop a series of cross calibrations, where the shortcoming of this approach is the anchoring decay system that pins down the accuracy for other chronometers. It is recognized (*Begemann et al.*, 2001; *Villa et al.*, 2015; *Ruedas*, 2017) that the half-life of ^{238}U (*Jaffey et al.*, 1971) is the most accurately known of the decay constants and thus acts as the anchor in these calculations. Table 7.2 highlights the differences in half-life values reported in a standard physics reference source NNDC (National Nuclear Data Center) and geology. Relative differences at the $\sim 1\%$ scale and greater are seen for ^{40}K, ^{87}Rb, ^{176}Lu, ^{187}Re and ^{190}Pt decay systems.

Radioactive decay involves the transition to a lower level energy state of a nuclear shell and the accompanied release of energy; requiring the conservation of energy, linear and angular momenta, charge, and nucleon number. The kinetic energies released by alpha particles are discrete and on the order of 4 to 8 MeV, whereas different forms of beta decay emit a spectrum with characteristic mean and maximum energies for a given decay and the (anti)neutrino carrying away a complementary part of the energy. The energy of the beta decay process is partitioned between the (electron)positron, the (anti)neutrino, and the recoiling nucleus. Differences in heat production from decay reported in different studies is largely due to differences in decay energies (minimal differences) and the energy carried off by (anti)neutrinos (large differences). This study differs from other recent efforts (*Dye*, 2012; *Ruedas*, 2017; *Usman et al.*, 2015; *Enomoto*, 2006b; *Fiorentini et al.*, 2007a) in its input assumptions; we use decay constants and branching ratios from geochronological studies and we calculate the beta decay energy spectrum for most of the SLR and ^{40}K decays. For the remaining LLR decays, we adopt the energy spectra from *Enomoto* (2006a).

The ^{40}K decay scheme is a good example of where differences in inputs occur. Many naturally occurring decay schemes have a single decay mode, whereas ^{40}K is a branch decay scheme with β^- and ε decays (see Figure 7.1), with emission of an $\bar{\nu_e}$ and ν_e, respectively, removing energy from the Earth. The amount of radioactive heating in the Earth from this branch decay scheme depends on the branching ratio and the energy removed by the ν_e and $\bar{\nu_e}$. Using only geological data, *Naumenko-Dèzes et al.* (2018) examined the ^{40}K decay system and report a probability for the

β^- branching between 89.25% and 89.62% and for the ε branching between 10.38% and 10.75%. They highlight that the errors on these values are non-Gaussian. The physics community reports the branching probabilities of β^- as 89.28(11)% and of ε as 10.72(11)% (*Chen*, 2017). Figure 7.1 reports the updated ^{40}K decay scheme, branching ratios, and average energy removed by the (anti)neutrinos and deposited by these decays.

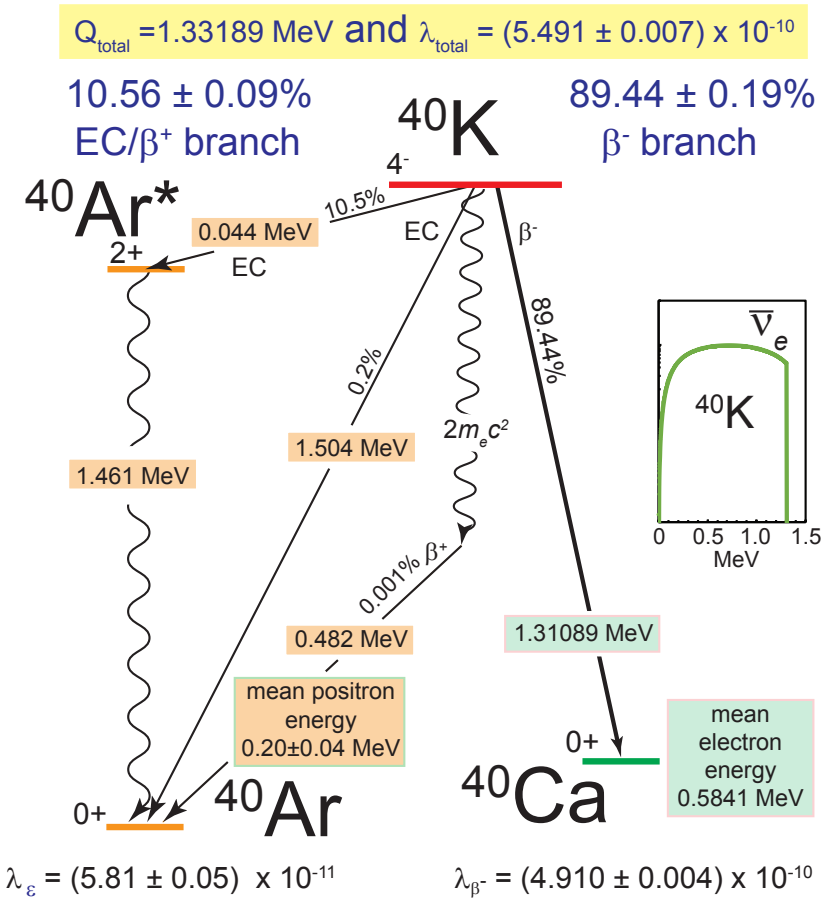

Figure 7.1: Decay scheme for ^{40}K. The beta-minus branch directly leads to ^{40}Ca in the ground state accompained by the emission of an $\bar{\nu_e}$, whereas the electron capture branch has the emission of a 45 keV ν_e and an excited state of ^{40}Ar*, with the latter undergoing an isomeric transition to the ground state of ^{40}Ar via the emission of a 1.46 MeV γ-ray. During β^- decay the energy is shared between the e^- and $\bar{\nu_e}$, with the latter particle removing on average 651 keV of energy from the Earth. Data for the branching ratios and the energies are from (*Chen*, 2017; *Renne et al.*, 2011; *Naumenko-Dèzes et al.*, 2018) and the antineutrino energy spectrum (with intensity in arbitrary units), shown in the inset, which uses the β^- shape factor from Leutz et al. (*Leutz et al.*, 1965) to account for the correction of the third unique forbidden transition.

Beta decay involves lepton conservation of two fermions (each spin 1/2) and lepton number ($e^- + \bar{\nu_e}$, $+1/-1$; $e^+ + \nu_e$, $-1/+1$; i.e. matter/antimatter, with this transformation accompanied by changes in the total orbital (L) and total spin (S^L) angular momenta of the nucleus. These transformations are either a Fermi or

Gamow-Teller transition. In the former transition, the spins of the emitted leptons (i.e., $e^-/\bar{\nu_e}$ or e^+/ν_e) are anti-parallel and there is no change in the angular momenta states of the nucleus (ΔL and $\Delta S^L = 0$). In the latter transition, the spin moments of the emitted leptons are aligned and coupled to the total change in the spin and the nuclear angular momenta states (i.e., the transforming baryon spin state changes before and after decay, $\Delta S^L = 1$). As the total change in orbital angular momentum increases so does the half-life ($t_{1/2}$) of the radionuclide. Changes in the angular momentum states during Gamow-Teller transitions need to be accounted for in the energy exchange (i.e., shape of a β spectrum) between the paired leptons during beta decay. Following Fermi's theory and working in units $\hbar = m_e = c = 1$, the shape of a β spectrum is calculated from

$$\frac{dN}{dw} \propto pwq^2 F(Z, w) S(w) \tag{7.2}$$

and normalized to the branching fraction of the specific β decay (*Enomoto*, 2005). In equation (7.2) $w = 1 + E$ is the total energy of the β-particle (E being its kinetic energy), $p = \sqrt{w^2 - 1}$ is the momentum of the β-particle, q is the total energy of the neutrino (equal to its momentum as the neutrino mass is negligible) satisfying $E + q = E_{\text{end}}$, where E_{end} is the endpoint energy of the transition (in the case of a transition to ground state, it is the Q-value), and Z is the charge of the daughter nucleus. The left-hand side of equation (7.2) is the probability of a β particle to be created with energy in the dw vicinity of w, where w goes from 1 to $1 + E_{\text{end}}$. The right-hand side is a product of three factors, the phase space factor

pwq^2, the Fermi function $F(Z,w)$, and the shape factor $S(w)$. The Fermi function

$$F(Z,w) \propto (w^2-1)^{\gamma-1} \mathrm{e}^{\pi\eta} \left|\Gamma(\gamma+i\eta)\right|^2, \tag{7.3}$$

where

$$\gamma = \sqrt{1-(\alpha Z)^2}, \tag{7.4}$$

$$\eta = \frac{\alpha Z w}{\sqrt{w^2-1}}, \tag{7.5}$$

α being the fine-structure constant, accounts for the Coulombic interaction between the daughter nucleus and the outgoing β-particle (*Enomoto*, 2005). The shape factor $S(w)$, often written at $S(p,q)$, is equal to 1 for allowed transitions and has a more complex energy-dependence in the case of forbidden transitions (i.e., forbidden decays, which really means suppressed decays, involving changes in nuclear spin state, L>1). For example, the ^{40}K decay scheme involves a third unique forbidden transition, whereas the ^{87}Rb decay scheme involves a third nonunique forbidden transition. Unique Gamow-Teller transitions are when total orbital and total spin angular momenta are aligned.

A review of many β^- decay energy spectra was recently given by *Mougeot* (2015), including the shape factors used for the forbidden transitions. We adopt these shape factors in our calculations, but also include additional β decays not studied by *Mougeot* (2015); the shape factors used here are listed in Table 7.4. We

have performed the β spectra evaluation and calculated the average energy removed by the ν_e and $\bar{\nu_e}$, which are reported as Q_ν (MeV) in Table 7.3 and can be calculated from $Q - Q_h$ in Table 7.4.

7.4 Radiogenic heat and geoneutrino luminosity of the Earth

Using decay constants for short-lived and long-lived radionuclides and ^{40}K branching ratio from the geological literature we calculate the heat production and geoneutrino luminosity of the bulk silicate Earth (BSE) based on a model composition (Tables 7.3 and 7.4 and references therein). Compositional models differ on the absolute amount of refractory elements (e.g., Ca and Al) in the Earth (see review in *McDonough* (2016)), which includes La, Sm, Lu, Re, Pt, Th, and U. The model composition for the BSE fixes the absolute abundances of the refractory elements at 2.75 times that in CI1 chondrites (*McDonough and Sun*, 1995). For critical volatile elements, there is a reasonable consensus for ratios with refractory elements. For example, *Arevalo et al.* (2009) reported the K/U value for the silicate Earth as $13,800 \pm 1,300$ (1 standard deviation). Constraints for Rb come from the constancy of the Ba/Rb and the Sr–Nd isotopic system (assumes the BSE has an ^{87}Sr/^{86}Sr between 0.7045 and 0.7054, based on the mantle array (*Hofmann*, 2007)) and the Rb/Sr values (Ba and Sr are refractory elements with abundances set at 2.75 times that in CI1 chondrites) for the bulk silicate Earth, leading to a Rb/Sr of 0.031 $\pm$ 0.002 (*McDonough et al.*, 1992).

Heat production and geoneutrino emission data for ^{40}K, ^{87}Rb, ^{147}Sm, ^{232}Th,

^{235}U, and ^{238}U are reported in Table 7.3, as these are the most significant present-day producers within the Earth. In fact, 99.5% of the Earth's radiogenic heat production comes from ^{40}K, ^{232}Th, ^{235}U, and ^{238}U alone. The fractional contributions to heat production from ^{138}La, ^{176}Lu, ^{187}Re, and ^{190}Pt add up to $< 3 \times 10^{-5}$ of the total radiogenic heat and 1% of the Earth's geoneutrino luminosity, with virtually all of this latter minor contributions coming from ^{187}Re. Figure 7.2 illustrates the present day relative contributions of heat production and geoneutrino luminosity from the major radionuclides reported in Table 7.3.

Table 7.3: Geoneutrino luminosity and heat production in the Earth

	^{238}U	^{235}U	^{232}Th	^{40}K	^{87}Rb	^{147}Sm
Decay mode	α, β^- chain	α, β^- chain	α, β^- chain	β^- or ε	β^-	α
Natural mole frac.$^{\#}$	0.992742	0.0072033	1.0000	1.167×10^{-4}	0.2783	0.14993
Nuclide mass ($g\,mol^{-1}$)	238.0508	235.0439	232.0381	39.9640	86.9092	146.9149
Atomic mass ($g\,mol^{-1}$)	238.0289	238.0289	232.038	39.098	85.468	150.362
Decay constant λ ($10^{-18}\,s^{-1}$)	4.916	31.223	1.558	17.400	0.443	0.207
Decay constant λ (yr^{-1})	1.5513×10^{-10}	9.8531×10^{-10}	4.916×10^{-11}	5.491×10^{-10}	1.397×10^{-11}	6.539×10^{-12}
Half-life $t_{1/2}$ (10^9 yr)*	4.4683	0.70348	14.1	1.262	49.61	106
1σ uncertainty on $t_{1/2}$ (10^9 yr)	0.0096	0.00020	0.1	0.002	0.16	1
n_α (α particles per decay)	8	7	6	0	0	1
$n_{\bar{\nu}_e}$ (antineutrinos per decay)	6	4	4	0.8944	1	0
n_{ν_e} (neutrinos per decay)	0	0	0	0.1056	0	0
Q (MeV)†	51.694	46.397	42.646	1.3313	0.2823	2.3112
Q (pJ)	8.2823	7.4335	6.8326	0.2133	0.0452	0.3703
Q_ν (MeV)	4.050	2.020	2.230	0.655	0.200	0
Q_ν (pJ)‡	0.649	0.324	0.357	0.105	0.032	0
Q_h (MeV)	47.6	44.4	40.4	0.676	0.082	2.311
Q_h (pJ)	7.633	7.110	6.475	0.108	0.013	0.370
Element mass frac. (kg/kg)**	2.00×10^{-8}	2.00×10^{-8}	7.54×10^{-8}	2.80×10^{-4}	6.00×10^{-7}	4.06×10^{-7}
Nuclide mass frac. (kg/kg)**	1.99×10^{-8}	0.0144×10^{-8}	7.54×10^{-8}	3.276×10^{-8}	1.67×10^{-7}	6.09×10^{-8}
$l'_{\bar{\nu}_e}$ (kg-element^{-1} s^{-1})	7.636×10^7		1.617×10^7	2.797×10^4	8.682×10^5	0
$L_{\bar{\nu}_e}$ (s^{-1})	5.99×10^{24}	1.84×10^{23}	4.93×10^{24}	3.17×10^{25}	2.11×10^{24}	0
% contribution to total $L_{\bar{\nu}_e}$	13%	0.41%	11%	71%	4.7%	0
L_{ν_e} (s^{-1})	0	0	0	3.74×10^{24}	0	0
h (μW/kg) nuclide	94.936	561.65	26.180	29.029	0.04082	0.3073
h' (μW/kg) element	94.247	4.046	26.180	0.003387	0.01136	0.04607
H (W)	7.62×10^{12}	3.27×10^{11}	7.98×10^{12}	3.84×10^{12}	2.77×10^{10}	7.56×10^{10}
% contribution to total H	38%	1.6%	40%	19%	0.1%	0.4%

Q is the energy released per decay, Q_ν is the energy carried away by the electron antineutrino or neutrino per decay, Q_h is the energy remaining to provide radiogenic heating per decay, "Nuclide mass frac." and "Element mass frac." are the abundances in silicate Earth within the reference Earth model (i.e., kg of nuclide or element per kg of rock), $l_{\bar{\nu}_e}$ and $l'_{\bar{\nu}_e}$ are the specific antineutrino luminosities of pure nuclide or element (i.e., number of $\bar{\nu}_e$ per kg of nuclide or element per second), $L_{\bar{\nu}_e}$ and L_{ν_e} are the antineutrino and neutrino luminosities of the Earth, h and h' are specific heat production rates of pure nuclide or element, H is the radiogenic heat production of the Earth. Mass of ^{4}He is 4.002603254 μ and conversion of amu to MeV is 931.494. Mass of silicate Earth of 4.042×10^{24} kg is used to calculate $L_{\bar{\nu}_e}$, L_{ν_e}, H. $^{\#}$values from Table 7.1; *values from Table 7.2 Geochronology section; **values from *McDonough and Sun* (1995); *Arevalo et al.* (2009) and Th/U ratio from *Wipperfurth et al.* (2018). ‡Energy removed from the Earth by the $\bar{\nu}_e$ in the U and Th decay chains was calculated by integrating the anti-neutrino spectrum reported by S. Enomoto: http://www.awa.tohoku.ac.jp/~sanshiro/research/geoneutrino/spectrum/

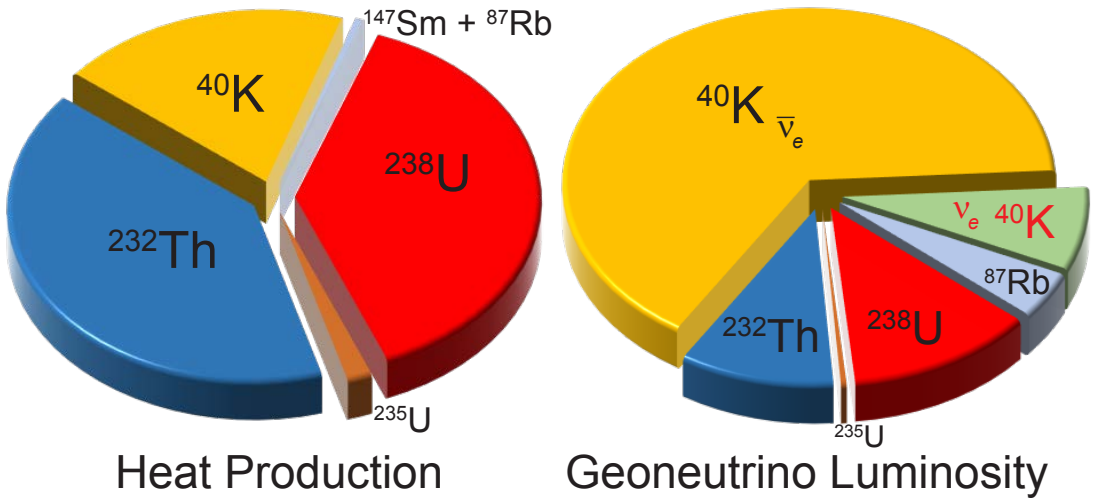

Figure 7.2: The relative contributions to radiogenic heat production and antineutrino luminosity of the Earth. Note the relative contributions of $\bar{\nu}_e$ and ν_e from ^{40}K in terms of geoneutrino luminosity.

A simple formula for the present-day radiogenic heating rate $\tilde{h}$ (in nanowatts per kilogram of rock) from long-lived radionuclides is presented in equation (7.6), where A is elemental concentration as mass fraction (kg-element/kg-rock; e.g., [K] is mass fraction of potassium), and the remaining parameters combine into numerical factors whose values are given (N_A is Avogadro's number, X is natural molar isotopic fraction, μ is molar mass of element, λ is decay constant, Q_h is radiogenic heat released per decay). Multiplying with the mass of the geochemical reservoir of interest M_{res} (to which the elemental concentrations apply), one gets the total radiogenic power H (in terawatts) in that reservoir as shown in equation (7.7). Similarly, the natural specific antineutrino and neutrino luminosities $\tilde{l}$ (in number of particles per second per kilogram of rock) are calculated from equations (7.8) and (7.9). Multiplication with a reservoir mass gives the total luminosities $L_{\bar{\nu}_e}$ and L_{ν_e} (equation 7.10; contributions from individual elements listed in Table 7.3).

$$\tilde{h}\ [\mathrm{nW\,kg^{-1}}] = \sum_{\mathrm{LLRs}} \frac{N_A X \lambda Q_h}{\mu} A$$
$$= 3.389\,[\mathrm{K}] + 11.41\,[\mathrm{Rb}] + 46.07\,[\mathrm{Sm}] + 26180\,[\mathrm{Th}] + 98292\,[\mathrm{U}] \tag{7.6}$$

$$H\ [\mathrm{TW}] = \tilde{h} \times M_{\mathrm{res}} \times 10^{-21} \tag{7.7}$$

$$\tilde{l}_{\bar{\nu}_e}\ [\mathrm{s^{-1}\,kg^{-1}}] = \sum_{\mathrm{LLRs}} \frac{N_A X \lambda n_{\bar{\nu}_e}}{\mu} A$$
$$= (2.797\,[\mathrm{K}] + 86.82\,[\mathrm{Rb}] + 1617\,[\mathrm{Th}] + 7636\,[\mathrm{U}]) \times 10^4 \tag{7.8}$$

$$\tilde{l}_{\nu_e}\ [\mathrm{s^{-1}\,kg^{-1}}] = \sum_{\mathrm{LLRs}} \frac{N_A X \lambda n_{\nu_e}}{\mu} A = 0.3302\,[\mathrm{K}] \times 10^4 \tag{7.9}$$

$$L\ [\mathrm{s^{-1}}] = \tilde{l} \times M_{\mathrm{res}} \tag{7.10}$$

To understand the evolution of the Earth's radiogenic heat and geoneutrino luminosity we must understand the initial starting abundances of the SLR in Table 7.4 in the solar system. At 4.57 Ga the local interstellar medium was populated with gas-dust clouds that were likely in secular equilibrium with ambient galactic sources prior to solar system formation. Recent calculations by *Wasserburg et al.* (2017) demonstrate that the proportional inventory of ^{26}Al, ^{60}Fe, ^{107}Pd, and ^{182}Hf in the

early solar system is unlikely to be a product from asymptotic giant branch (AGB) star. Moreover, supernova sources would likely provide abundant ^{26}Al and ^{60}Fe, whereas the early solar system content of ^{60}Fe is equivalent to the measly ambient galactic supply (*Trappitsch et al.*, 2018). More recent suggestions envisage stellar winds from a massive Wolf-Rayet star injecting ^{26}Al to complement the local inventory of ambient galactic sources (*Young*, 2014; *Gounelle, M. and Meynet, G.*, 2012; *Dwarkadas et al.*, 2017). At the same time, the enhanced abundance of ^{53}Mn and the presence of very short half life isotopes (e.g.,^{41}Ca $t_{1/2} = 0.1$ Ma) present challenges to be explained by models invoking Wolf-Rayet stars (*Vescovi et al.*, 2018). Thus, the addition of mass and momentum from such a stellar source could cause a gravitational collapse of a molecular gas-dust cloud, which may have triggered our solar system formation and explain the observed proportions of short-lived radionuclides.

The total heat production and geoneutrino luminosity for models of the BSE are plotted with respect to time in Figure 7.3, which were calculated using results from Tables 7.3 and 7.4 and updated values for the BSE (*McDonough and Sun*, 1995; *Arevalo et al.*, 2009) and equations (7.6-7.10). The uncertainties for the BSE element abundances reported in Table 7.3 is ±10% (*Wipperfurth et al.*, 2018) with correlations between K, Th and U. Using this Earth model, the present days fluxes are 19.9 ± 3.0 TW for radiogenic heat and the total geoneutrino luminosity is $4.91 \pm 0.75 \times 10^{25}$ $\bar{\nu_e}$+ν_e s^{-1}. The results shown in Figure 7.3 are directly scalable for different size planetary bodies with a bulk Earth composition; lowering the mass of a planet by a factor of 10 results in a decease by a factor of 10 in the heat production and (anti)neutrino luminosity. The most important factors are the amount

of refractory elements and the volatility curve for the planet. The Earth has an Fe/Al value of 20 ± 2 (*McDonough and Sun*, 1995; *Allègre et al.*, 1995), comparable to the chondritic ratio, which is 19 ± 4 (less the 35 value for EH chondrites). The Fe/Al value sets the proportion of refractory elements (Al) to one of the 4 major elements (i.e., O, Fe, Mg and Si) that make up ∼93% of the mass of a terrestrial planet. A K/U or K/Th value sets the volatile depletion curve for the planet. Using $\tilde{h}/A$ factors given in Table 7.4 and equations (7.6) and (7.7), one can readily model the thermal history of various size bodies in the solar system and exoplanets.

We can also compare these results for the present-day flux (i.e., only $\bar{\nu}_e$ from K, Rb, Th and U) versus that reported in the literature. In our comparison and where possible, we used the abundances and masses reported in Table 7.3 to carry out these comparisons. The calculated BSE heat flux in the models of *Enomoto* (2006b), *Dye* (2012), and *Ruedas* (2017) differs from our values by -0.2%, 0.5%, and 0.3%, respectively. The antineutrino luminosity of the modeled BSE from this study and that calculated using the numbers in *Enomoto* (2006b), *Dye* (2012), and *Usman et al.* (2015) yields a 68%, 67%, and 25% difference, respectively; we note that *Dye* (2012), and *Usman et al.* (2015) did not include ^{87}Rb in their calculations, which contributes 5% of the flux.

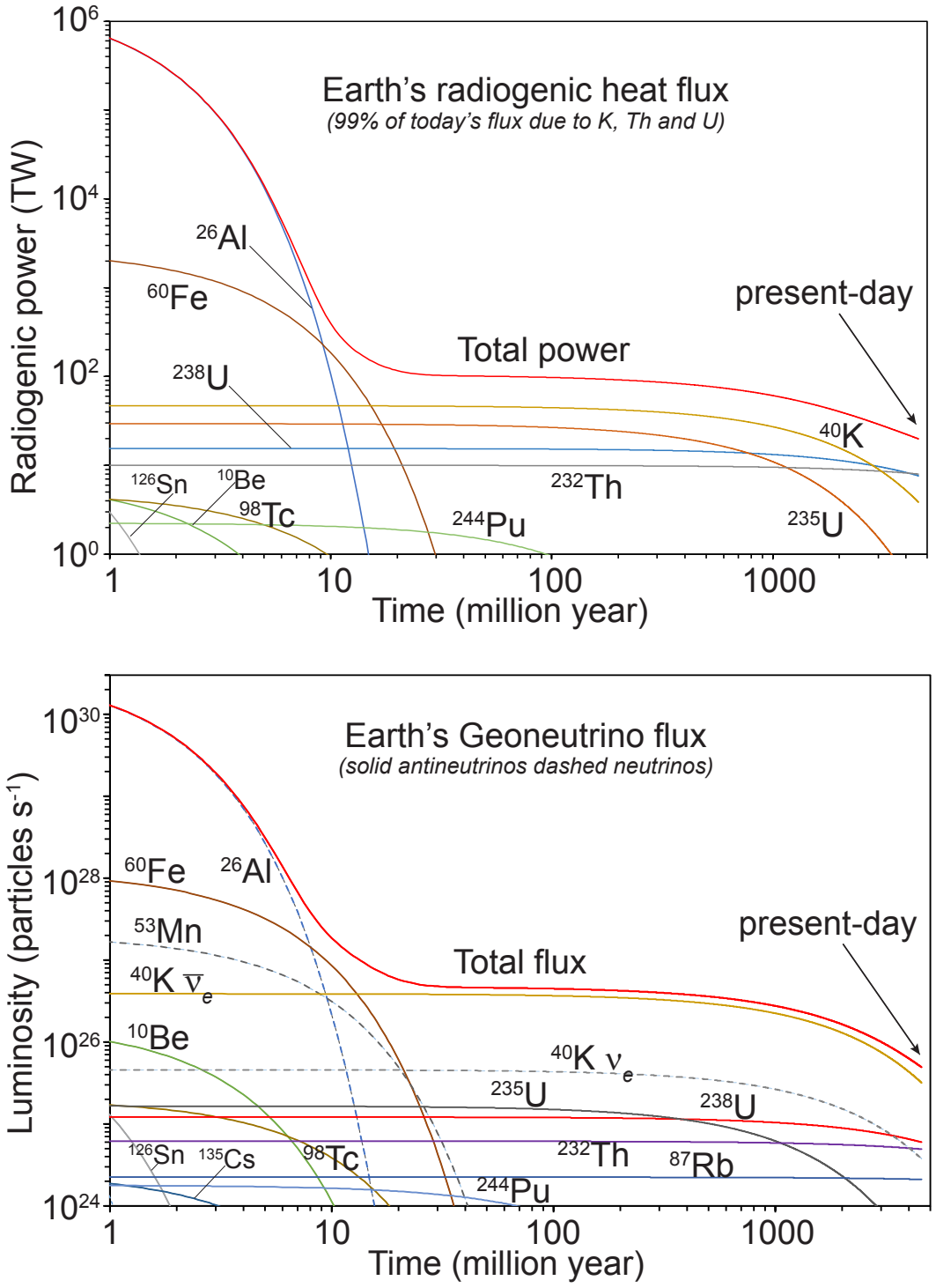

Figure 7.3: The Earth's radiogenic power (upper panel) and geoneutrino flux (lower panel) over the last 4568 million years. These figures assume an Earth mass of 6×10^{24} kg at all times. The power and geoneutrino flux is scalable; if one assumes 1/10 the planetary mass, it has 1/10 the power and luminosity, for an Earth bulk composition.

7.5 Secular variation in the heat and luminosity of the Earth

Secular evolution of the Earth's heat production reveals that only two of the short-lived radionuclides, ^{26}Al, and ^{60}Fe, contribute any significant amount of additional heating to the accreting Earth above the power coming from the long-lived radionuclides (Figure 7.4). Formation and growth of the Earth is envisaged as a process that occurred on timescales of 10^6 to 10^7 years, with planetary growth increasing exponentially according to

$$\frac{m}{M}(t) = 1 - \exp^{-t/\tau}, \tag{7.11}$$

m/M being the fractional mass of the Earth at time t and τ the characteristic accretion time. We show a series of plausible growth curves in Figure 7.4 (inset). Assuming $\tau = 10$ (red curve), then the Earth's mean mass ($\sim 63\%$) is accreted in 10 million years and is virtually fully accreted at about ~ 50 million years after $t_{\text{zero}} = t_{\text{CAI}}$ (i.e., formation time of CAIs), approximately the timing of a putative *Giant impact* event followed by Moon formation (*Barboni et al.*, 2017).

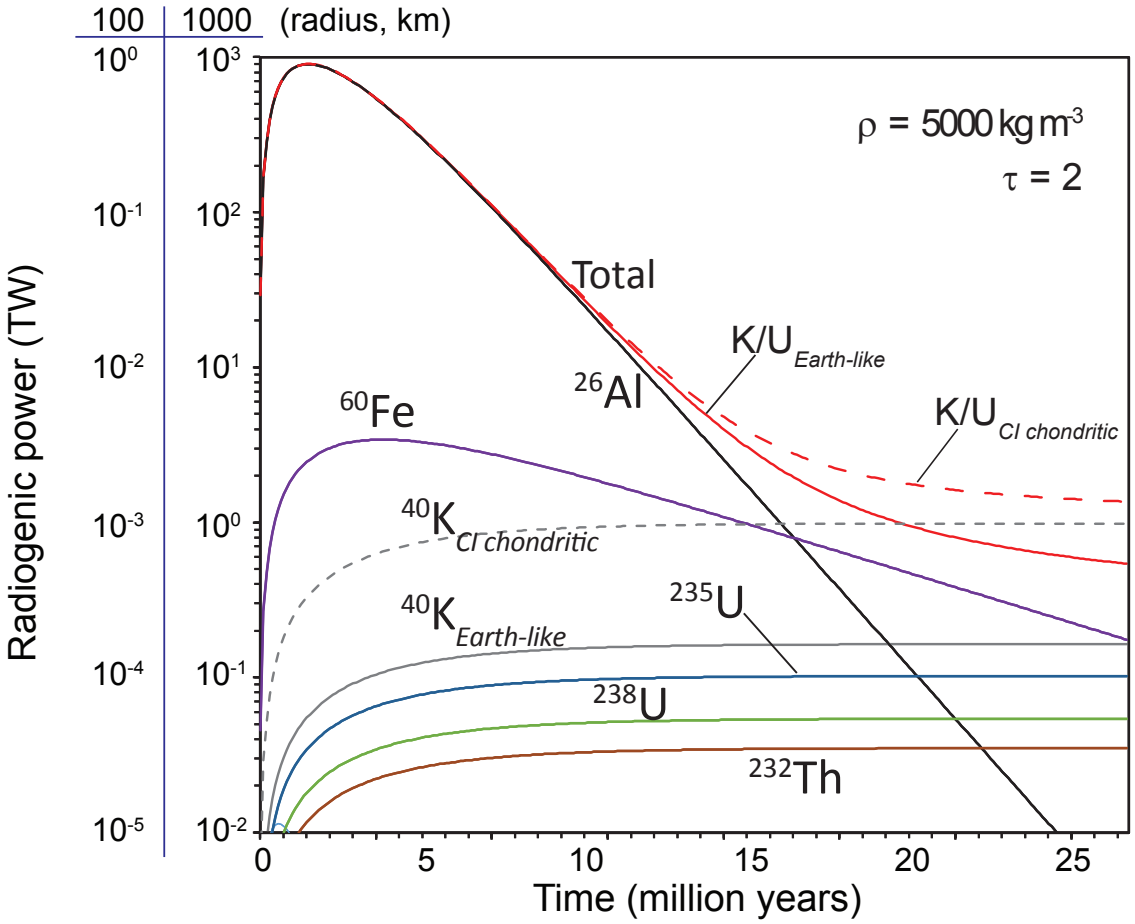

Figure 7.5: A plot of the relative contributions of radiogenic heat to a model terrestrial body (i.e., planet or asteroid) during accretion over the first 25 million years of solar system history. [In the bottom-most left corner of the plot is a tiny dark green peak from SRL ^{126}Sn, which provides a perspective for heat production from all of the remaining contributors.] Two model compositions are shown for K/U = 14,000 (Earth-like, solid lines) and K/U = 85,000 (CI chondrite, dashed lines); both models assume refractory elements at about 2 times that in CI chondrite, which is equivalent to an Earth-like water and CO_2 budget. The terrestrial body is modeled as having a τ value of 2 and a density of 5,000 kg/m^3. The left y-axis (radiogenic power) has two scales, one for a body with a 100 km radius and another having a 1000 km radius. Differences in scales reflex the r^3 dependence of volume and also shows that the result are scalable for any size radius planet or asteroid.

The calculated radiogenic power of the Earth is plotted as a function of accretion time (Figure 7.4). The peak radiogenic heating occurs at about 1 to 5 million years after t_{CAI}, equivalent to the time scale for Mars accretion, when the proto-

Earth produces 5×10^3 to 5×10^4 TW of power, mostly from the decay of ^{26}Al. This power is added on top of the kinetic energy accompanying accretion.

Some core formation models, particularly those invoking continuous metal-silicate segregation, suggest a mean age of core separation of $\approx$ 10 million years after t_{CAI} (*Kleine et al.*, 2009). At this time the combined heat production from ^{26}Al and ^{60}Fe accounts for $\sim$ 90% of the $\sim$ 300 TW of radiogenic power in the Earth. Between 10 and 15 million years after t_{CAI}, heat production from ^{60}Fe exceeds that of ^{26}Al and the long-lived radionuclides, despite the recent low estimate for the initial $(^{60}\mathrm{Fe}/^{56}\mathrm{Fe})_i$ of $(3.8 \pm 6.9) \times 10^{-8}$ (*Trappitsch et al.*, 2018). These findings leave little doubt as to the early hot start of the Earth and the likely melting temperatures experienced by both the forming Fe-rich core and surrounding silicate mantle. Moreover, isolating 90%+ of the Earth's iron into the core at this time results in a superheated condition, given contributions from radiogenic and primordial (i.e., gravitational and accretion) sources.

There is a positive correlation between the Earth's radiogenic power and its geoneutrino flux, with the former given in TW (i.e., 10^{12} watts) and the latter given in number of (anti)neutrinos per cm^2 per second (cm^{-2} s^{-1}). The Earth's geoneutrino signal is also often reported in TNU, which stands for terrestrial neutrino units, and is the number of geoneutrinos counted over a 1-year exposure in a detector having 10^{32} free protons ($\sim$1 kiloton detector of liquid scintillation oil) and 100% counting efficiency. The KamLAND experiment recently reported the geoneutrino flux (*Watanabe*, 2016), based on a fixed Th/U = 3.9. We conducted a Monte Carlo simulation to determine the total signal at the KamLAND experiment, based on a

reference lithospheric model for the local and global contributions to the total flux (Chapter 5). We assumed the following architecture of the BSE: lithosphere underlain by the Depleted Mantle (source of mid-ocean ridge basalt, MORB), with an underlying Enriched Mantle (source of ocean island basalts, OIB) and the volume fraction of Depleted Mantle to Enriched Mantle is 5:1. Input assumption for the MC simulation include: (1) U abundance in the BSE (6 to 40 ng/g), (2) BSE Th/U ($3.776^{+0.122}_{-0.075}$; *Wipperfurth et al.* (2018)) and K/U ($13,800 \pm 1,300$; *Arevalo et al.* (2009)), and (3) accept results with abundances of $U_{\text{Depleted Mantle}} \leqslant U_{\text{Enriched Mantle}}$. Figure 7.6 shows the intersection of the MC model and the measured signal; the ensemble of acceptable BSE models includes the intersection of the best fit line (MC results) and the measurement field determined by the KamLAND experiment (i.e., total power of 10 to 25 TW).

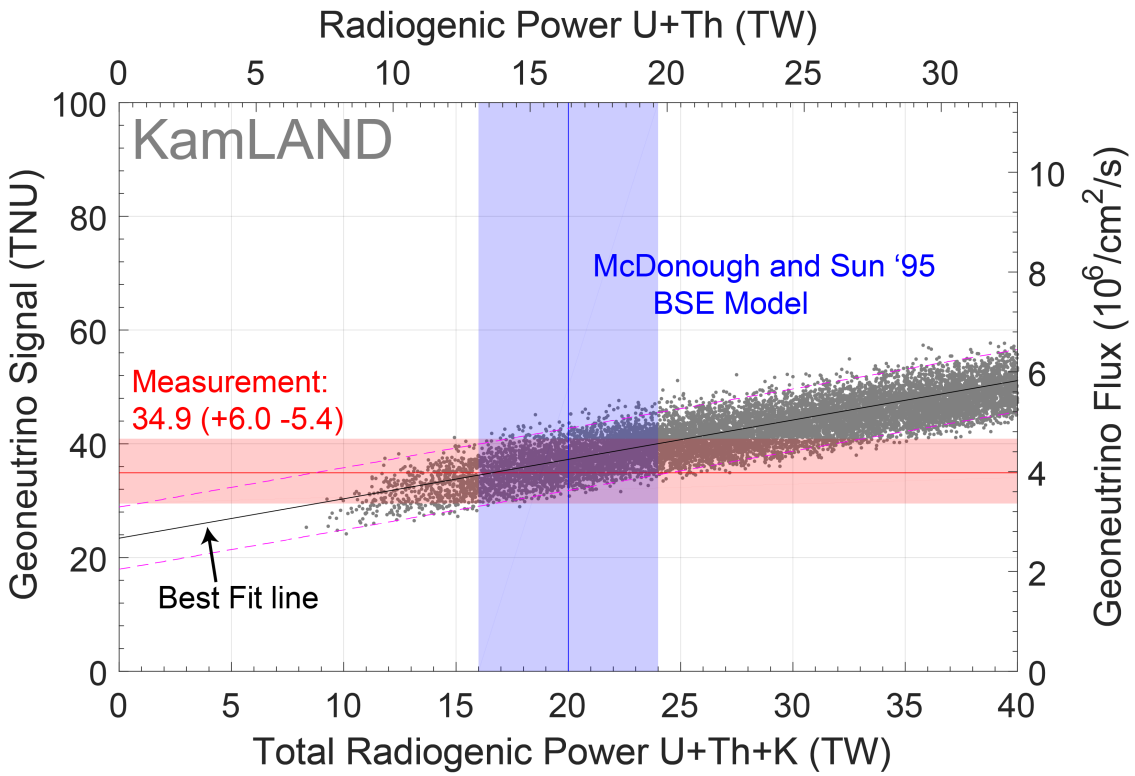

Figure 7.6: The TNU signal (left y-axis) or geoneutrino flux (in cm^{-2} s^{-1}; right y-axis) for the KamLAND experiment versus the total radiogenic power (bottom x-axis) or only radiogenic power from Th + U (upper x-axis)(in TW) within the modeled BSE. The sloped array of points (along with best fit and 2σ limits) are the 1-sigma accepted (15,000 cases) predictions generated with a Monte Carlo model using a reference lithosphere of the local and global contributions to the total geoneutrino flux for the KamLAND location (Chapter 5). The minimum solution (leftmost points) is set by the $8.1^{+2.7}_{-2.0}$ TW lithospheric model and negligible radiogenic power in the mantle. Measured data reported by the KamLAND experiment (horizontal red band) is from *Watanabe* (2016). Vertical blue band represents the model BSE from *McDonough and Sun* (1995), with line representing the central value and total spread of 20% uncertainty. See text for definition of TNU.

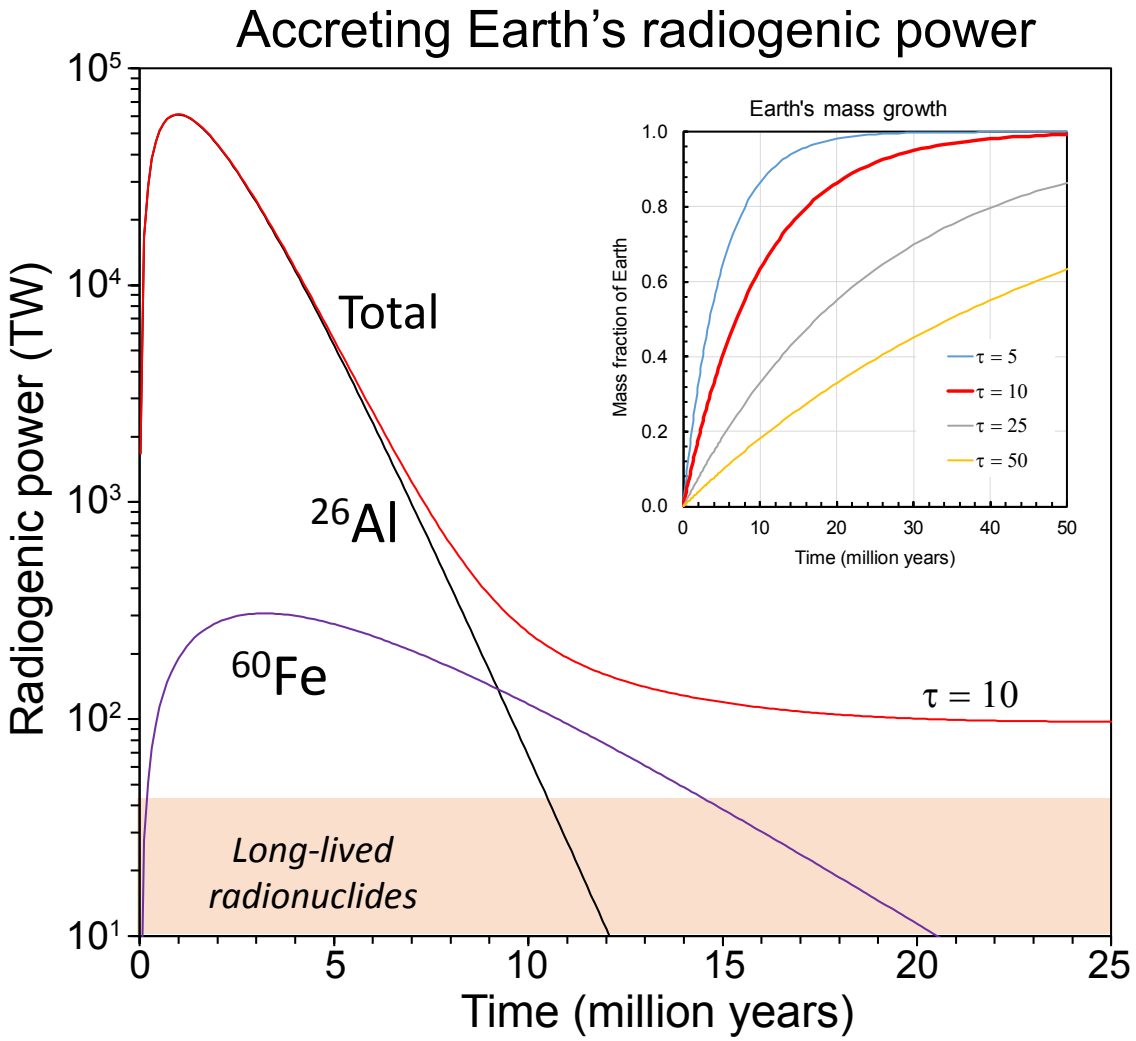

Figure 7.4: A plot of the relative contributions of radiogenic heat to the Earth during accretion over the first 25 million years of Solar system history. The long-lived radionuclides include: ^{40}K, ^{232}Th, ^{235}U, and ^{238}U. Figure 7.3 shows that other short-lived radionuclides contribute negligible amounts of power than what is shown here. Inset diagram shows a series of exponential growth curves $(m/M)(t) = 1 - \exp(-t/\tau)$ for planets. Given an age of Mars of between 2 and 5 million years (*Dauphas and Pourmand*, 2011; *Bouvier et al.*, 2018), its accretion history can be modeled assuming $\tau \leqslant 5$. For the Earth we assume $\tau \approx 10$, however the absolute τ value is not significant, as there is only a 40% reduction in radiogenic power at the peak between a Mars and Earth accretion model.

Table 7.4: Short-lived radioactive decay systems for the Earth.

Decay system	Decay mode	Shape factor $S(p,q)$	Q (MeV)	Q_h (MeV)	$t^{\ddagger}_{1/2}$	$(\tilde{h}/A)$ [nW/kg-elem] at $t_{\rm zero}$ (CAI)	Mole frac. (%) parent nuclide	ref
^{41}Ca $\rightarrow$ ^{41}K	EC	–	0.4217	0	$9.94(15) \times 10^4$	0	$(^{41}\mathrm{Ca}/^{40}\mathrm{Ca})_i = (4.2\pm1.9)\times10^{-9}$	L'17
^{99}Tc $\rightarrow$ ^{99}Ru	β^-	$0.54p^2 + q^2$ [M'15]	0.2975	0.0957	$2.111(12) \times 10^5$	46.71	$(^{99}\mathrm{Tc}/^{100}\mathrm{Ru})_i = <3.9\times10^{-5}$	W'94
^{81}Kr $\rightarrow$ ^{81}Br	EC	–	0.2809	0.0008	$2.29(11) \times 10^5$	–	*not available*	–
^{126}Sn $\rightarrow$ ^{126}Te	β^-, β^-	1$^!$, NuDat$^!$	4.0502	2.8597	$2.35(7) \times 10^5$	3.773×10^4	$(^{126}\mathrm{Sn}/^{124}\mathrm{Sn})_i = \leqslant3\times10^{-3}$	B'17
^{36}Cl $\rightarrow$ ^{36}Ar	β^- (98.1%)	from M'15	0.7095	0.3343	$3.01(2) \times 10^5$	0.9557	$(^{36}\mathrm{Cl}/^{35}\mathrm{Cl})_i = (1.9\pm0.5)\times10^{-8}$	T'13
^{36}Cl $\rightarrow$ ^{36}S	ε (1.9%)	NuDat$^!$	1.1421$^{\rm EC}$	7×10^{-6}	$3.01(2) \times 10^5$	2.011×10^{-5}	"	"
^{79}Se $\rightarrow$ ^{79}Br	β^-	$p^2 + q^2$ [th.]	0.1506	0.0559	$3.26(28) \times 10^5$	–	*not available*	–
^{26}Al $\rightarrow$ ^{26}Mg	EC (18.3%)	–	4.0044	0.3610	$\lambda_{\rm EC}/\lambda = 0.1827$	2057		
^{26}Al $\rightarrow$ ^{26}Mg	β^+ (81.7%)	$p^4 + \frac{10}{3}p^2q^2 + q^4$ [th.]	2.9824	2.7593	$\lambda_{\beta^+}/\lambda = 0.8173$	1.572×10^4		
^{26}Al $\rightarrow$ ^{26}Mg	Overall			3.1203	$7.17(24) \times 10^5$	1.777×10^4	$(^{26}\mathrm{Al}/^{27}\mathrm{Al})_i = (5.2\pm0.2)\times10^{-5}$	K'13
^{10}Be $\rightarrow$ ^{10}B	β^-	$p^4 + \frac{10}{3}p^2q^2 + q^4$ [th.]	0.5568	0.2527	$1.387(12) \times 10^6$	2.270×10^4	$(^{10}\mathrm{Be}/^{9}\mathrm{Be})_i = (5.3\pm1.0)\times10^{-4}$	L'10
^{93}Zr $\rightarrow$ ^{93}Nb	β^-	$p^2 + q^2$ [th.]	0.0903	0.0456	$1.61(5) \times 10^6$	–	*not available*	–
^{150}Gd $\rightarrow$ ^{146}Sm	α	–	2.8077	2.8077	$1.79(8) \times 10^6$	–	*not available*	–
^{135}Cs $\rightarrow$ ^{135}Ba	β^-	$0.10p^2 + q^2$ [M'15]	0.2688	0.0615	$2.3(3) \times 10^6$	119.4	$(^{135}\mathrm{Cs}/^{133}\mathrm{Cs})_i = (2.8\pm2)\times10^{-4}$	B'14
^{60}Fe $\rightarrow$ ^{60}Ni	β^-, β^-	1$^!$, NuDat$^!$	3.0598	2.7077	$2.62(4) \times 10^6$	1.367	$(^{60}\mathrm{Fe}/^{56}\mathrm{Fe})_i = (3.8\pm6.9)\times10^{-8}$	T'18
^{154}Dy $\rightarrow$ ^{150}Gd	α	–	2.9451	2.9451	$3.0(15) \times 10^6$	–	*not available*	–
^{53}Mn $\rightarrow$ ^{53}Cr	EC	–	0.5968	0	$3.74(4) \times 10^6$	0	$(^{53}\mathrm{Mn}/^{55}\mathrm{Mn})_i = (6.5\pm1.9)\times10^{-6}$	T'08
^{98}Tc $\rightarrow$ ^{98}Ru	β^-	1$^!$	1.794	1.5165	$4.2(3) \times 10^6$	1449	$(^{98}\mathrm{Tc}/^{98}\mathrm{Ru})_i = <1.5\times10^{-3}$	B'03
^{97}Tc $\rightarrow$ ^{97}Mo	EC	–	0.3247	0	$4.21(16) \times 10^6$	0	$(^{97}\mathrm{Tc}/^{98}\mathrm{Ru})_i = <2\times10^{-5}$	D'03
^{107}Pd $\rightarrow$ ^{107}Ag	β^-	$p^2 + q^2$ [th.]	0.0341	0.0133	$6.5(3) \times 10^6$	0.2768	$(^{107}\mathrm{Pd}/^{108}\mathrm{Pd})_i = (2.573\pm0.07)\times10^{-5}$	M'17
^{182}Hf $\rightarrow$ ^{182}W	β^-, β^-	$p^2 + q^2$ [th.], NuDat$^!$	2.1958	1.8276	$8.90(9) \times 10^6$	87.07	$(^{182}\mathrm{Hf}/^{180}\mathrm{Hf})_i = (1.018\pm0.043)\times10^{-4}$	K'14
^{129}I $\rightarrow$ ^{129}Xe	β^-	$p^2 + 3.16q^2$ [M'15]	0.1889	0.0853	$1.57(4) \times 10^7$	12.71	$(^{129}\mathrm{I}/^{127}\mathrm{I})_i = (1.4\pm0.1)\times10^{-4}$	G'17
^{205}Pb $\rightarrow$ ^{205}Tl	EC	–	0.05067	0	$1.73(7) \times 10^7$	0	$(^{205}\mathrm{Pb}/^{204}\mathrm{Pb})_i = (1.0\pm0.4)\times10^{-3}$	B'10
^{92}Nb $\rightarrow$ ^{92}Zr	EC	–	2.0059	1.4956	$3.47(24) \times 10^7$	16.71	$(^{92}\mathrm{Nb}/^{93}\mathrm{Nb})_i = (1.7\pm0.6)\times10^{-5}$	I'16
^{244}Pu $\rightarrow$ ^{232}Th	$\alpha^{\dagger}$	NuDat$^!$	17.0845	15.6264	$8.11(3) \times 10^7$	1.363×10^4	$(^{244}\mathrm{Pu}/^{238}\mathrm{U})_i = 0.008$	T'07
^{146}Sm $\rightarrow$ ^{142}Nd	α	–	2.5288	2.5288	$1.03(5) \times 10^8$	0.0754	$(^{146}\mathrm{Sm}/^{144}\mathrm{Sm})_i = (8.28\pm44)\times10^{-3}$	M'14,M'87

Q is the energy of transition (Q value) not accounting for possible branching; Q_h is the energy that remains in the Earth to provide radiogenic heating per decay, accounting for branching. $^!$In some cases, we use shape factors equal to 1 or NuDat-tabulated mean electron energies for forbidden transitions, due to lack of better inputs. $^{\rm EC}$Reports the Q value of EC branch. ‡Half-lives are from NNDCs www.nndc.bnl.gov. Sources in the table are as follows: L'17(*Liu*, 2017), M'15 (*Mougeot*, 2015), W'94(*Wasserburg et al.*, 1994), B'17(*Brennecka et al.*, 2017), T'13 (*Turner et al.*, 2013), K'13 (*Kita et al.*, 2013), L'10 (*Liu et al.*, 2010), B'14 (*Bermingham et al.*, 2014), T'18 (*Trappitsch et al.*, 2018), T'08 (*Trinquier et al.*, 2008), B'03 (*Becker and Walker*, 2003), D'03 (*Dauphas et al.*, 2003), M'17 (*Matthes et al.*, 2017), K'14 (*Kruijer et al.*, 2014), G'17 (*Gilmour and Crowther*, 2017), B'10 (*Baker et al.*, 2010), I'16 (*Iizuka et al.*, 2016), T'07 (*Turner et al.*, 2007), M'14 (*Marks et al.*, 2014), M'87 (*Meissner et al.*, 1987).

7.6 Reflections and applications

Tables 7.3 and 7.4 and equations (7.6–7.10) can be used to calculate heat production and (anti)neutrino luminosity in terrestrial bodies in the solar system and exoplanets, given assumptions about the body's bulk composition. A chondritic Fe/Al (19 ± 4) sets the proportion of refractory elements (e.g., Al, Th and U) to one of the 4 major elements (i.e., O, Fe, Mg and Si) that make up the mass of terrestrial planets. These latter elements are not in fixed chondritic proportions, as is the case for the refractory elements, thus, the mass proportion of O, Fe, Si and Mg can be approximated as 30:30:20:20 (or 50:15:15:15 for atomic proportions), respectively, with proportional differences leading to variations in the metal/silicate mass fraction and fraction of olivine (Mg_2SiO_4) to pyroxene ($MgSiO_3$) in the silicate shell. Figure 7.5 presents the heat production for two different bulk compositional models of small terrestrial planets (or asteroidal body). One model assume a bulk Earth-like composition (*McDonough*, 2014) with an Fe/Al = 20 and depletions in moderately volatile elements, while the other model assumes the same composition, except with moderately volatile elements set by a CI chondrite K/U value of 85,000. A small difference in heat production for these two models in the first 15 million years of solar system history is revealed.

The 1 TW of radiogenic power in the first 2 million years of solar system history for a 100 km radius body (i.e., a size commensurate with estimates of some parent bodies of iron meteorites (*Goldstein et al.*, 2009) is sufficient to induce melting and enhance the effectiveness of metal-silicate fractionation. As noted (*Kleine et al.*,

2009) these bodies will have molten cores and mantles. Thus, their $\epsilon^{182}W$ model ages ($t_{\mathrm{CAI}} + 1$ to 4 million years) reflects metal-silicate fractionation, whereas ages from lithophile and siderophile isotope systems reflect closure of isotopic diffusion.

Acknowledgements

WFM gratefully acknowledges NSF support (EAR1650365), SAW acknowledges support from NSF (EAPSI grant) and Japanese Society for the Promotion of Science (SP17054), and OŠ acknowledges Czech Science Foundation support (GAČR 17-01464S) for this research. We thank the many geo-, nuclear, and particle physics friends who have helped us to understand many of the details of these calculations, especially, Béda Roskovec, Steve Dye, John Learned, Sanshiro Enomoto, Hiroko Watanabe, Katherine Bermingham, and Richard Ash.

Chapter 8: Conclusions and Future Perspectives

Geoneutrinos are currently the only method to directly measure the U and Th abundance in the inaccessible mantle. Their study is therefore also the only direct way to test various models for the composition of the bulk-silicate Earth. Interpretation of the geoneutrino signal from the deep Earth requires an understanding of the amount and distribution of the heat production of the accessible surface and near-surface continental crust on a regional and global scale.

This dissertation explored various topics of the detection and interpretation of the geoneutrino signal including the propagation of particles through matter, the U and Th budget of the core, the heat producing element (HPE) abundance and distribution within the crust, and the energies associated with HPE decay. An overview of each chapter as well as the main conclusions of this dissertation are included here. A brief overview of future perspectives in the field of geoneutrino science follows.

8.1 Summary of Conclusions

- ***Shielding Cave (Ch. 2)***. A simulation of the particle flux which accompanies a nuclear reactor and the effective attenuation of these particles through

a 22 ton shielding Cave was conducted. In developing this "clean room" environment next to the reactor this study demonstrated an order of magnitude reduction in the ambient particle flux as a function of the particle energy.

- ***SNO+ Regional Model (Ch. 3)***. Samples were collected and used to create a 3D model of the 50×50 km region surrounding the SNO+ detector in Sudbury, Canada. The geoneutrino signal from this region yields $7.7^{+7.7}_{-3.0}$ TNU with a bulk-crustal geoneutrino signal of $31.1^{+8.0}_{-4.5}$ TNU. Uncertainty on this signal is large and restricts the usefulness of the SNO+ measurement in the discrimination between bulk-silicate Earth compositional models.

- ***Crustal Heat Production Inferred from Heat Flux (Ch. 4)***. The heat production of the upper and bulk continental crust was calculated from measured surface heat flux and assumed mantle heat flux. Large ranging and spatially heterogeneous heat producing element abundances in the upper crust not consistent with comprehensive crustal studies was observed. Calculated bulk-continental crust heat production was consistent with previous studies when seismically calculated mantle heat flux was included, albeit with large uncertainty.

- ***Reference Models for Earth's Geoneutrino Flux (Ch. 5)***. A global crustal model was created using three different geophysical models, literature geochemical estimates, and a compressional wave speed-SiO^2-HPE correlation for the middle and lower crust. Estimated geoneutrino signal uncertainties from the reference model are on the order of ∼20%, with proportional geo-

physical and geochemical inputs contributing ∼30% and ∼70%, respectively. The use of these different geophysical models yields negligibly different signals at detector locations, even when only taking into account the geophysical uncertainty.

- ***Earth's chondritic Th/U (Ch. 6)***. A dataset of many thousand measured ^{232}Th/^{238}U (κ) and time-integrated ratios from Pb isotopes (κ_{Pb}) for the continental crust, mid-ocean ridge basalts (MORB), and ocean island basalts (OIB) was compiled. Each reservoir (Earth, crust, mantle, and core) was attributed a κ_{Pb} from representative samples with associated weighting factor from the estimated mass of U. The maximum heat power of U and Th in the core was constrained to < 1 TW at 95% confidence limits, with a median value of 0.03 TW.

- ***Radiogenic power and luminosity of the Earth (Ch. 7)***. The energy emitted during decay of both short and long-lived radionuclides was re-evaluated. Total heat production and geoneutrino luminosity for each isotope were calculated for the start of Earth's history using estimates of isotope abundances at solar system formation 4.57 Gyr. The decay of these elements through time was accounted for and the temporal change in heat production and luminosity was calculated.

8.2 Future Perspectives

Geoneutrino science aims to resolve a century-long question of the composition and heat power of the Earth. Increasingly new and larger geoneutrino detectors are being built with each detector requiring a regional model of the crustal geoneutrino signal. The contents of this dissertation have interrogated the geoneutrino signal at active and future detectors, with different models for the estimated signal at KamLAND (Japan) and SNO+ (Canada) in disagreement of the expected crustal signal.

The longest-running detector, KamLAND, needs high-resolution geophysical surveys to map the 3D geologic structure of the closest 100 km. The critical domain of regional crust is represented by the upper crust ($\sim$ top 15 km), where the most heat generation is occurring. Similarly, *Strati et al.* (2017) showed that any improvement of the regional model surrounding SNO+ would be inefficient without characterization of the depth-structure of the sub-groups of the Huronian Supergroup, the largest source of uncertainty on the predicted regional geoneutrino signal.

Geoneutrinos coming from the global crust, which account for $\sim$35% of the total signal, are dependent on estimates of the abundance of HPE within the upper crust. The current generation of global crustal models adopt sigma-mean uncertainties for abundances in the upper crust rather than standard deviation (used for all other uncertainties). Any regional or global geoneutrino modeling should adopt consistent error estimators — be it standard deviation or sigma mean — or justify

the treatment of the upper crust separately from other portions of the crust.

Appendix A1: Appendix to Chapter 3

A1.1 Introduction

The supporting information contain detailed information about geologic features of the collected samples and about the results of measurements performed by gamma-ray spectrometry and ICPMS techniques as well as the ICPMS instrument parameters and the results of external calibration. Data from compiled geochemical databases used characterized particular reservoirs are provided with available information.

A1.2 Tables

RF power	1350 W
HV	10 kV
Cool gas flow rate	16 L/min Ar
Auxiliary gas flow rate	1.5 L/min Ar
Carrier gas flow rate	0.95 L/min Ar
Torch	Quartz glass torch
Sample cone	Aluminum, 1.0 mm aperture
Skimmer cone	Aluminum, 0.5 mm aperture
UO^+/U^+	0.7%
Nebulizer	Microflow PFA
Spray chamber	Apex IR desolvation system
Sample uptake rate	0.05 mL/min
Detector mode	Dual
Dwell time/mass	Variable (5 to 10ms)
Scan type	Electronic sweep through selected masses, 10 points per peak for low and medium resolution
Mass resolution	Low (300) and medium (4000)
Isotopes	^{23}Na, ^{24}Mg, ^{39}K, ^{43}Ca,^{45}Sc, ^{47}Ti, ^{51}V, ^{53}Cr, ^{55}Mn, ^{57}Fe, ^{59}Co, ^{60}Ni, ^{63}Cu, ^{93}Nb, ^{115}In,^{133}Cs, ^{137}Ba, ^{139}La, ^{140}Ce, ^{141}Pr, ^{146}Nd, ^{147}Sm, ^{151}Eu, ^{153}Eu, ^{157}Gd, ^{159}Tb, ^{163}Dy, ^{165}Ho,^{166}Er, ^{169}Tm, ^{172}Yb, ^{175}Lu, ^{178}Hf, ^{180}Ta, ^{181}Ta, ^{184}W, ^{205}Tl, ^{204}Pb, ^{206}Pb,^{207}Pb,^{208}Pb, ^{232}Th, ^{238}U.

Table A1.1: ICP-MS instrument parameters of the Thermo-Finnigan Element2 HR-ICP-MS (University of Maryland).

ID	Latitude WGS84	Longitude WGS84	Geocode	Lithology	U [µg/g]	σ(U) [µg/g]	RSD(U) [%]	Th [µg/g]	σ(Th) [µg/g]	RSD(Th) [%]
SNO_006	46.61	-81.46	11	gneiss	0.04	0.001	1.98	0.04	0.002	3.09
SNO_007	46.61	-81.48	11	tonalite	0.15	0.05	2.73	0.15	0.01	3.11
SNO_009	46.62	-81.44	11	tonalite	0.18	0.01	3.23	0.18	0.01	3.82
SNO_010	46.61	-81.43	29b	norite	1.06	0.05	4.79	1.06	0.25	4.27
SNO_013	46.62	-81.42	11	tonalite	0.15	0.003	2.20	0.15	0.002	2.06
SNO_018	46.59	-81.32	28b	siltstone	1.11	0.03	2.54	1.11	0.11	2.56
SNO_033	46.36	-81.43	19a	siltstone	7.42	0.22	2.58	7.42	0.48	2.99
SNO_035	46.39	-81.38	18a	siltstone	6.64	0.30	4.34	6.64	0.77	4.55
SNO_046	46.47	-80.97	19a	sandstone	1.03	0.05	4.68	1.03	0.19	4.64
SNO_051	46.40	-80.98	23d	noritc quartz gabbro	0.11	0.04	3.53	0.11	0.01	3.73
SNO_070	46.53	-81.10	29b	gabbro	0.62	0.03	4.67	0.62	0.14	4.24
SNO_074	46.50	-81.03	18c	ryolitic flow	9.49	0.30	3.04	9.49	0.91	3.18
SNO_076	46.41	-81.04	19a	quartz sandstone	1.95	0.10	5.46	1.95	0.45	5.26
SNO_089	46.48	-81.21	29b	norite gabbro	0.83	0.03	4.12	0.83	0.28	3.06

Table A1.2: Results of Standard Addition analysis for 14 samples reported as concentration (μg/g) of U and Th. One sigma (σ;μg/g) uncertainty and relative standard deviation (RSD;%) are also reported.

ID Sample	Rock type and location	U [µg/g]	Th [µg/g]
93PCL-340	MM-G Granophyre	3.32	15.52
93PCL-299	MM-G-CAP SEC	3.53	16.49
93PCL-335	MM-G-CAP SEC	2.96	13.22
93PCL-312	MM-G-CAP SEC	3.22	14.41
93PCL-296	MM-G-CAP-SEC	3.51	15.98
93PCL-337	MM-G Granophyre	3.06	13.22
93PCL-313	MM-G-CAP SEC	3.16	14.19
93PCL-336	MM-G Granophyre	3.09	13.45
93PCL-317	MM-G-CAP SEC	3.23	14.57
93PCL-294	MM-G-CAP SEC	3.47	15.77
93PCL-338	MM-G Granophyre	3.06	13.61
93PCL-311	MM-G-CAP SEC	3.21	14.75
93PCL-302	MM-G-CAPSEC	3.36	15.93
93PCL-334	MM-G-CAPSEC	3.08	13.5
93PCL-298	MM-G-CAP SEC	3.48	16.06
93PCL-303	MM-G-CAP SEC	3.45	15.9
93PCL-301	MM-G-CAP SEC	3.31	15.22
93PCL-339	MM-G Granophyre	3.40	15.85
93PCL-316	MM-G-CAPSEC	3.18	14.19
93PCL-297	MM-G-CAPSEC	3.43	15.83
93PCL-293	MM-G-CAP SEC	3.20	15.39
93PCL-315	MM-G-CAP-SEC	3.23	14.65
93PCL-314	MM-G-CAP SEC	3.19	14.29
93PCL-310	MM-G-CAPSEC	3.17	14.83
93PCL-295	MM-G-CAP SEC	3.31	15.62

Table A1.3: Additional samples used for the characterization of GN taken from *Lightfoot et al.* (1997), with the available information about rock type, location, and the U and Th abundances.

Appendix A2: Appendix to Chapter 5

A2.1 Joint Probability Analysis

Huang et al. (2013) calculates the abundance of heat producing elements (HPE) in the middle and lower crust. Given a compressional wave velocity (Vp) from a geophysical model (e.g. LITHO1.0; *Pasyanos et al.* (2014)), an SiO_2 abundance is calculated first from a negative Vp and SiO_2 relationship. Next the HPE abundance is calculated from a positive SiO_2 and HPE abundance trend. Samples of mafic and felsic amphibolite (N = 134; middle crust) and granulite (N = 73; lower crust) have been measured in the laboratory for Vp and SiO_2. A simplifying assumption is that all middle and lower crustal rocks fall within mafic and felsic end-members and that the trend between the end-members is linear (Figure A2.1). The calculation of HPE abundance from Vp is as follows:

$$V_{model} = V_f f + V_m m \tag{A2.1}$$

$$1 = f + m \tag{A2.2}$$

$$a_{output} = a_f f + a_m m \tag{A2.3}$$

where V_f,V_m, a_f, and a_m are the Vp and abundance of the felsic and mafic end-members of amphibolite and granulite, and f and m are the mass proportions of felsic and mafic end-members. Given a Vp from a geophysical model (e.g. LITHO1.0), the HPE abundance is calculated. As discussed in Section 5.4 of this dissertation, the simplifying assumptions of *Huang et al.* (2013) are not valid for portions of the crust.

A joint probability analysis, where the probability density functions of Vp and SiO_2 are compared, would largely avoid crustal tiles from falling outside the end-members from the *Huang et al.* (2013) method (see Chapter 5 for details). In the joint probability analysis, amphibolite and granulite samples are placed into bins based on their measured Vp or SiO_2 abundance (Figure A2.2 and A2.3). Bin sizes are selected using Sturges rule ($N_{bins} = \log_2(N) + 1$)(*Sturges*, 1926). The probability of any SiO_2 bin is determined by the number of samples with a given Vp. For example, a Vp of 7.3 km/s (within Vp bin 7.2-7.4 km/s) in a amphibolite sample would have a 50% probability of having SiO_2 = 45-50 wt%, and 50% probability of having SiO_2 = 50-55 wt% (Figure A2.2).

There exist more samples which contain both HPE and SiO_2 than have measured Vp and SiO_2. Samples with both HPE and SiO_2 were binned by their SiO_2 abundance with the same bins that were used in the Vp vs SiO_2 analysis. These sub-distributions of HPE were fit with log-normal distributions as some sub-distributions

had little number of samples. The distributions of U for each SiO_2 bin are shown in Figure A2.4 and A2.5 for amphibolite and granulite, respectively. Generally, as SiO_2 increases the central value of the sub-distribution fits increases. However, due to the poor correlation between HPE and SiO_2 this was not always the case.

The implementation of the joint probability method is similar to that used by *Huang et al.* (2013). Given a Vp from the geophysical model (e.g. LITHO1.0), there is a probability of the sample having some SiO_2 abundance (Figure A2.2 and A2.3). For each SiO_2 bin, the HPE abundance is randomly chosen based on the probability density function for each U sub-distribution (Figure A2.4 and A2.5). When implemented in a Monte-Carlo simulation this method will sample the entire amphibolite and granulite sample space. The MATLAB code which used to create the data reported in Chapter 5 has already implemented the joint probability method.

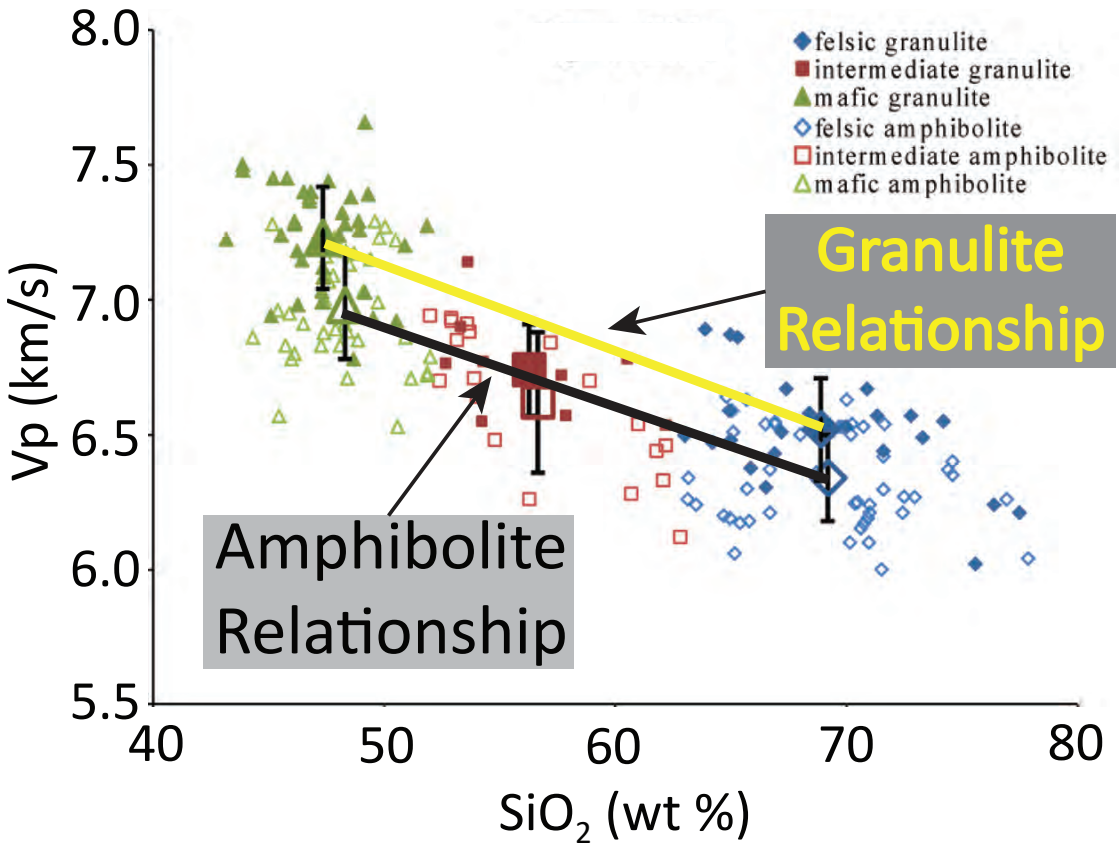

Figure A2.1: Vp (km/s) vs SiO_2 for amphibolite (hollow symbols) and granulite (filled symbols) samples used in this study. Figure adapted from *Huang et al.* (2013).

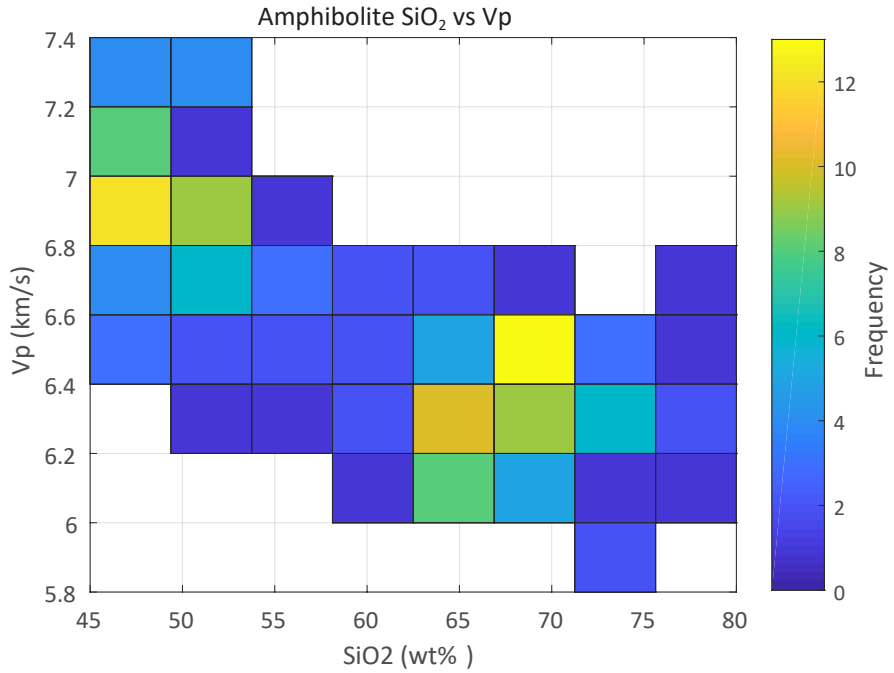

Figure A2.2: Frequency diagram of Vp (km/s) vs SiO_2 (wt%) for amphibolite samples. Vp bin width is 0.2 km/s and SiO_2 bin width is 4.375 wt%. Color indicates frequency of samples which fall within a cell, with maximum frequeny of 13 samples/cell. N = 138.

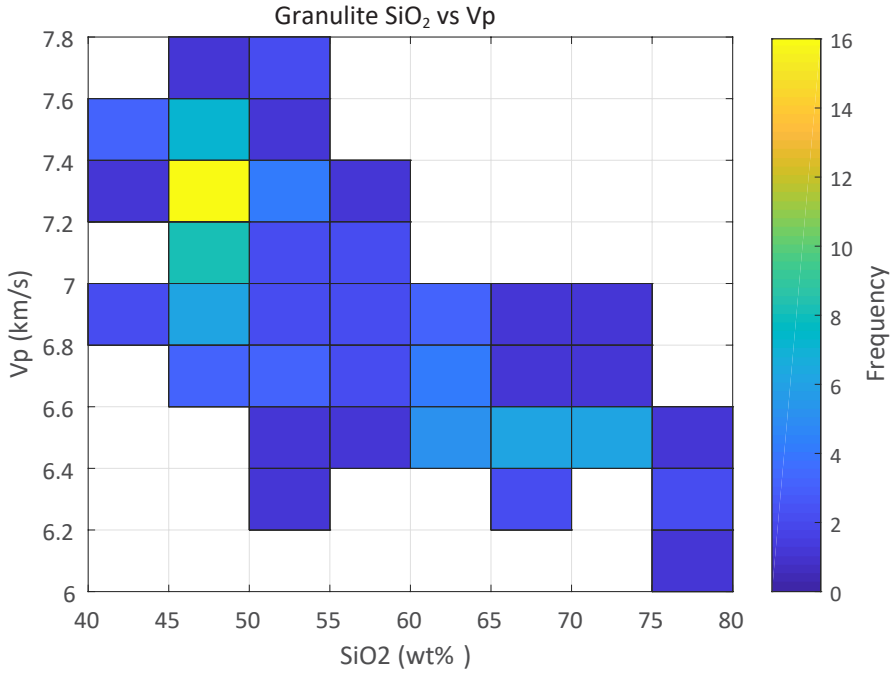

Figure A2.3: Frequency diagram of Vp (km/s) vs SiO_2 (wt%) for granulite samples. Vp bin width is 0.2 km/s and SiO_2 bin width is 5 wt%. Color indicates frequency of samples which fall within a cell, with maximum frequeny of 16 samples/cell. Total N = 105.

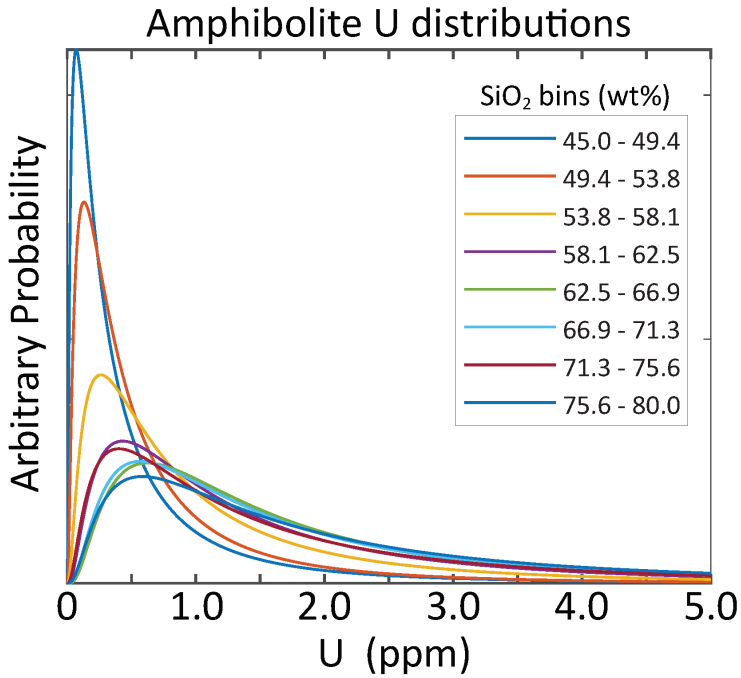

Figure A2.4: Log-normal distributions of U abundance from amphibolite samples binned by SiO_2 abundance. N = 1136. Number of samples per each SiO_2 bin is: N = 16, 197, 90, 75, 133, 194, 180, and 107, respectively for the SiO_2 bin order in the figure.

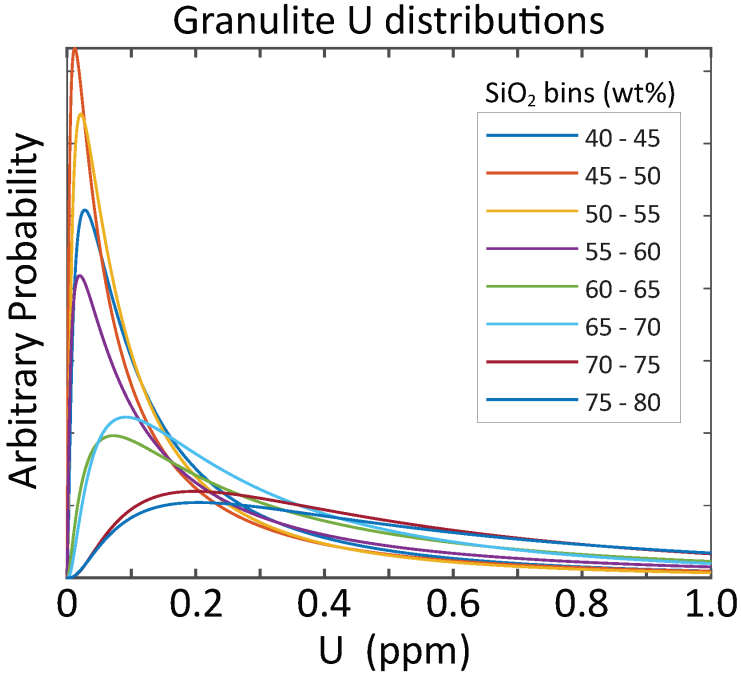

Figure A2.5: Log-normal distributions of U abundance from granulite samples binned by SiO_2 abundance. N = 681. Number of samples per each SiO_2 bin is: N = 9, 206, 182, 74, 70, 49, 73, 18, respectively for the SiO_2 bin order in the figure.

The joint probability method results in HPE abundances in the middle and lower crust lower than those calculated using the *Huang et al.* (2013) method, although within uncertainty. Calculated relative uncertainties are larger than those from the *Huang et al.* (2013) method. The joint probability method is not robust given the limited number of samples which have both measured Vp and SiO_2, which results in Vp-SiO_2 bins which have only one sample (Figure A2.2 and A2.3). The integration of a thermodynamic modeling software, such as Perple_X (*Connolly*, 2005), and the calculation of Vp from the samples with both HPE and SiO_2 abundance, would significantly increase the robustness of the method. Additionally, the frequency binning method used to bin the Vp and SiO_2 data could be applied to the HPE and SiO_2 data to be consistent and to avoid assumption of the probability density function of the HPE data.

A2.2 Geoneutrino Detector Information

Detector	Country	Latitude	Longitude	Depth (m)	Size (kton)	Status
KamLAND	Japan	36.43	137.31	1000	1	On
Borexino	Italy	42.45	13.57	1400	0.3	On
SNO+	Canada	46.475	-81.201	2092	1	(On)
JUNO	China	22.118	112.518	700	20	Const.
Jinping	China	28.15	101.71	2400	4	Prop.
Hawaii	U.S.A.	19.72	-156.32	0	∼	∼

Table A2.1: Geoneutrino detectors information including name, location (country, latitude, longitude), depth below surface, size (in kton of liquid scintillator), and current operating status. SNO+ is collecting data but is not at full efficiency. JUNO is currently under construction. Jinping is in the proposal stage of funding. Hawaii is only a hypothetical location.

A2.3 Dimensional Analysis

The geoneutrino flux unit balance is as follows:

$$\frac{dN(E_{\bar{\nu}_e})}{dE_{\bar{\nu}_e}} = proton * s \frac{\frac{atom}{mol}\frac{decay}{s*atom}}{\frac{kg}{mol}} * \frac{m^2}{proton} * \frac{\bar{\nu}_e}{decay} * m^3 * \frac{\frac{kg}{kg}\frac{kg}{m^3}}{m^2} \tag{A2.4}$$

$$\frac{dN(E_{\bar{\nu}_e})}{dE_{\bar{\nu}_e}} = \cancel{proton * s} \frac{\frac{\cancel{atom}}{\cancel{mol}}\frac{\cancel{decay}}{\cancel{s*atom}}}{\frac{\cancel{kg}}{\cancel{mol}}} * \frac{\cancel{m^2}}{\cancel{proton}} * \frac{\bar{\nu}_e}{\cancel{decay}} * \cancel{m^3} * \frac{\frac{\cancel{kg}}{\cancel{kg}}\frac{\cancel{kg}}{\cancel{m^3}}}{\cancel{m^2}} \tag{A2.5}$$

The resulting signal is number of $\bar{\nu}_e$ interactions. Included is one year exposure

of 10^{32} protons and a detection efficiency of 100%, where one interaction is equivalent to one terrestrial neutrino unit (TNU)(*Mantovani et al.*, 2004).

A2.4 Geoneutrino Fluxes

The following tables provide predicted fluxes (in Terrestrial Neutrino Unit (TNU)) at the six detectors outlined in Table A2.1 (KamLAND: A2.2, Borexino: A2.3, SNO+: A2.4, JUNO: A2.4, Jinping: A2.6, Hawaii: A2.7). Each table includes fluxes from U, Th, and combined U + Th for the layers of the reference model. 1-sigma uncertainty is reported for each value.

KamLAND	CRUST2.0			CRUST1.0			LITHO1.0		
	S(U)	S(Th)	S(U + Th)	S(U)	S(Th)	S(U + Th)	S(U)	S(Th)	S(U + Th)
Sed cc	1.07 $\pm$0.15	0.34 $\pm$0.05	1.41 $\pm$0.19	0.34 $\pm$0.04	0.11 $\pm$0.01	0.45 $\pm$0.06	0.49 $\pm$0.06	0.15 $\pm$0.02	0.64 $\pm$0.09
UC	13.4 $\pm$3.5	3.5 $\pm$0.6	17.0 $\pm$4.0	14.1 $\pm$3.6	3.7 $\pm$0.6	17.8 $\pm$4.2	15.9 $\pm$4.1	4.2 $\pm$0.7	20.1 $\pm$4.7
MC	$2.4^{+2.5}_{-1.2}$	$0.6^{+1.1}_{-0.4}$	$3.1^{+3.5}_{-1.6}$	$3.2^{+2.9}_{-1.5}$	$1.1^{+1.5}_{-0.6}$	$4.3^{+4.3}_{-2.2}$	$3.0^{+3.0}_{-1.5}$	$0.9^{+1.4}_{-0.6}$	$4.0^{+4.3}_{-2.1}$
LC	$0.4^{+0.6}_{-0.2}$	$0.1^{+0.3}_{-0.1}$	$0.6^{+0.9}_{-0.3}$	$0.5^{+0.8}_{-0.3}$	$0.2^{+0.5}_{-0.2}$	$0.8^{+1.4}_{-0.5}$	$0.6^{+0.8}_{-0.3}$	$0.2^{+0.5}_{-0.1}$	$0.8^{+1.3}_{-0.5}$
LM	$1.1^{+1.5}_{-0.6}$	$0.3^{+0.6}_{-0.2}$	$1.4^{+2.1}_{-0.9}$	$1.2^{+1.7}_{-0.7}$	$0.4^{+0.6}_{-0.2}$	$1.5^{+2.3}_{-0.9}$	$0.6^{+0.9}_{-0.4}$	$0.2^{+0.3}_{-0.1}$	$0.8^{+1.2}_{-0.5}$
Sed oc	0.13 $\pm$0.02	0.04 $\pm$0.01	0.17 $\pm$0.02	0.11 $\pm$0.01	0.03 $\pm$0.00	0.14 $\pm$0.02	0.11 $\pm$0.01	0.03 $\pm$0.00	0.14 $\pm$0.02
OC	0.08 $\pm$0.02	0.02 $\pm$0.00	0.10 $\pm$0.02	0.09 $\pm$0.02	0.02 $\pm$0.00	0.11 $\pm$0.03	0.12 $\pm$0.03	0.02 $\pm$0.01	0.14 $\pm$0.04
Bulk cc	$17.6^{+4.8}_{-3.8}$	$5.0^{+1.3}_{-1.0}$	$22.7^{+5.9}_{-4.7}$	$18.5^{+5.2}_{-4.1}$	$5.6^{+1.7}_{-1.3}$	$24.2^{+6.7}_{-5.2}$	$20.4^{+5.7}_{-4.5}$	$6.0^{+1.6}_{-1.3}$	$26.4^{+7.1}_{-5.6}$
Bulk Crust	$17.8^{+4.8}_{-3.8}$	$5.1^{+1.3}_{-1.0}$	$23.0^{+5.9}_{-4.7}$	$18.7^{+5.2}_{-4.1}$	$5.6^{+1.7}_{-1.3}$	$24.4^{+6.7}_{-5.2}$	$20.6^{+5.7}_{-4.5}$	$6.0^{+1.7}_{-1.3}$	$26.7^{+7.1}_{-5.6}$
Near-Field Crust	$12.0^{+3.2}_{-2.5}$	$3.3^{+0.8}_{-0.6}$	$15.3^{+3.8}_{-3.1}$	$12.9^{+3.6}_{-2.8}$	$3.8^{+1.0}_{-0.8}$	$16.7^{+4.5}_{-3.5}$	$14.0^{+3.9}_{-3.1}$	$4.0^{+1.0}_{-0.8}$	$18.0^{+4.7}_{-3.7}$
Far-Field Crust	$5.9^{+1.6}_{-1.3}$	$1.8^{+0.6}_{-0.4}$	$7.6^{+2.2}_{-1.7}$	$5.9^{+1.7}_{-1.3}$	$1.8^{+0.6}_{-0.5}$	$7.7^{+2.2}_{-1.7}$	$6.6^{+1.9}_{-1.5}$	$2.0^{+0.7}_{-0.5}$	$8.6^{+2.5}_{-1.9}$
Bulk LS	$19.4^{+5.1}_{-4.0}$	$5.6^{+1.5}_{-1.2}$	$25.0^{+6.4}_{-5.1}$	$20.4^{+5.6}_{-4.4}$	$6.2^{+1.8}_{-1.4}$	$26.7^{+7.1}_{-5.6}$	$21.6^{+5.8}_{-4.6}$	$6.3^{+1.7}_{-1.3}$	$27.9^{+7.3}_{-5.8}$
DM	3.9 $\pm$1.2	1.0 $\pm$0.7	4.9 $\pm$1.8	3.9 $\pm$1.2	1.0 $\pm$0.7	4.9 $\pm$1.8	4.0 $\pm$1.2	1.0 $\pm$0.7	5.0 $\pm$1.9
EM	3.6 $\pm$1.8	0.9 $\pm$0.5	4.6 $\pm$2.3	3.8 $\pm$1.9	1.0 $\pm$0.5	4.7 $\pm$2.4	3.7 $\pm$1.8	1.0 $\pm$0.5	4.6 $\pm$2.3
Grand Total	$27.1^{+4.6}_{-3.9}$	$7.6^{+1.5}_{-1.2}$	$34.7^{+5.8}_{-5.0}$	$28.3^{+5.0}_{-4.2}$	$8.3^{+1.8}_{-1.5}$	$36.6^{+6.5}_{-5.5}$	$29.4^{+5.2}_{-4.4}$	$8.4^{+1.7}_{-1.4}$	$37.9^{+6.6}_{-5.6}$

Table A2.2: Geoneutrino flux (in TNU) at KamLAND using CRUST2.0, CRUST1.0, and LITHO1.0 geophysical models with 1-sigma uncertainty. S(U), S(Th), and S(U + Th) is the geoneutrino flux from U, Th, and combined U + Th, respectively. Layers include sediment above continental crust ('Sed cc'), upper crust ('UC'), middle crust ('MC'), lower crust ('LC'), lithospheric mantle ('LM'), sediment above oceanic crust ('Sed oc'), oceanic crust ('OC'), bulk continental crust ('Bulk cc'), bulk crust, Near-field crust, Far-Field crust, bulk lithosphere ('Bulk LS'), depleted mantle ('DM'), enriched mantle ('EM'), and total signal ('Grand Total').

Borexino	CRUST2.0			CRUST1.0			LITHO1.0		
	S(U)	S(Th)	S(U + Th)	S(U)	S(Th)	S(U + Th)	S(U)	S(Th)	S(U + Th)
Sed cc	1.42 $\pm$0.18	0.46 $\pm$0.06	1.88 $\pm$0.25	1.28 $\pm$0.16	0.41 $\pm$0.05	1.69 $\pm$0.22	3.08 $\pm$0.40	0.97 $\pm$0.13	4.05 $\pm$0.53
UC	16.5 $\pm$4.3	4.4 $\pm$0.7	20.9 $\pm$4.9	16.5 $\pm$4.3	4.3 $\pm$0.7	20.8 $\pm$4.9	14.9 $\pm$3.9	3.9 $\pm$0.6	18.9 $\pm$4.4
MC	$3.9^{+3.6}_{-1.9}$	$1.3^{+1.8}_{-0.8}$	$5.3^{+5.3}_{-2.7}$	$3.8^{+3.5}_{-1.8}$	$1.3^{+1.8}_{-0.7}$	$5.1^{+5.2}_{-2.6}$	$3.9^{+3.6}_{-1.9}$	$1.3^{+1.7}_{-0.7}$	$5.2^{+5.2}_{-2.6}$
LC	$0.9^{+1.1}_{-0.5}$	$0.4^{+0.9}_{-0.3}$	$1.3^{+2.0}_{-0.8}$	$0.8^{+1.0}_{-0.4}$	$0.4^{+0.8}_{-0.3}$	$1.2^{+1.9}_{-0.7}$	$0.8^{+1.1}_{-0.5}$	$0.4^{+0.8}_{-0.2}$	$1.2^{+1.9}_{-0.7}$
LM	$1.5^{+2.1}_{-0.9}$	$0.5^{+0.8}_{-0.3}$	$1.9^{+2.8}_{-1.1}$	$1.4^{+2.0}_{-0.8}$	$0.4^{+0.7}_{-0.3}$	$1.8^{+2.7}_{-1.1}$	$0.6^{+0.9}_{-0.4}$	$0.2^{+0.3}_{-0.1}$	$0.8^{+1.3}_{-0.5}$
Sed oc	0.19 $\pm$0.02	0.06 $\pm$0.01	0.25 $\pm$0.03	0.30 $\pm$0.04	0.10 $\pm$0.01	0.40 $\pm$0.05	0.29 $\pm$0.04	0.09 $\pm$0.01	0.38 $\pm$0.05
OC	0.05 $\pm$0.01	0.01 $\pm$0.00	0.06 $\pm$0.01	0.07 $\pm$0.02	0.01 $\pm$0.00	0.09 $\pm$0.02	0.10 $\pm$0.02	0.02 $\pm$0.00	0.12 $\pm$0.03
Bulk cc	$23.3^{+6.3}_{-5.0}$	$7.2^{+2.1}_{-1.6}$	$30.5^{+8.1}_{-6.4}$	$22.8^{+6.2}_{-4.9}$	$7.0^{+2.0}_{-1.6}$	$29.9^{+8.0}_{-6.3}$	$23.3^{+5.9}_{-4.7}$	$7.1^{+2.0}_{-1.6}$	$30.5^{+7.7}_{-6.2}$
Bulk Crust	$23.5^{+6.3}_{-5.0}$	$7.2^{+2.1}_{-1.7}$	$30.8^{+8.2}_{-6.5}$	$23.2^{+6.2}_{-4.9}$	$7.1^{+2.1}_{-1.6}$	$30.4^{+8.0}_{-6.3}$	$23.7^{+6.0}_{-4.8}$	$7.3^{+2.0}_{-1.6}$	$31.0^{+7.8}_{-6.2}$
Near-Field Crust	$13.1^{+3.5}_{-2.8}$	$4.0^{+1.1}_{-0.8}$	$17.1^{+4.4}_{-3.5}$	$13.2^{+3.5}_{-2.8}$	$3.9^{+1.0}_{-0.8}$	$17.1^{+4.3}_{-3.5}$	$12.7^{+3.0}_{-2.4}$	$3.9^{+0.9}_{-0.8}$	$16.6^{+3.8}_{-3.1}$
Far-Field Crust	$10.4^{+2.9}_{-2.3}$	$3.3^{+1.1}_{-0.8}$	$13.7^{+3.9}_{-3.0}$	$10.0^{+2.8}_{-2.2}$	$3.2^{+1.1}_{-0.8}$	$13.2^{+3.7}_{-2.9}$	$11.0^{+3.0}_{-2.4}$	$3.4^{+1.1}_{-0.8}$	$14.4^{+4.0}_{-3.1}$
Bulk LS	$25.6^{+6.7}_{-5.3}$	$7.9^{+2.3}_{-1.8}$	$33.6^{+8.7}_{-6.9}$	$25.2^{+6.6}_{-5.2}$	$7.8^{+2.2}_{-1.7}$	$33.0^{+8.6}_{-6.8}$	$24.6^{+6.1}_{-4.9}$	$7.6^{+2.1}_{-1.6}$	$32.3^{+7.9}_{-6.4}$
DM	3.7 $\pm$1.1	1.0 $\pm$0.7	4.7 $\pm$1.8	3.8 $\pm$1.2	1.0 $\pm$0.7	4.8 $\pm$1.8	4.0 $\pm$1.2	1.0 $\pm$0.7	5.0 $\pm$1.9
EM	3.6 $\pm$1.8	0.9 $\pm$0.5	4.6 $\pm$2.3	3.8 $\pm$1.9	1.0 $\pm$0.5	4.8 $\pm$2.4	3.7 $\pm$1.8	1.0 $\pm$0.5	4.6 $\pm$2.3
Grand Total	$33.2^{+6.0}_{-5.1}$	$9.9^{+2.2}_{-1.8}$	$43.2^{+8.0}_{-6.7}$	$33.0^{+6.0}_{-5.1}$	$9.8^{+2.2}_{-1.8}$	$42.9^{+7.9}_{-6.6}$	$32.5^{+5.5}_{-4.7}$	$9.6^{+2.1}_{-1.7}$	$42.1^{+7.3}_{-6.2}$

Table A2.3: Geoneutrino flux at Borexino (in TNU) using CRUST2.0, CRUST1.0, and LITHO1.0 geophysical models with 1-sigma uncertainty. Layer abbreviations are the same as Table A2.2

SNO+	CRUST2.0			CRUST1.0			LITHO1.0		
	S(U)	S(Th)	S(U + Th)	S(U)	S(Th)	S(U + Th)	S(U)	S(Th)	S(U + Th)
Sed cc	0.44 $\pm$0.06	0.14 $\pm$0.02	0.58 $\pm$0.08	0.36 $\pm$0.05	0.11 $\pm$0.01	0.47 $\pm$0.06	0.37 $\pm$0.05	0.12 $\pm$0.02	0.49 $\pm$0.06
UC	22.4 $\pm$5.8	5.9 $\pm$0.9	28.3 $\pm$6.6	18.3 $\pm$4.7	4.8 $\pm$0.8	23.1 $\pm$5.4	19.6 $\pm$5.1	5.2 $\pm$0.8	24.7 $\pm$5.8
MC	$4.5^{+4.4}_{-2.2}$	$1.4^{+2.2}_{-0.8}$	$5.9^{+6.5}_{-3.1}$	$4.8^{+4.7}_{-2.4}$	$1.5^{+2.4}_{-0.9}$	$6.4^{+6.9}_{-3.3}$	$4.6^{+4.5}_{-2.3}$	$1.4^{+2.1}_{-0.8}$	$6.0^{+6.5}_{-3.1}$
LC	$0.8^{+1.1}_{-0.5}$	$0.3^{+0.8}_{-0.2}$	$1.2^{+1.9}_{-0.7}$	$0.9^{+1.3}_{-0.6}$	$0.4^{+1.1}_{-0.3}$	$1.4^{+2.4}_{-0.9}$	$0.9^{+1.2}_{-0.5}$	$0.3^{+0.8}_{-0.2}$	$1.2^{+2.1}_{-0.8}$
LM	$1.4^{+1.9}_{-0.8}$	$0.4^{+0.7}_{-0.3}$	$1.8^{+2.7}_{-1.1}$	$1.4^{+2.0}_{-0.8}$	$0.4^{+0.7}_{-0.3}$	$1.8^{+2.7}_{-1.1}$	$1.6^{+2.3}_{-0.9}$	$0.5^{+0.8}_{-0.3}$	$2.1^{+3.1}_{-1.2}$
Sed oc	0.10 $\pm$0.01	0.03 $\pm$0.00	0.13 $\pm$0.02	0.13 $\pm$0.02	0.04 $\pm$0.01	0.18 $\pm$0.02	0.13 $\pm$0.02	0.04 $\pm$0.01	0.17 $\pm$0.02
OC	0.04 $\pm$0.01	0.01 $\pm$0.00	0.05 $\pm$0.01	0.05 $\pm$0.01	0.01 $\pm$0.00	0.06 $\pm$0.02	0.06 $\pm$0.02	0.01 $\pm$0.00	0.08 $\pm$0.02
Bulk cc	$28.7^{+8.1}_{-6.3}$	$8.5^{+2.5}_{-1.9}$	$37.3^{+10.2}_{-8.0}$	$25.1^{+7.3}_{-5.7}$	$7.7^{+2.6}_{-2.0}$	$32.9^{+9.6}_{-7.4}$	$26.1^{+7.5}_{-5.8}$	$7.7^{+2.4}_{-1.8}$	$33.8^{+9.6}_{-7.5}$
Bulk Crust	$28.9^{+8.1}_{-6.3}$	$8.5^{+2.5}_{-1.9}$	$37.5^{+10.2}_{-8.0}$	$25.3^{+7.3}_{-5.7}$	$7.8^{+2.6}_{-2.0}$	$33.1^{+9.6}_{-7.4}$	$26.3^{+7.5}_{-5.8}$	$7.8^{+2.4}_{-1.8}$	$34.1^{+9.6}_{-7.5}$
Near-Field Crust	$17.2^{+4.9}_{-3.8}$	$5.0^{+1.3}_{-1.0}$	$22.3^{+5.9}_{-4.7}$	$14.7^{+4.2}_{-3.3}$	$4.4^{+1.3}_{-1.0}$	$19.2^{+5.4}_{-4.2}$	$15.1^{+4.3}_{-3.3}$	$4.5^{+1.3}_{-1.0}$	$19.6^{+5.4}_{-4.2}$
Far-Field Crust	$11.6^{+3.4}_{-2.6}$	$3.5^{+1.2}_{-0.9}$	$15.2^{+4.4}_{-3.4}$	$10.6^{+3.1}_{-2.4}$	$3.3^{+1.3}_{-0.9}$	$14.0^{+4.3}_{-3.3}$	$11.2^{+3.3}_{-2.5}$	$3.3^{+1.1}_{-0.8}$	$14.5^{+4.3}_{-3.3}$
Bulk LS	$30.8^{+8.4}_{-6.6}$	$9.2^{+2.6}_{-2.0}$	$40.1^{+10.6}_{-8.4}$	$27.3^{+7.6}_{-6.0}$	$8.4^{+2.8}_{-2.1}$	$35.9^{+10.1}_{-7.9}$	$28.5^{+8.0}_{-6.2}$	$8.5^{+2.6}_{-2.0}$	$37.1^{+10.3}_{-8.0}$
DM	3.8 $\pm$1.1	1.0 $\pm$0.7	4.7 $\pm$1.8	3.8 $\pm$1.1	1.0 $\pm$0.7	4.8 $\pm$1.8	3.7 $\pm$1.1	1.0 $\pm$0.7	4.7 $\pm$1.8
EM	3.6 $\pm$1.8	0.9 $\pm$0.5	4.6 $\pm$2.3	3.8 $\pm$1.9	1.0 $\pm$0.5	4.7 $\pm$2.4	3.7 $\pm$1.8	1.0 $\pm$0.5	4.6 $\pm$2.3
Grand Total	$38.5^{+7.6}_{-6.3}$	$11.2^{+2.5}_{-2.0}$	$49.8^{+9.7}_{-8.1}$	$35.2^{+6.9}_{-5.8}$	$10.5^{+2.7}_{-2.1}$	$45.7^{+9.3}_{-7.7}$	$36.2^{+7.2}_{-6.0}$	$10.5^{+2.5}_{-2.0}$	$46.8^{+9.4}_{-7.8}$

Table A2.4: Geoneutrino flux at SNO+ (in TNU) using CRUST2.0, CRUST1.0, and LITHO1.0 geophysical models with 1-sigma uncertainty. Layer abbreviations are the same as Table A2.2

JUNO	CRUST2.0			CRUST1.0			LITHO1.0		
	S(U)	S(Th)	S(U + Th)	S(U)	S(Th)	S(U + Th)	S(U)	S(Th)	S(U + Th)
Sed cc	0.98 $\pm$0.13	0.31 $\pm$0.04	1.30 $\pm$0.17	0.45 $\pm$0.06	0.14 $\pm$0.02	0.59 $\pm$0.08	0.44 $\pm$0.06	0.14 $\pm$0.02	0.58 $\pm$0.08
UC	15.6 $\pm$4.0	4.1 $\pm$0.7	19.7 $\pm$4.6	16.0 $\pm$4.1	4.2 $\pm$0.7	20.2 $\pm$4.8	17.0 $\pm$4.4	4.5 $\pm$0.7	21.5 $\pm$5.0
MC	$3.7^{+3.4}_{-1.8}$	$1.2^{+1.7}_{-0.7}$	$4.9^{+5.0}_{-2.5}$	$3.8^{+3.4}_{-1.8}$	$1.3^{+1.7}_{-0.7}$	$5.1^{+5.1}_{-2.5}$	$3.7^{+3.5}_{-1.8}$	$1.2^{+1.7}_{-0.7}$	$4.9^{+5.1}_{-2.5}$
LC	$0.7^{+0.9}_{-0.4}$	$0.3^{+0.7}_{-0.2}$	$1.1^{+1.7}_{-0.7}$	$0.8^{+1.0}_{-0.4}$	$0.4^{+0.8}_{-0.2}$	$1.1^{+1.8}_{-0.7}$	$0.8^{+1.0}_{-0.4}$	$0.3^{+0.8}_{-0.2}$	$1.1^{+1.8}_{-0.7}$
LM	$1.4^{+2.0}_{-0.8}$	$0.4^{+0.7}_{-0.3}$	$1.9^{+2.8}_{-1.1}$	$1.4^{+1.9}_{-0.8}$	$0.4^{+0.7}_{-0.3}$	$1.8^{+2.6}_{-1.1}$	$0.5^{+0.7}_{-0.3}$	$0.1^{+0.2}_{-0.1}$	$0.6^{+0.9}_{-0.4}$
Sed oc	0.07 $\pm$0.01	0.02 $\pm$0.00	0.10 $\pm$0.01	0.12 $\pm$0.02	0.04 $\pm$0.01	0.16 $\pm$0.02	0.12 $\pm$0.02	0.04 $\pm$0.01	0.16 $\pm$0.02
OC	0.04 $\pm$0.01	0.01 $\pm$0.00	0.05 $\pm$0.01	0.07 $\pm$0.02	0.02 $\pm$0.00	0.09 $\pm$0.02	0.10 $\pm$0.02	0.02 $\pm$0.01	0.12 $\pm$0.03
Bulk cc	$21.5^{+5.9}_{-4.6}$	$6.5^{+1.9}_{-1.5}$	$28.1^{+7.5}_{-5.9}$	$21.4^{+6.0}_{-4.7}$	$6.6^{+2.0}_{-1.5}$	$28.0^{+7.7}_{-6.1}$	$22.4^{+6.3}_{-4.9}$	$6.7^{+2.0}_{-1.5}$	$29.2^{+8.0}_{-6.3}$
Bulk Crust	$21.6^{+5.9}_{-4.6}$	$6.5^{+1.9}_{-1.5}$	$28.2^{+7.6}_{-6.0}$	$21.6^{+6.0}_{-4.7}$	$6.6^{+2.0}_{-1.5}$	$28.3^{+7.7}_{-6.1}$	$22.7^{+6.3}_{-4.9}$	$6.8^{+2.0}_{-1.5}$	$29.5^{+8.0}_{-6.3}$
Near-Field Crust	$12.8^{+3.5}_{-2.7}$	$3.8^{+1.0}_{-0.8}$	$16.6^{+4.3}_{-3.4}$	$12.8^{+3.6}_{-2.8}$	$3.8^{+1.1}_{-0.8}$	$16.7^{+4.5}_{-3.5}$	$13.2^{+3.7}_{-2.9}$	$3.8^{+1.0}_{-0.8}$	$17.1^{+4.5}_{-3.6}$
Far-Field Crust	$8.8^{+2.5}_{-1.9}$	$2.7^{+0.9}_{-0.7}$	$11.6^{+3.3}_{-2.6}$	$8.8^{+2.5}_{-1.9}$	$2.8^{+0.9}_{-0.7}$	$11.6^{+3.3}_{-2.6}$	$9.5^{+2.7}_{-2.1}$	$2.9^{+1.0}_{-0.7}$	$12.4^{+3.6}_{-2.8}$
Bulk LS	$23.7^{+6.3}_{-5.0}$	$7.2^{+2.1}_{-1.6}$	$31.0^{+8.1}_{-6.4}$	$23.6^{+6.4}_{-5.0}$	$7.3^{+2.2}_{-1.7}$	$30.9^{+8.3}_{-6.5}$	$23.3^{+6.4}_{-5.0}$	$7.0^{+2.0}_{-1.6}$	$30.4^{+8.1}_{-6.4}$
DM	3.8 $\pm$1.1	1.0 $\pm$0.7	4.8 $\pm$1.8	3.8 $\pm$1.2	1.0 $\pm$0.7	4.8 $\pm$1.8	4.0 $\pm$1.2	1.0 $\pm$0.7	5.1 $\pm$1.9
EM	3.6 $\pm$1.8	0.9 $\pm$0.5	4.6 $\pm$2.3	3.7 $\pm$1.9	1.0 $\pm$0.5	4.7 $\pm$2.4	3.7 $\pm$1.9	1.0 $\pm$0.5	4.6 $\pm$2.4
Grand Total	$31.3^{+5.7}_{-4.8}$	$9.2^{+2.0}_{-1.7}$	$40.5^{+7.4}_{-6.3}$	$31.4^{+5.8}_{-4.9}$	$9.3^{+2.1}_{-1.7}$	$40.7^{+7.6}_{-6.4}$	$31.3^{+5.7}_{-4.8}$	$9.1^{+2.0}_{-1.6}$	$40.4^{+7.4}_{-6.3}$

Table A2.5: Geoneutrino flux at JUNO (in TNU) using CRUST2.0, CRUST1.0, and LITHO1.0 geophysical models with 1-sigma uncertainty. Layer abbreviations are the same as Table A2.2

Jinping	CRUST2.0			CRUST1.0			LITHO1.0		
	S(U)	S(Th)	S(U + Th)	S(U)	S(Th)	S(U + Th)	S(U)	S(Th)	S(U + Th)
Sed cc	0.92 $\pm$0.12	0.29 $\pm$0.04	1.22 $\pm$0.16	0.59 $\pm$0.08	0.19 $\pm$0.03	0.78 $\pm$0.10	0.62 $\pm$0.08	0.20 $\pm$0.03	0.82 $\pm$0.11
UC	24.7 $\pm$6.4	6.5 $\pm$1.0	31.2 $\pm$7.3	28.4 $\pm$7.3	7.5 $\pm$1.2	35.9 $\pm$8.4	27.9 $\pm$7.2	7.4 $\pm$1.2	35.3 $\pm$8.3
MC	$5.8^{+5.2}_{-2.8}$	$2.1^{+2.7}_{-1.2}$	$7.9^{+7.8}_{-3.9}$	$6.0^{+5.3}_{-2.8}$	$2.2^{+2.8}_{-1.2}$	$8.2^{+8.0}_{-4.1}$	$6.8^{+5.6}_{-3.1}$	$2.6^{+2.9}_{-1.4}$	$9.3^{+8.4}_{-4.4}$
LC	$0.6^{+0.9}_{-0.4}$	$0.2^{+0.5}_{-0.2}$	$0.9^{+1.5}_{-0.6}$	$0.7^{+1.0}_{-0.4}$	$0.3^{+0.8}_{-0.2}$	$1.1^{+1.7}_{-0.7}$	$1.0^{+1.3}_{-0.6}$	$0.5^{+1.1}_{-0.4}$	$1.6^{+2.4}_{-0.9}$
LM	$1.4^{+2.0}_{-0.8}$	$0.4^{+0.7}_{-0.3}$	$1.9^{+2.7}_{-1.1}$	$1.4^{+1.9}_{-0.8}$	$0.4^{+0.7}_{-0.3}$	$1.8^{+2.6}_{-1.1}$	$0.7^{+1.0}_{-0.4}$	$0.2^{+0.4}_{-0.1}$	$0.9^{+1.3}_{-0.5}$
Sed oc	0.06 $\pm$0.01	0.02 $\pm$0.00	0.07 $\pm$0.01	0.11 $\pm$0.01	0.03 $\pm$0.00	0.14 $\pm$0.02	0.10 $\pm$0.01	0.03 $\pm$0.00	0.14 $\pm$0.02
OC	0.03 $\pm$0.01	0.01 $\pm$0.00	0.04 $\pm$0.01	0.05 $\pm$0.01	0.01 $\pm$0.00	0.06 $\pm$0.01	0.06 $\pm$0.02	0.01 $\pm$0.00	0.07 $\pm$0.02
Bulk cc	$32.6^{+9.1}_{-7.1}$	$9.8^{+2.8}_{-2.2}$	$42.5^{+11.5}_{-9.1}$	$36.2^{+10.2}_{-7.9}$	$11.0^{+3.0}_{-2.4}$	$47.2^{+12.7}_{-10.0}$	$36.9^{+10.3}_{-8.0}$	$11.5^{+3.3}_{-2.6}$	$48.5^{+13.1}_{-10.3}$
Bulk Crust	$32.7^{+9.1}_{-7.1}$	$9.8^{+2.8}_{-2.2}$	$42.6^{+11.5}_{-9.1}$	$36.3^{+10.2}_{-7.9}$	$11.0^{+3.0}_{-2.4}$	$47.4^{+12.7}_{-10.0}$	$37.0^{+10.3}_{-8.0}$	$11.5^{+3.3}_{-2.6}$	$48.7^{+13.1}_{-10.3}$
Near-Field Crust	$19.9^{+5.5}_{-4.3}$	$5.8^{+1.5}_{-1.2}$	$25.7^{+6.8}_{-5.4}$	$22.2^{+6.3}_{-4.9}$	$6.5^{+1.6}_{-1.3}$	$28.8^{+7.7}_{-6.1}$	$23.2^{+6.5}_{-5.1}$	$7.0^{+1.8}_{-1.4}$	$30.2^{+7.9}_{-6.3}$
Far-Field Crust	$12.8^{+3.7}_{-2.9}$	$4.0^{+1.4}_{-1.0}$	$16.8^{+4.9}_{-3.8}$	$14.1^{+4.0}_{-3.1}$	$4.4^{+1.4}_{-1.1}$	$18.6^{+5.2}_{-4.1}$	$13.9^{+3.9}_{-3.1}$	$4.5^{+1.6}_{-1.2}$	$18.4^{+5.4}_{-4.2}$
Bulk LS	$34.8^{+9.4}_{-7.4}$	$10.5^{+2.9}_{-2.3}$	$45.4^{+11.9}_{-9.4}$	$38.3^{+10.4}_{-8.2}$	$11.7^{+3.2}_{-2.5}$	$50.1^{+13.1}_{-10.4}$	$38.1^{+10.3}_{-8.1}$	$11.9^{+3.3}_{-2.6}$	$50.0^{+13.2}_{-10.4}$
DM	3.7 $\pm$1.1	1.0 $\pm$0.7	4.7 $\pm$1.8	3.8 $\pm$1.1	1.0 $\pm$0.7	4.8 $\pm$1.8	3.9 $\pm$1.2	1.0 $\pm$0.7	4.9 $\pm$1.8
EM	3.6 $\pm$1.8	0.9 $\pm$0.5	4.6 $\pm$2.3	3.8 $\pm$1.9	1.0 $\pm$0.5	4.7 $\pm$2.4	3.7 $\pm$1.8	1.0 $\pm$0.5	4.6 $\pm$2.3
Grand Total	$42.4^{+8.5}_{-7.1}$	$12.5^{+2.8}_{-2.3}$	$55.0^{+10.9}_{-9.1}$	$46.1^{+9.6}_{-7.9}$	$13.7^{+3.1}_{-2.5}$	$59.9^{+12.1}_{-10.1}$	$45.9^{+9.5}_{-7.9}$	$13.9^{+3.2}_{-2.6}$	$59.9^{+12.2}_{-10.1}$

Table A2.6: Geoneutrino flux at Jinping (in TNU) using CRUST2.0, CRUST1.0, and LITHO1.0 geophysical models with 1-sigma uncertainty. Layer abbreviations are the same as Table A2.2

Hawaii	CRUST2.0			CRUST1.0			LITHO1.0		
	S(U)	S(Th)	S(U + Th)	S(U)	S(Th)	S(U + Th)	S(U)	S(Th)	S(U + Th)
Sed cc	0.09 $\pm$0.01	0.03 $\pm$0.00	0.12 $\pm$0.02	0.08 $\pm$0.01	0.02 $\pm$0.00	0.10 $\pm$0.01	0.07 $\pm$0.01	0.02 $\pm$0.00	0.10 $\pm$0.01
UC	1.2 $\pm$0.3	0.3 $\pm$0.1	1.5 $\pm$0.4	1.0 $\pm$0.3	0.3 $\pm$0.0	1.3 $\pm$0.3	1.2 $\pm$0.3	0.3 $\pm$0.0	1.5 $\pm$0.3
MC	$0.4\ ^{+0.4}_{-0.2}$	$0.1\ ^{+0.2}_{-0.1}$	$0.5\ ^{+0.5}_{-0.2}$	$0.4\ ^{+0.3}_{-0.2}$	$0.1\ ^{+0.2}_{-0.1}$	$0.5\ ^{+0.5}_{-0.2}$	$0.4\ ^{+0.3}_{-0.2}$	$0.1\ ^{+0.2}_{-0.1}$	$0.5\ ^{+0.5}_{-0.2}$
LC	$0.1\ ^{+0.1}_{-0.0}$	$0.0\ ^{+0.1}_{-0.0}$	$0.1\ ^{+0.2}_{-0.1}$	$0.1\ ^{+0.1}_{-0.0}$	$0.0\ ^{+0.1}_{-0.0}$	$0.1\ ^{+0.2}_{-0.1}$	$0.1\ ^{+0.1}_{-0.0}$	$0.0\ ^{+0.1}_{-0.0}$	$0.1\ ^{+0.2}_{-0.1}$
LM	$0.2\ ^{+0.4}_{-0.1}$	$0.1\ ^{+0.1}_{-0.0}$	$0.3\ ^{+0.5}_{-0.2}$	$0.2\ ^{+0.3}_{-0.1}$	$0.1\ ^{+0.1}_{-0.0}$	$0.2\ ^{+0.3}_{-0.1}$	$0.1\ ^{+0.2}_{-0.1}$	$0.0\ ^{+0.1}_{-0.0}$	$0.2\ ^{+0.2}_{-0.1}$
Sed oc	0.09 $\pm$0.01	0.03 $\pm$0.00	0.12 $\pm$0.02	0.10 $\pm$0.01	0.03 $\pm$0.00	0.13 $\pm$0.02	0.10 $\pm$0.01	0.03 $\pm$0.00	0.14 $\pm$0.02
OC	0.30 $\pm$0.06	0.06 $\pm$0.01	0.36 $\pm$0.08	0.37 $\pm$0.09	0.08 $\pm$0.02	0.45 $\pm$0.11	0.38 $\pm$0.10	0.08 $\pm$0.02	0.46 $\pm$0.11
Bulk cc	$1.8\ ^{+0.5}_{-0.4}$	$0.5\ ^{+0.2}_{-0.1}$	$2.3\ ^{+0.7}_{-0.5}$	$1.6\ ^{+0.5}_{-0.4}$	$0.5\ ^{+0.2}_{-0.1}$	$2.1\ ^{+0.6}_{-0.5}$	$1.7\ ^{+0.5}_{-0.4}$	$0.5\ ^{+0.2}_{-0.1}$	$2.2\ ^{+0.7}_{-0.5}$
Bulk Crust	$2.2\ ^{+0.6}_{-0.4}$	$0.6\ ^{+0.2}_{-0.2}$	$2.8\ ^{+0.7}_{-0.6}$	$2.1\ ^{+0.5}_{-0.4}$	$0.6\ ^{+0.2}_{-0.1}$	$2.7\ ^{+0.7}_{-0.5}$	$2.2\ ^{+0.5}_{-0.4}$	$0.6\ ^{+0.2}_{-0.1}$	$2.8\ ^{+0.7}_{-0.6}$
Near-Field Crust	$0.2\ ^{+0.0}_{-0.0}$	$0.1\ ^{+0.0}_{-0.0}$	$0.3\ ^{+0.1}_{-0.0}$	$0.2\ ^{+0.1}_{-0.1}$	$0.1\ ^{+0.0}_{-0.0}$	$0.3\ ^{+0.1}_{-0.1}$	$0.2\ ^{+0.1}_{-0.0}$	$0.0\ ^{+0.0}_{-0.0}$	$0.3\ ^{+0.1}_{-0.1}$
Far-Field Crust	$2.0\ ^{+0.5}_{-0.4}$	$0.6\ ^{+0.2}_{-0.1}$	$2.6\ ^{+0.7}_{-0.6}$	$1.8\ ^{+0.5}_{-0.4}$	$0.6\ ^{+0.2}_{-0.1}$	$2.4\ ^{+0.6}_{-0.5}$	$2.0\ ^{+0.5}_{-0.4}$	$0.6\ ^{+0.2}_{-0.1}$	$2.6\ ^{+0.7}_{-0.5}$
Bulk LS	$2.6\ ^{+0.7}_{-0.5}$	$0.8\ ^{+0.3}_{-0.2}$	$3.3\ ^{+0.9}_{-0.7}$	$2.3\ ^{+0.6}_{-0.5}$	$0.7\ ^{+0.2}_{-0.2}$	$3.0\ ^{+0.8}_{-0.6}$	$2.4\ ^{+0.6}_{-0.5}$	$0.7\ ^{+0.2}_{-0.2}$	$3.1\ ^{+0.8}_{-0.6}$
DM	4.1 $\pm$1.2	1.1 $\pm$0.7	5.2 $\pm$2.0	4.2 $\pm$1.3	1.1 $\pm$0.8	5.3 $\pm$2.0	4.2 $\pm$1.3	1.1 $\pm$0.8	5.3 $\pm$2.0
EM	3.6 $\pm$1.8	0.9 $\pm$0.5	4.6 $\pm$2.3	3.8 $\pm$1.9	1.0 $\pm$0.5	4.7 $\pm$2.4	3.6 $\pm$1.8	1.0 $\pm$0.5	4.6 $\pm$2.3
Grand Total	$10.2\ ^{+2.0}_{-1.7}$	$2.7\ ^{+0.8}_{-0.6}$	$12.9\ ^{+2.8}_{-2.3}$	$10.2\ ^{+2.0}_{-1.7}$	$2.7\ ^{+0.8}_{-0.6}$	$12.9\ ^{+2.8}_{-2.3}$	$10.1\ ^{+2.0}_{-1.7}$	$2.7\ ^{+0.8}_{-0.6}$	$12.8\ ^{+2.7}_{-2.3}$

Table A2.7: Geoneutrino flux at Hawaii (in TNU) using CRUST2.0, CRUST1.0, and LITHO1.0 geophysical models with 1-sigma uncertainty. Layer abbreviations are the same as Table A2.2

Appendix A3: Appendix for Chapter 6

A3.1 Kappa

U has three, naturally occurring, long-lived ($>10^5$ years) isotopes:^{234}U, ^{235}U, and ^{238}U, where at present ^{238}U accounts for 99.2743% of the total U isotope composition. Th has one, naturally occurring, long-lived ($>10^5$ years) isotope, ^{232}Th.

κ values are calculated using equation A3.1:

$$\kappa = \frac{^{232}Th}{^{238}U} = \frac{Th}{U * 0.992743} = \frac{1}{0.992743}\frac{a_{Th}}{a_U}\frac{\mu_U}{\mu_{Th}} \tag{A3.1}$$

where a_U and a_{Th} are the abundance of U and Th, respectively; μ_U and μ_{Th} are the molar mass of U and Th, respectively.

A3.2 Kappa-Pb

κ_{Pb} values are calculated from the measured lead isotopic composition of the sample minus it's primordial lead contribution. First, following the method of *Tatsumoto et al.* (1973), the lead isotopic composition of a primitive iron meteorite troilite is subtracted from the sample's lead isotopic composition. Troilite is an iron sulfide (FeS) mineral that is uncommon on the Earth, but common to iron mete-

orites. It is a mineral rich in Pb and has un-measureable amounts of Th and U. In addition, iron meteorites represent some of the earliest solids formed in the solar system (*Kleine and Walker*, 2017) and thus, the Pb isotopic composition of these troilites are frozen into the mineral at the time of its crystallization. Therefore, these meteoritic troilites record the most primordial Pb isotopic values of the solar system.

The corrected lead composition, referred to as the "radiogenic lead ratio", is calculated by comparing the ^{208}Pb/^{204}Pb and ^{206}Pb/^{204}Pb of the sample and that of Canyon Diablo meteorite (CD). ^{208}Pb$*$/^{206}Pb$*$ is calculated using equation A3.2:

$$\frac{^{208}Pb*}{^{206}Pb*} = \frac{(\frac{^{208}Pb}{^{204}Pb})meas - (\frac{^{208}Pb}{^{204}Pb})CD}{(\frac{^{206}Pb}{^{204}Pb})meas - (\frac{^{206}Pb}{^{204}Pb})CD} \tag{A3.2}$$

where the subscripts "meas" and "CD" represent the measured lead isotope ratios of the sample and Canyon Diablo, respectively. We adopt Canyon Diablo lead values of $(^{208}\text{Pb}/^{204}\text{Pb})_{CD} = 29.476$ and $(^{206}\text{Pb}/^{204}\text{Pb})_{CD} = 9.307$ (*Tatsumoto et al.*, 1973; *Blichert-Toft et al.*, 2010). In a closed system, the development of the radiogenic lead ratio only depends on time and the Th and U concentration.

Finally, κ_{Pb}can be calculated using equation A3.2:

$$\kappa_{Pb} = \frac{(\frac{^{208}Pb*}{^{206}Pb*}) \times (e^{\lambda_{238}T} - 1)}{e^{\lambda_{232}T} - 1} \tag{A3.3}$$

where the T is the age of the Earth (assumed to be 4.568 Ga), and λ is the decay constant of the isotope.

A3.3 Linear regression

Since Th has a smaller bulk distribution coefficient then U, one expects a positive linear trend between κ and SiO_2. In order to avoid possible sampling bias in our dataset, the linear regression approach to estimate continental crust's κ has been taken. The κ datasets were binned according to their average SiO_2 (wt%) values, starting at 40 wt%, with a bin width of 5 wt%. For each bin, the median value of κ and 68% confidence limit were calculated. The best-fit lines were calculated using the least squares cost function:

$$\Phi(m,d) = \sum_{i=1}^{N} |d_{obs-i} - d_{prd-i}|^2 \tag{A3.4}$$

where

m = model parameters, i.e., slope and intersect of the regression line;

d = data, specifically:

d_{obs-i} = i-th observed datum;

d_{prd-i} = i-th model predicted datum;

N = number of the data;

Minimizing the cost function Φ approximates a solution to an overdetermined problem (κ values) by minimizing the sum of the squares of the residuals between observation and prediction. Results are plotted in Figure A3.1.

A3.4 CRUST1.0 crust type weighting

We grouped crustal (igneous and metamorphic combined datasets) κ and κ_{Pb} values by 31 continental crust types (defined by CRUST1.0 geophysical model)(*Laske et al.*, 2013) based on sample longitude and latitude. We performed a Monte Carlo calculation to weigh κ and κ_{Pb} by the mass of U within each crust type. Within the Monte Carlo a value for κ, κ_{Pb}, and a U concentration (correlated to κ) were randomly selected for each crust type. The weight of each crust type was determined by the ratio of the mass of U within an individual crust type and the total U mass of the crust (from a summation of U mass of all crust types). Summation of the weighted κ and κ_{Pb} yield a U mass weighted value for the CC. The calculation proceeds as

$$\kappa^{CC} = \sum_{i=1}^{29} \kappa_i X_i + \kappa_{i+1} X_{i+1} \tag{A3.5}$$

where X is the proportional weight of crust type i. Results are tabulated in Table A3.2.

A3.5 Mass Balance: κ of combined reservoirs

We describe mass balance of a geochemical reservoir Z, combined from two reservoirs X and Y, i.e., Z = X + Y (for example, BSE = CC + MM).

Notation:

M^{res} = mass of reservoir "*res*" in kg.

m_{el}^{res} = mass of element "el" reservoir "res" in kg.

a_{el}^{res} = abundance, as mass fraction, of element "el" in reservoir "res" in kg-element/kg-rock.

Mass balance equations for rock, Th, and U are

$$M^Z = M^X + M^Y \tag{A3.6}$$

$$M^Z a_{Th}^Z = M^X a_{Th}^X + M^Y a_{Th}^Y \qquad or \qquad m_{Th}^Z = m_{Th}^X + m_{Th}^Y \tag{A3.7}$$

$$M^Z a_U^Z = M^X a_U^X + M^Y a_U^Y \qquad or \qquad m_U^Z = m_U^X + m_U^Y \tag{A3.8}$$

The ratio of the last two equations yields

$$(\frac{a_{Th}}{a_U})^Z = \frac{m^X a_{Th}^X + m^Y a_{Th}^Y}{m^Z a_U^Z} = (\frac{a_{Th}}{a_U})\frac{m^{MM} a_U^{MM}}{m^{BSE} a_U^{BSE}} + (\frac{a_{Th}}{a_U})^{CC}\frac{m^{CC} a_U^{CC}}{m^{BSE} a_U^{BSE}}$$

$$= (\frac{a_{Th}}{a_U})^{MM}\frac{m_U^{MM}}{m_U^{BSE}} + (\frac{a_{Th}}{a_U})^{CC}\frac{m_U^{CC}}{m_U^{BSE}} \tag{A3.9}$$

and using equation A3.1 we write:

$$\kappa^Z = \kappa^X \frac{m_U^X}{m_U^Z} + \kappa^Y \frac{m_U^Y}{m_U^Z} \tag{A3.10}$$

Therefore, the individual reservoir κ's are weighted by U mass contributions.

One could choose to use weights based on Th masses, in which case one would write the "mixing" equation for κ^{-1}:

$$\frac{1}{\kappa^Z} = \frac{1}{\kappa^X}\frac{m^X_{Th}}{m^Z_{Th}} + \frac{1}{\kappa^Y}\frac{m^Y_{Th}}{m^Z_{Th}} \tag{A3.11}$$

The same exercise for $(\frac{a_{208Pb*}}{a_{206Pb*}})^Z$, assuming that the exponential decay factors in the definition of κ_{Pb} use the same t (i.e., time since the birth of the Earth), leads to

$$\kappa^Z_{Pb} = \kappa^X_{Pb}\frac{m^X_{206Pb*}}{m^Z_{206Pb*}} + \kappa^Y_{Pb}\frac{m^Y_{206Pb*}}{m^Z_{206Pb*}} \tag{A3.12}$$

and the proper weights are the normalized masses of ^{206}Pb$*$, the radiogenic lead-206. But we do not know how much radiogenic lead-206 there is in each reservoir. We make the assumption that the present day m_{206Pb*} is calculated from present day m_U using decay law, and U masses are used as weights (as in κ; equation A3.10),

$$\kappa^Z_{Pb} = \kappa^X_{Pb}\frac{m^X_U}{m^Z_U} + \kappa^Y_{Pb}\frac{m^Y_U}{m^Z_U} \tag{A3.13}$$

We appreciate that this assumption is equivalent to asserting that in each of the reservoirs $\kappa = \kappa_{Pb}$, which is not accurate as evidenced by the differences between κ and κ_{Pb} in a given reservoir. In the case of reservoirs which constitute the BSE, the assumption is proven reasonable a posteriori by the results (i.e., essentially identical values of κ_{Pb} in all reservoirs). In the case of the core, the assumption of no exchange

of Th, U nor Pb with the mantle since core formation is also reasonable. The validity of our approach is further corroborated by obtaining essentially the same results using equation A3.13 on one hand, and the κ_{Pb} counterpart of equation A3.11 on the other.

A3.6 Constraint on U in the core

Specifically, the mass balances for the Earth are

$$M^{\oplus} = M^{CC} + M^{MORB} + M^{OIB} + M^{core} \tag{A3.14}$$

$$m_{Th}^{\oplus} = m_{Th}^{CC} + m_{Th}^{MORB} + m_{Th}^{OIB} + m_{Th}^{core} \tag{A3.15}$$

$$m_{U}^{\oplus} = m_{U}^{CC} + m_{U}^{MORB} + m_{U}^{OIB} + m_{U}^{core} \tag{A3.16}$$

where CC is continental crust, MORB is MORB-source mantle, OIB is OIB-source mantle. One of the last two equations can be replaced by their combination in terms of κ_{Pb} ratios, either

$$\kappa_{Pb}^{\oplus} m_{206Pb*}^{\oplus} = \kappa_{Pb}^{CC} m_{206Pb*}^{CC} + \kappa_{Pb}^{MORB} m_{206Pb*}^{MORB} + k_{Pb}^{OIB} m_{206Pb*}^{OIB} + \kappa_{Pb}^{core} m_{206Pb*}^{core} \tag{A3.17}$$

Where the weights are $^{206}Pb*$ masses, or alternatively with $^{208}Pb*$ weights

$$\frac{1}{\kappa^{\oplus}_{Pb}} m^{\oplus}_{208Pb*} = \frac{1}{\kappa^{CC}_{Pb}} m^{CC}_{208Pb*} + \frac{1}{\kappa^{MORB}_{Pb}} m^{MORB}_{208Pb*} + \frac{1}{k^{OIB}_{Pb}} m^{OIB}_{208Pb*} + \frac{1}{\kappa^{core}_{Pb}} m^{core}_{208Pb*} \quad \text{(A3.18)}$$

In fact, since $\kappa^{MORB}_{Pb} \approx \kappa^{OIB}_{Pb}$, we can simply consider the modern mantle (MM). We thus avoid the need to make assumptions about the size of OIB-source reservoir and its enrichment in U or Th relative to the MORB-source mantle. We make the assumption, discussed in previous paragraph, that ratios of $^{206}Pb*$ and $^{208}Pb*$ masses in reservoirs can be approximated by ratios of U and Th masses, respectively. κ^{core}_{Pb} isinferred from the assumption that $D_{Th} \equiv \frac{Th^{core}}{Th^{BSE}}$ is an order of magnitude smaller than D_U and we define

$$D_{\kappa} = \frac{D_{Th}}{D_U} = (\frac{Th}{U})^{Core} (\frac{U}{Th})^{BSE} = \frac{\kappa^{core}}{\kappa^{BSE}} \quad \text{(A3.19)}$$

We now have

$$M^{\oplus} = M^{cc} + M^{MM} + M^{core} \quad \text{(A3.20)}$$

plus a set of these three equations,

$$m^{\oplus}_{U} = m^{CC}_{U} + m^{MM}_{U} + m^{core}_{U} \quad \text{(A3.21)}$$

$$\kappa^{\oplus}_{Pb} = \kappa^{CC}_{Pb} \frac{m^{CC}_{U}}{m^{\oplus}_{U}} + \kappa^{MM}_{Pb} \frac{m^{MM}_{U}}{m^{\oplus}_{U}} + \kappa^{core}_{Pb} \frac{m^{core}_{U}}{m^{\oplus}_{U}} \quad \text{(A3.22)}$$

$$\kappa_{Pb}^{core} = D_\kappa \kappa_{Pb}^{BSE} = D_\kappa (\kappa_{Pb}^{CC} \frac{m_U^{CC}}{m_U^{BSE}} + \kappa_{Pb}^{MM} \frac{m_U^{MM}}{m_U^{BSE}}) \tag{A3.23}$$

Or alternatively these three,

$$m_{Th}^{\oplus} = m_{Th}^{CC} + m_{Th}^{MM} + m_{Th}^{core} \tag{A3.24}$$

$$\frac{1}{\kappa_{Pb}^{\oplus}} = \frac{1}{\kappa_{Pb}^{CC}} \frac{m_{Th}^{CC}}{m_{Th}^{\oplus}} + \frac{1}{\kappa_{Pb}^{MM}} \frac{m_{Th}^{MM}}{m_{Th}^{\oplus}} + \frac{1}{\kappa_{Pb}^{core}} \frac{m_{Th}^{core}}{m_{Th}^{\oplus}} \tag{A3.25}$$

$$\frac{1}{\kappa_{Pb}^{core}} = \frac{1}{D_\kappa} (\frac{1}{\kappa_{Pb}^{CC}} \frac{m_{Th}^{CC}}{m_{Th}^{BSE}} + \frac{1}{\kappa_{Pb}^{MM}} \frac{m_{Th}^{MM}}{m_{Th}^{BSE}}) \tag{A3.26}$$

where $m_U^{BSE} = m_U^{CC} + m_U^{MM}$ and similarly for m_{Th}^{BSE}. The four independent values ($M^{MM}, m_U^{MM}, \kappa_{Pb}^{\oplus}, and \kappa_{Pb}^{core}$) are calculated for a given value of the free parameter (m_{Th}^{core}) using the four equations [A3.20, and either A3.21,A3.22, and A3.23 or A3.24,A3.25, and A3.26], the other inputs assumed known (see Table A3.3). Equations A3.21 and A3.24 can be substituted into A3.22 to eliminate m_U^{MM} and κ_{Pb}^{core}. This yields

$$\kappa_{Pb}^{\oplus} = [\kappa_{Pb}^{CC} \frac{m_U^{CC}}{m_U^{\oplus}} + \kappa_{Pb}^{MM} (1 - \frac{m_U^{CC}}{m_U^{\oplus}} - X)](1 + D_\kappa \frac{X}{1-x}) \tag{A3.27}$$

written in terms of the small parameter

$$X \equiv \frac{m_U^{core}}{m_U^{\oplus}} \tag{A3.28}$$

the ratio of U mass in the core to U mass in the Earth. The coefficients of the Taylor series at X = 0,

$$\kappa_{Pb}^{\oplus}(X) = A_0 = A_1 X + A_2 X^2 + A_3 X^3 + \ldots, \tag{A3.29}$$

are

$$A_0 = \kappa_{Pb}^{CC} \frac{m_U^{CC}}{m_U^{\oplus}} + \kappa_{Pb}^{MM}(1 - \frac{m_U^{CC}}{m_U^{\oplus}}) \equiv^0 \kappa_{Pb}^{BSE} \tag{A3.30}$$

$$A_1 = D_\kappa \, {}^0\kappa_{Pb}^{BSE} - \kappa_{Pb}^{MM} \tag{A3.31}$$

$$A_2 = D_\kappa({}^0\kappa_{Pb}^{BSE} - \kappa_{Pb}^{MM}) \tag{A3.32}$$

$$A_j = D_\kappa(\kappa_{Pb}^{CC} - \kappa_{Pb}^{MM}) \frac{m_U^{CC}}{m_U^{\oplus}} for j \geqslant 3 \tag{A3.33}$$

The 0^{th} order coefficient is, as expected, the κ_{Pb} of the BSE under the assumption of no U in the core, therefore denoted ${}^0\kappa_{Pb}^{BSE}$. The 1^{st} order coefficient is the slope of the curve at X = 0. It is negative for $D_\kappa < \kappa_{Pb}^{MM} \; / \; {}^0\kappa_{Pb}^{BSE}$ and positive otherwise. Since $\kappa_{Pb}^{MM} \; / \; {}^0\kappa_{Pb}^{BSE}$ is just marginally smaller than 1 (i.e., 3.87/3.89 = 0.995), any D_κ value $\ll 1$ will result in a negative slope. The sign of the 2^{nd} order

coefficient determines the orientation of the parabola (convex or concave) in the 2^{nd} order approximation to the curve. Given that ${}^{0}\kappa_{Pb}^{BSE} > \kappa_{Pb}^{MM}$ (albeit by a hairpin), the curve is convex (u-shaped).

A3.7 Additional Figures and Tables

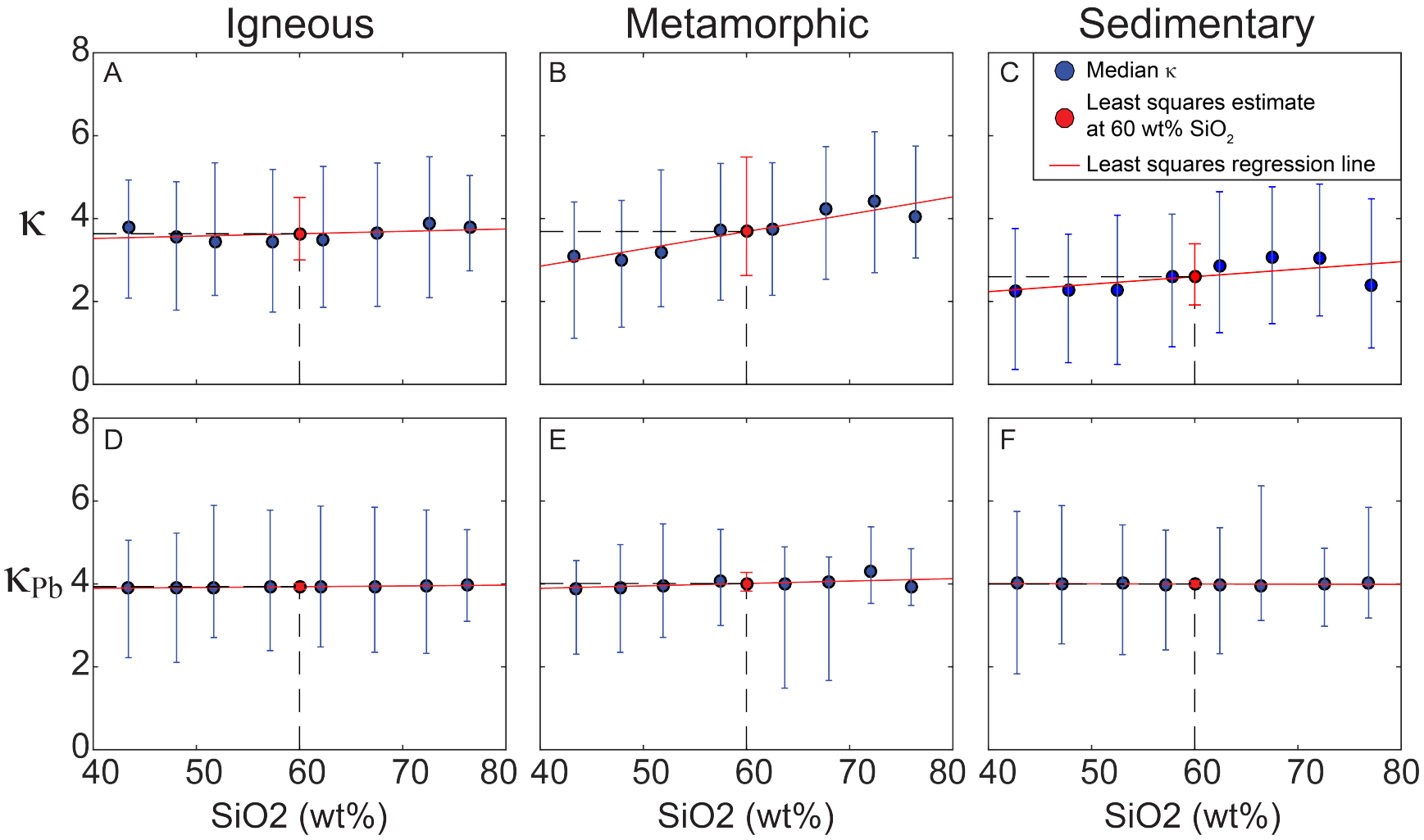

Figure A3.1: Linear regression line of SiO_2 vs κ^{CC} and κ^{CC}_{Pb} for igneous, metamorphic, and sedimentary data sets. Data (blue circles) is binned every five wt% SiO_2. Red lines are least squares fit with the red circle being the least squares estimate at 60 wt% SiO_2. See Supplementary Material Section 3 for details.

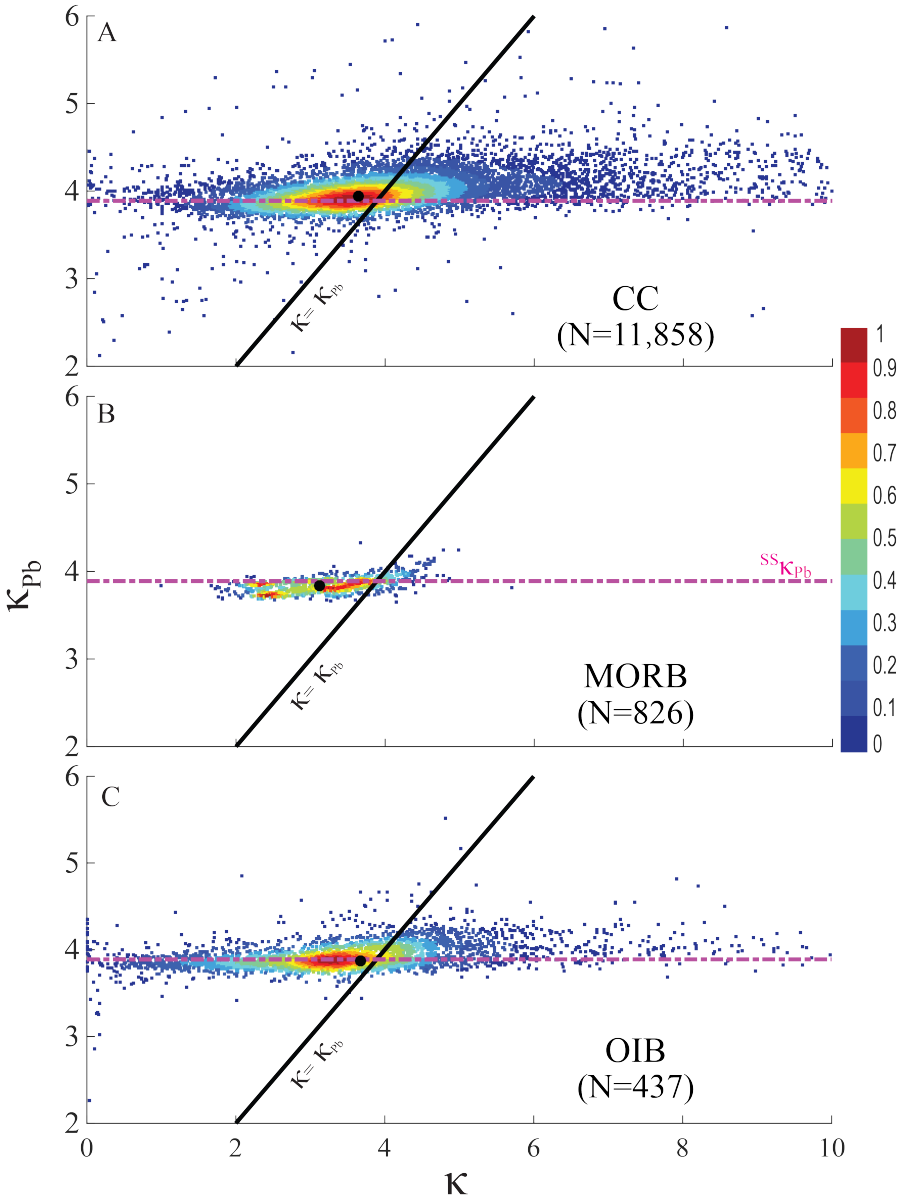

Figure A3.2: Density plot of κ vs κ_{Pb} in continental crust, MORB, and OIB. Density of data points is shown in color on a scale from 0 to 1 (arbitrary units). The black line is the 1:1 correspondence line indicating $\kappa = \kappa_{Pb}$ while the horizontal dashed line represents the solar system κ_{Pb}. A) 7,093 data located on the left of the 1:1 line ($\kappa < \kappa_{Pb}$) and 4,765 on the right ($\kappa > \kappa_{P}b$), B) 675 data have $\kappa < \kappa_{P}b$, while 151 have $\kappa > \kappa_{Pb}$, and C) 331 data have $\kappa < \kappa_{Pb}$, while 106 have $\kappa > \kappa_{Pb}$. The black circle in each panel shows the median κ and κ_{Pb} values.

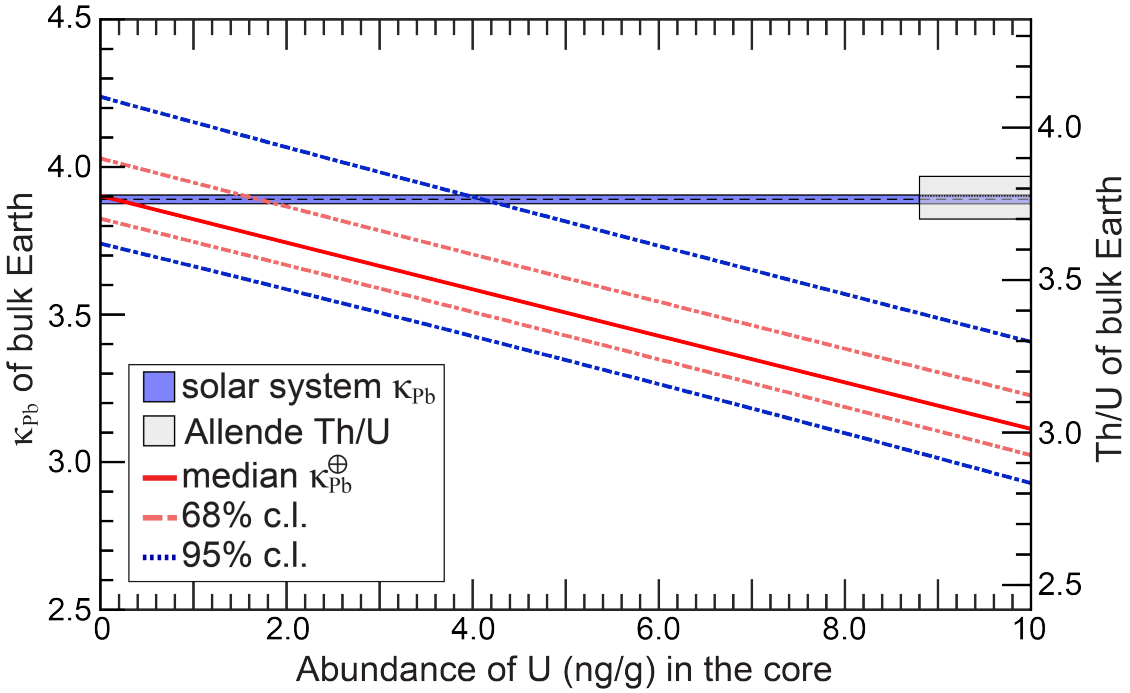

Figure A3.3: Modeled U abundance (in ng/g) in the core vs. κ_{Pb} of the the Bulk Earth (left y-axis) and Th/U (mass ratio) of the bulk Earth (right y-axis). The median (red solid), 68% confidence limit (c.l.; red dashed), and 95% c.l. (blue dashed) are plotted against the solar-system κ_{Pb} (blue shaded horizontal region with 1-sigma bounds; *Blichert-Toft et al.* (2010)) and Allende meteorite (grey shaded region along right side with 1-sigma bounds and arbitrary x-axis size; *Pourmand and Dauphas* (2010)).

		U concentration (μg/g)				Th concentration (μg/g)			
Reservoir	# of data	Mean	Geometric mean	Median	SiO_2 at 60 wt%	Mean	Geometric mean	Median	SiO_2 at 60 wt%
				Modern Mantle					
MORB	2,558	0.14	0.095	$0.093^{+0.13}_{-0.05}$		0.46	0.28	$0.26^{+0.50}_{-0.15}$	
OIB	10,599	1.6	0.7	$0.77^{+2.0}_{-0.56}$		5.7	2.6	$2.9^{+7.1}_{-2.2}$	
				Continental Crust					
igneous	120,836	7	1.5	$1.7^{+3.9}_{-1.2}$	$2.2^{+1.5}_{-0.9}$	19	5.2	$5.9^{+15}_{-4.5}$	$8.0^{+4.9}_{-3.2}$
metamorphic	8,287	27	1.4	$1.6^{+2.8}_{-1.3}$	$1.5^{+1.7}_{-0.7}$	25	4.3	$6.0^{+11}_{-5.2}$	$5.8^{+3.8}_{-2.5}$
sedimentary	11,682	410	4.5	$3.2^{+9.8}_{-1.9}$	$3.8^{+198}_{-3.5}$	48	6.7	$7.7^{+8.7}_{-4.9}$	$8.8^{+4.4}_{-2.7}$

Table A3.1: Summary of U and Th concentration in continental crust (igneous, metamorphic, and sedimentary), MORB, and OIB data.

		κ			κ_{Pb}			
Reservoir	# of data	Mean	Geometric mean	Median	# of data	Mean	Geometric mean	Median
Cont. Crust	129,123	5.27	3.68	$3.73^{+1.66}_{-1.22}$	22,982	3.99	3.97	$3.95^{+0.19}_{-0.13}$

Table A3.2: Summary of κ and $\kappa_P b$ for continental crust (combined igneous and metamorphic datasets) weighted by mass of U within each crust type (see Supplementary Material Section 4 for details). 68% confidence limits are reported alongside the median value for κ and $\kappa_P b$.

Quantity	Value	Source
$M^{\oplus}$	$5.97218 \pm 0.00060 \times 10^{24}$ kg	(Chambat et al., 2010)
M^{CC}	$20.6 \pm 2.5 \times 10^{21}$ kg	(Huang et al., 2013)
M^{MM}	$4.02 \pm 0.058 \times 10^{24}$	Calculated from eqn. A3.20
M^{core}	$1.93 \pm 0.058 \times 10^{24}$	(Yoder, 1995) with arbitrary uncertainty of 3%
$m_U^{\oplus}, m_{Th}^{\oplus}$	$(8.49 \pm 0.42, 32.0 \pm 0.42) \times 10^{16}$	(McDonough and Sun, 1995)
m_U^{CC}, m_{Th}^{CC}	$(1.94^{+2.31}_{-1.34}, 6.60^{+9.33}_{-4.89}) \times 10^{16}$ kg	Data
m_U^{MM}, m_{Th}^{MM}		Calculated from eqn. A3.21 or A3.24
$m_U^{core}, m_{Th}^{core}$	[0-10 ng/g]	Free parameter
$\kappa_{Pb}^{\oplus}$		Calculated from eqn. A3.22 or A3.25
κ_{Pb}^{CC}	$3.95^{+0.19}_{-0.13}$	Data
κ_{Pb}^{MM}	$3.87^{+0.15}_{-0.07}$	Data
κ_{Pb}^{core}		Calculated from eqn. A3.23 or A3.27

Table A3.3: Quantities, values, and sources used within the mass balance calculation. Values left blank are dependent on U abundance in the core. Values in parentheses contain both U and Th masses, respectively.

Appendix A4: (publication) Revealing the Earth's mantle from the tallest mountains using the Jinping Neutrino Experiment

[1] O. Šrámek and W. F. McDonough conceived the study, B. Roskovec and O. Šrámek developed the geoneutrino emission models and produced results. Benchmark testing of crustal models were carried out by O. Šrámek, B. Roskovec, S.A. Wipperfurth. and Y. Xi. O. Šrámek and W.F. McDonough wrote the manuscript using inputs from all co-authors. All authors discussed and reviewed the manuscript.

[2] This chapter has been published as:

Šrámek, O., B. Roskovec, S. A. Wipperfurth, Y. Xi, and W. F. McDonough (2016), Revealing the Earth's mantle from the tallest mountains using the Jinping Neutrino Experiment, *Scientific Reports*, *6*, 33,034, doi:10.1038/srep33034

A4.1 Abstract

The Earth's engine is driven by unknown proportions of primordial energy and heat produced in radioactive decay. Unfortunately, competing models of Earth's

composition reveal an order of magnitude uncertainty in the amount of radiogenic power driving mantle dynamics. Recent measurements of the Earth's flux of geoneutrinos, electron antineutrinos from terrestrial natural radioactivity, reveal the amount of uranium and thorium in the Earth and set limits on the residual proportion of primordial energy. Comparison of the flux measured at large underground neutrino experiments with geologically informed predictions of geoneutrino emission from the crust provide the critical test needed to define the mantle's radiogenic power. Measurement at an oceanic location, distant from nuclear reactors and continental crust, would best reveal the mantle flux, however, no such experiment is anticipated. We predict the geoneutrino flux at the site of the Jinping Neutrino Experiment (Sichuan, China). Within 8 years, the combination of existing data and measurements from soon to come experiments, including Jinping, will exclude end-member models at the 1σ level, define the mantle's radiogenic contribution to the surface heat loss, set limits on the composition of the silicate Earth, and provide significant parameter bounds for models defining the mode of mantle convection.

A4.2 Introduction

Recent cosmochemical observations have produced a range of compositional models for the silicate Earth and its prediction for the amount of radiogenic power in the Earth (*Boyet and Carlson*, 2005; *Burkhardt et al.*, 2016; *Campbell and St C. O'Neill*, 2012; *Fukai and Yokoyama*, 2016; *Jellinek and Jackson*, 2015). Likewise, new insights on the thermal and electrical conductivity of the Earth's core (*de Koker et al.*,

2012; *Gomi et al.*, 2013; *Pozzo et al.*, 2012; *Seagle et al.*, 2013; *Konôpková et al.*, 2016; *Ohta et al.*, 2016) have greatly revised our understanding of the core-mantle boundary heat flux, which in turn has significant implications on the nature of the Earth's surface heat flux. These findings permit a broad range of estimates of the radiogenic power available in the silicate Earth. Of the 46 TW of heat output from the Earth's interior(*Jaupart et al.*, 2015; *Davies*, 2013), anywhere between ∼10 TW and ∼30 TW are attributed to the decay of long-lived radionuclides (i.e., 40K, 232Th, and 238U) within existing compositional models (*Šrámek et al.*, 2013). The continental lithosphere accounts for 8 TW (*Huang et al.*, 2013) leaving negligible (2 TW; i.e., 10 TW-8 TW) to significant (22 TW) amounts of radiogenic power contributing to mantle dynamics (*Korenaga*, 2008; *Deschamps et al.*, 2010; *Lenardic et al.*, 2011; *Nakagawa and Tackley*, 2012; *Höink et al.*, 2013). The complex and inaccessible deep Earth system, where mantle dynamics is coupled to processes in the metallic core, has so far resisted efforts to better constrain the K, Th, U abundance in the Earth.

Compositional models of the Earth have been categorized into three groups based on the available radiogenic power (*Dye et al.*, 2015; *McDonough*, 2016): low-Q models (10-15 TW), medium-Q models (17-22 TW), and high-Q models (<25 TW). Low-Q models assume a low K, Th, and U concentration in the material that formed the Earth (the enstatite chondrite model and the non-chondritic model) or invoke an impact-induced loss of early differentiated crust enriched in heat-producing elements (the collisional erosion model). Medium-Q models estimate the silicate Earth composition using elemental fractionation patterns between melt (basalt) and melt

residue (peridotite) while constraining the ratios of refractory lithophile elements to abundances in C1 chondritic meteorites. High-Q estimates are the high end-member of physical models which rely on simple relationship between the heat output from the convecting mantle and the vigor of convection, described as a balance between thermal buoyancy driving the dynamics and thermal and momentum diffusion hindering the flow.

The recent breakthrough in detection of terrestrial electron antineutrinos, created in β- decays of 232Th and 238U decay chains of natural thorium and uranium, has offered an exciting new framework for studying the shallow and the deep Earth's composition and for tightening constraints on the amount of radiogenic heat available for driving Earth's dynamics. It took 26 years from Wolfgang Pauli's original proposal of a neutrino in 1930 to the first detection of antineutinos by Reines and Cowan in 1956 (*Cowan et al.*, 1956b). An additional almost 50 years passed before the first detection of geoneutrinos with the KamLAND 1-kiloton liquid scintillator detector at Kamioka Underground Laboratory in Japan in 2005 (*Araki et al.*, 2005). A few years later the Borexino collaboration released their initial measurement of the Earth's geoneutrino flux with the 0.3-kton detector at Gran Sasso (Italy) (*Bellini et al.*, 2010).

These two neutrino experiments will be soon joined by the 1-kton SNO+ detector at SNOLAB (Ontario, Canada)(*Chen*, 2006) and a fourth experiment, the 20-kton JUNO detector, which is under construction in Jiangmen (China)(*An et al.*, 2016). In addition, a prototype detector is currently being built at the China Jinping Laboratory (CJPL; Fig. A4.1). Following this testing phase the Jinping Neutrino

Experiment (*Beacom et al.*, 2016)(hereafter Jinping) is designed to build a 4-kton detector for low-energy neutrino physics, astrophysics and geophysics at the CJPL. Importantly, CJPL is the world's deepest underground physics laboratory where a rock overburden of ∼2400 m (6700 meters water equivalent)(*Beacom et al.*, 2016) results in the lowest flux of cosmic ray muons, thus minimizing the unwanted cosmogenic background in antineutrino detection. Furthermore, CJPL is remote from nuclear reactors which also emit electron antineutrinos, with the nearest operating reactor 1400 km away. Jinping will thus give an unprecedented antineutrino measurement dominated by the geoneutrino signal (*Beacom et al.*, 2016), unlike any other geoneutrino detecting experiment (*Baldoncini et al.*, 2015).

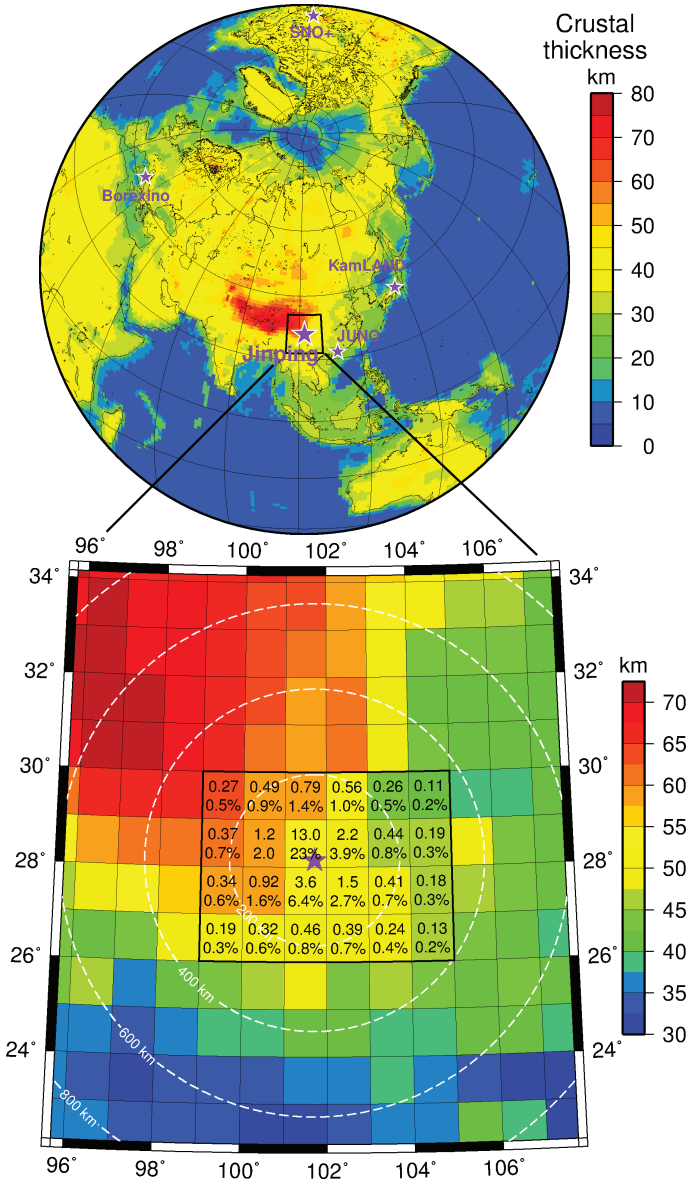

Figure A4.1: Top: Location of Jinping and other geoneutrino detectors. Crustal thickness from CRUST1.0 (*Laske et al.*, 2013) model plotted in color. Bottom: 1° longitude × 1° latitude tiles of CRUST1.0 model around Jinping. Within the 6° × 4° region centered at the detector location (somewhat arbitrarily defined and termed near-field crust in past studies) we show TNU (Terrestrial Neutrino Units (*Mantovani et al.*, 2004)) and % contributions from the lithosphere (i.e., Continental Crust + Continental Lithospheric Mantle) in each tile to the total geoneutrino signal at Jinping. White dashed circles contour distance from Jinping. Map created using The Generic Mapping Tools, Version 4.5.14 (http://gmt.soest.hawaii.edugmt.soest.hawaii.edu).

KamLAND (KL) and Borexino (BX) geoneutrino measurements (*Araki et al.*,

2005; *Bellini et al.*, 2010; *Gando et al.*, 2013, 2011; *Bellini et al.*, 2013; *Agostini et al.*, 2015) are broadly consistent with existing models of Earth's architecture and its chemical composition, thus independently validating the geoscientific paradigms i.e., Bulk Silicate Earth (BSE) Th and U abundance estimates, and enrichment of the heat-producing elements in the crust. These experiments have also demonstrated that the existing budget of heat producing elements is insufficient to account for the 46 TW of surface heat flow (*Gando et al.*, 2011), thus requiring the presence of residual primordial energy, which includes the heat of accretion and the transformation of gravitation energy of core formation into thermal energy. Furthermore, an upper limit has been placed on thermal power of a nuclear geo-reactor at depth31, proposed by some (*Herndon*, 1996; *De Meijer and Van Westrenen*, 2008). Geoneutrino research is now entering the exciting next stage where geoneutrino measurements begin to address the large uncertainty in estimates of radiogenic power driving mantle convection, stemming from various models of Earth's composition. Most recently the signal of geoneutrinos from the mantle has been reported (*Agostini et al.*, 2015; *Ludhova and Zavatarelli*, 2013; *Usman et al.*, 2015), although with a considerable uncertainty.

In this report, we calculate the prediction of the geoneutrino flux at Jinping. We demonstrate the power which the Jinping measurement will bring in combination with results of the earlier geoneutrino experiments. Moreover, we make a case for the critical role of constructing an accurate crustal emission model from nearby crust at Jinping, in resolving the mantle signal.

A4.3 Emission model and results

Our global model for geoneutrino emission (see Methods section) integrates the three-dimensional spatial structure and rock density from CRUST1.0 (*Laske et al.*, 2013) (C1) with estimates of chemical composition in various reservoirs: layers of Continental Crust (CC) and Oceanic Crust (OC) including sediment layers, Continental Lithospheric Mantle (CLM), and the convecting mantle composed of the Depleted MORB-source Mantle (DM; source for mid-oceanic ridge basalts), and the Enriched Mantle (EM). The EM is introduced in order to satisfy the mass balance of elements in the Bulk Silicate Earth (BSE) and is a source of oceanic intraplate basalts (OIB). We do not make a distinction between several types of enriched chemical reservoirs in the deep Earth as seen by geochemistry (e.g., the EM1, EM2, and HIMU reservoirs3 (*Hofmann*, 2014)), as such compositional differences will remain beyond detection sensitivity (*Šrámek et al.*, 2013). Various compositional estimates result in a suite of models whose calculated antineutrino emission can be tested with geoneutrino measurements. Here we calculate the geoneutrino predictions for a typical Earth model (*Huang et al.*, 2013) as a reference, whereas the Supplementary information reviews the consideration for the complete spectrum of competing Earth models.

Table A4.1 lists geoneutrino fluxes at the Jinping location, 28.15°N, 101.71°E, that come from the distinct geochemical reservoirs of the Earth model. Uncertainty in the predicted flux are dominated by unknowns in the chemical composition of the layers, whereas uncertainties in crustal thickness are uncorrelated and estimated

to be <10%, while not reported in C1. Accounting for the uncertainty in crustal structure is expected to increase the uncertainty in lithospheric geoneutrino flux prediction by a few percent, resulting in a larger relative uncertainty of the mantle flux, given the ratio of lithospheric to mantle flux at Jinping and other continental locations of neutrino experiment. The total predicted geoneutrino signal at Jinping is $58.5^{+7.4}_{-7.2}$ TNU (Terrestrial Neutrino Units40), with 86% of the signal from the lithosphere (crust + CLM) and 14% from the convecting mantle (DM + EM).

	Geoneutrino flux in TNU†		
Reservoir	**Th**	**U**	**Th + U**
Upper CC + sediments	7.37 ± 0.74	28.3 ± 6.0	35.7 ± 6.7
Middle CC	2.70 ± 0.22	8.1 ± 2.5	10.8 ± 2.7
Lower CC	0.292 ± 0.088	0.72 ± 0.22	1.02 ± 0.31
OC sediments	0.032 ± 0.002	0.102 ± 0.005	0.134 ± 0.008
OC crust	0.009 ± 0.003	0.045 ± 0.013	0.054 ± 0.016
CC + OC	10.40 ± 0.77	37.3 ± 6.5	47.7 ± 7.2
CLM	$0.40^{+0.56}_{-0.25}$	$1.4^{+1.7}_{-0.8}$	$1.8^{+2.3}_{-1.1}$
CC + OC + CLM	$11.0^{+1.1}_{-0.9}$	39.3 ± 6.8	$50.4^{+7.8}_{-7.6}$
Depleted Mantle (DM)	$0.67^{+0.15}_{-0.17}$	$3.68^{+0.83}_{-0.93}$	$4.35^{+0.99}_{-1.10}$
Enriched Mantle* (EM)	$0.87^{+0.44}_{-0.34}$	$2.6^{+2.2}_{-1.6}$	$3.5^{+2.6}_{-2.0}$
DM + EM	$1.59^{+0.43}_{-0.47}$	$6.6^{+2.1}_{-2.2}$	$8.1^{+2.5}_{-2.7}$
TOTAL	$12.6^{+1.0}_{-0.9}$	45.9 ± 6.4	$58.5^{+7.4}_{-7.2}$

Table A4.1: Prediction of geoneutrino flux at Jinping location: 28.15°N, 101.71°E, 2400 m depth, based on CRUST1.038 model of the crustal structure. *See text for details on how the EM was determined to satisfy BSE model. See text for details on units. CC = Continental Crust; OC = Oceanic Crust; CLM = Continental; Lithospheric Mantle.

A4.4 Resolving mantle

Determining the amount of radiogenic heat production in Earth's mantle is a major goal in the field. Such a constraint will transform our understanding of the composition of the silicate Earth, mantle dynamics and the cooling history of the planet. To be able to unambiguously define the mantle-only geoneutrino signal means deploying a detector deep in the oceans (or buried on an ocean island) far away from nuclear reactors and continental lithosphere. Both the reactor antineutrino background and the lithospheric signal prediction must be subtracted from the total antineutrino measurement and reducing these contributions increases the relative proportion of mantle signal while reducing uncertainty. Such an ocean-going experiment has been proposed, i.e., Hanohano (*Learned et al.*, 2008). However, it may take decades before Hanohano or a similar experiment is approved and operational. In the absence of a detector located in the middle of the ocean, Jinping is our best solution as it will provide critical data in defining the mantle contribution.

The power of the Jinping experiment comes from the potential of a precise geoneutrino detection, given developments in the field in the last decade and the specifics of its location. Jinping will detect the largest geoneutrino flux (TNU signal) of all geoneutrino detectors (Fig. A4.2). Because of low cosmogenic and reactor antineutrino background, Jinping is expected to measure geoneutrinos with the greatest precision of all detectors, quantified as relative uncertainty of 4% after an exposure of a 3-kiloton target mass over 5 years (*Beacom et al.*, 2016). The limiting factor of resolving the mantle geoneutrino flux using Jinping measurement is the

uncertainty in the prediction of the lithospheric signal, which must be subtracted from the total measurement. In our geoneutrino emission model the uncertainty in the lithospheric flux simply scales with the lithospheric flux magnitude and is therefore comparatively large at Jinping.

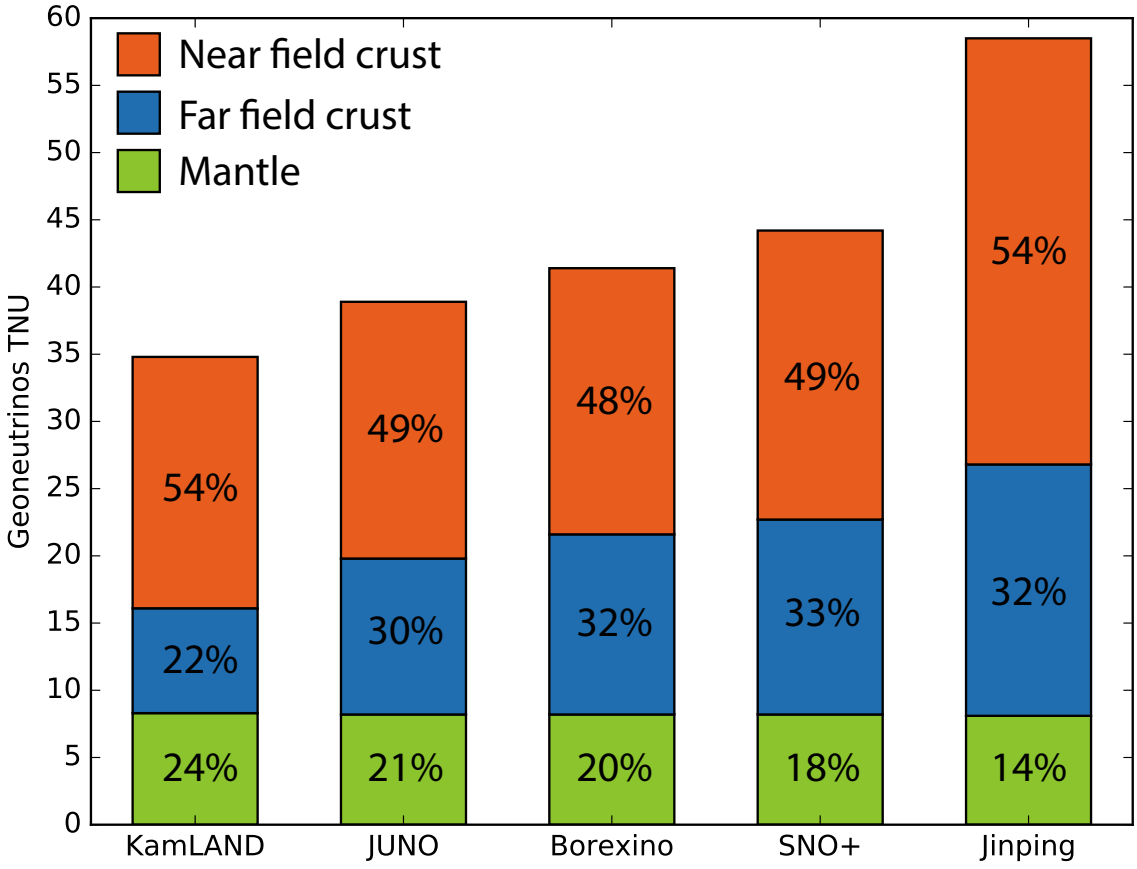

Figure A4.2: Geoneutrino flux predictions at geoneutrino detectors, showing contributions from Near-field crust (NFC), Far-field crust (FFC), and the convecting Mantle (DM + EM). NFC is a 6° longitude by 4° latitude region centered at the detector location. NFC and FFC include the small contribution (<2 TNU) from the underlying Continental Lithospheric Mantle (CLM). See Fig. A4.1 for detector locations and TNU.

It has been recognized that a large fraction of the expected geoneutrino flux at a detector originates from the closest few hundred km surrounding a detector (*Araki et al.*, 2005). Figure A4.1 shows the lithospheric contribution to the geoneutrino flux

coming from the surrounding 1° longitude × 1° latitude tiles of the C1 discretization. Almost a quarter of the signal (23%) originates in the tile in which Jinping sits. The plot of cumulative geoneutrino flux versus distance to emitter (Fig. A4.3) at Jinping shows the steepest sloping curve of all detectors, where 50% of signal originates within 300 km distance, 60% within 500 km, and 70% within 1000 km. Thus, it is fundamentally important to characterize the local geology as it represents the largest contributor to the signal and uncertainty on the total expected flux. The geoneutrino flux estimates from the local lithosphere must become constrained by multiple geophysical and geochemical observables including existing heat flow data, seismic observations, gravity data, and measured element abundances in rocks. Local crustal studies have been performed around KamLAND, Borexino, and SNO+ and constitute an urgent challenge for geoscience in geoneutrino research at Jinping and JUNO.

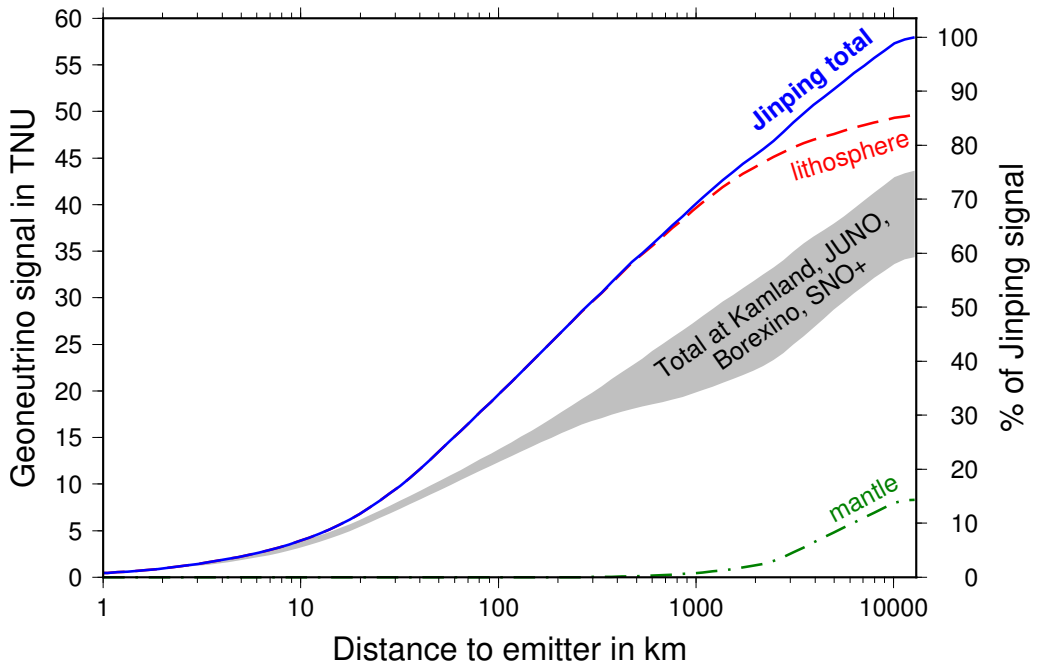

Figure A4.3: Cumulative geoneutrino signal vs. distance to emission location at Jinping. Showing both TNU (left vertical axis) and % of total signal (right axis). Total signal and contributions from lithosphere (crust + CLM) and mantle (DM + EM) are plotted. Grey shaded area envelops signals at detectors KamLAND (lower bound), JUNO, Borexino, and SNO + (upper bound).

The area around Jinping has been heavily studied because of the many devastating earthquakes that have occurred in the region, with the most recent ones being the 2008 Wenchuan (Sichuan) earthquake and the 2013 Lushan earthquake (*Wang et al.*, 2007; *Meng et al.*, 2008; *Chen et al.*, 2013; *Wang et al.*, 2014; *Zhang et al.*, 2014). Furthermore, Jinping is sited on the eastward facing ramp of the Tibetan Plateau that abuts the Sichuan Basin and is known to be located in one of the world's fastest moving geological regions, with vertical uplift rates reaching up to 6 mm/yr and horizontal movements exceeding 10 mm/yr (*Hao et al.*, 2014). Hundreds of GPS measurements and identification of the many major tectonic faults reveal large scale tectonic block rotation and crustal flow in the region (*Li et al.*, 2012; *Liu*

et al., 2014; *Sun et al.*, 2015; *Kong et al.*, 2016). This region has been and continues to be intensely studied for both understanding the fundamental processes of plate tectonics and to improve our abilities to predict the occurrence and consequences of major earthquakes.

Even though the mantle signal at Jinping is a small fraction (14%) of the total geoneutrino signal, the power of combining the Jinping measurement with other experiments is unprecedented. Figure A4.4 illustrates this feature with a plot that compares the measured geoneutrino flux (ordinate, physics only input) versus the geological estimate of the flux from the lithosphere (i.e., crust + CLM; abscissa), with the flux from convecting mantle (DM + EM) being the remaining contribution. Consequently, fitting the data with a line of slope 1 yields the y-intercept, which identifies the mantle contribution to the total signal, and provides its uncertainty as a function of the unknowns in the geoneutrino measurements (i.e., the experimental neutrino physics uncertainty) and in the lithospheric flux predictions (i.e., the uncertainty in geological model). This analysis can be repeated for each experiment individually or any combination of experiments. Analyses on the existing data (KL and BX combined) provides a result with a large uncertainty on the mantle flux (i.e., 6.0 $\pm$ 7.2 TNU for the y-intercept; Fig. A4.4, top; see Supplementary information for details). By the time Jinping produces a measurement, other detectors will have accumulated additional data.

The existing geoneutrino experiments are statistics limited, so with more exposure the relative uncertainties in their signal drop as the inverse square root of the measurement following Poisson's statistics. The annual geoneutrino count rate

is predicted to be about 400 at JUNO, 100 at Jinping, 20 at SNO+, and it has been measured as 14 at KamLAND and 4.2 at Borexino. Given the marked reduction in the reactor signal following the Tohoku 2011 earthquake, KamLAND is on track to reach 11% uncertainty in 7 more years of counting (*Watanabe*, 2016). The 20-kton JUNO detector will provide a significant annual flux of geoneutrino events and improvements in characterizing and subtracting the reactor signal (estimated at 3% uncertainty) will yield a geoneutrino measurement with 6% uncertainty after 5 years of live time (*Han et al.*, 2016). Extrapolating the statistics of current Borexino measurements (*Bellini et al.*, 2010, 2013; *Agostini et al.*, 2015), we predict an uncertainty of 13% after 6 additional years. SNO+ detector's assumed count rate of 20 geoneutrinos per year gives an estimate of 9% measurement uncertainty after 6 years (*Chen*, 2006; *Baldoncini et al.*, 2016). A projection for the year 2025, based on all of the detectors expected to be online (KL, BX, SNO+ , JUNO, and Jinping), reduces the uncertainty of the result of mantle flux, 8.2 $\pm$ 2.9 TNU, down to 35% relative uncertainty for the tested model (Fig. A4.4, bottom). With this reduction in uncertainty on the mantle flux, by a factor of 2.5 relative to the current result using KL and BX data, we will clearly discriminate between models of silicate Earth composition and put narrow bounds on radiogenic power in the mantle. It is also seen in Fig. A4.4 that while the measurement uncertainty at Jinping is the smallest, the uncertainty in the lithospheric flux prediction is the largest of all detectors, as in the present model it simply scales with the flux magnitude. Its reduction offers the greatest potential to further pin down the mantle contribution.

The Jinping detector and Fig. A4.4 offers critical insights into the nature of

geoneutrino science. Each of these five detectors can independently see the mantle given the slope 1 requirement. Differences in the intercept value reflect one of three potential considerations: (1) biases in the detectors, (2) variations in the mantle flux, and/or (3) biases in the predicted crustal flux. Assuming that instrumental calibrations reduce detector bias and total variation in mantle fluxes is expected to be at the 10% level (*Šrámek et al.*, 2013), then deviations in the y-intercepts can be in turn used to interrogate the assumed crustal model for the detector. Coupling data from continental based detectors with constraints from an oceanic based detector will provide unprecedented opportunities to critically evaluate competing models of crust composition. In this regard Jinping represents a significant test case with its exceptionally thick crust and distinctly bright geoneutrino flux.

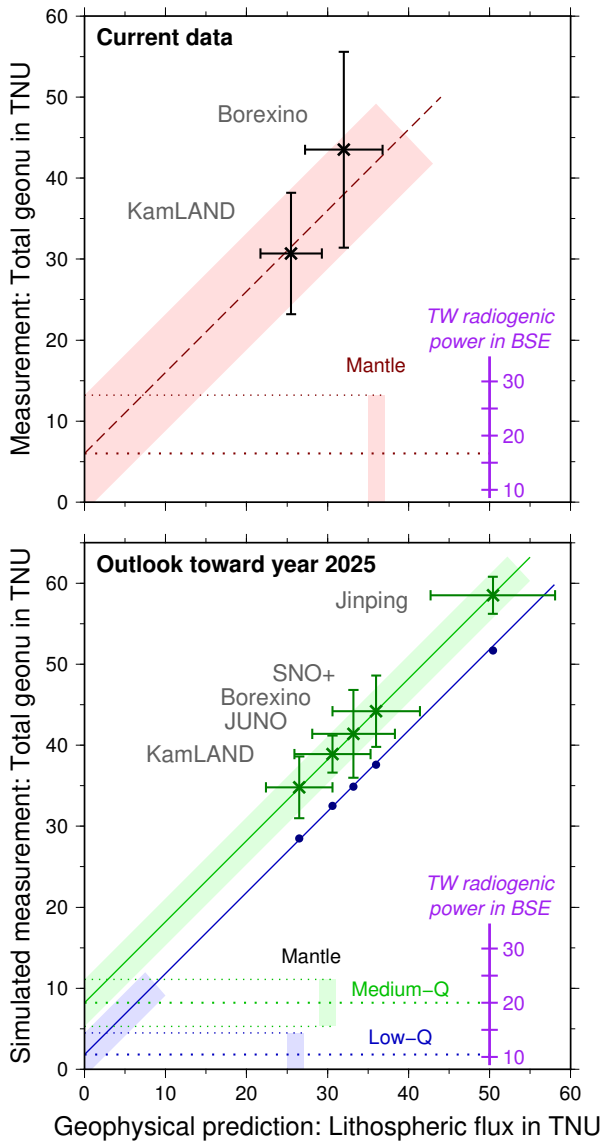

Figure A4.4: Top: Most recent measurement of total geoneutrino flux at KamLAND (KL)(*Gando et al.*, 2013) and Borexino (BX)(*Agostini et al.*, 2015) (vertical axis) vs. lithospheric flux prediction (this study). Best fit of slope 1 line shown as red dashed line, including $\pm$ 1σ uncertainty (red band). The y-intercept reveals signal from the convecting mantle (DM + EM), which scales with radiogenic power in BSE (purple). Bottom: Simulated measurements in year 2025 (vertical axis) vs. lithospheric predictions at geoneutrino detectors KL, JUNO, BX, SNO+ , and Jinping (JP). Assumes that detectors measure the nominal value predicted by the emission model, and measurement uncertainty is assumed to be 11% (KL)(*Watanabe*, 2016), 6% (JUNO)(*Han et al.*, 2016), 13% (BX), 9% (SNO+), and 4% (JP)(*Beacom et al.*, 2016), respectively. We show results for two BSE compositional estimates, previously termed medium-Q and low-Q models (*Dye et al.*, 2015; *Engel et al.*, 2016). The solution of mantle flux for the medium-Q model translates into 12 $\pm$ 4 TW of radiogenic power in the mantle.

Recent advances in antineutrino detection technology have been in directionality studies (*Tanaka and Watanabe*, 2014). Being able to evaluate directionality, even at 180° resolution, provides a powerful documentation of the sources of the geoneutrino signal (i.e., distinguishing near field crustal contributions that can be up to 50% of the signal). Primary focus in geoneutrino directionality analyses has been the variation of the crust and mantle signals with the incoming dip angle (*Fields and Hochmuth*, 2006; *Dye*, 2010). In Fig. A4.5 we predict the normalized azimuthal distribution of the geoneutrino signal at the various detectors. The asymmetric azimuthal signal at KamLAND, Borexino, and JUNO detectors reflects their settings on the margins of continents. The least variable azimuthal signal is seen for SNO+ , which sits in the center of the North American plate. The asymmetry in Jinping's azimuthal signal reflects the exceptionally thick continental crust of the Himalayas to the west and the normal ∼40 km crust of eastern China. While currently unable to measure geoneutrino directionality, predictions of azimuthal signal intensity provide insight into the geology of the local crust and inform mapping and sampling efforts for regional geologic models.

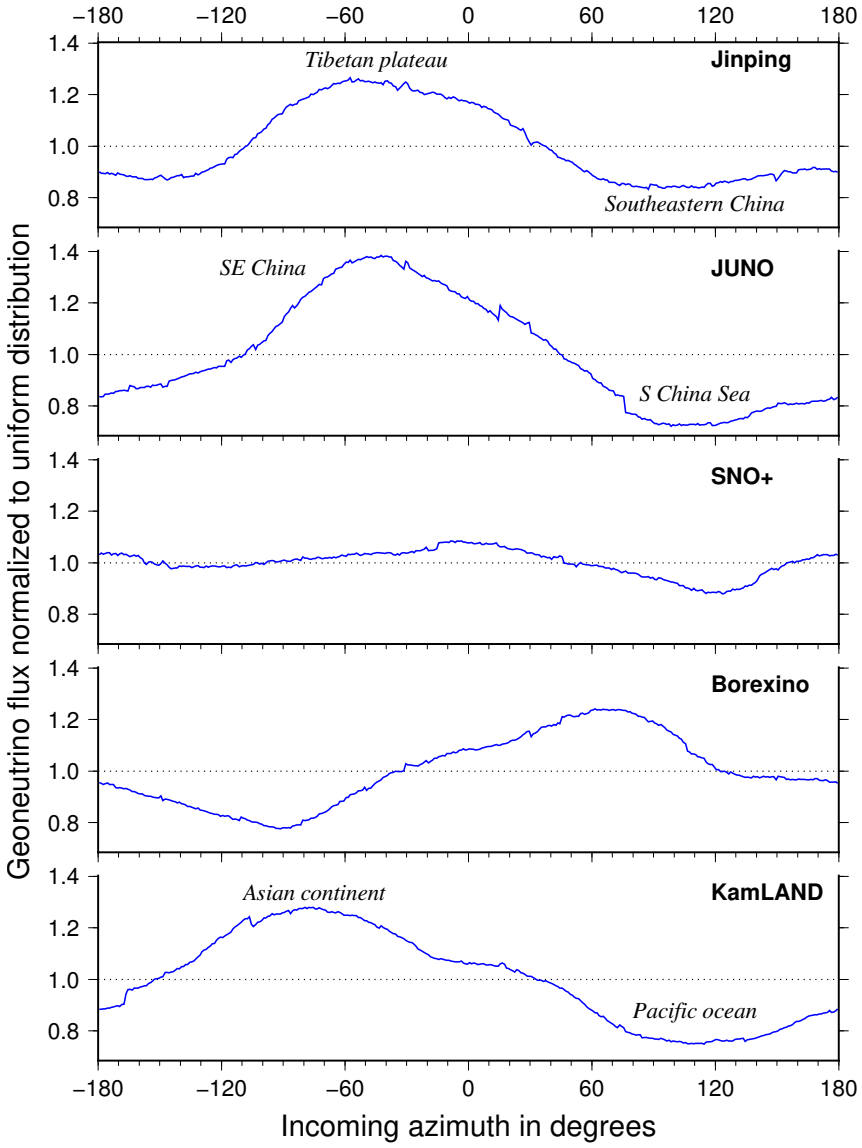

Figure A4.5: Predicted signal at geoneutrino detectors as a function of azimuth of incoming geoneutrino. Normalized to uniform distribution at each detector.

A4.5 Conclusion

The predicted geoneutrino signal for the proposed Jinping Neutrino Experiment is $58.5^{+7.4}_{-7.2}$ TNU, of which $50.4^{+7.8}_{-7.6}$ is from the Crust + Continental Lithospheric Mantle and $8.1^{+2.5}_{-2.7}$ TNU is from the Depleted + Enriched Mantle. The Jinping measurement, combined with geoneutrino measurements at other continental sites,

is currently our best chance at resolving the mantle signal. Dedicated geophysical effort toward an accurate local lithospheric model is required. This is a realistic goal, given the wealth of geophysical data in this well studied seismogenic region at the boundary between the Tibetan Plateau and the Sichuan Basin. Refinement to model predictions of the lithospheric flux are crucial to reducing the uncertainty estimates of the mantle flux. The strategy mapped out here reveals that geoneutrino data will constrain the amount of radiogenic heat production in the mantle by combining all measurements from continental detection sites to reduce the uncertainty. Reference model predicts that constraining the mantle's radiogenic heat production to 12 $\pm$ 4 TW is achievable within 8 years. Such a strategy will successfully discriminate between models of the Earth's composition, i.e., the previously described low-Q, medium-Q, and high-Q models predicting anywhere from 2 TW to <20 TW of radiogenic power in the mantle (*Šrámek et al.*, 2013; *Dye et al.*, 2015; *McDonough*, 2016). These data will place limits on the amount of heat producing elements inside the Earth, describe the planetary abundances of the refractory lithophile elements, and thus define the building blocks of the Earth (*Engel et al.*, 2016). Moreover, by setting a limit on the radiogenic heat production in the mantle we will constrain the Urey ratio of the convecting mantle (Ur = radiogenic heat/total mantle heat flux), a parameter that is considerably debated (i.e., estimates of Ur from 0.2 to 0.7) in the literature (*Korenaga*, 2008; *Deschamps et al.*, 2010; *Lenardic et al.*, 2011; *Nakagawa and Tackley*, 2012; *Höink et al.*, 2013).

A4.6 Methods

The geoneutrino flux at Jinping location is calculated in the usual way (*Usman et al.*, 2015; *Mantovani et al.*, 2004; *Enomoto et al.*, 2007; *Fiorentini et al.*, 2007a). Flux ϕ at location $\vec{r}$ is the integral

$$\phi(\vec{r}) = \frac{X\lambda N_A}{\mu} n_\nu \langle P_{ee} \rangle \int\int\int \frac{A(\vec{r}\prime)\rho(\vec{r}\prime)}{4\pi|\vec{r}-\vec{r}\prime|^2} d\vec{r}\prime, \tag{A4.1}$$

where meanings of various quantities are described in Table A4.2. As we assume negligible Th, U in the core (*McDonough*, 2014), the integration domain is the Earth's crust and mantle, where antineutrino emitters reside. We average the effect of neutrino oscillations by using the average survival probability Pee. We use CRUST1.0 model (*Laske et al.*, 2013) (C1) to describe the geometry and rock density in the crust. C1 parametrizes the crust as 1° latitude by 1° longitude stacks of 6 tiles (excluding ice and water layers) of a given thickness and uniform density. Depth-dependent density in the mantle is taken from PREM (*Dziewonski and Anderson*, 1981). We divide the crust into Oceanic Crust (OC; 'A' and 'B' type tiles of C1) and Continental Crust (CC). Continental Crust is underlain by the Continental Lithospheric Mantle (CLM), which is assumed to extend to 175 km depth (*Huang et al.*, 2013). The bulk of the mantle is divided into two reservoirs, the Depleted Mantle (DM) and the Enriched Mantle (EM) where EM is a layer of uniform thickness at the base of the mantle containing 18% of mantle mass (*Arevalo et al.*, 2013)(i.e., layering at radius of 4200 km). Within each of the chemical reservoirs (i.e., layers

of the crust in CC and OC, CLM, DM, EM), the abundance of Th, U is assumed uniform, with values and their uncertainties adopted from several compositional estimates (see Table A4.3). Abundances in EM are calculated to balance the overall inventory in BSE. Uncertainty on the structure and rock density is not available within CRUST1.0, and is not considered in the emission model. Uncertainty in the input abundances of Th and U is propagated using a Monte Carlo approach. The selection of CLM abundances is assumed to follow a log-normal distribution (*Huang et al.*, 2013). Abundances in other reservoirs (layers of CC and OC, DM, BSE) are assumed to follow the normal distribution (*Rudnick and Gao*, 2014). We assume that Th and U abundances within a reservoir are fully correlated when performing their Monte Carlo fluctuations. We further assume that abundances are uncorrelated between the following reservoirs: BSE, CLM, layers of CC and OC. We find, however, that some degree of correlation must be introduced between abundances in DM and the rest of the model, in order to prevent unphysical situations where abundances in EM are below DM values or even negative. The somewhat smaller absolute uncertainty in the total predicted geoneutrino flux compared to the lithospheric flux (Table A4.1) results from the anti-correlation between abundances in EM and abundances in layers of the lithosphere and in DM when balancing the inventory of elements in BSE.

Quantity	Symbol	^{40}K	^{232}Th	^{235}U	^{238}U
Natural isotopic mole fraction	X	0.000117	1	0.007204	0.992742
Standard atomic mass (g/mol)	μ	39.0983	232.038	238.029	238.029
Half-life (10^9yr)	$t_{1/2}$	1.248	14.0	0.704	4.468
Decay constant (s^{-1})	λ				
Number of $\bar{\nu}_e$'s per decay	n_ν	0.8928	4	4	6
Heat per decay (10^{-12}J)		0.110	6.475	7.108	7.648
Elemental abundance (mass fraction)	A				
Rock density (g/cm^3)	ρ				
Avogadro's number (mol^{-1})	N_A				
Average survival probability	P_{ee} = 0.553				
$cm^{-2}\,\mu s^{-1}$ to TNU conversion factors	^{232}Th:	$0.25\,cm^{-2}\,\mu s^{-1}\,TNU^{-1}$			
	^{238}U:	$0.076\,cm^{-2}\,\mu s^{-1}\,TNU^{-1}$			

Table A4.2: Quantities used is geoneutrino flux calculations.

	K	Th	U	Ref.
Upper CC+ sediments	$(2.32\pm 8\%)\times 10^{-2}$	$(10.5\pm 10\%)\times 10^{-6}$	$(2.7\pm 21\%)\times 10^{-6}$	RG'14
Middle CC	$(1.91\pm 14\%)\times 10^{-2}$	$(6.5\pm 8\%)\times 10^{-6}$	$(1.3\pm 31\%)\times 10^{-6}$	RG'14
Lower CC	$(0.51\pm 30\%)\times 10^{-2}$	$(1.2\pm 30\%)\times 10^{-6}$	$(0.2\pm 30\%)\times 10^{-6}$	RG'14
OC sediments	$(1.83\pm 7\%)\times 10^{-2}$	$(8.10\pm 7\%)\times 10^{-6}$	$(1.73\pm 5\%)\times 10^{-6}$	P'14
OC crust	$(716\pm 30\%)\times 10^{-6}$	$(0.21\pm 30\%)\times 10^{-6}$	$(0.07\pm 30\%)\times 10^{-6}$	WK'14
CLM	$315^{+432}_{-183}\times 10^{-6}$	$150^{+277}_{-97}\times 10^{-9}$	$33^{+49}_{-20}\times 10^{-9}$	H'13
Depleted Mantle	$(152\pm 20\%)\times 10^{-6}$	$(21.9\pm 20\%)\times 10^{-9}$	$(8.0\pm 20\%)\times 10^{-9}$	A'10
Enriched Mantle*	$402^{+350}_{-238}\times 10^{-6}$	$147^{+74}_{-57}\times 10^{-9}$	$30^{+24}_{-18}\times 10^{-9}$	
Bulk Silicate Earth	$(280\pm 21\%)\times 10^{-6}$	$(80\pm 15\%)\times 10^{-9}$	$(20\pm 20\%)\times 10^{-9}$	A'09

Table A4.3: Abundance estimates (in kg/kg) used as inputs in the geoneutrino emission model. *Abundance in Enriched Mantle calculated from balance of each element (BSE = CC + OC + CLM + DM + EM) where EM is 18% by mass of the convecting mantle (*Arevalo et al.*, 2013). References refer to: RG'14 = *Rudnick and Gao* (2014), P'14 = *Plank* (2014), WK'14 = (*White and Klein*, 2014), H'13 = *Huang et al.* (2013), A'10 = *Arevalo and McDonough* (2010), and A'09 = *Arevalo et al.* (2009).

A4.7 Acknowledgements

We thank the editor Afu Lin, two reviewers, and Fabio Mantovani for insightful comments which guided us in improving this manuscript. WFM thanks Stan Hart

for his constant support of geoneutrino studies. This study was funded by National Science Foundation Grant EAR-1067983/1068097 and by Fundamental Research Grants for Central Public Research Organizations, Chinese Academy of Geological Sciences, YYWF201623.

Appendix A5: (publication) Invited Article: miniTimeCube

[1] My contribution to this work was the simulation of particle background fluxes onto the mTC detector (Section A5.4.2).

[2] This chapter has been published as:

Li, V. A., R. Dorrill, M. J. Duvall, J. Koblanski, S. Negrashov, M. Sakai, S. A. Wipperfurth, K. Engel, G. R. Jocher, J. G. Learned, L. Macchiarulo, S. Matsuno, W. F. McDonough, H. P. Mumm, J. Murillo, K. Nishimura, M. Rosen, S. M. Usman, and G. S. Varner (2016), Invited Article: miniTimeCube, *Review of Scientific Instruments*, *87*(2), 021,301, doi:10.1063/1.4942243

A5.1 Abstract

We present the development of the miniTimeCube (mTC), a novel compact neutrino detector. The mTC is a multipurpose detector, aiming to detect not only neutrinos but also fast/thermal neutrons. Potential applications include the counter-proliferation of nuclear materials and the investigation of antineutrino short-baseline effects. The mTC is a plastic 0.2% ^{10}B–doped scintillator $(13\text{ cm})^3$ cube surrounded by 24 Micro-Channel Plate (MCP) photon detectors, each with an 8×8 anode to-

taling 1536 individual channels/pixels viewing the scintillator. It uses custom-made electronics modules which mount on top of the MCPs, making our detector compact and able to both distinguish different types of events and reject noise in real time. The detector is currently deployed and being tested at the National Institute of Standards and Technology (NIST) Center for Neutron Research (NCNR) nuclear reactor (20 MW_{th}) in Gaithersburg MD. A shield for further tests is being constructed, and calibration and upgrades are ongoing. The mTCs improved spatiotemporal resolution will allow for determination of incident particle directions beyond previous capabilities.

A5.2 Introduction: The motivation behind compact neutrino detectors and the mTC

A number of fundamental mysteries remain in the field of neutrino physics, for instance the structure of the mass hierarchy of the three known neutrinos, and the possible existence of sterile neutrinos that interact only through mixing. Further, their ultimate nature as Majorana or Dirac fermions has yet to be determined. At the same time, our understanding of neutrinos has reached a turning point where practical applications of neutrino detection are becoming increasingly feasible. This understanding, combined with recent developments in the areas of fast photodetectors, high-quality doped scintillators, electronics, and computing, have led to the possibility of a new generation of compact, highly instrumented neutrino detectors that were previously impractical and unaffordable. These detectors will allow ex-

ploration of fundamental neutrino properties, as well as practical applications in the fields of reactor safety and nuclear security.

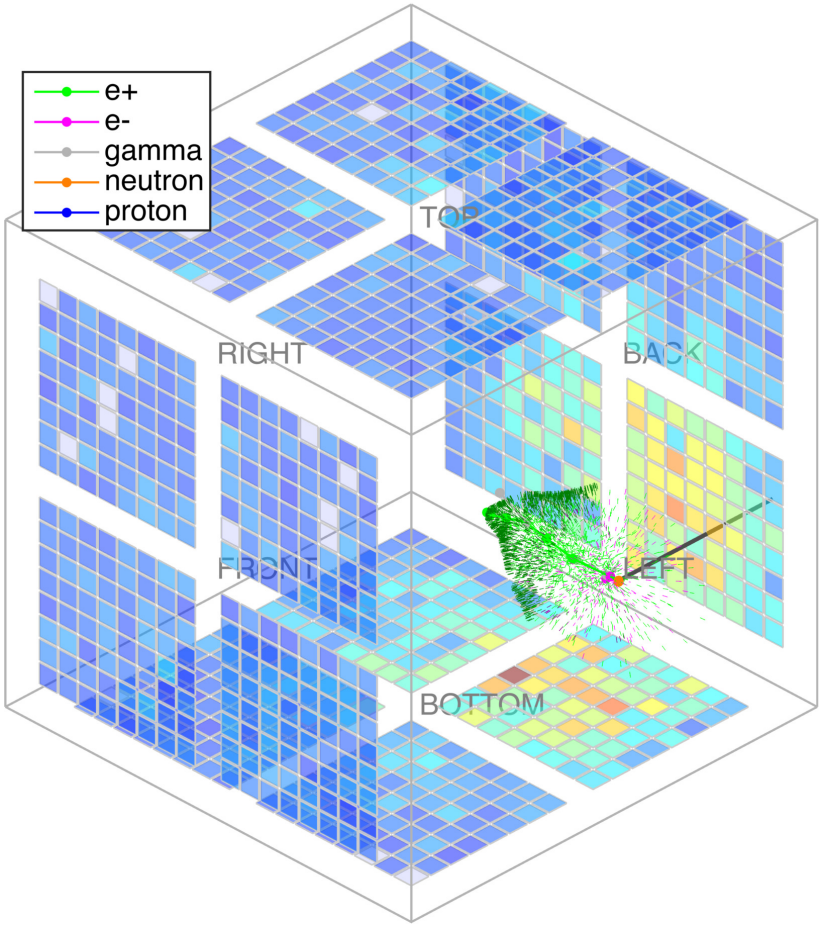

Figure A5.1: GEANT and MATLAB simulation of a 10 MeV $\bar{\nu}_e$ interaction in the 13 cm cubical mTC. Photons colored identically to parent particles.

Specifically, measurements of reactor antineutrinos provide a number of scientific opportunities, such as the detailed study of neutrino oscillations at very short baselines, and investigation of the reactor antineutrino anomaly, which may be connected to the existence of sterile neutrinos(*Vogel et al.*, 2015b). The miniTimeCube (mTC), shown in simulation in Fig. A5.1, represents a new step in this direction. The mTC is a compact ($\sim$ 2200 cm^3 active volume), densely instrumented, fast timing plastic-scintillator detector designed as a proof-of-concept for future reactor

antineutrino detectors. In addition to these scientific studies, the mTC is also designed for practical applications, such as directional neutrino detection and reactor monitoring for non-proliferation.

A5.2.1 The History and Inception of the mTC

The motivation for a compact neutrino detector began with a study involving National Geospatial-Intelligence Agency (NGA), Integrity Applications Incorporated (IAI), and UH personnel in 2011. It is an evolution of a CCD-based detection concept,(*Learned*, 2009a; *Watanabe*, 2010) which was found to have issues with scalability to large detection volumes. To avoid similar problems, the mTC utilizes time as an extra dimension to reconstruct the event kinematics. In the mTC concept, a Fermat surface is defined by the first light arrival, leading to spatial and angular resolutions well below what one would expect from the scintillator decay times (*Learned*, 2009b). This leads to particle location resolutions on the order of millimeters instead of the meter scale one would naively expect from scintillator decay time constants.

A5.2.2 Technological Context

The mTC concept requires excellent single photon timing resolution, which is achieved using commercial micro-channel plate photomultiplier tubes with excellent intrinsic timing ($\sim$ 50 ps). Combined with readout electronics we expect single photon timing resolutions of 100 ps or better, corresponding to about 2 cm spatial

resolution in the scintillator. Further improvement is achieved by multiple pixel constraints, roughly scaling as $1/\sqrt{N_{\mathrm{pe}}}$.

The mTC's state-of-the-art fast-timing and pixelization allow many novel measurements. Although its small size may prohibit full investigation of some of the proposed applications, it serves as a proof-of-concept and model for future detectors such as NuLat (*Lane et al.*, 2015).

The preliminary design of the detector and initial performance simulations were conducted in 2011, with construction starting the same year. The initial version of the detector, shown in Fig. A5.2, was completed at the end of 2013. In January 2014 we started testing and calibrating the detector at NIST. A number of upgrades have been performed or are underway as a result of lessons learned from these initial studies. We expect to begin operation at the NIST reactor, pending installation of a shielding cave to reduce neutron backgrounds, in late 2015.

A5.2.3 Design of the mTC

The core detection volume of the mTC is a $(13\ \mathrm{cm})^3$ cube of plastic scintillator (Eljen Technology EJ-254), doped with 1% natural boron (0.2% ^{10}B)(*ELJEN*). The scintillator decay constant is 2.2 ns.

A total of 24 PLANACON MCP-PMTs (PHOTONIS XP85012), hereafter referred to as simply "MCPs," shown in Fig. A5.4(*PHOTONIS*, 2013), are used to detect photons from the scintillator volume. They are coupled to the scintillator cube using optical grease (Eljen Technology EJ-550), and clamped in place to the

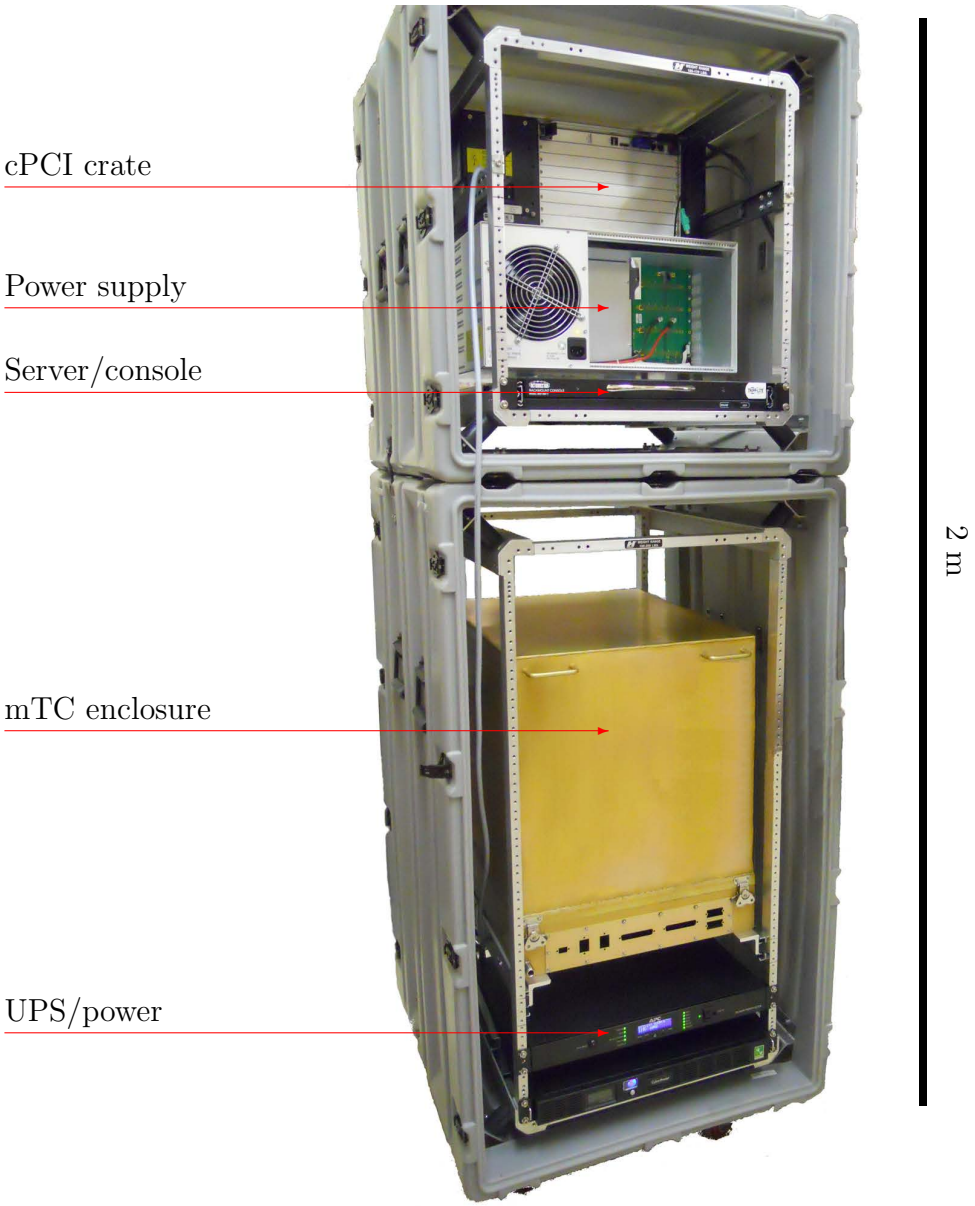

Figure A5.2: Photograph of mTC's mount-racks, light-tight aluminum enclosure, data acquisition system, and power supplies.

cube for mechanical stability. The anode plane of each MCP is segmented into 64 pixels, leading to a total of 1536 readout channels. The scintillation and Cherenkov spectra expected for EJ-254 are shown in Fig. A5.3, along with the typical quantum efficiency (QE) curve of the MCP, showing matching of the QE to the scintillation spectrum. The sensitivity of the scintillator, including coverage factors and detection efficiency of the MCPs, is $\sim$ 1000 photoelectrons / MeV.

The 1536 MCP readout channels are instrumented with custom electronics developed at the University of Hawaii. These electronics mount directly to the MCPs, providing multi-gigasample per second sampling and on-board digitization of the MCP signals with a timing resolution of $<$ 100 ps. By preserving the excellent timing resolution of the MCPs, we retain the ability to study advanced reconstruction techniques (e.g., incorporation of the shape of the scintillator decay time distribution and the fast timing of the Cherenkov photons). A model of the scintillator cube with one face of photodetectors and corresponding readout electronics populated is shown in Fig. A5.5. The compact nature of the readout electronics keeps the core of the mTC compact. The net dimensions of the cube, MCPs and electronics fit inside a $\sim 1/8$ m^3 volume. The electronics is discussed in more detail in Section A5.5.

The main detector, ancillary electronics, and power supplies fit in stacked plastic cases, with a clearance footprint of 0.75 m wide by 1.2 m deep by 2.5 m high, and requires only 115 VAC and a network connection for remote operation. The assembled and integrated mTC, including associated servers for data acquisition, is shown in Fig. A5.2. A water-based chiller, with flow around 8 LPM, provides cooling needed for operation in the shielded enclosure. The power consumption is roughly

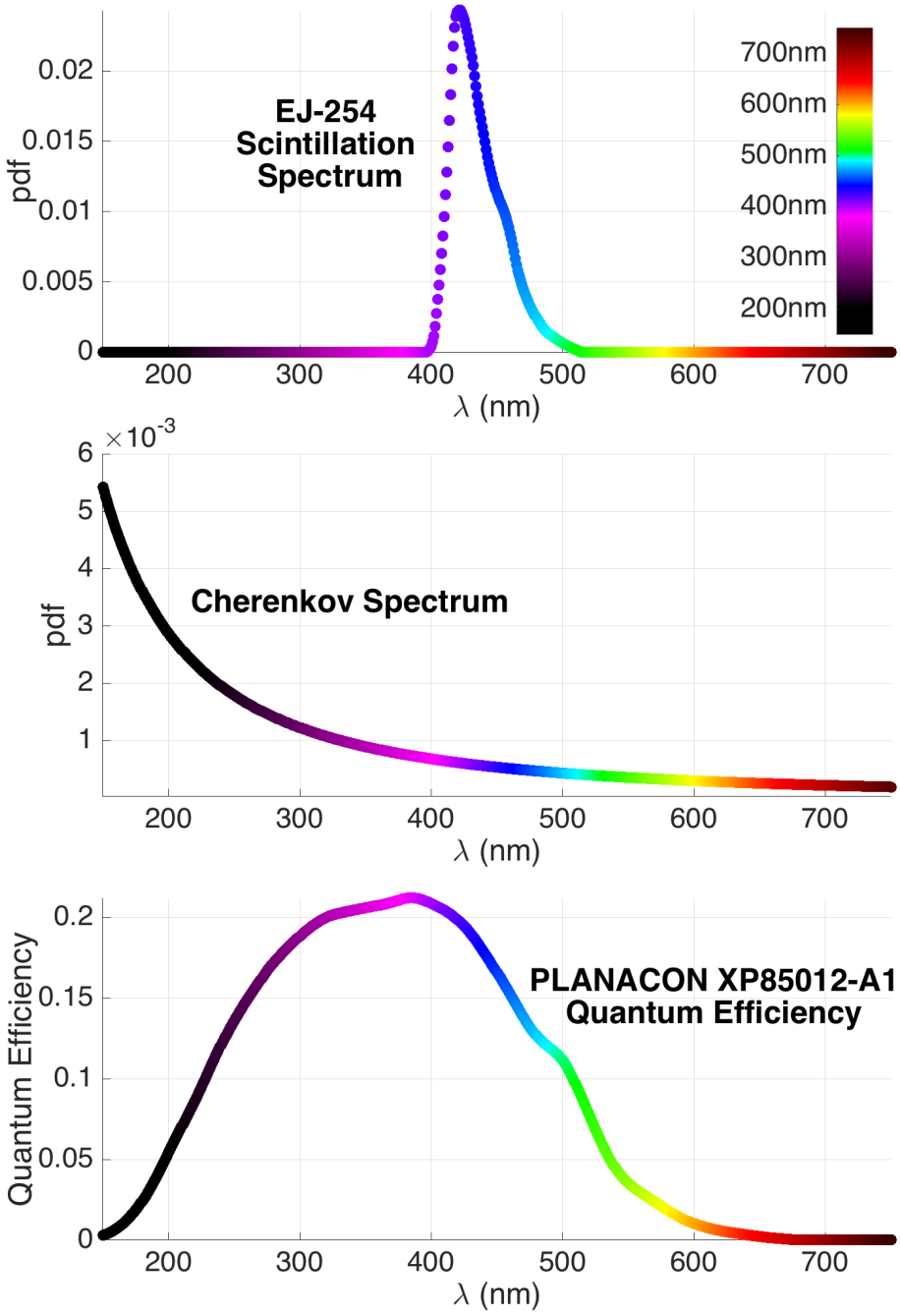

Figure A5.3: Scintillation, Cherenkov and QE spectra for the mTC. GEANT and MATLAB MC models include all effects of chromatic dispersion. Most Cherenkov photons in the UV region attenuate very quickly and are not observed.

2 kW, including $\sim$ 1 kW from the chiller itself. The size and power consumption make this a relatively portable detector, capable of being operated from a truck or a ship.

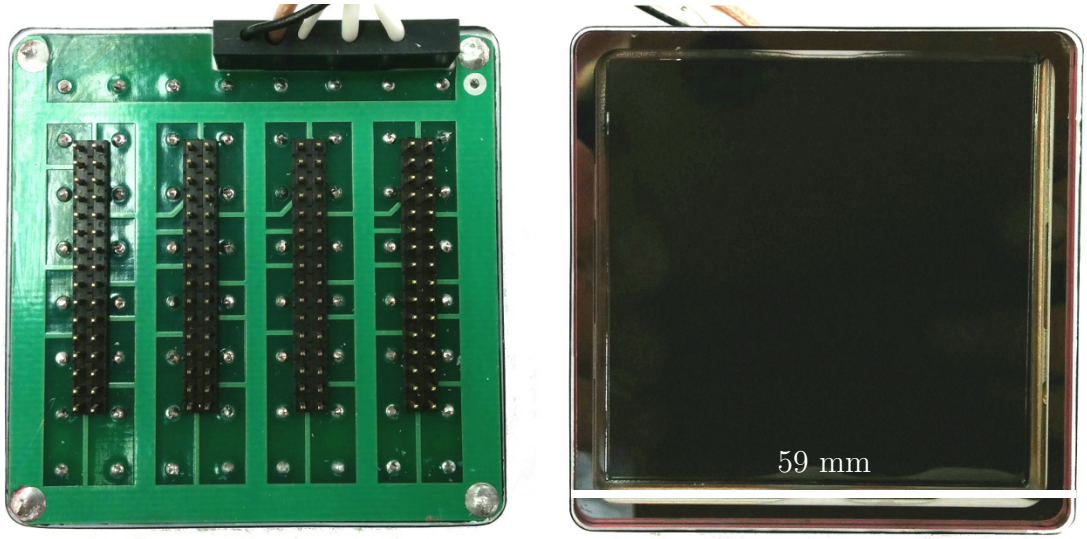

Figure A5.4: Photograph of a PHOTONIS PLANACON MCP XP 85012, one of 24 MCPs used in the mTC.

A5.3 Neutrinos in mTC

The process of identifying a neutrino interaction in the mTC is similar to the one first used in the Reines & Cowan experiment (*Cowan et al.*, 1956a; *Reines and Cowan*, 1956) in 1956, and used by many experiments since.

An electron antineutrino emitted from a nuclear reactor interacts with a proton inside the plastic scintillator medium, producing a positron and a neutron via inverse beta-decay (IBD):

$$\bar{\nu}_e + p \rightarrow e^+ + n \tag{A5.1}$$

This reaction has a cross-section of $\sigma_{tot} \cong 5 \times 10^{-43}$ cm^2 at a neutrino energy

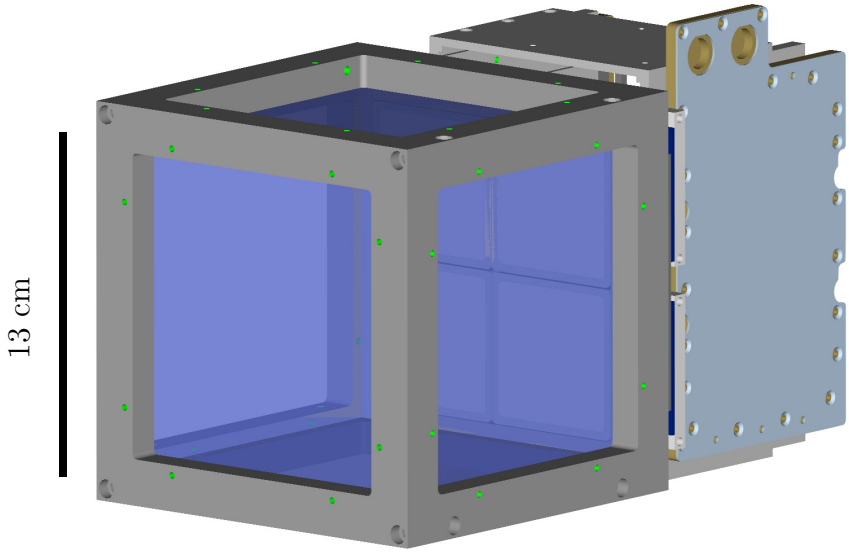

Figure A5.5: CAD of the mTC scintillator cube with one face populated with four MCPs and two electronics board stacks connected.

E_ν = 2 MeV and an energy threshold of E_ν = 1.806 MeV (in the lab frame, where the proton is at rest). The characteristic time-scale between *prompt* (positron annihilation) and *delayed* (neutron capture) signals is used as the primary signature for identifying neutrino events. As outlined below, the positrons scatter nearly isotropically after the neutrino interaction, with the positron taking most of the kinetic energy and the neutron taking most of the momentum. If one records the direction and energy of the positron and the first scatter of the neutron, one can back-reconstruct the incident direction of neutrino. Additionally, further scatters of the neutron can also be used to improve the reconstruction.

A5.3.1 Prompt Signal

The IBD prompt signal generates anywhere from several hundred to several thousand Photo-Electrons (PEs) in the mTC, as shown in Figs. A5.6 and A5.7.

The energy of this signal is used to reconstruct the incoming $\bar{\nu}_e$ energy, and the location of the signal may be used for directional determination of the $\bar{\nu}_e$ angle, however weakly, by pairing it with the delayed signal location. The prompt signal is composed of a short positron track ($\sim$ 1 cm), any electrons it may interact with, and two equal and opposite 511 keV gammas produced upon positron annihilation.

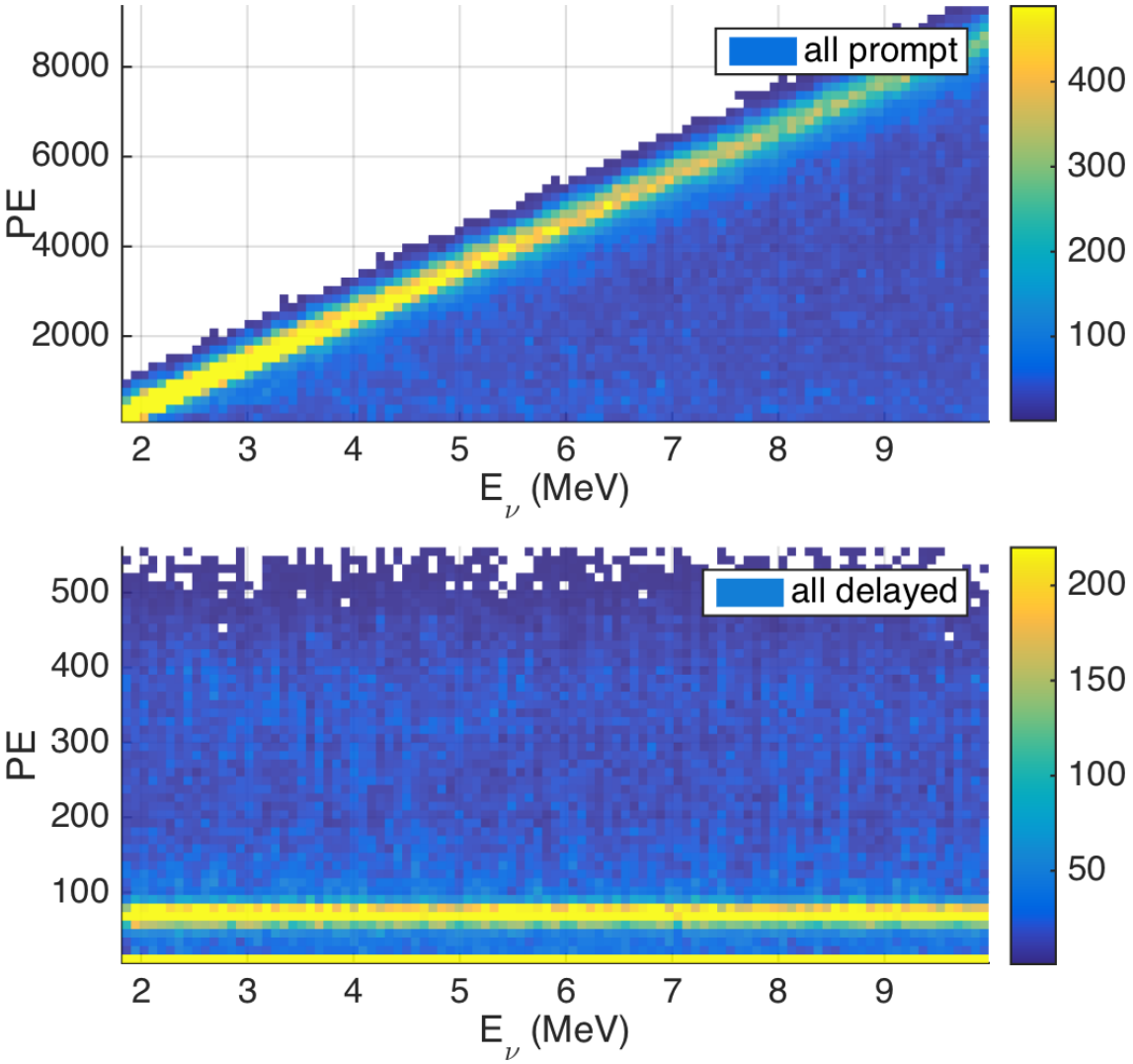

Figure A5.6: Simulated distributions of the number of PE produced as a function of $\bar{\nu}_e$ energy for the prompt signal (top) and delayed signal (bottom). In top figure, a long tail of under-estimated energies is produced by longer positrons leaving the detector. In the bottom figure, the long tail of higher energy delayed events is due to the 478 keV gamma produced on neutron capture depositing part of its energy randomly inside the detector.

Simulation projects that the mTC reach about 10-15% $\bar{\nu}_e$ energy resolution, ultimately limited by its small size. The positron track at the lower range of the $\bar{\nu}_e$ energy spectrum is on the order of a cm, though higher energy $\bar{\nu}_e$'s will produce longer tracks proportional to their energy above the $E_{\bar{\nu}_e} > 1.8$ MeV threshold. As a result, higher energy $\bar{\nu}_e$'s tend to produce positrons which leave the detector with ever greater likelihood, causing a certain amount of energy under-estimation at higher $\bar{\nu}_e$ energies.

In addition to severed positron tracks, a second problem arises at all $\bar{\nu}_e$ energies: uncertainty in prompt signal is introduced via the two 511 keV gammas. In a larger detector such as KamLAND, the annihilation gammas typically deposit their full energy within the scintillation volume. In a very small detector like mTC, these gammas deposit varying amounts of energy from event to event, smearing the prompt energy resolution. On average the annihilation gammas deposit about 1/3 of their energy in the mTC, but the proportion varies event to event, and is impossible to predict *a priori* for a specific IBD event.

More information on expected energy resolutions can be found in Section A5.7.

A5.3.2 Delayed Signal

The neutron from the neutrino interaction scatters elastically on the scintillator medium and, after thermalizing, captures on the ^{10}B embedded in the scintillator. On average, the neutron travels for a few centimeters before being captured, as shown in Fig. A5.8.

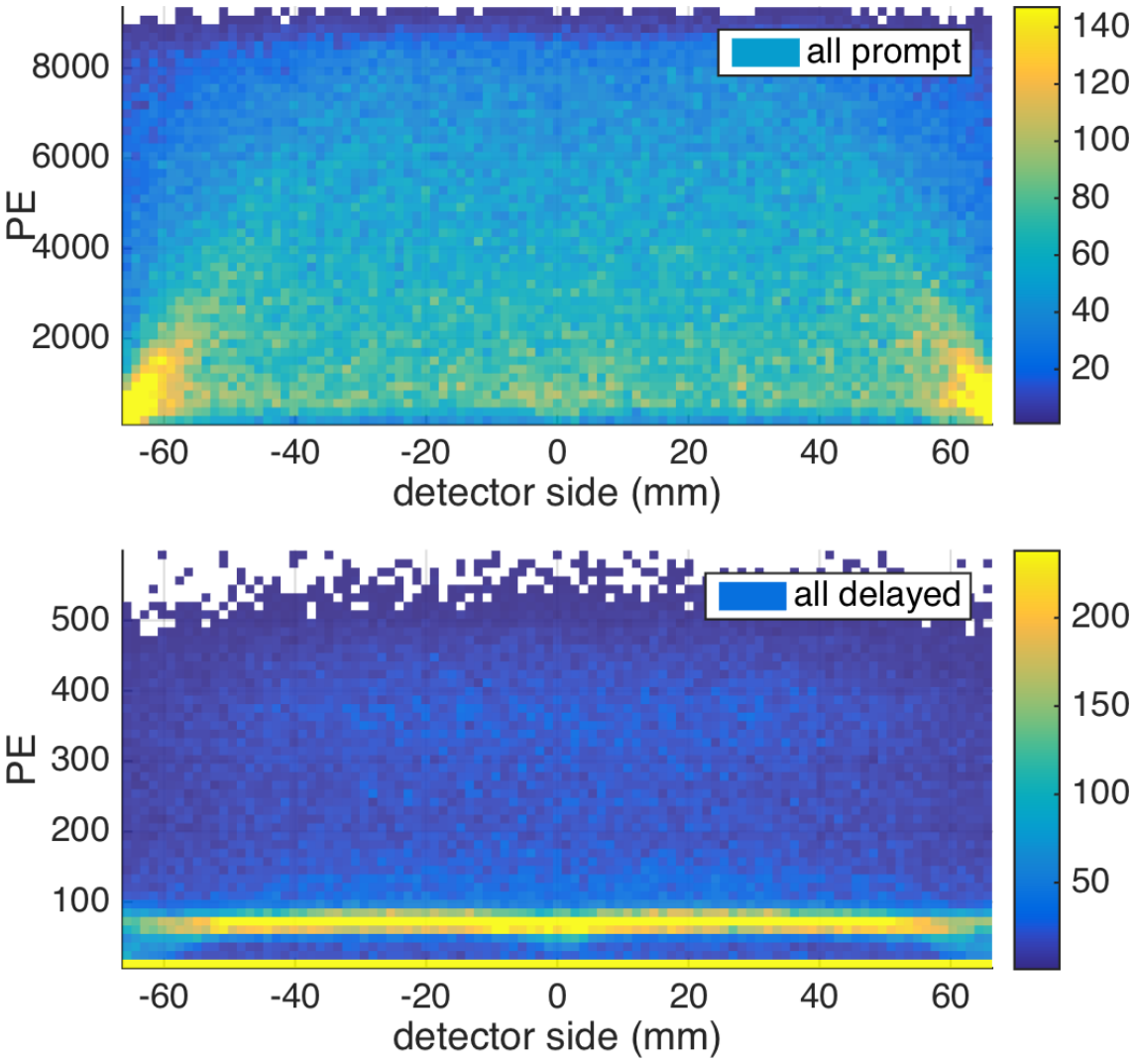

Figure A5.7: Simulated distributions of the number of PE produced for the prompt signal (top) and delayed signal (bottom) as a function of vertex location. 0 mm is the center of the detector, and 67 mm is at the edge.

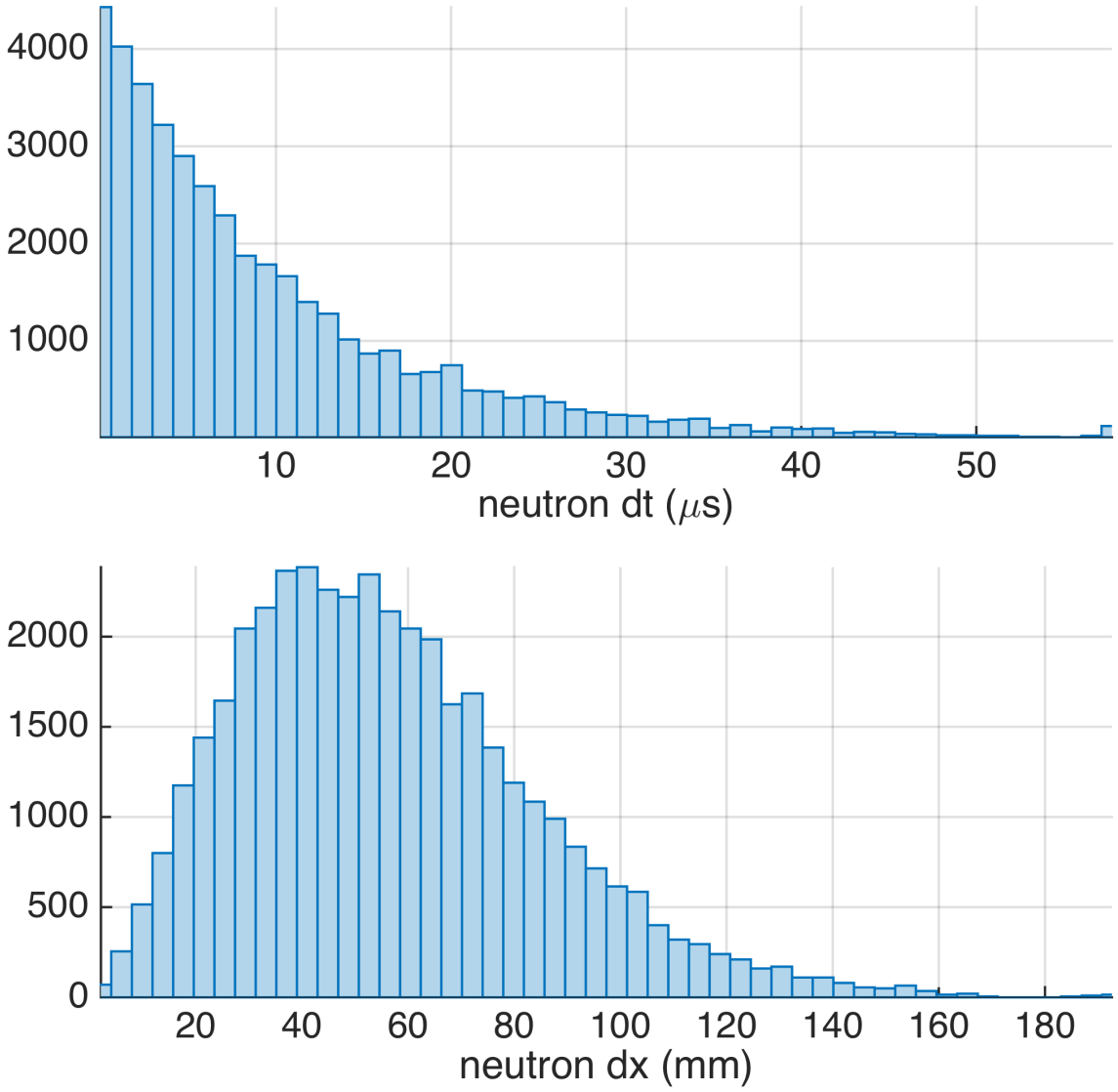

Figure A5.8: Simulated frequencies, in arbitrary units, of Monte Carlo generated IBD events as a function of time and distance of neutron production to neutron capture in the mTC scintillator.

The primary reaction for neutron capture is:*Knoll* (2000); *Pawelczak et al.* (2014); *Wright et al.* (2011)

$$\begin{aligned} n + {}^{10}\mathrm{B} \rightarrow & {}^{7}\mathrm{Li}(1015\ \mathrm{keV}) + {}^{4}\mathrm{He}(1775\ \mathrm{keV}), \quad \sim 6\% \\ \rightarrow & {}^{7}\mathrm{Li}^{*} + {}^{4}\mathrm{He}(1471\ \mathrm{keV}), \quad \sim 94\% \\ \hookrightarrow & {}^{7}\mathrm{Li}^{*} \rightarrow {}^{7}\mathrm{Li}(839\ \mathrm{keV}) + \gamma(478\ \mathrm{keV}) \end{aligned} \tag{A5.2}$$

The cross-section for neutron capture on ^{10}B as well as the linear attenuation coefficient as a function of neutron energy have been studied (*ELJEN*; *Wright et al.*, 2011; *Crane and Baker*, 1991; *ENDF*, 2011). For a completely thermal neutron (E_n = 0.025 eV), the total cross-section is equal to 3836 barns. The neutron from an IBD reaction can also be captured on a proton in $\sim$ 180 μs, resulting in 2.2 MeV γ's depositing energy via Compton scattering(*Olive et al.*, 2014). The fraction of thermal neutrons captured on ^{10}B is 25.6 times larger than on ^{1}H (*ELJEN*).

To confirm our understanding of the Monte Carlo results shown in Fig. A5.8, we can estimate the detector's neutron-capture efficiency analytically. Because the majority of neutrons capturing on ^{10}B is so large, neutron thermalization and capture on ^{10}B is the dominating process in determining the detector's neutron-capture efficiency. We can therefore get a rough estimate of this number by considering a typical neutron undergoing this process. For this calculation, we treat the neutron's path as a random-walk series of elastic scatters on ^{1}H in two parts: 1) production to thermalization, and 2) thermalization to capture. Combining these two results will give us a general idea of where neutrons are likely to be lost and therefore what

fraction of neutrons should capture without escaping the cube.

We will take a typical IBD neutron to have $K_{init} \sim 4$ keV. At these neutron energies, we can safely use nonrelativistic kinematics: $K \sim \mathcal{O}(1 \text{ keV}) \ll m_0$.

1) Production to thermalization, d_{therm}:

$$d_{therm} \sim \lambda_{es}\sqrt{N_{therm}}, \tag{A5.3}$$

where λ_{es} is the mean free path (MFP) for elastic scattering and N_{therm} is the number of steps to thermalization. We can get λ_{es} from the cross-section σ_{es} (20 barns for hydrogen) and the volume density of targets n_H:

$$\lambda_{es} \sim \frac{1}{n_H \ \sigma_{es}} \tag{A5.4}$$

To find N_{therm}, we assume that on average the neutron loses half its excess KE on each collision with a proton. Then N_{therm} is simply:

$$N_{therm} \sim \log_2\left(\frac{K_{init}}{K_{therm}}\right) \tag{A5.5}$$

Combining the above equations and data from the scintillator manufacturer (*ELJEN*), we get ~ 17 steps at ~ 1 cm each for a distance of:

$$d_{therm} \sim 4 \text{ cm} \tag{A5.6}$$

2) Thermalization to capture, d_{cap}:

Once thermalized, the neutron will typically capture after traveling the corresponding MFP, λ_{cap}. Because this distance is longer than λ_{es} above, the neutron will continue its elastic scattering on H during this time, with a number of steps equal to $\lambda_{cap}/\lambda_{es}$. The displacement for this part of the process is therefore:

$$d_{cap} \sim \lambda_{es}\sqrt{\frac{\lambda_{cap}}{\lambda_{es}}} \sim \lambda_{es}\sqrt{\frac{1}{\lambda_{es}}\cdot\frac{1}{n_{B10}\,\sigma_{cap}}} \sim 1.5 \text{ cm} \tag{A5.7}$$

3) Total (production to capture), d_{tot}:

Finally, taking d_{therm} and d_{cap} to be two steps of a random walk, we have:

$$d_{tot} \sim \langle d\rangle\sqrt{N} = \frac{d_{therm}+d_{cap}}{2}\sqrt{2} \sim 4 \text{ cm}, \tag{A5.8}$$

as the typical total distance between production and capture (again, ignoring corrections for effects like capture before thermalization, capture on hydrogen, etc.).

4) Neutron-capture Efficiency, $n_{captured}/n_{total}$:

We can use an imaginary sphere of radius $d_{tot} \sim 4$ cm to roughly estimate the capture rates in various regions of the cube. For example, a neutron produced at the surface of the cube but near the center of a face will generally have $\sim 1/2$ probability to move inward and capture or to move outward and escape; however, a neutron produced deeper than $d_{tot} \sim 4$ cm into the face will most likely capture inside the cube. Averaging over the depth indicates that $\sim 3/4$ of the neutrons produced in this region should capture inside the cube. We can make similar estimates for the rates in the other regions of the cube (i.e., edges, corners, and interior) and combine

these estimates to get our final result:

$$\frac{n_{captured}}{n_{total}} \sim \frac{1}{2} \tag{A5.9}$$

This is in general agreement with simulations indicating that $\sim 55\%$ of the neutrons produced inside the cube capture without escaping.

Using this same approach, we can get a rough estimate for how long this process might take: $t_{tot} = t_{therm} + t_{cap}$. It is relevant to keep in mind that N_{therm} depends on K_{init} as discussed above.

1) Production to thermalization, t_{therm}:

As in the distance calculation, we will assume that on average, the neutron loses half of its kinetic energy on each collision. (For this calculation, we approximate $K_{therm} \sim 0$). After n collisions, this becomes $K_n = 2^{-n} K_{init}$. We then immediately have:

$$v_n = \sqrt{\frac{2K_n}{m}} = 2^{-n/2}\sqrt{\frac{2K_{init}}{m}} = 2^{-n/2}\, v_{init} \tag{A5.10}$$

Since the distance travelled in each step is λ_{es} from above, the time for each step is:

$$t_n = \frac{\lambda_{es}}{v_n} = 2^{n/2}\frac{\lambda_{es}}{v_{init}} \tag{A5.11}$$

The total time to thermalization is then the sum of these steps over N_{therm} terms:

$$t_{therm} \sim \sum t_n = \sum_{n=0}^{N_{therm}} 2^{n/2}\, \frac{\lambda_{es}}{v_{init}} \sim 10\ \mu\text{s} \tag{A5.12}$$

2) Thermalization to capture, t_{cap}:

The average speed after thermalization is constant by definition, so the time to capture will be λ_{cap} from above divided by this speed:

$$t_{cap} \sim \frac{\lambda_{cap}}{v_{N_{therm}}} = 2^{N_{therm}/2}\frac{\lambda_{cap}}{v_{init}} \sim 10\ \mu\text{s} \tag{A5.13}$$

3) Total (production to capture), t_{tot}:

Combining these results gives us:

$$t_{tot} = t_{therm} + t_{cap} \sim 20\ \mu\text{s}, \tag{A5.14}$$

which is also in general agreement with the Monte Carlo.

Reconstruction of the neutrino's direction largely depends on the neutron direction reconstruction, improved by the positron direction and energy. Having one or more neutron scatters improves the resolution, but even the neutron capture location after many scatters retains information on the initial neutron direction, as was demonstrated in the CHOOZ experiment (*Abe et al.*, 2014). Full reconstruction algorithms, currently under development, will take all the information into account in solving for incoming neutrino direction.

The light yield of these neutron scatters can present some difficulty when detecting and reconstructing events. Ionization density quenching on two charged particles (^{4}He and ^{7}Li) with $\gtrsim 2.3$ MeV kinetic energy in the reaction, Eq. (A5.2), results in a small total light output, about 60 keV electron-equivalent energy de-

position (*de Meijer et al.*, 2005). However, due to the small size of the detector and high MCP surface coverage, mTC has the high light collection efficiency crucial to detect the weak light from these delayed signals. As a result, only in relatively small-volume (∼Liter sized) ^{10}B-doped scintillator detectors can incident antineutrino direction currently be reconstructed based on neutron directionality (*de Meijer et al.*, 2005).

A5.3.3 mTC at NIST Reactor

The mTC currently sits on-site at the NIST Center for Neutron Research (NCNR), which houses the NIST 20 MW_{th} split-core research reactor. This reactor has a compact core (Figs. A5.9–A5.10) with 30 fuel elements, each containing 2 segments of highly-enriched uranium fuel U_3O_8/Al (^{235}U, 93% enrichment). Fuel elements are submerged in heavy water which serves as a moderator and coolant. The upper and lower fuel segments, each 27.9 cm high, are separated by a 17.8 cm unfueled gap which serves as a "flux trap" to minimize the fast-neutron and gamma backgrounds in the neutron beam lines. The overall dimensions of the core are 1.12 m in diameter by 0.74 m in height. The NIST reactor cycle is 38 days on followed by 10 days off for refueling.

Full Monte Carlo N-particle (MCNP) simulations of the core are available to onsite collaborations (*Cheng et al.*, 2004; *Hanson and Diamond*, 2011).

Using a total thermal power of 20 MW_{th}, an average number of 6 $\bar{\nu}_e$ produced per fission (with $\sim$ 1.5 $\bar{\nu}_e$ above IBD threshold), and thermal energies released per

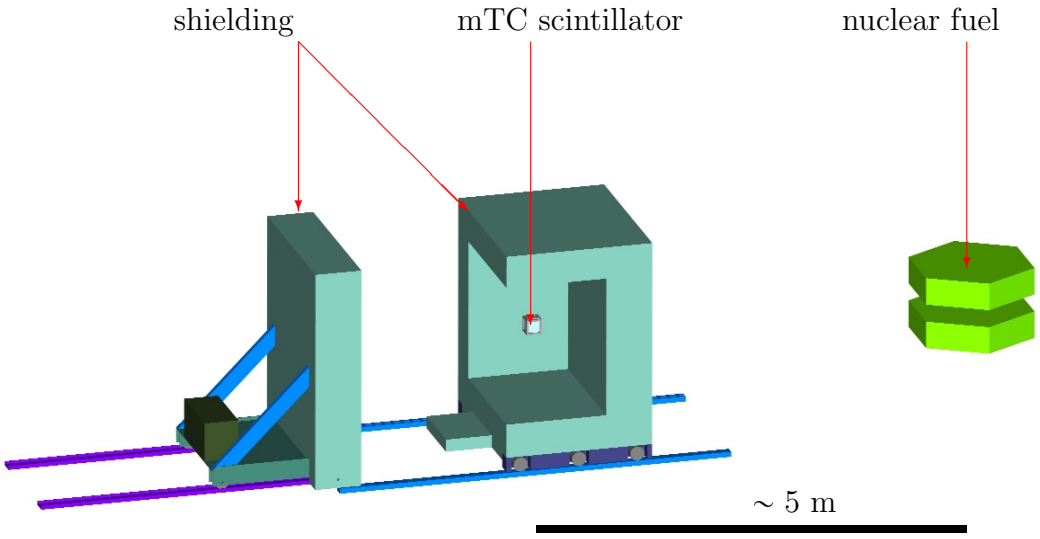

Figure A5.9: Relative location of the scintillator cube inside the movable cave (one face made transparent) with respect to the reactor core (upper and lower fuel segments are approximated by two hexagonal prisms).

fission of ^{235}U and ^{238}U, one can roughly estimate the total number of neutrinos produced at the reactor core to be $\sim 4 \times 10^{18}$ s^{-1} $\bar{\nu}_e$. This corresponds to a flux of $\sim 1.1 \times 10^{12}$ cm^{-2} s^{-1} $\bar{\nu}_e$ at the miniTimeCube location ~ 5 m away from the center of the reactor core, Fig. A5.11. It further corresponds to a number of antineutrino interactions with ^{1}H via IBD reaction in the plastic scintillator on the order of a few events per day.

More precisely, the total number of expected antineutrinos from the reactor observed in the detector is given by

$$N_{\bar{\nu}_e}^{\text{obs}} = \frac{N_p}{4\pi L^2} \int \epsilon_{det} P(\bar{\nu}_e \to \bar{\nu}_e) \frac{d\sigma(E_{e^+}, E_{\bar{\nu}_e})}{dE_{e^+}} \times \frac{d^2 N_{\bar{\nu}_e}(E_{\bar{\nu}_e}, t)}{dE_{\bar{\nu}_e} dt} dE_{e^+} dE_{\bar{\nu}_e} dt, \tag{A5.15}$$

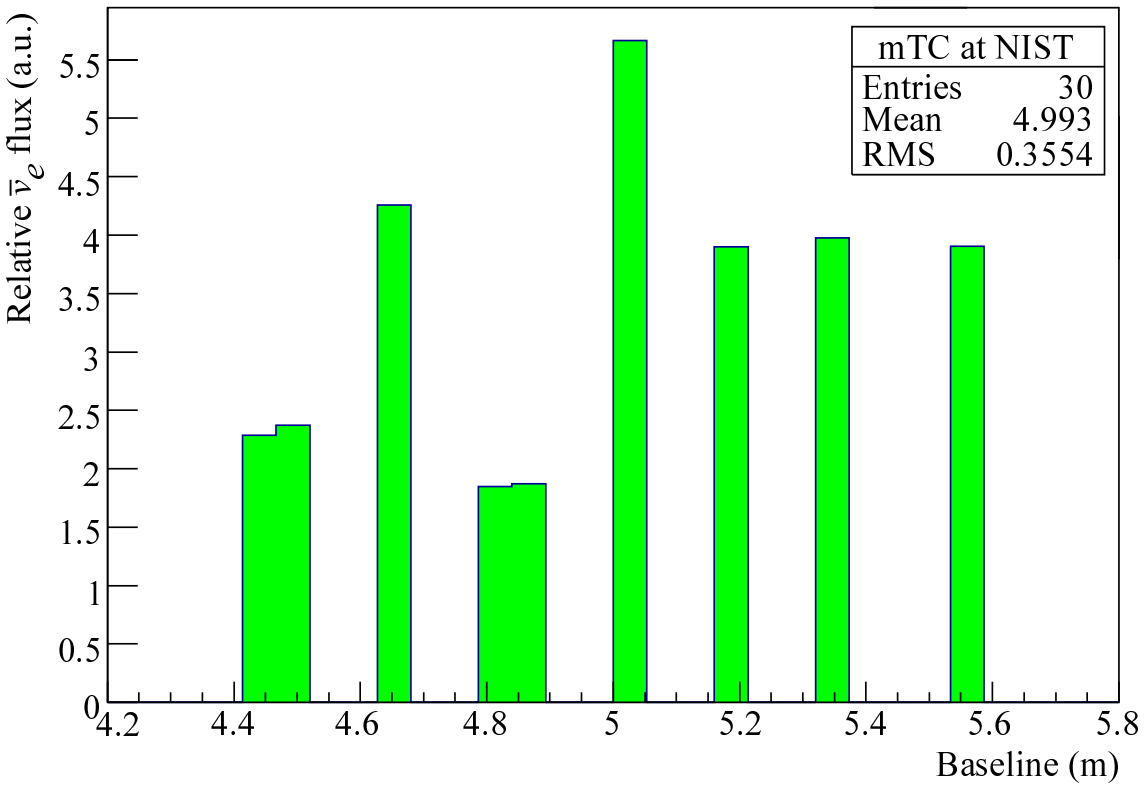

Figure A5.10: Relative distribution of $\bar{\nu}_e$ flux as a function of baseline from a nominal mTC position to each fuel element in the core. The mean source location of flux is at $\sim$ 5 m and the effective spread is 0.36 m, or an inherent smearing of about 7 % on the baseline. Specifics of this distribution will vary by fuel loading conditions.

Figure A5.11: Photograph of the mTC shielding next to the reactor.

where N_p — number of hydrogen atoms in the scintillator ("free protons"); L — distance between production and detection points of the antineutrino, ϵ_{det} — detector efficiency $\sim$ 30 % based on MC simulations for IBD detection in the mTC; $P(\bar{\nu}_e \rightarrow \bar{\nu}_e)$ — survival probability of electron antineutrino(*Olive et al.*, 2014; *Lane et al.*, 2015); and $\frac{d\sigma(E_{e^+}, E_{\bar{\nu}_e})}{dE_{e^+}}$ — differential cross-section of the IBD process as a function of positron energy E_{e^+} and antineutrino energy $E_{\bar{\nu}_e}$ (*Vogel and Beacom*, 1999).

Further details on antineutrino production at reactor facilities can be found in the literature, including: fuel time-dependence for the NIST nuclear reactor (*Cheng et al.*, 2004; *Hanson and Diamond*, 2011), evaluation of thermal energies released per fission of the four main isotopes (*Kopeikin et al.*, 2004), and spectrum of antineutrinos produced from the four main isotopes (*Dwyer and Langford*, 2015; *Mueller et al.*, 2011).

In addition to NIST, we have actively considered two other deployment sites: Typical Power Reactors (TPR) and nuclear-powered ships. Their parameters are listed in Table A5.1.

Table A5.1: Approximate parameters at potential mTC deployment sites, including NIST, a typical power reactor, and a nuclear-powered ship. "Compact core" indicates a core where all fuel elements are contained within a few meter radius.

Parameter	NIST	TPR
Power, GW_{th}	0.02	3
$\langle$Baseline$\rangle$, m	5	25
Fuel	HEU	mixed
Fuel cycle, on/off days	38/10	400/10
Compact core	X	X
$\langle$Event rate$\rangle$, $\bar{\nu}_e$/ day	$\sim$ 1	$\sim$ 10

A5.4 Backgrounds

Backgrounds in the mTC come from several sources. First there are the "natural sources", most prominently cosmic radiation. Of those, which consist of high energy neutrons, gammas, and muons, along with their collisional products, potentially the most serious for IBD detectors is the nearly irreducible background of some long lived muon-produced isotopes as we discuss below in Section A. The local environmental backgrounds, such as radioactivity, are not as much of a problem as the cosmic ray associated backgrounds. In Section B we discuss backgrounds relevant to a reactor and specifically the NIST reactor location.

A5.4.1 Cosmic Ray Backgrounds

Cosmic rays produce an inescapable background for IBD detectors. Unfortunately, all the reactors to which we may have access are at best a few meters water equivalent (mwe) under the surface. About 2 mwe is enough to shield from extensive air showers, clearing the remnant hadrons and most electromagnetic components. Muons, however, penetrate to the greatest depths, in ever decreasing numbers but increasing mean energies. These muons may generate local particles, and so shielding is somewhat of a double edged sword. Sea-level muons make neutrons and other hadrons in nuclear interactions, though with something on the order of a 2 km radiation length. The mean muon energy at the Earth's surface is about 2 GeV with a penetrating power of about 10 mwe. Muons coming through the mTC (at about 1/s) often (~10%) come with knock-on electrons (Fig. A5.12). More dangerous are

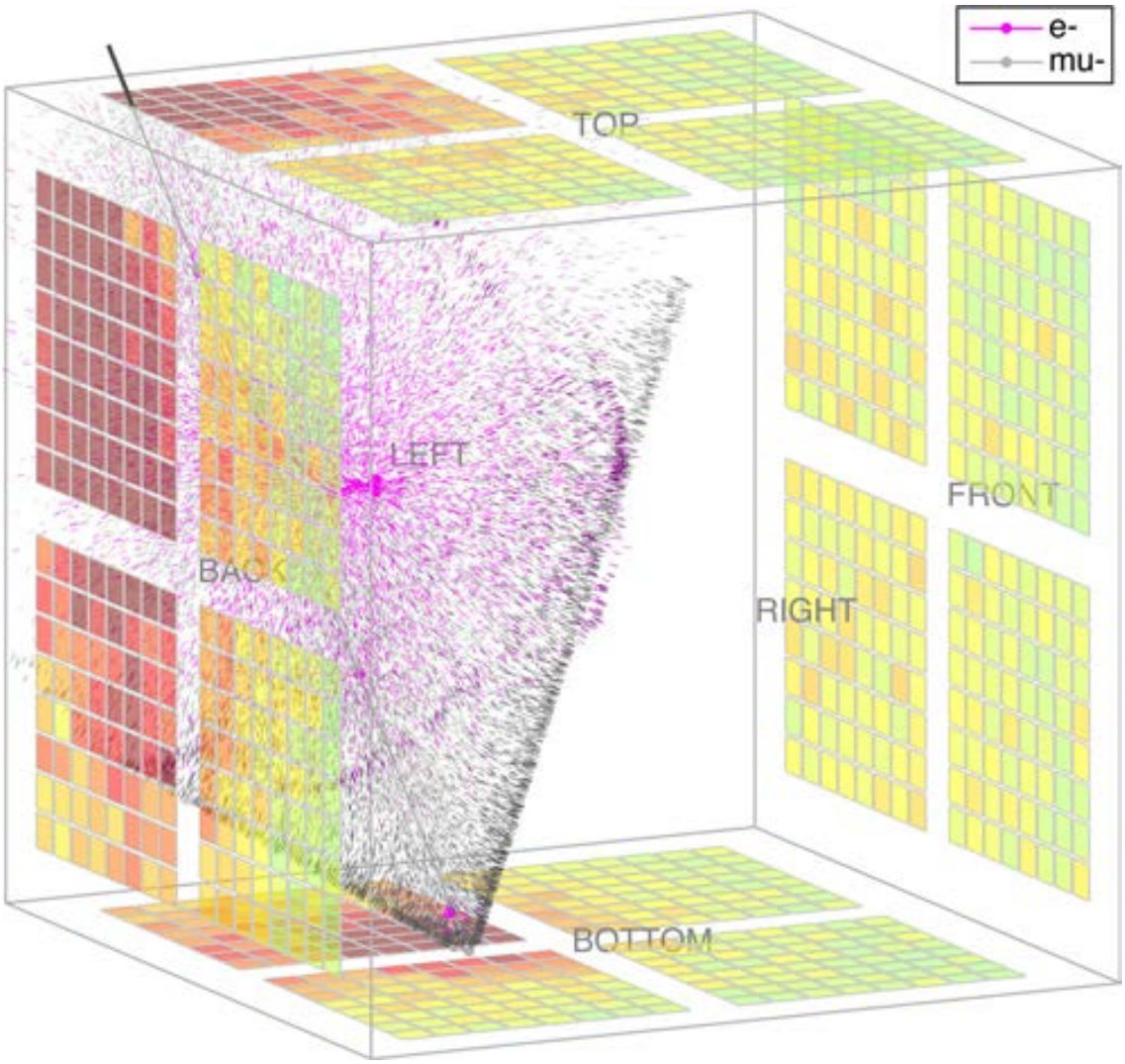

Figure A5.12: A simulated muon traversing the mTC, with scintillation photons and Cherenkov cone visible.

gammas and neutrons, which can fake the prompt signature of a neutrino.

Precise calculations of these rates are difficult because they depend upon details of the overburden, the local geometry, and shielding in particular. Isotopes and various spallation products of cosmic-ray muons can be a serious background for neutrino signals. Although many of the isotopes can be filtered from analysis using various cuts, long-lived isotopes such as ^{8}He and ^{9}Li may have lifetimes on the order of a second and decay by beta emission into neutron-unstable daughters.

These are two backgrounds that can mimic IBD events in the mTC, but are in fact negligible, as we show below.

In order to study this problem in more detail, a GEANT4 (*Agostinelli et al.*, 2003) simulation of the EJ-254 plastic scintillator was conducted. Sea-level spectrum cosmic ray muons were incident on a $(10 \times 10 \times 10)$ m^3 cube of scintillator. The isotope yield per muon event for this simulation run is tallied and shown in Fig. A5.13.

Figure A5.14 shows the average secondary particle yield per unit muon track length per unit medium density for simulated cosmic ray muons using a sea-level energy spectrum. The result implies an isotope yield of $\sim 6.86 \times 10^{-10}$ cm^2/g for ^{9}Li and $\sim 9.79 \times 10^{-11}$ cm^2/g for ^{8}He. The atmospheric muon rate traversing the 13 cm cube is about 1/s (depending upon overhead shielding), and so the rate of these events being produced in the mTC is estimated to be less than 1 event per year. In addition, the general behavior of typical sea-level spectrum muons shown by the black points involves a relatively constant production of secondaries with respect to energies above a few hundred MeV; whereas a trend of increasing daughter production is clearly seen for those producing ^{9}Li. This suggests that the ^{9}Li isotope is most likely produced in showering muon events at high energies, which can be easily vetoed. Rejection of backgrounds associated with ^{8}He will require more statistics and further investigation.

Peripheral geometries of the detector and its in-situ environment pose a non-negligible contribution to the cosmogenic backgrounds and a more accurate study with these effects fully taken into account will need to be conducted in the future.

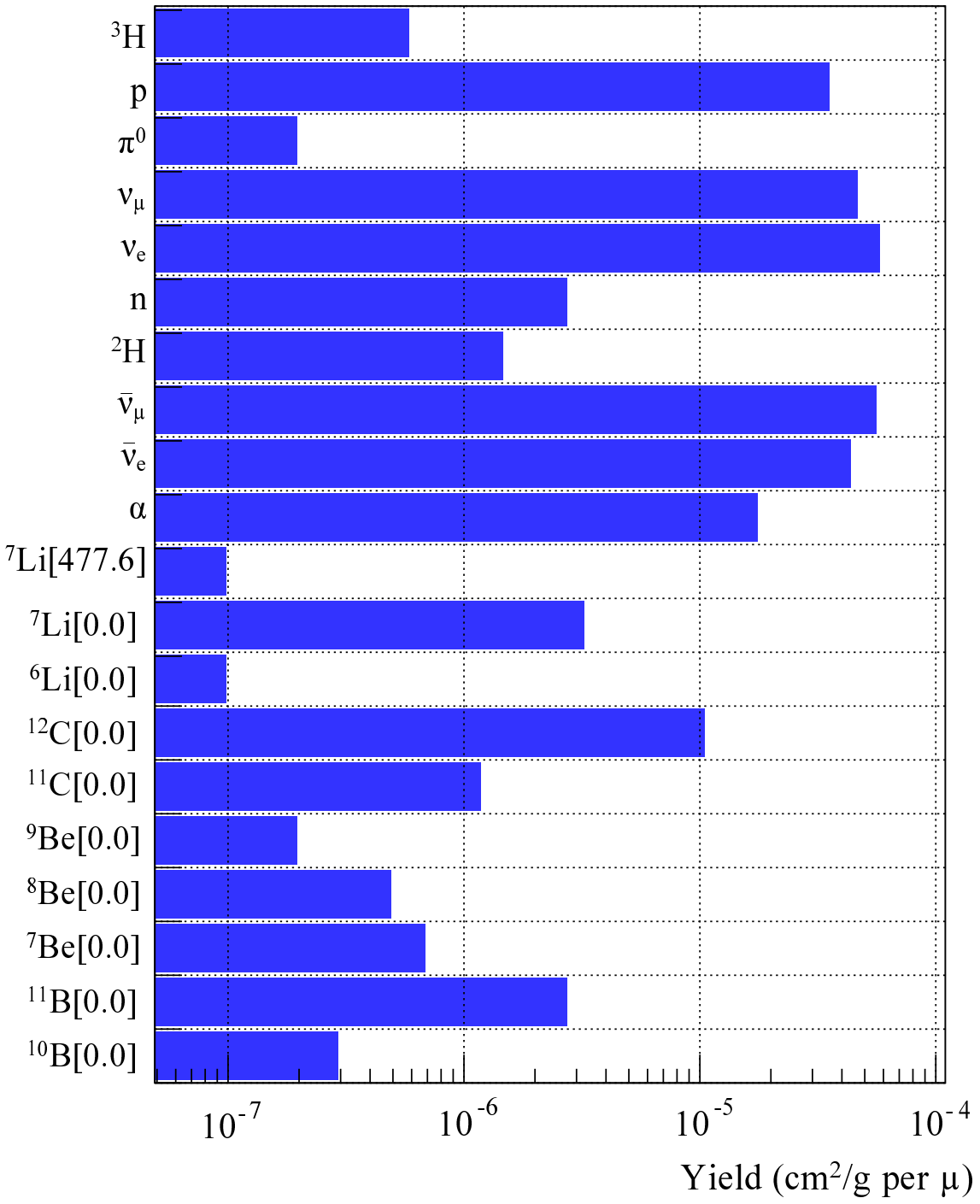

Figure A5.13: Cosmogenic isotope production yield due to sea-level spectrum μ^-s passing through 10 m of EJ-254 plastic. 10^4 events were simulated for this result. The number enclosed in brackets in the labels along the y-axis is the excitation energy of the isotope in units of keV. ^{9}Li and ^{8}He were not observed.

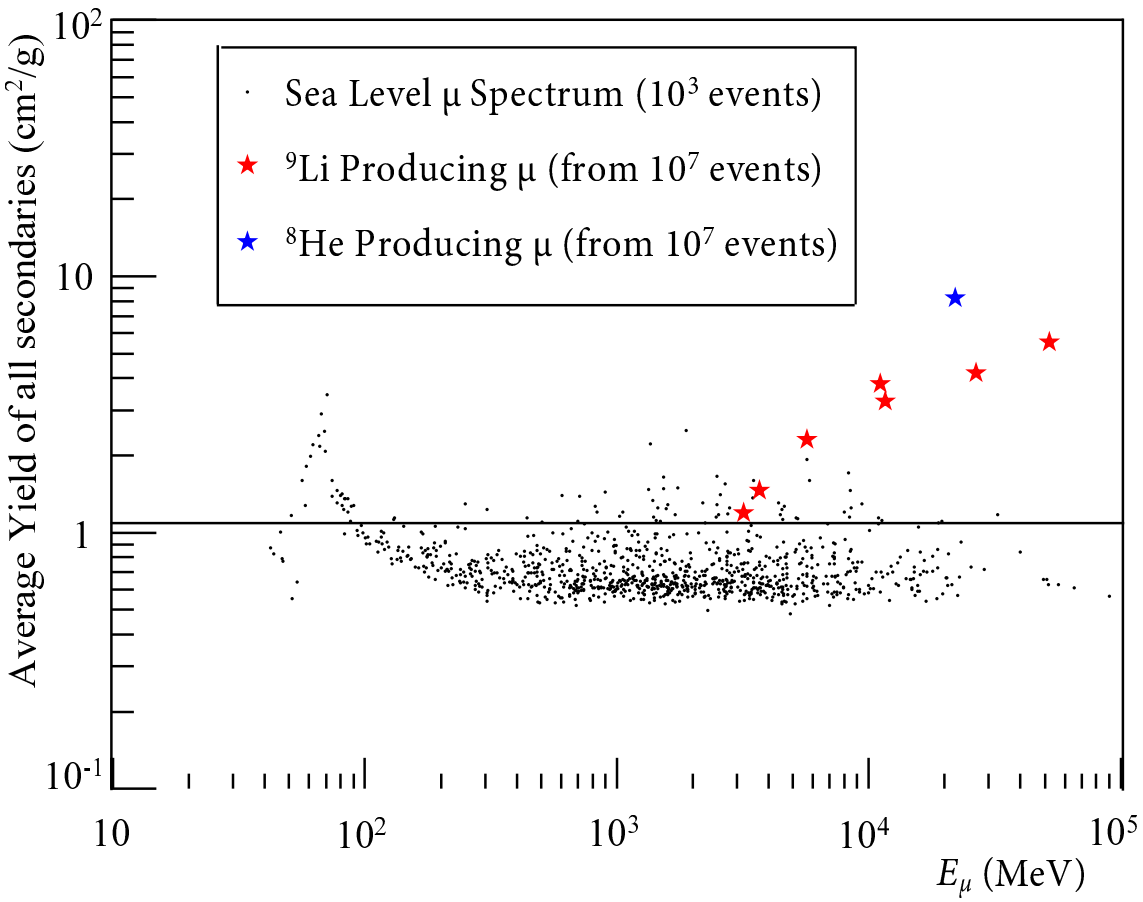

Figure A5.14: Average yield per unit muon track length per unit medium density of all non-photon secondary particles versus muon energy. The black points show the result of a run of 10^3 sea-level spectrum muons. Superimposed on the figure are eight specific muon events that had produced a ^{8}He or ^{9}Li daughter depicted by the colored stars. These eight events were extracted from a much larger ensemble with an increased statistics of 10^7 events in order to produce the rare events.

Design and production of the shielding cave is currently underway and these background studies will be pursued in parallel as development continues.

Finally, with an mTC-type detector, it is straightforward to implement additional vetos to reject backgrounds if needed. This can be accomplished by installing scintillator paddles around the mTC and feeding additional trigger signals to the trigger/clock distribution board.

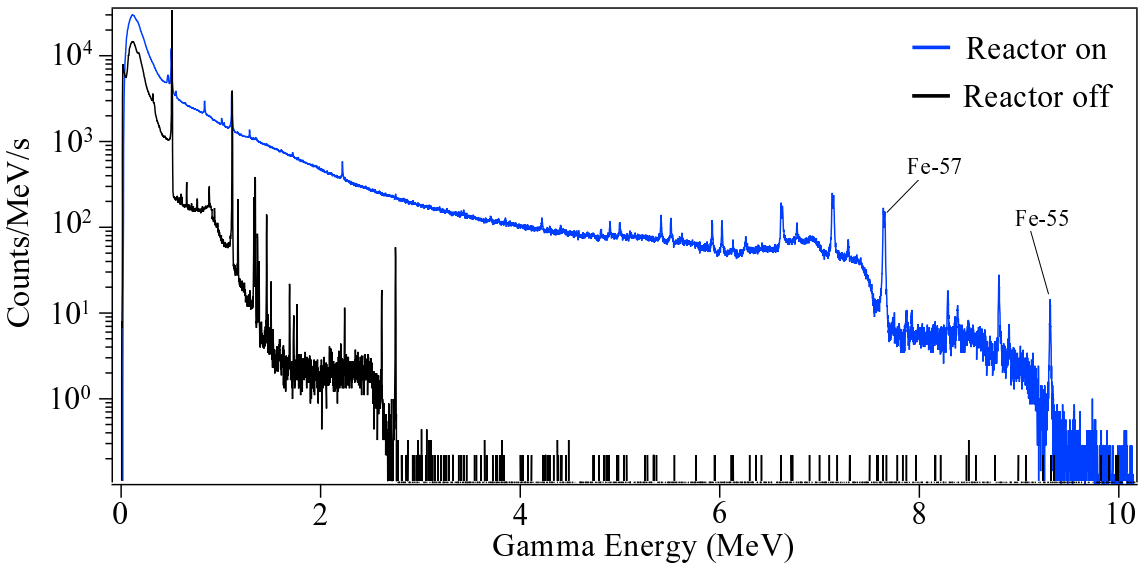

Figure A5.15: High Purity Germanium (HPGe) gamma-ray spectrometer response at the mTC location adjacent to the NIST reactor. HPGe spectrometer is 55 mm in length and 62.5 mm in diameter. The observed Fe lines are from neutron capture on surrounding shielding and structural materials.

A5.4.2 Backgrounds at the NIST Reactor Location

Detailed background studies must be performed at a particular reactor site, since all venues differ and the backgrounds depend in detail upon local conditions. A group preparing for the PROSPECT experiment carried out a detailed background survey in the mTC location.(*Ashenfelter et al.*, 2015)

Figure A5.15 shows the gamma spectrum at the proposed mTC location without shielding. The difference between the reactor on/off spectra is readily visible. The "reactor on" spectrum extends to relatively high energies due to prompt gammas from neutron capture thus posing additional challenges for shielding.

Deployment of mTC as an antineutrino detector at the NIST reactor, where the backgrounds are particularly high due to adjacent neutron scattering instruments, requires shielding from various background signals that could overwhelm or

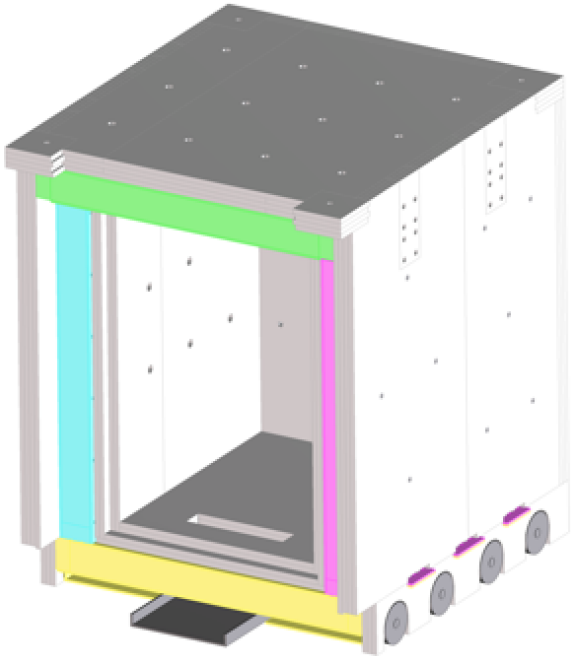

Figure A5.16: CAD of the multi-layer shielding for the mTC.

create false events within the scintillating volume (e.g., high-energy gammas, thermal neutrons, fast neutrons, cosmic ray induced muons and their decay products). In most other anticipated deployment locations we do not expect shielding to be critical.

Towards that effort a multi-layered shielding cave was designed to encase the mTC and most of its associated electronics during the testing at the NIST reactor. The mTC detector will be deployed inside this shielding cave and together they will be placed against the face of the reactor biological shield. The shielding cave is comprised of six nested cubes, with the outermost dimensions yielding a footprint of $\sim$ 1.8 m $\times$ 2 m $\times$ 2.7 m and a total internal wall thickness of roughly 0.4 m. From exterior to interior, the layers are as follows (Fig. A5.16):

1. 10 cm of 5% borated polyethylene sheet

2. 1 cm of A36 steel plate
3. 15 cm of steel shot and paraffin wax mixture
4. 1 cm of A36 steel plate
5. 10 cm of 5% borated polyethylene sheet
6. Interior cavity for housing the mTC and associated electronics (dimensions 1 m $\times$ 1.2 m $\times$ 1.5 m)

Borated polyethylene was chosen for its neutron absorbing properties while the layer of steel shot and wax acts as both a neutron and gamma absorber. All layers serve to attenuate the muon flux, albeit less efficiently. The overlapping construction removes potential line-of-sight and the hermetic design inhibits the penetration of thermal neutrons, which exhibit gas like properties.

The shielding cave is 20 tons. The entire weight of the cave is supported on rails already laid into the floor at the NCNR, which allows the cave to be moved across different baselines.

The interior of the shielding cave will house the mTC, complete with its electronics rack containing high voltage power supplies and support electronics. The system requires less than 2 kW of 115 VAC power, and has its own uninterruptible power supply system. Accommodations for cooling of the electronics will be used, with access for cooling and electricity through a floor tray. During mTC operation access to the interior of the cave is expected to be infrequent.

We use GEANT4 to estimate effectiveness of the different shielding layers in attenuating potential backgrounds. The modeled environment includes the shielding

cave, a 0.5 m thick concrete roof above the area, and a concrete reactor bio-shield next to the shielding cave.Three primary particles (muons, neutrons, and gammas) and two particle sources (atmospheric and reactor), including their relevant energy spectra and fluxes, were used.

Atmospheric gamma and muon energy spectra were calculated using the Cosmic-RaY shower Library (CRY) (*Hagmann et al.*, 2012b).We use the spectrum and flux for atmospheric neutrons from *Gordon et al.* (2004c) A Maxwell-Boltzmann distribution at 600 K with an integrated flux of 3-4 neutrons cm^{-2} s^{-1} was used to represent reactor neutrons outside the shielding cave. The integrated flux was chosen to match energy-insensitive Bonner ball measurements taken *in situ*. Because the neutron energy spectrum was not measured, a higher characteristic temperature (vs 298 K) allows the simulation to conservatively account for a portion of the reactor neutrons not being thermalized. The reactor gamma spectrum and flux ($\sim$200 cm^{-2} s^{-1} above 100 keV) comes from a measurement at NIST adjacent to the proposed mTC site with the reactor on.

For the purposes of preliminary Monte Carlo work, atmospheric particles were assumed to follow a $\cos^2\theta$ angular distribution. Reactor particles were assumed to be isotropic, although significant spatial variation coming from localized source has been measured, and if needed will be incorporated in later work.

Preliminary estimates of the resultant particle fluxes through the mTC volume with and without the cave present are shown in Table A5.2. These include secondaries produced within the shielding material itself. Measurements taken *in situ* useful for Monte Carlo validation are planned and will be reported in a future

publication.

Table A5.2: Particle fluxes through the mTC volume with and without the shielding cave present. The neutron flux is dominated by near-thermal neutrons hence the large attenuation factor. Muons are incident on the mTC at a rate of less than 3.5 Hz, and are not significantly affected by the shielding cave.

	normal	shielded	normal	shielded	attenuation
Type	#/mTC/s		#/cm^2/s		%
Neutron	3391	0.082	4.0	9.7×10^{-5}	99.9%
Gamma	169015	325	2.0×10^2	3.8×10^{-1}	99.8%

The Monte Carlo model of the mTC using the shielded fluxes in Table A5.2 shows a signal to background (for uncorrelated events only) of roughly 1:1. These uncorrelated events are usually composed of two independent gammas entering the detector within our 12 μs time window, the first creating a false prompt signal and the second a false delayed signal. An order of magnitude less likely are uncorrelated backgrounds in which a neutron creates a false delayed signal instead of a gamma. These simulation results indicate that accidental coincidences from uncorrelated backgrounds will likely not be our dominant background source, and we are beginning to focus more on correlated secondaries originating from high-energy cosmogenic neutrons and muons.

A5.5 Electronics

The mTC concept puts stringent requirements on the channel density, timing performance, synchronization, and power consumption of the detector. In order to fully utilize the spatial information provided by the pixelization of the 24 MCP-PMTs, all 1536 channels must be separately instrumented. The readout for each

pixel must preserve the $\mathcal{O}$(100ps) timing provided by the photodetector, and to avoid further timing degradation the timing of all detector channels must be synchronized to one another at a level significantly below the transit time spread of the MCP-PMT. An online trigger system is required to isolate physics interactions of interest from backgrounds.

A5.5.1 Front-end Electronics

The core of the front-end electronics functionality is provided by the IRS, a family of application specific integrated circuits (ASICs) developed at the University of Hawaii. The IRS has been used in a variety of projects that require fast sampling and deep buffering (*Dey et al.*, 2014; *Bechtol et al.*, 2012; *Allison et al.*, 2012).

Table A5.3: Operating parameters for the IRS family of ASICs, and nominal ASIC operating conditions for the mTC. Full performance parameters will be reported in a future publication.

Parameter	IRS Range	mTC Setting
Channels	8	
Sampling cells	128	
Storage depth	32,768	
Analog bandwidth	$>$ 300 MHz	
Digitization	on-chip Wilkinson	
Quantization	12(9)-bits logged(effective)	
Dynamic range	$\sim$ 2 V	
Typical noise	$\sim$ 1 mV_{RMS}	
Sampling rate	1–4 GSa/s	2.73 GSa/s
Master clock	8–31 MHz	21.3 MHz
Buffer time	$(8-32)\mu$s	12.0 μs
Conversion time	$>$ 2 μs	6.2 μs

The IRS ASIC architecture is shown schematically in Fig. A5.17, and a list of operating parameters can be found in Table A5.3. The ASIC has 8 analog in-

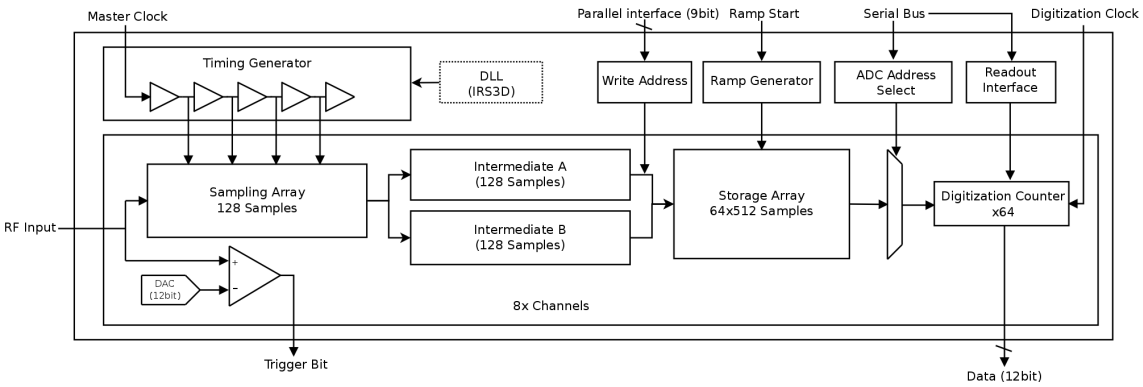

Figure A5.17: Block diagram of the IRS ASIC architecture. Eight channels of analog input are received by a set of eight sampling arrays, with sampling timing based on a common timing generator, driven by an external clock. This timing generator also determines timing of transfers from the sampling arrays to intermediate and storage arrays. The target location for the transfer from the intermediate to storage array is controlled by the user with a 9-bit parallel bus. A separate pin is used to start an internal voltage ramp, used to digitize 64-samples of the storage array for all eight channels in parallel. Selection of the storage address to digitize is controlled through a serial interface. A clock for the Wilkinson digitization process is generated internally (IRS3B) or provided externally (IRS3D). Once data is digitized, the channel and sample to readout are controlled by a second independent serial interface. Digitized data is available on a parallel 12-bit bus. A number of DACs and internal timing parameters are controlled by a third serial register interface.

put channels, each with a sampling stage, intermediate and deep storage stages, on-chip digitization, and per-channel threshold triggers. The sampling stage is a multi-GSa/s switched capacitor array (SCA) waveform sampler, similar to other ASICs, (*Delagnes et al.*, 2006; *Ritt et al.*, 2010; *Oberla et al.*, 2014) in which a sampling clock propagates down a delay line, with subsequent delay stages utilized to create short, GHz-scale timing intervals to sample the input signal onto capacitors. Unlike other SCA waveform samplers, this sampling array is connected to deeper buffers to allow for higher trigger latencies and larger time records per-event. Buffer amplifiers are used to drive the stored voltages from the sampling array into a deep sampling array consisting of 32,768 storage capacitors per channel. This transfer occurs via an intermediate storage array to accommodate the settling time of the buffer amplifiers. Signals required to coordinate the intermediate transfers are provided by an internal timing generator, and the final location of the samples in the deep storage array is provided by a parallel address bus that is driven by the user, allowing for flexible and user-defined memory management schemes. The IRS includes 12-bit Wilkinson ADCs, which digitize 64-sample blocks of the storage array for all 8 channels in parallel. Readout of the digitized data is done one sample at a time through a 12-bit parallel bus. Selection of the channel and sample number is provided by the user via a serial interface. A typical digitized MCP pulse in the mTC system is shown in Fig. A5.18.

Analog inputs for each channel are also monitored by a comparator, with the digital trigger bits available to the user. These bits can be used to monitor which sections of analog memory have signals above a user-defined threshold, allowing the

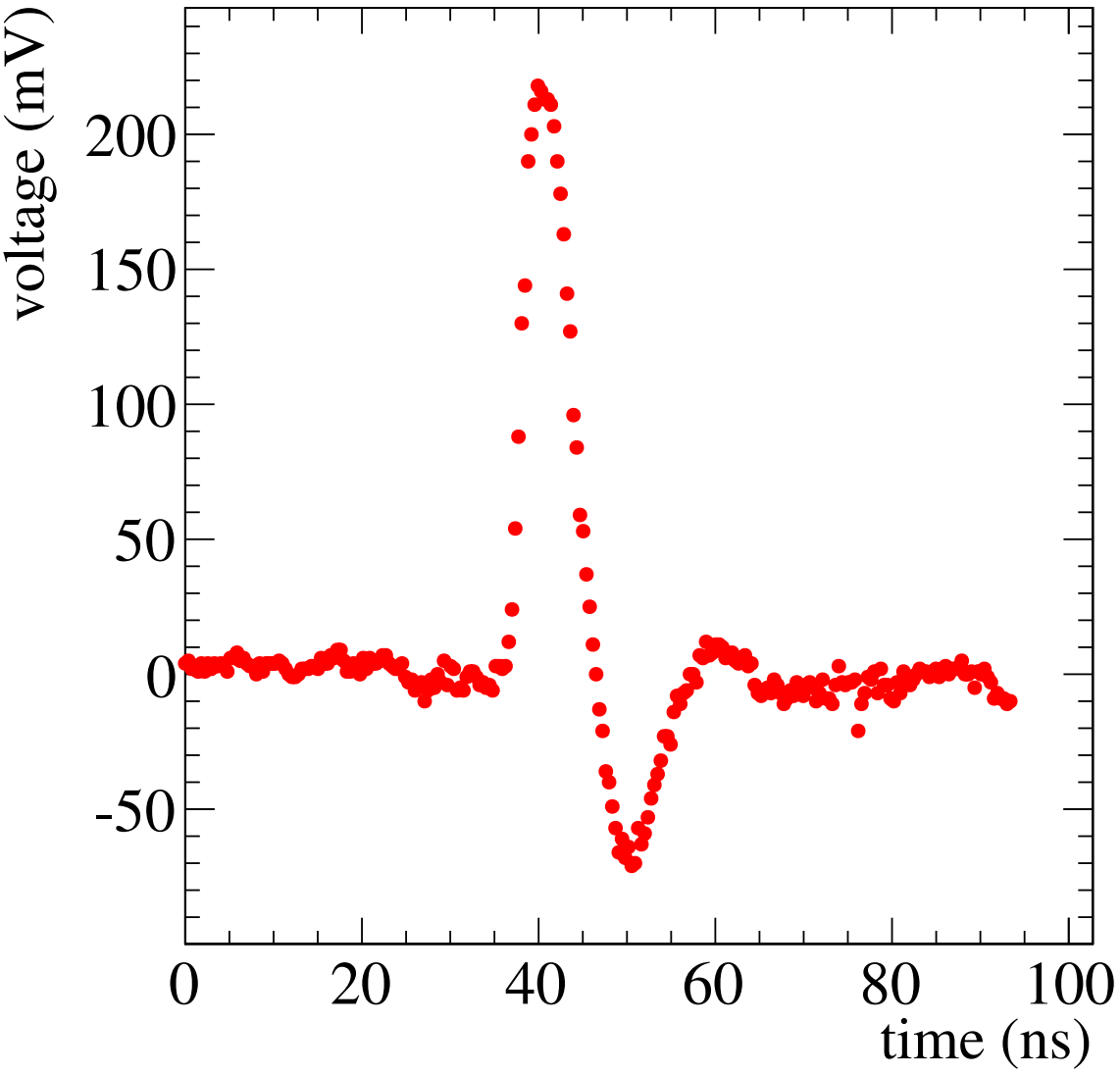

Figure A5.18: Example MCP pulse digitized with the IRS3B. Times for each point are calculated based on a nominal sampling rate of 2.73 GSa/s. Voltages are calculated based on a nominal conversion factor of 0.6 mV/ADC count, and represent the signal after passing through an external amplifier.

user to select only those windows which have signals of interest to be read out. Further details on the IRS ASICs and their performance will be presented in an upcoming publication.

One front-end electronics module, or "board stack," shown in Fig. A5.19, includes 16 IRS ASICs (128 total input channels from 2 MCPs). Each analog input is amplified by an RF amplifier before arriving at the IRS ASIC. The initial version of the mTC was developed with the IRS3B ASIC, and an upgrade is in progress to move to new board stacks using the IRS3D, a new revision of the ASIC that includes improvements to reduce noise and improve timing stability. In both versions of the front-end electronics, a single FPGA (Xilinx XC6SLX150T) on each board stack provides all control signals necessary to operate and readout the ASICs and other auxiliary devices. The FPGA interfaces to the back-end data acquisition system for register control and data transmission via fiberoptic cable. To coordinate timing between the 12 modules of the mTC, each board stack accepts a central distributed clock via RJ45 connector. Another RJ45 connector is wired to the FPGA JTAG interfaces, allowing remote programming of the FPGA firmware in-situ.

A5.5.2 Clock Distribution and Triggering

All 12 board stacks communicate with a custom PCB, designated Clock and JTAG In PCI (CAJIPCI), over differential pairs of CAT7a cable. The CAJIPCI provides a low jitter ($\sigma_t < 2$ ps) clock to the front-end modules. Front-end board stacks provide a module-level trigger to the CAJIPCI over another differential pair

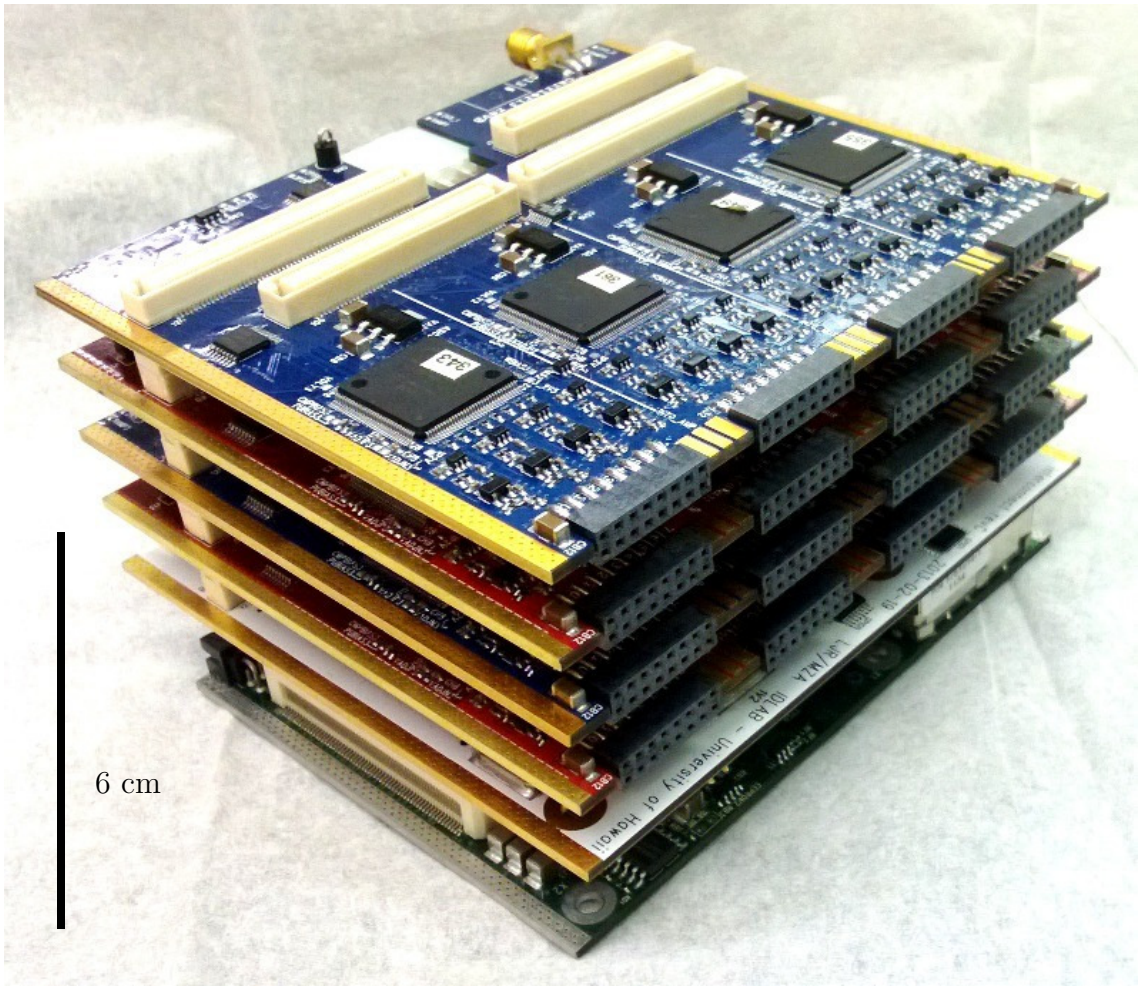

Figure A5.19: A photograph of one of the twelve board stack assemblies. The 128 MCP signals are input via connectors shown. Each board stack instruments a pair of MCPs and is enclosed in an aluminum cage surrounded by chiller plates.

on the same cable, and the CAJIPCI responds with a system level trigger over a third pair. The final differential pair can be used to perform flow control and limit trigger rates to the front-end electronics.

Three separate trigger levels are defined for the experiment. The lowest level trigger is a level 0 (L0) trigger, defined as a single channel trigger bit from an IRS ASIC. Thresholds for these triggers can be set via adjustment of an on-chip DAC. The 128 L0 triggers on a board stack are monitored by the FPGA. When the number of coincident triggers falls between two user programmable thresholds, a level 1 (L1) trigger is issued and sent to the CAJIPCI. The CAJIPCI, in turn, monitors L1 triggers from the 12 front-end board stacks, and issues a level 2 (L2) trigger to the front-end modules under user-defined conditions.

A basic L2 trigger can be calculated based on the number of coincident L1 triggers. This basic trigger is appropriate for signals that fall mainly in a narrow time window (e.g., neutrons, gammas, and cosmic ray muons). A neutrino L2 trigger must monitor for both a prompt and delayed signal, so it includes an initial "arming" period when it detects a prompt signal, and a second stage to issue a trigger upon receipt of a delayed signal. This logic is shown in Fig. A5.20. The timeout for the delayed trigger is typically set to ~ 12 μs, the length of the IRS storage array. Longer times between prompt and delayed signals are possible based on the analog memory management scheme used for the IRS, and this may be explored in future upgrades.

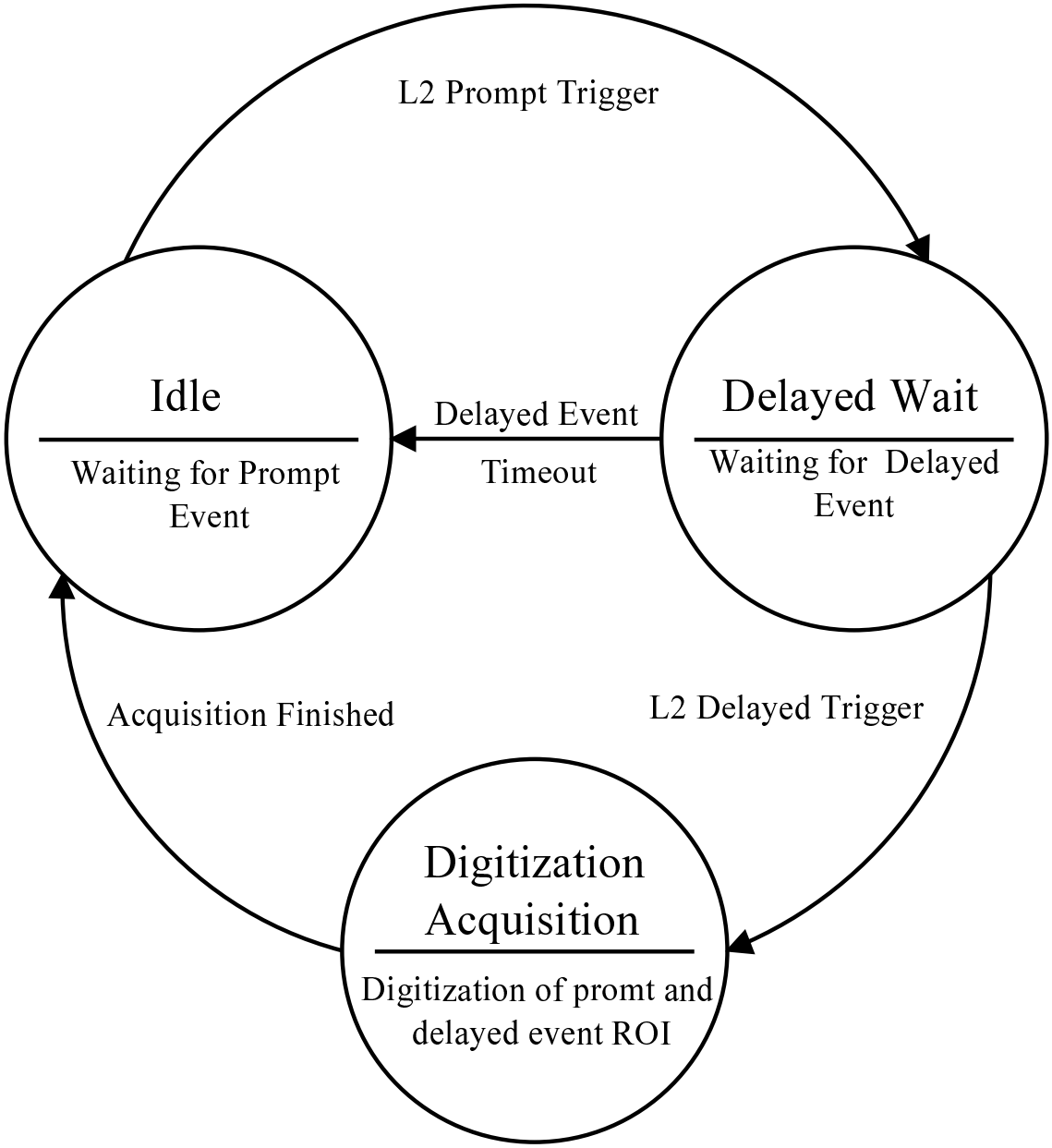

Figure A5.20: State machine diagram of the neutrino trigger.

A5.5.3 Data Acquisition and Software

Upon receipt of an L2 trigger, data from the front-end modules is digitized, readout by the front-end FPGA, and sent over fiberoptic cables using a gigabit Ethernet (1 GbE) interface. This data is received by commercial PCIe Ethernet cards, running on a rack-mount server, which can be operated directly or via a network connection. Operations from powering up to collecting data may be performed remotely over this network, with an aim for full remote control.

Data acquisition is implemented primarily in C++, with a Python API to the system that can be used for configuration as well as monitoring and slow control of the detector. Several algorithms and programs have been developed to perform automated startup, initialization, and real-time fine tuning of the electronics. Before physics data acquisition begins, threshold scans and pedestals are collected for each channel and stored in files for each board stack. Timing parameters for each chip are taken, adjusted, and stored to ensure optimum calibration. Once this procedure is completed, the files can be used for repeated data runs. For more detail on the required electronics calibrations, see Section A5.6.

Once the detector is initialized and data is taken, the data can be observed and analyzed with tools developed by the collaboration. Several event viewers have been developed and analytical methods for analysis and event reconstruction are being employed using packages such as MATLAB, C++, and ROOT.

A5.5.4 Support Systems

Power is supplied by high voltage (HV) and low voltage (LV) units from modular power supplies. These are mounted in the rack underneath the mTC's aluminum enclosure and are operated remotely. The front-end power consumption is approximately 330 W, so cooling of the electronics is crucial. Commercially available hard-drive chiller plates are used and mounted on the electronics card cages with deionized water as a coolant at a total flow rate of $\sim$ 2 GPM. When the detector is operating, the temperature of the ASICs is monitored during operation to ensure the safety and stability of the electronics, and typically is stable in the range $\sim$ 30–35 ℃, depending on ASIC position.

A5.6 Calibration

A number of calibrations are required to operate the detector and remove systematic biases, including electronics effects (both amplitude and timing), MCP efficiency and gain, and calibration with physics processes. We describe each in more detail here.

A5.6.1 Electronics Calibrations

The architecture of the IRS ASIC utilizes individual capacitors and comparators for each of the 32,768 storage cells of an input channel. Variations in the fabrication process create sample-to-sample differences in threshold voltages for the comparators, resulting in a fixed-pattern voltage structure that must be removed

from digitized waveforms. These are known as "pedestals" and are evaluated by collecting events with no signal input. This may be done, for example, with the MCP high voltage turned off, or with the high voltage on but using software triggers that are uncorrelated with any signal inputs. Pedestals are typically collected at the beginning of a run period. Over 50×10^6 pedestals are required to run all channels of the detector at their full sampling depth. An example waveform following pedestal subtraction can be seen in Fig. A5.18.

Further feature extraction is performed on pedestal subtracted data, including estimates of pulse height and pulse times. Pulse timing is estimated using an offline, software-based, constant-fraction discrimination method, with time defined by the crossing of the signal over a set percentage of the pulse height, typically around 50%. Linear interpolation is used to determine this time with much higher granularity than the 370 ps spacing of the individual samples. To achieve the best possible timing resolution, further calibrations are necessary to remove ASIC fabrication effects. The delay line used to generate the fast sampling signals within the ASIC is a current-starved inverter chain. As with the storage cell comparators, process variations cause threshold variations in these inverters, leading to non-uniform timing distributions from sample-to-sample. This manifests as a fixed-pattern timing structure that is unique to each ASIC, which we refer to as the "fine timing calibration." A total of 128 timing offsets must be calculated for each ASIC, one for each stage of the delay line. Typical spreads in timing values are 10-15% of the nominal sampling delay. For example, in our standard operating mode with the IRS running at 2.7 GSa/s, the mean timing delay is 370 ps, with a spread of roughly $\sigma_t \approx 13 - 55$ ps.

To perform this timing calibration we inject MCP-like pulses into the electronics at known delays relative to the sampling clock. By stepping the delay of these pulses in fine increments (as low as 15 ps) we can calculate a pulse time in units of sampling cells and cross reference it against the known delay, allowing us to map out the fine time structure within the ASIC. A total of 24,576 of these timing values (128 sample delays $\times$ 16 ASICs $\times$ 12 board stacks) are stored for the full detector.

Following these fine timing calibrations, we must then align all channels of the mTC to a common time reference. Although all channels sample synchronously based on the distributed master clock, various skews are introduced throughout the system from the ASIC structure, PCB routing delays, cable lengths, etc. To characterize these delays, we use a laser system, described below, to inject signal at fixed times into each face of the detector. By aligning timing of pulses for all channels relative to one another, we can measure these skews for each of the 1536 channels and remove them for any subsequent analysis.

A5.6.2 Laser Sources

A precision timing laser system (Advanced Laser Systems EIG1000D) can inject signal into any of the 6 faces of the mTC through a 'needle' fiber connector installed in the space between the MCPs. Variable neutral density filters can be inserted between the laser diode output and the input to the fiberoptic connections that inject into the mTC. This allows studies at adjustable light levels, from single

PE and up. Stepper motors can be used to move optical elements and select the injection point of the laser, or adjust the laser attenuation. The laser controller is triggered by the timing distribution board, allowing optical pulses to be injected at adjustable times relative to the master sampling clock. These features allow the laser to be used as an automated in-situ calibration or validation source.

A5.6.3 MCP Gains

All 24 MCPs operate on independent high voltage channels, allowing selection of gain independently for each tube. A specification from the manufacturer is provided for each MCP unit with HV settings at 10^5 gain. We have further measured gain curves by observing the common-last-dynode of each MCP for laser and cosmic ray muon signals. Specific HV settings vary by operating mode, as the expected number of PE detected covers a very broad range from tens of thousands of PE (e.g., for cosmic ray muons fully traversing the detector), to under 100 PE (for the delayed neutron capture from IBD).

Since gain can vary considerably across the pixels of an MCP, we must further calibrate the gains of each individual channel. This is typically done by measuring single PE signals across the detector, either injected using the laser or by observing MCP dark pulses, and normalizing their mean amplitudes to one another. This further provides a conversion factor from digitized counts to an estimated number of PE for each recorded pulse. Quantum efficiency can be similarly calibrated on a pixel-by-pixel basis, using the calibration laser running in a mode where we collect

primarily single PE pulses.

An example of a gain map obtained from laser data is shown in Fig. A5.21.

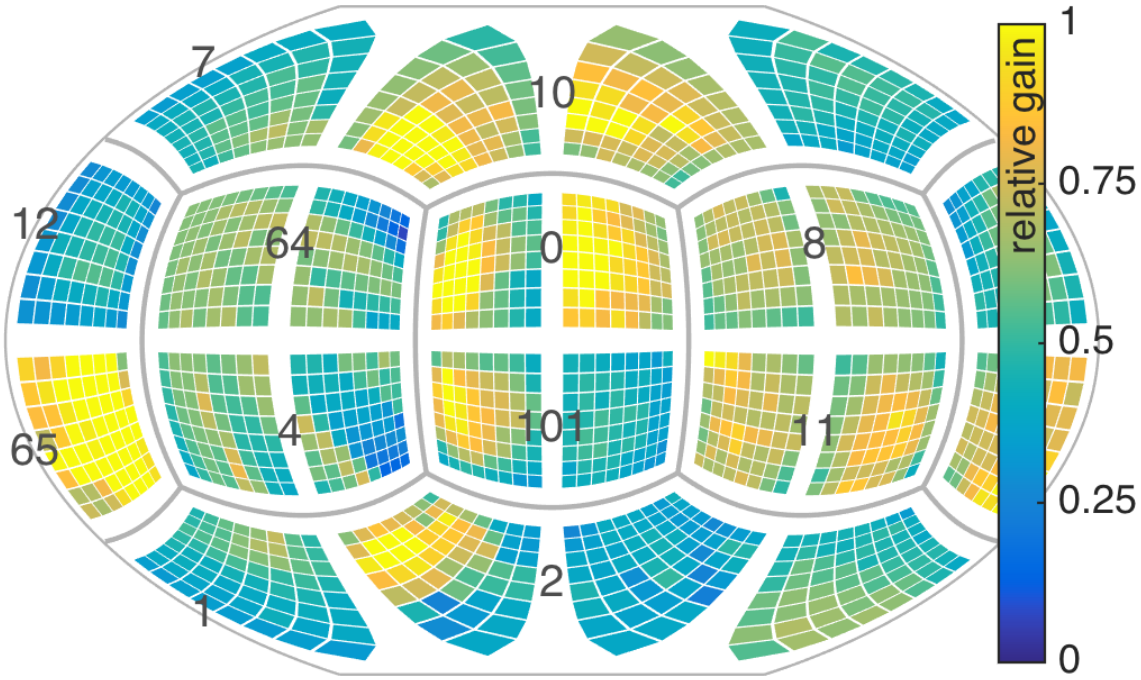

Figure A5.21: Display of a preliminary relative gain map obtained from laser data. This includes electronics effects, such as variation in amplifier gain.

A5.6.4 Cosmic Muons

Cosmic ray muons provide one method for validating the calibrated performance of the detector, as they have a known energy deposition and time-stable rate. The fairly stable flux at sea level ($\sim$ 1 Hz through the detector) has a mean energy of about 2 GeV and is peaked near the vertical but falls off towards the horizon gently with a $\cos^2$ of zenith angle. In typical running conditions one would expect some variation due to the local overburden. The minimum ionizing energy loss rate for polyvinyltoluene (*Olive et al.*, 2014) (the plastic in the mTC's scintillator) is 1.956 MeV cm^2/g with density 1.02 g/cm^3, so the net (mean) energy loss

rate in the cube should be about $dE/dx = 2.3$ MeV/cm.

To acquire muon data, a low gain is set on the MCPs to avoid saturation, and the trigger levels are changed accordingly. The previously determined electronics and gain calibrations are used to analyze the resulting data, and muon tracks can be fitted through the detector, as shown in Fig. A5.22. An example of reconstructed muon parameters for a preliminary data set is shown in Fig. A5.23.

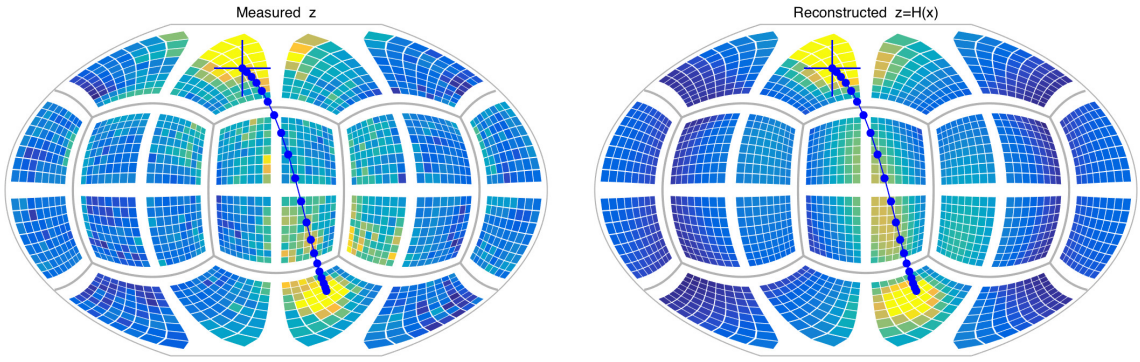

Figure A5.22: Event display for a muon measured in mTC (left) and the expected light distribution for the best fit reconstructed path of the muon (right).

A5.7 Reconstruction

The fast timing of the mTC's electronics, coupled with the excellent spatial resolution of the MCP channels, allows for high-quality reconstruction of subatomic events. Reconstruction is generally subdivided into two categories: unconstrained and constrained. *Unconstrained reconstruction* techniques like simple back-projection make possible the recovery in space and time of any arbitrarily-distributed pattern of energy, while *constrained reconstruction* techniques – the simplest being a single point-source fit – allow for the exploitation of *a priori* knowledge about the

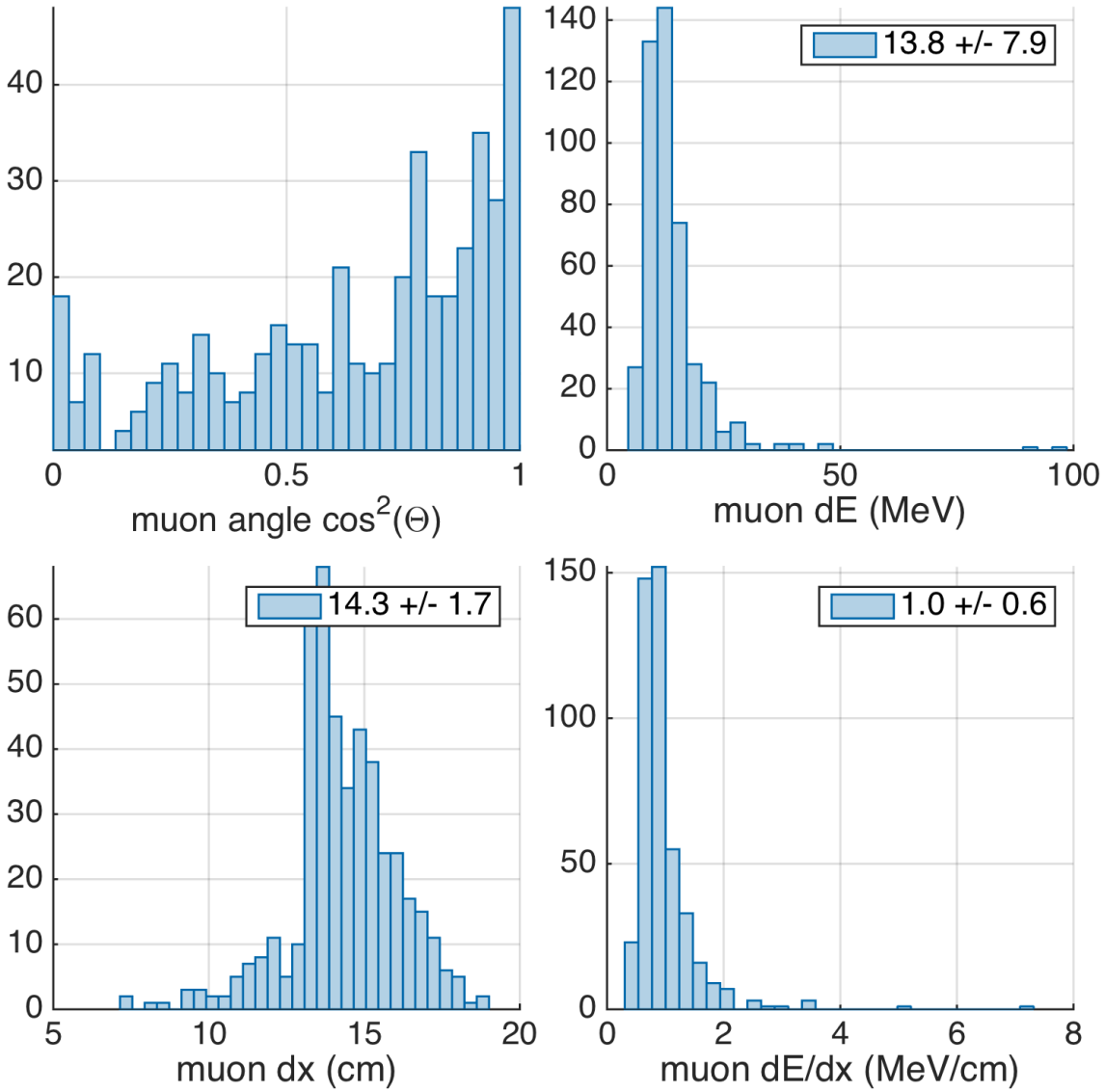

Figure A5.23: Preliminary distributions of reconstructed cosmic ray muon parameters using data collected with the mTC, showing reconstructed incident angle (top left), energy deposition (top right), muon track length within the mTC (bottom left), and muon energy deposition per unit track length (bottom right). These distributions reflect a 500 event data sample. Results are expected to improve as calibrations continue.

event, and provide more accurate reconstructions as long as correct assumptions are applied (*Jocher et al.*, 2015).

In general, the likelihood of observing a single photo-electron (PE) z from a single point-source θ is

$$p\left(z|\theta\right) = \Lambda_t P_\Omega P_\gamma P_T Q \tag{A5.16}$$

where Λ_t is the temporal likelihood, P_Ω is the solid angle probability, P_γ is the unattenuated energy probability, P_T is the transmission (or non-reflecting) probability, and Q is the PMT quantum efficiency. Equation A5.16 then forms the basis of our likelihood function, defining the likelihood of point-source θ given measurements z:

$$p(\theta|z) = \prod_j p\left(z_j|\theta\right) p\left(\theta\right) \tag{A5.17}$$

where the likelihood $p(z_j|\theta)$ of measurement j with prior $p\left(\theta\right)$ is simply an evaluation of the measurement space created by θ at z_j. Equation A5.17 extends to multiple point sources as well:

$$p(\theta|z) = \prod_j \sum_i w_i p\left(z_j|\theta_i\right) p\left(\theta_i\right) \tag{A5.18}$$

For point source i, the likelihood $p(z_j|\theta_i)$ of measurement j given source i with weight w_i and prior $p\left(\theta_i\right)$ is simply an evaluation of the measurement space created by θ_i at z_j. This measurement space is defined by a point source position P_θ at time t_θ, and is a function of several detector and scintillator characteristics including:

- Scintillation spectrum, yield and decay constant(s)
- Cherenkov spectrum

- Quenching factors for heavy particles
- Scintillator attenuation length
- Re-emission efficiency of attenuated photons
- Refraction indices of the scintillator and PMT glass
- PMT QE
- Time and energy calibrations

Equation A5.18 forms the basis for a variety of parameter estimators in the mTC. Any number of complex shapes (i.e. muon tracks, neutron scatters, a complete antineutrino event) can be built up by using a collection of these simple point sources.

A5.7.1 Candidate Cuts

Measured events in the mTC pass through several candidate cuts before they are considered as possible $\bar{\nu}_e$ candidates. These cuts, and their related candidate efficiencies are shown in Fig. A5.24. The cuts are implemented to both improve the quality of the $\bar{\nu}_e$ events and also to reduce the likelihood of backgrounds entering into the $\bar{\nu}_e$ candidate dataset.

The 5 mm edge cuts reject events with either prompt or delayed vertices <5 mm from the wall. Since the mTC is a single volume detector, the MCPs are directly adjacent to the scintillation volume. Points which are fit too close to the wall tend to suffer from low reconstruction quality, and this cut serves to reject these potentially unreliable fits. Another reason for the edge cut is to reduce the

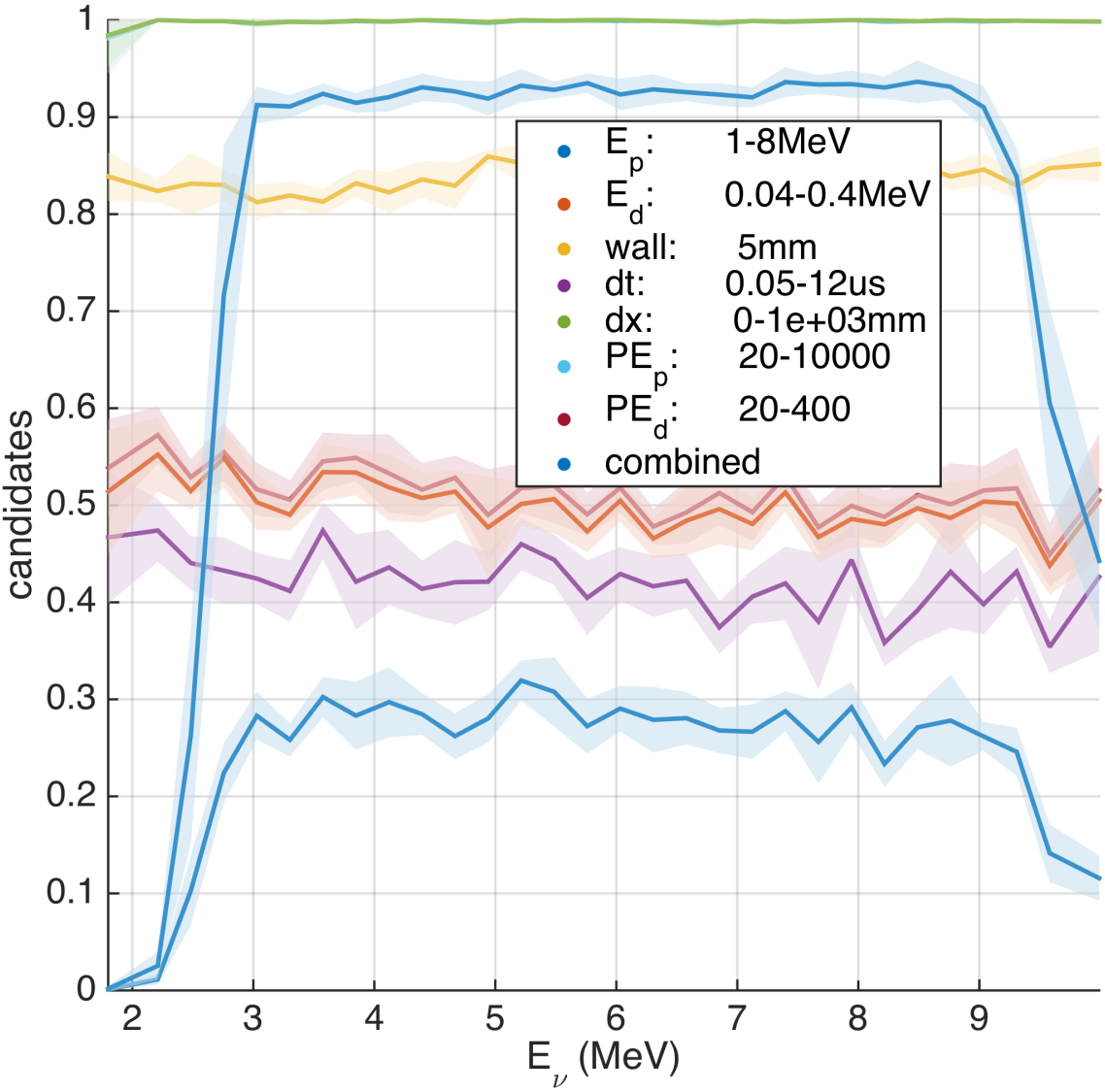

Figure A5.24: Simulated mTC $\bar{\nu}_e$ candidate efficiency vs. $\bar{\nu}_e$ energy.

likelihood of a positron from leaving the detector volume, which could result in severe underestimation of the $\bar{\nu}_e$ energy. This edge cut reduces the detector fiducial volume by 20%, from 2.2 to 1.7 liters.

There are time cuts on the prompt-delayed dt as well; these are a 50 ns floor and a 12 μs ceiling (hardware imposed). The floor is designed to prevent late prompt PE's from entering the delayed signal dataset.

We impose energy and PE cuts as well. For the prompt signal we accept energies of 1-8 MeV and PE counts between 20 and 10,000 PEs. The delayed signal has much stricter energy cuts, as it has a more consistent energy output; we accept delayed candidates with between 20-400 PEs and 40-400 keV.

$\bar{\nu}_e$ candidates must meet all these requirements in order to be accepted into the $\bar{\nu}_e$ candidate pool. In the mTC we find about 30% $\bar{\nu}_e$ candidate efficiency at 3-4 MeV. The dominant source of efficiency loss is neutrons leaving the detector volume, which happens 45% of the time, and from neutrons leaving the 12 μs time window, which happens 30% of the time. These two causes alone reduce the mTC $\bar{\nu}_e$ candidate efficiency to <40%; the other cuts only have minor effect.

A5.7.2 Performance

While the mTC has not yet detected any real world antineutrinos, its performance has been modeled through many GEANT and MATLAB Monte Carlo (MC) simulations. Figure A5.25 shows the expected $\bar{\nu}_e$ energy resolution of the mTC across the 2-10 MeV reactor $\bar{\nu}_e$ energy spectrum, which peaks at 3-4 MeV. Our

mean energy resolution is about 11% 1σ, including outliers in the long tail, or as low as 5% if outliers are ignored. Most outliers are due to higher energy positrons leaving the detector, resulting in significant under-estimation of their true energy. The prevalence of these occurrences decreases as the wall cuts are expanded.

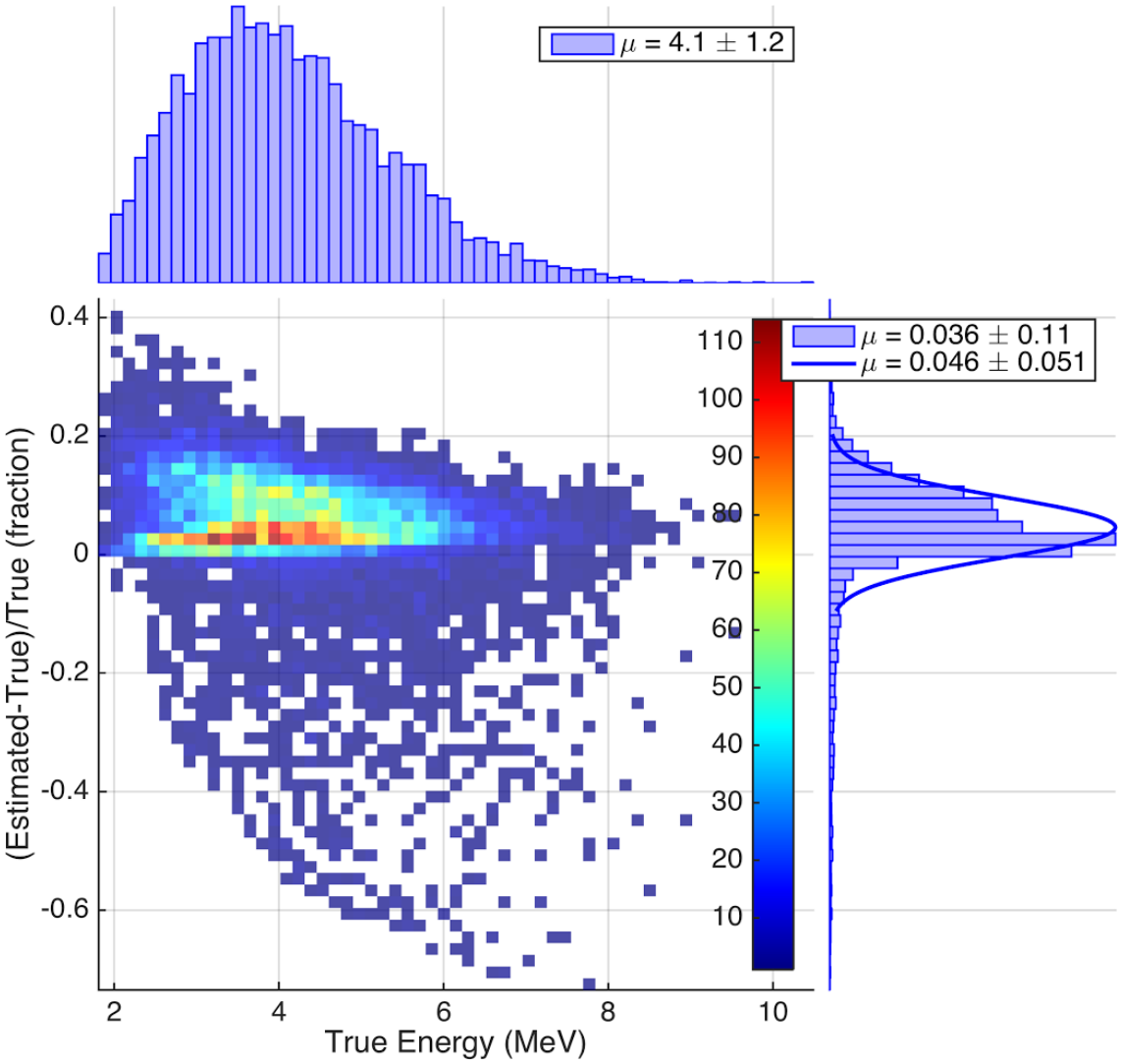

Figure A5.25: Monte Carlo (MC) simulation results showing $\bar{\nu}_e$ energy resolution in mTC (y axis) over the reactor antineutrino spectrum (x axis).

Figure A5.26 shows the corresponding energy resolution as a function of $\bar{\nu}_e$ energy rather than weighted by the reactor spectrum as in Fig. A5.25. A nice coincidence is seen here: the best energy resolution is enjoyed at the peak of the reactor

spectrum, with the resolution suffering at lower energies due to lack of light, and suffering at higher energies due to the high energy positron tracks leaving the detector more frequently. Figure A5.27 shows the same energy resolution values vs. vertex within the detector, indicating that resolution suffers near the detector walls.

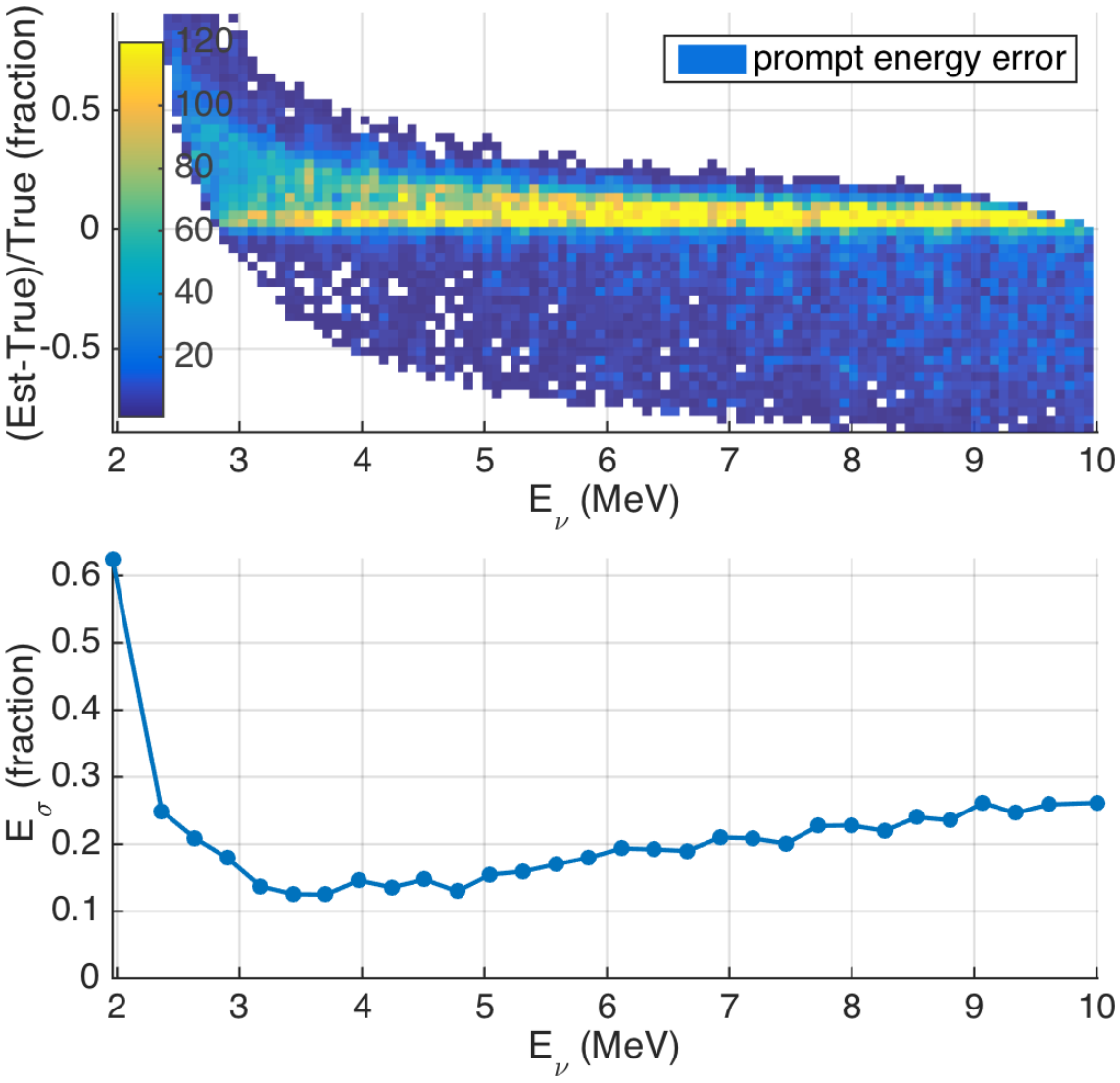

Figure A5.26: Simulated mTC $\bar{\nu}_e$ energy resolution vs. $\bar{\nu}_e$ energy.

Figure A5.28 shows the prompt and delayed vertex resolution as a function of $\bar{\nu}_e$ energy. In this context 'vertex' means the $\bar{\nu}_e$ interaction point for the prompt signal (the start of the e^+ track), and the capture location of the neutron for the

delayed signal. The prompt vertex fits tend to bias towards the center of the e^+ track rather than its start, and both the prompt and delayed vertex location fits are smeared by the spatially dispersed energy depositions of the prompt (2× 511 keV) and delayed (1× 470 keV) gammas.

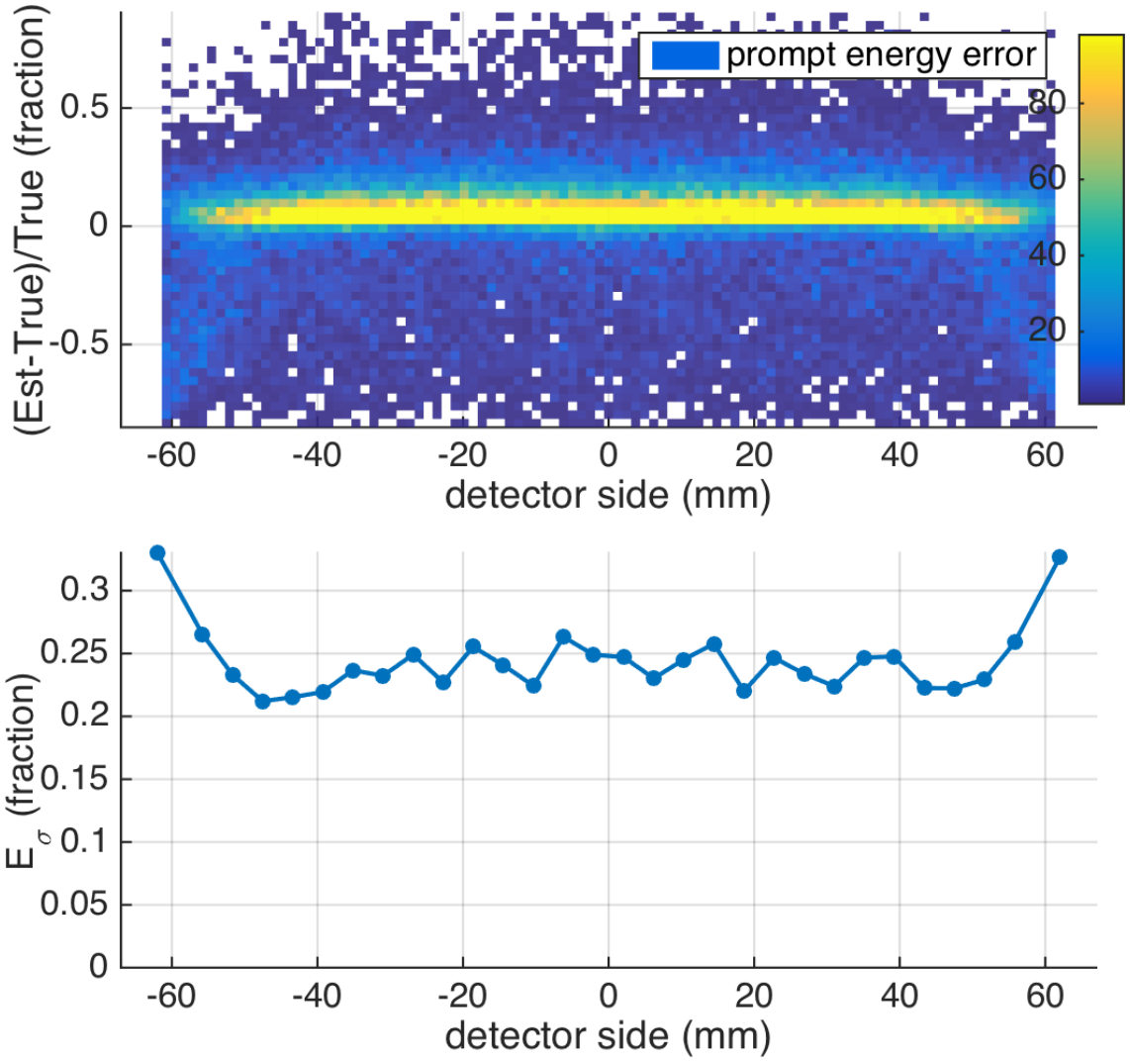

Figure A5.27: Simulated mTC $\bar{\nu}_e$ energy resolution vs. vertex location, averaged over $\bar{\nu}_e$ energy with a flat input spectrum. The detector center is at 0 mm, and the detector wall is at 67 mm.

Figure A5.28 also shows that the prompt vertex resolution suffers at low $\bar{\nu}_e$ energies due to lack of light, and at higher $\bar{\nu}_e$ energies due to longer e^+ tracks (as the

center of the track distances itself from its start point). Figure A5.29 shows Monte Carlo $\bar{\nu}_e$ angle reconstructions in the mTC and puts the mTC angular resolution in context by comparison with the CHOOZ detectors (*Abe et al.*, 2014) and hypothetical 138 kT TREND detector (*Jocher et al.*, 2013).

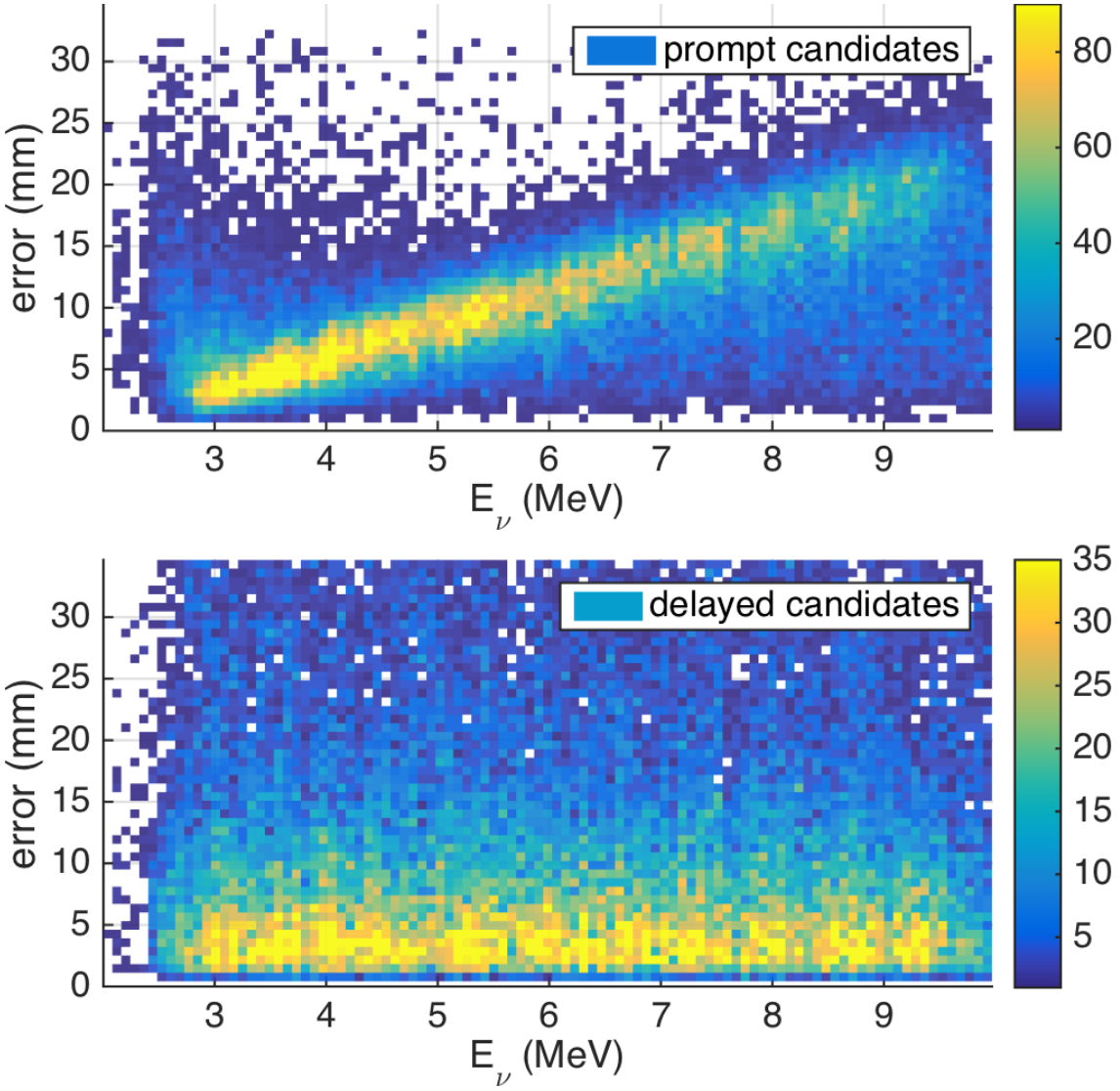

Figure A5.28: Simulated mTC $\bar{\nu}_e$ prompt and delayed vertex resolution vs. $\bar{\nu}_e$ energy.

Figure A5.29 shows the angle error distributions of mTC, CHOOZ, and TREND over the -1 to 1 $\cos(\theta)$ range, where $\cos(\theta) = 1$ corresponds to zero error and

$cos(\theta) = -1$ corresponds to 180° of angle error. The color maps on the unit sphere represent several thousand reconstructions of Monte Carlo events, and serve as a more intuitive measure of how well the mTC reconstructs direction. Though the mTC hypothetically exceeds the $\bar{\nu}_e$ angular resolution of the CHOOZ detector, they are both in reality extremely poor at directional determination from a single $\bar{\nu}_e$, and require great statistics to reduce the uncertainty on any angle fit.

The angular resolution metric we employ is the vector Signal to Noise Ratio (vector SNR). The vector SNR is the magnitude of the vector mean divided by the standard deviation in any of the 3 dimensions (which should all share similar uncertainties) for a given population of vectors. In our application these vectors are the reconstruction vectors connecting the delayed signal vertices to the prompt signal vertices. Such a group of vectors should, with some uncertainty, point back towards the $\bar{\nu}_e$ source.

We use this metric rather than the more common angle 1σ because the uncertainty is so great as to wrap completely around the sphere, rendering simpler 1-dimensional methods meaningless. An alternative metric for directional statistics is the von Mises–Fisher distribution, which provides a 'concentration parameter' that increases as the angular distribution decreases.

In the mTC, our mean reconstruction vector (from delayed vertex to prompt vertex) is 10 mm long, and the 1σ standard deviation of these vectors is 32 mm, giving us a vector SNR of 10 mm / 32 mm = 0.3. In the CHOOZ $\bar{\nu}_e$ detector, the mean reconstruction vector is 17 mm long with a 190 mm 1σ uncertainty about each axis, producing an SNR of 17 mm / 190 mm = 0.09. The simulated TREND SNR

is 0.05. Figure A5.29 shows the angular distributions for these 3 detectors plotted over the -1 to 1 $\cos(\theta)$ range, as well as wrapped around a unit sphere on a common colormap. Also, a hypothetical mTC-detector is shown with 1.5% ^{6}Li-loaded plastic scintillator.

Per Fig. A5.29, the chances of reconstructing a $\bar{\nu}_e$ as originating from the correct hemisphere (i.e. forward or backward) is 62% in the mTC, 54% in CHOOZ, and 52% in TREND. These values are obtained by simply integrating the 0-1 $\cos(\theta)$ probabilities in Figure A5.29.

The analytical equation defining the vector SNR distributions shown in Fig. A5.29 is Equation 44 in *Jocher et al.* (2013) This equation defines a proper analytical PDF (one that normalizes to unity) over the -1 to 1 $\cos(\theta)$ range, and was derived specifically for the purpose of describing $\bar{\nu}_e$ directional resolution. We could not find evidence of its use previously in the field of directional statistics.

A5.8 Conclusions

The compact size of the miniTimeCube gives it the potential for many novel measurements. Preliminary results indicate the mTC should attain a 1:1 $\bar{\nu}_e$ signal-to-noise ratio inside the shielding cave at the NIST reactor site. The mTC is designed to exploit fast timing for event reconstruction. While the fiducial volume may be smaller than desirable in certain aspects, the sizing, coupled with the fast $\sim$ 100 ps electronics and high spatial resolution enable high levels of imaging and reconstruction not attainable by larger detectors. Our modeled antineutrino vertex

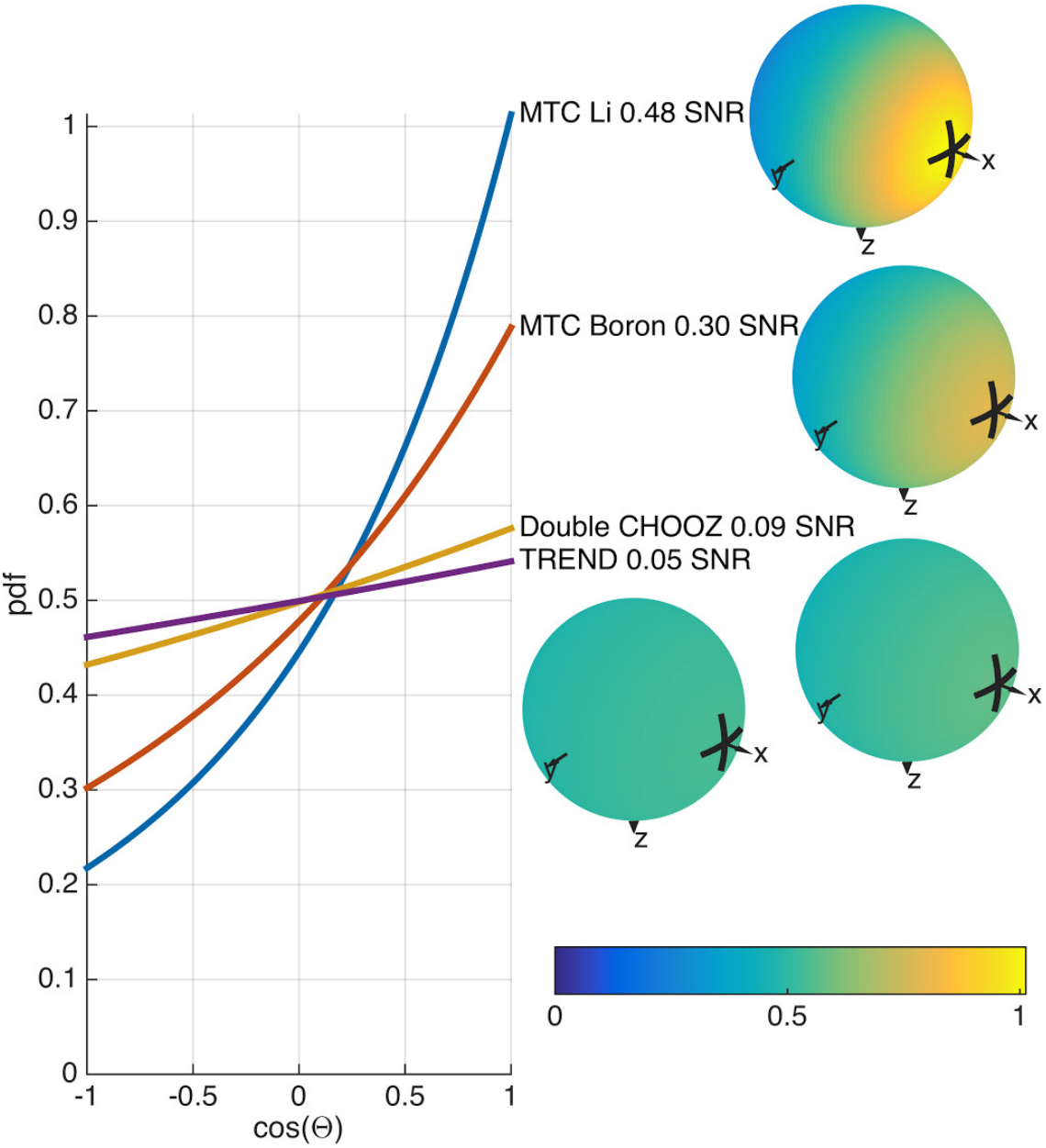

Figure A5.29: Angular $\bar{\nu}_e$ resolution comparison between mTC, CHOOZ and TREND. CHOOZ and Double CHOOZ detectors both provide nearly identical angular resolutions as a result of identical near and far detector designs.

and angular resolutions (10 mm vector and 32 mm of noise) indicate that the mTC should enjoy ∼3 times better directional resolution than existing large $\bar{\nu}_e$ detectors.

mTC energy resolution, at 11% (or 5% without outliers), is on par with other large antineutrino detectors, despite the challenges faced by uncertain gamma energy deposition from one IBD event to the next. The efficiency of the detector, at 30%, may be improved significantly by the addition of higher levels of neutron capture doping material, which would solve many of the current problems with neutron retention in time and space.

One could scale the mTC concept up to a larger detector — as is planned with NuLat — or build a networked array of such small detectors. These could be used to perform in-depth studies ranging from neutrino oscillation with novel detector arrangements at very short baselines or to explore nuclear security applications. Upgrades to the mTC are ongoing, with continuing calibration, electronics improvements, and reactor tests planned. Ultimately we believe the mTC provides exciting opportunities for fast timing exploitation, and we look forward to publishing future results as they become available.

A5.9 Acknowledgments

We gratefully acknowledge the funding for the mTC project provided by NGA, the U.S. Department of Energy HEP, the National Science Foundation, and the University of Hawaii.

We also acknowledge the support of the NIST, US Department of Commerce,

in providing support for facilities used in this work.

We would like to thank NIST personnel for hosting our detector and making the mTC lab at NIST Center for Neutron Research our second home, the UH Instrumentation Development Laboratory team for their commitment to improving the electronics, NGA for providing guidance, Integrity Applications Incorporated, the UH Physics Department workshop team, the UH Applied Research Laboratory, the UH Physics Department IT specialists, Photonis and WIENER's technical support teams, Prof. Stephen Dye from Hawaii Pacific University, UH project manager Andrew Druetzler, Sharon Messina at the NGA for help with graphic design, graduate student Stefanie Smith, undergraduate students Andrew Carpenter and Yenmy Truong who were involved in the project in its early stages, and NIST summer high school student Jason Siegel who worked on the neutron background simulations for the mTC's shielding.

Disclaimer

Certain trade names and company products are mentioned in the text or identified in illustrations in order to adequately specify the experimental procedure and equipment used. In no case does such identification imply recommendation or endorsement by the National Institute of Standards and Technology, nor does it imply that the products are necessarily the best available for the purpose.

Bibliography

Abe, Y., et al. (2014), Improved measurements of the neutrino mixing angle $_{13}$ with the Double Chooz detector, *JHEP*, *1410*, 086, doi:10.1007/JHEP02(2015)074, 10.1007/JHEP10(2014)086.

Abrefah, R. G., B. J. B. Nyarko, E. H. K. Akaho, S. A. Sampong, and R. B. M. Sogbadji (2010), Axial and radial distribution of thermal and epithermal neutron fluxes in irradiation channels of the Ghana Research Reactor-1 using foil activation analysis, *Annals of Nuclear Energy*, *37*(8), 1027–1035, doi:10.1016/j.anucene.2010.04.017.

Adam, E., G. Perron, B. Milkereit, J. Wu, A. J. Calvert, M. Salisbury, P. Verpaelst, and D.-J. Dion (2000), A review of high-resolution seismic profiling across the Sudbury, Selbaie, Noranda, and Matagami mining camps, *Canadian Journal of Earth Sciences*, *37*(2-3), 503–516, doi:10.1139/e99-064.

Adam, T., F. An, G. An, Q. An, N. Anfimov, V. Antonelli, G. Baccolo, M. Baldoncini, E. Baussan, M. Bellato, L. Bezrukov, D. Bick, S. Blyth, S. Boarin, A. Brigatti, T. Brugière, R. Brugnera, M. B. Avanzini, J. Busto, A. Cabrera, H. Cai, X. Cai, A. Cammi, D. Cao, G. Cao, J. Cao, J. Chang, Y. Chang, M. Chen, P. Chen, Q. Chen, S. Chen, S. Chen, S. Chen, X. Chen, Y. Chen, Y. Cheng, D. Chiesa, A. Chukanov, M. Clemenza, B. Clerbaux, D. D'Angelo, H. de Kerret, Z. Deng, Z. Deng, X. Ding, Y. Ding, Z. Djurcic, S. Dmitrievsky, M. Dolgareva, D. Dornic, E. Doroshkevich, M. Dracos, O. Drapier, S. Dusini, M. A. Díaz, T. Enqvist, D. Fan, C. Fang, J. Fang, X. Fang, L. Favart, D. Fedoseev, G. Fiorentini, R. Ford, A. Formozov, R. Gaigher, H. Gan, A. Garfagnini, G. Gaudiot, C. Genster, M. Giammarchi, F. Giuliani, M. Gonchar, G. Gong, H. Gong, M. Gonin, Y. Gornushkin, M. Grassi, C. Grewing, V. Gromov, M. Gu, M. Guan, V. Guarino, W. Guo, X. Guo, Y. Guo, M. Göger-Neff, P. Hackspacher, C. Hagner, R. Han, Z. Han, J. Hao, M. He, D. Hellgartner, Y. Heng, D. Hong, S. Hou, Y. Hsiung, and B. Hu (2015), JUNO Conceptual Design Report.

Agius, M. R., and S. Lebedev (2017), Complex, multilayered azimuthal anisotropy beneath Tibet: Evidence for co-existing channel flow and pure-shear crustal thickening, *Geophysical Journal International*, *210*(3), 1823–1844, doi:10.1093/gji/ggx266.

Agostinelli, S., and with the GEANT Collaboration (2003), GEANT4 — a simulation toolkit, *Nuclear Instruments and Methods in Physics Research Section A: Accelerators, Spectrometers, Detectors and Associated Equipment*, *506*(3), 250–303, doi:10.1016/S0168-9002(03)01368-8.

Agostinelli, S., et al. (2003), GEANT4: A Simulation toolkit, *Nucl.Instrum.Meth.*, *A506*, 250–303, doi:10.1016/S0168-9002(03)01368-8.

Agostini, M., S. Appel, G. Bellini, J. Benziger, D. Bick, G. Bonfini, D. Bravo, B. Caccianiga, F. Calaprice, A. Caminata, et al. (2015), Spectroscopy of geoneutrinos from 2056 days of Borexino data, *Physical Review D*, *92*(3), 031,101, doi:https://doi.org/10.1103/PhysRevD.92.031101.

Ahrens, L. H. (1954), The lognormal distribution of the elements (A fundamental law of geochemistry and its subsidiary), *Geochimica et Cosmochimica Acta*, *5*(2), 49–73, doi:10.1016/0016-7037(54)90040-X.

Allègre, C. J., B. Dupré, and E. Lewin (1986), Thorium/uranium ratio of the Earth, *Chemical Geology*, *56*(3), 219–227, doi:10.1016/0009-2541(86)90005-7.

Allègre, C. J., E. Lewin, and B. Dupré (1988), A coherent crust-mantle model for the uranium-thorium-lead isotopic system, *Chemical Geology*, *70*(3), 211–234, doi:10.1016/0009-2541(88)90094-0.

Allègre, C. J., J.-P. Poirier, E. Humler, and A. W. Hofmann (1995), The chemical composition of the Earth, *Earth and Planetary Science Letters*, *134*(3), 515–526, doi:https://doi.org/10.1016/0012-821X(95)00123-T.

Allison, P., et al. (2012), Design and Initial Performance of the Askaryan Radio Array Prototype EeV Neutrino Detector at the South Pole, *Astropart. Phys.*, *35*, 457–477, doi:10.1016/j.astropartphys.2011.11.010.

An, F., G. An, Q. An, V. Antonelli, E. Baussan, J. Beacom, L. Bezrukov, S. Blyth, R. Brugnera, M. B. Avanzini, J. Busto, A. Cabrera, H. Cai, X. Cai, A. Cammi, G. Cao, J. Cao, Y. Chang, S. Chen, S. Chen, Y. Chen, D. Chiesa, M. Clemenza, B. Clerbaux, J. Conrad, D. D'Angelo, H. D. Kerret, Z. Deng, Z. Deng, Y. Ding, Z. Djurcic, D. Dornic, M. Dracos, O. Drapier, S. Dusini, S. Dye, T. Enqvist, D. Fan, J. Fang, L. Favart, R. Ford, M. Göger-Neff, H. Gan, A. Garfagnini, M. Giammarchi, M. Gonchar, G. Gong, H. Gong, M. Gonin, M. Grassi, C. Grewing, M. Guan, V. Guarino, G. Guo, W. Guo, X.-H. Guo, C. Hagner, R. Han, M. He, Y. Heng, Y. Hsiung, J. Hu, S. Hu, T. Hu, H. Huang, X. Huang, L. Huo, A. Ioannisian, M. Jeitler, X. Ji, X. Jiang, C. Jollet, L. Kang, M. Karagounis, N. Kazarian, Z. Krumshteyn, A. Kruth, P. Kuusiniemi, T. Lachenmaier, R. Leitner, C. Li, J. Li, W. Li, W. Li, X. Li, X. Li, Y. Li, Y. Li, Z.-B. Li, H. Liang, G.-L. Lin, T. Lin, Y.-H. Lin, J. Ling, I. Lippi, D. Liu, H. Liu, H. Liu, J. Liu, J. Liu, J. Liu, Q. Liu, S. Liu, S. Liu, P. Lombardi, Y. Long, H. Lu, J. Lu, J. Lu, J. Lu, B. Lubsandorzhiev, L. Ludhova, S. Luo, Vladimir Lyashuk, R. Möllenberg, X. Ma, F. Mantovani,

Y. Mao, S. M. Mari, W. F. McDonough, G. Meng, A. Meregaglia, E. Meroni, M. Mezzetto, L. Miramonti, Thomas Mueller, D. Naumov, L. Oberauer, J. P. Ochoa-Ricoux, A. Olshevskiy, F. Ortica, A. Paoloni, H. Peng, Jen-Chieh Peng, E. Previtali, M. Qi, S. Qian, X. Qian, Y. Qian, Z. Qin, G. Raffelt, G. Ranucci, B. Ricci, M. Robens, A. Romani, X. Ruan, X. Ruan, G. Salamanna, M. Shaevitz, Valery Sinev, C. Sirignano, M. Sisti, O. Smirnov, M. Soiron, A. Stahl, L. Stanco, J. Steinmann, X. Sun, Y. Sun, D. Taichenachev, J. Tang, I. Tkachev, W. Trzaska, S. van Waasen, C. Volpe, V. Vorobel, L. Votano, C.-H. Wang, G. Wang, H. Wang, M. Wang, R. Wang, S. Wang, W. Wang, Y. Wang, Y. Wang, Y. Wang, Z. Wang, Z. Wang, Z. Wang, Z. Wang, W. Wei, L. Wen, C. Wiebusch, B. Wonsak, Q. Wu, C.-E. Wulz, M. Wurm, Y. Xi, D. Xia, Y. Xie, Zhi-zhong Xing, J. Xu, B. Yan, C. Yang, C. Yang, G. Yang, L. Yang, Y. Yang, Y. Yao, U. Yegin, F. Yermia, Z. You, B. Yu, C. Yu, Z. Yu, S. Zavatarelli, L. Zhan, C. Zhang, H.-H. Zhang, J. Zhang, J. Zhang, Q. Zhang, Y.-M. Zhang, Z. Zhang, Z. Zhao, Y. Zheng, W. Zhong, G. Zhou, J. Zhou, L. Zhou, R. Zhou, S. Zhou, W. Zhou, X. Zhou, Y. Zhou, Y. Zhou, and J. Zou (2016), Neutrino physics with JUNO, *Journal of Physics G: Nuclear and Particle Physics*, *43*(3), 030,401, doi:10.1088/0954-3899/43/3/030401.

Andersen, M. B., T. Elliott, H. Freymuth, K. W. W. Sims, Y. Niu, and K. A. Kelley (2015), The terrestrial uranium isotope cycle, *Nature*, *517*(7534), 356–359, doi:10.1038/nature14062.

Araki, T., S. Enomoto, K. Furuno, Y. Gando, K. Ichimura, H. Ikeda, K. Inoue, Y. Kishimoto, M. Koga, Y. Koseki, T. Maeda, T. Mitsui, M. Motoki, K. Nakajima, H. Ogawa, M. Ogawa, K. Owada, J.-S. Ricol, I. Shimizu, J. Shirai, F. Suekane, A. Suzuki, K. Tada, S. Takeuchi, K. Tamae, Y. Tsuda, H. Watanabe, J. Busenitz, T. Classen, Z. Djurcic, G. Keefer, D. Leonard, A. Piepke, E. Yakushev, B. E. Berger, Y. D. Chan, M. P. Decowski, D. A. Dwyer, S. J. Freedman, B. K. Fujikawa, J. Goldman, F. Gray, K. M. Heeger, L. Hsu, K. T. Lesko, K.-B. Luk, H. Murayama, T. O'Donnell, A. W. P. Poon, H. M. Steiner, L. A. Winslow, C. Mauger, R. D. McKeown, P. Vogel, C. E. Lane, T. Miletic, G. Guillian, J. G. Learned, J. Maricic, S. Matsuno, S. Pakvasa, G. A. Horton-Smith, S. Dazeley, S. Hatakeyama, A. Rojas, R. Svoboda, B. D. Dieterle, J. Detwiler, G. Gratta, K. Ishii, N. Tolich, Y. Uchida, M. Batygov, W. Bugg, Y. Efremenko, Y. Kamyshkov, A. Kozlov, Y. Nakamura, H. J. Karwowski, D. M. Markoff, K. Nakamura, R. M. Rohm, W. Tornow, R. Wendell, M.-J. Chen, Y.-F. Wang, and F. Piquemal (2005), Experimental investigation of geologically produced antineutrinos with KamLAND, *Nature*, *436*(7050), 499–503, doi:10.1038/nature03980.

Arevalo, R., and W. F. McDonough (2010), Chemical variations and regional diversity observed in MORB, *Chemical Geology*, *271*(1), 70–85, doi:10.1016/j.chemgeo.2009.12.013.

Arevalo, R., W. F. McDonough, and M. Luong (2009), The K/U ratio of the silicate

Earth: Insights into mantle composition, structure and thermal evolution, *Earth and Planetary Science Letters*, *278*(3-4), 361–369, doi:10.1016/j.epsl.2008.12.023.

Arevalo, R., W. F. McDonough, A. Stracke, M. Willbold, T. J. Ireland, and R. J. Walker (2013), Simplified mantle architecture and distribution of radiogenic power, *Geochemistry, Geophysics, Geosystems*, *14*(7), 2265–2285, doi:10.1002/ggge.20152.

Ashenfelter, J., and with the PROSPECT Collaboration (2016), Background Radiation Measurements at High Power Research Reactors, *Nuclear Instruments and Methods in Physics Research Section A: Accelerators, Spectrometers, Detectors and Associated Equipment*, *806*, 401–419, doi:10.1016/j.nima.2015.10.023.

Ashenfelter, J., et al. (2015), Background Radiation Measurements at High Power Research Reactors.

Ayer, J., J. Chartrand, N. Trowell, and A. Wilson (2010), GIS compilation of the Maple Mountain area, Abitibi greenstone belt., *Preliminary Map P.3620, Scale 1:100 000. 272*, Ontario Geologic Survey, Toronto, ON.

Bai, Z., S. Zhang, and C. Braitenberg (2013), Crustal density structure from 3D gravity modeling beneath Himalaya and Lhasa blocks, Tibet, *Journal of Asian Earth Sciences*, *78*, 301–317, doi:10.1016/j.jseaes.2012.12.035.

Baker, R. G. A., M. Schonbachler, M. Rehkamper, H. M. Williams, and A. N. Halliday (2010), The thallium isotope composition of carbonaceous chondrites — New evidence for live ^{205}Pb in the early solar system, *Earth and Planetary Science Letters*, *291*(1-4), 39–47, doi:10.1016/J.EPSL.2009.12.044.

Baldoncini, M., I. Callegari, G. Fiorentini, F. Mantovani, B. Ricci, V. Strati, and G. Xhixha (2015), Reference worldwide model for antineutrinos from reactors, *Physical Review D*, *91*(6), doi:10.1103/PhysRevD.91.065002.

Baldoncini, M., V. Strati, S. Wipperfurth, G. Bellini, F. Mantovani, W. McDonough, and B. Ricci (2016), Geoneutrinos and reactor antineutrinos at SNO+, *Journal of Physics: Conference Series*, *718*, 062,003, doi:10.1088/1742-6596/718/6/062003.

Barboni, M., P. Boehnke, B. Keller, I. E. Kohl, B. Schoene, E. D. Young, and K. D. McKeegan (2017), Early formation of the Moon 4.51 billion years ago, *Science Advances*, *3*(1), doi:10.1126/sciadv.1602365.

Bassin, C., G. Laske, and T. G. Masters (2000), The current limits of resolution for surface wave tomography in North America, *Eos Trans. AGU*.

Beacom, J. F., S. Chen, J. Cheng, S. N. Doustimotlagh, Y. Gao, S.-F. Ge, G. Gong, H. Gong, L. Guo, R. Han, et al. (2016), Letter of Intent: Jinping Neutrino Experiment, *arXiv preprint arXiv:1602.01733*.

Beakhouse, G. P. (2011), Geology, petrography, geochemistry and photographs of the south of Gogama area., *Tech. Rep. 285*, Ontario Geologic Survey, Toronto, ON.

Bechtol, K., S. Funk, A. Okumura, L. Ruckman, A. Simons, et al. (2012), TARGET: A multi-channel digitizer chip for very-high-energy gamma-ray telescopes, *Astropart.Phys.*, *36*, 156–165, doi:10.1016/j.astropartphys.2012.05.016.

Becker, H., and R. J. Walker (2003), Efficient mixing of the solar nebula from uniform Mo isotopic composition of meteorites, *Nature*, *425*(6954), 152–155, doi:10.1038/nature01975.

Begemann, F., K. R. Ludwig, G. W. Lugmair, K. Min, L. E. Nyquist, P. J. Patchett, P. R. Renne, C. Y. Shih, I. M. Villa, and R. J. Walker (2001), Call for an improved set of decay constants for geochronological use, *Geochimica et Cosmochimica Acta*, *65*(1), 111–121, doi:10.1016/S0016-7037(00)00512-3.

Bellini, G., J. Benziger, S. Bonetti, M. B. Avanzini, B. Caccianiga, L. Cadonati, F. Calaprice, C. Carraro, A. Chavarria, F. Dalnoki-Veress, D. D'Angelo, S. Davini, H. de Kerret, A. Derbin, A. Etenko, G. Fiorentini, K. Fomenko, D. Franco, C. Galbiati, S. Gazzana, C. Ghiano, M. Giammarchi, M. Goeger-Neff, A. Goretti, E. Guardincerri, S. Hardy, A. Ianni, A. Ianni, M. Joyce, V. V. Kobychev, Y. Koshio, G. Korga, D. Kryn, M. Laubenstein, M. Leung, T. Lewke, E. Litvinovich, B. Loer, P. Lombardi, L. Ludhova, I. Machulin, S. Manecki, W. Maneschg, G. Manuzio, Q. Meindl, E. Meroni, L. Miramonti, M. Misiaszek, D. Montanari, V. Muratova, L. Oberauer, M. Obolensky, F. Ortica, M. Pallavicini, L. Papp, L. Perasso, S. Perasso, A. Pocar, R. S. Raghavan, G. Ranucci, A. Razeto, A. Re, B. Ricci, P. Risso, A. Romani, D. Rountree, A. Sabelnikov, R. Saldanha, C. Salvo, S. Schönert, H. Simgen, M. Skorokhvatov, O. Smirnov, A. Sotnikov, S. Sukhotin, Y. Suvorov, R. Tartaglia, G. Testera, D. Vignaud, R. B. Vogelaar, F. von Feilitzsch, J. Winter, M. Wojcik, A. Wright, M. Wurm, J. Xu, O. Zaimidoroga, S. Zavatarelli, and G. Zuzel (2010), Observation of geo-neutrinos, *Physics Letters B*, *687*(4), 299–304, doi:10.1016/j.physletb.2010.03.051.

Bellini, G., A. Ianni, L. Ludhova, F. Mantovani, and W. F. McDonough (2013), Geo-neutrinos, *Progress in Particle and Nuclear Physics*, *73*, 1–34, doi:10.1016/j.ppnp.2013.07.001.

Berger, B. R. (2012), Lithogeochemical data for Abitibi Subprovince intermediate to felsic intrusive rocks., *Tech. Rep. 292*, Ontario Geologic Survey, Toronto, ON.

Bermingham, K. R., K. Mezger, S. J. Desch, E. E. Scherer, and M. Horstmann (2014), Evidence for extinct ^{135}Cs from Ba isotopes in Allende CAIs?, *Geochimica et Cosmochimica Acta*, *133*, 463–478, doi:10.1016/J.GCA.2013.12.016.

Bertou, X. (2012), The ANDES underground laboratory, *The European Physical Journal Plus*, *127*(9), 104, doi:10.1140/epjp/i2012-12104-1.

Blanchard, I., J. Siebert, S. Borensztajn, and J. Badro (2017), The solubility of heat-producing elements in Earth's core, *Geochemical Perspectives Letters*, pp. 1–5, doi:10.7185/geochemlet.1737.

Blichert-Toft, J., B. Zanda, D. S. Ebel, and F. Albarède (2010), The Solar System primordial lead, *Earth and Planetary Science Letters*, *300*(1), 152–163, doi:10.1016/j.epsl.2010.10.001.

Bouvier, L. C., M. M. Costa, J. N. Connelly, N. K. Jensen, D. Wielandt, M. Storey, A. A. Nemchin, M. J. Whitehouse, J. F. Snape, J. J. Bellucci, F. Moynier, A. Agranier, B. Gueguen, M. Schönbächler, and M. Bizzarro (2018), Evidence for extremely rapid magma ocean crystallization and crust formation on Mars, *Nature*, *558*(7711), 586–589, doi:10.1038/s41586-018-0222-z.

Boyet, M., and R. W. Carlson (2005), 142Nd Evidence for Early (>4.53 Ga) Global Differentiation of the Silicate Earth, *Science*, *309*(5734), 576–581, doi:10.1126/science.1113634.

Braun, M., Y. M. Georgiev, T. Schönherr, H. Wilsenach, and K. Zuber (2017), A new precision measurement of the α-decay half-life of ^{190}Pt, *Physics Letters B*, *768*, 317–320, doi:10.1016/j.physletb.2017.02.052.

Brennecka, G. A., L. E. Borg, S. J. Romaniello, A. K. Souders, Q. R. Shollenberger, N. E. Marks, and M. Wadhwa (2017), A renewed search for short-lived ^{126}Sn in the early Solar System: Hydride generation MC-ICPMS for high sensitivity Te isotopic analysis, *Geochimica et Cosmochimica Acta*, *201*, 331–344, doi:10.1016/j.gca.2016.10.003.

Burkhardt, C., L. E. Borg, G. A. Brennecka, Q. R. Shollenberger, N. Dauphas, and T. Kleine (2016), Meteoritic Nd Isotope Constraints on the Origin and Composition of the Earth, in *Lunar and Planetary Science Conference*, vol. 47, p. 1908.

Calcagno, P., J. P. Chilès, G. Courrioux, and A. Guillen (2008), Geological modelling from field data and geological knowledge: Part I. Modelling method coupling 3D potential-field interpolation and geological rules, *Physics of the Earth and Planetary Interiors*, *171*(1), 147–157, doi:10.1016/j.pepi.2008.06.013.

Cammarano, F., and M. Guerri (2017), Global thermal models of the lithosphere, *Geophysical Journal International*, doi:10.1093/gji/ggx144.

Cammarano, F., S. Goes, P. Vacher, and D. Giardini (2003), Inferring upper-mantle temperatures from seismic velocities, *Physics of the Earth and Planetary Interiors*, *138*(3-4), 197–222, doi:10.1016/S0031-9201(03)00156-0.

Campbell, I. H., and H. St C. O'Neill (2012), Evidence against a chondritic Earth, *Nature*, *483*(7391), 553–558, doi:10.1038/nature10901.

Cano-Ott, D., J. Tain, A. Gadea, B. Rubio, L. Batist, M. Karny, and E. Roeckl (1999a), Monte Carlo simulation of the response of a large NaI (Tl) total absorption spectrometer for β-decay studies, *Nuclear Instruments and Methods in Physics Research Section A: Accelerators, Spectrometers, Detectors and Associated Equipment*, *430*(2), 333–347, doi:10.1016/S0168-9002(99)00217-X.

Cano-Ott, D., J. Tain, A. Gadea, B. Rubio, L. Batist, M. Karny, and E. Roeckl (1999b), Pulse pileup correction of large NaI (Tl) total absorption spectra using the true pulse shape, *Nuclear Instruments and Methods in Physics Research Section A: Accelerators, Spectrometers, Detectors and Associated Equipment*, *430*(2), 488–497, doi:10.1016/S0168-9002(99)00216-8.

Capozzi, F., E. Di Valentino, E. Lisi, A. Marrone, A. Melchiorri, and A. Palazzo (2017), Global constraints on absolute neutrino masses and their ordering, *Physical Review D*, *95*(9), 096,014, doi:10.1103/PhysRevD.95.096014.

Castillo, P. R. (2016), A proposed new approach and unified solution to old Pb paradoxes, *Lithos*, *252-253*(Supplement C), 32–40, doi:10.1016/j.lithos.2016.02.015.

Chapman, D. S. (1986), Thermal gradients in the continental crust, *Geological Society, London, Special Publications*, *24*(1), 63–70.

Chen, B., C. Chen, M. K. Kaban, J. Du, Q. Liang, and M. Thomas (2013), Variations of the effective elastic thickness over China and surroundings and their relation to the lithosphere dynamics, *Earth and Planetary Science Letters*, *363*, 61–72, doi:10.1016/j.epsl.2012.12.022.

Chen, J. (2017), Nuclear Data Sheets for A=40, *Nuclear Data Sheets*, *140*, 1–376, doi:10.1016/j.nds.2017.02.001.

Chen, M. C. (2006), Geo-neutrinos in SNO+, *Earth, Moon, and Planets*, *99*(1-4), 221–228, doi:10.1007/s11038-006-9116-4.

Cheng, L., A. Hanson, D. Diamond, J. Xu, J. Carew, and D. Rorer (2004), Physics and Safety Analysis for the NIST Research Reactor, *Technical Report BNL-NIST-0803, Rev. 1.*

Chidester, B. A., Z. Rahman, K. Righter, and A. J. Campbell (2017), Metal–silicate partitioning of U: Implications for the heat budget of the core and evidence for reduced U in the mantle, *Geochimica et Cosmochimica Acta*, *199*, 1–12, doi:10.1016/j.gca.2016.11.035.

Christensen, N. I. (1965), Compressional wave velocities in metamorphic rocks at pressures to 10 kilobars, *Journal of Geophysical Research*, *70*(24), 6147–6164, doi:10.1029/JZ070i024p06147.

Christensen, N. I., and W. D. Mooney (1995), Seismic velocity structure and composition of the continental crust: A global view, *Journal of Geophysical Research: Solid Earth*, *100*(B6), 9761–9788, doi:10.1029/95JB00259.

Coltorti, M., R. Boraso, F. Mantovani, M. Morsilli, G. Fiorentini, A. Riva, G. Rusciadelli, R. Tassinari, C. Tomei, G. Di Carlo, and V. Chubakov (2011), U and Th content in the Central Apennines continental crust: A contribution to the determination of the geo-neutrinos flux at LNGS, *Geochimica et Cosmochimica Acta*, *75*(9), 2271–2294, doi:10.1016/j.gca.2011.01.024.

Connolly, J. A. D. (2005), Computation of phase equilibria by linear programming: A tool for geodynamic modeling and its application to subduction zone decarbonation, *Earth and Planetary Science Letters*, *236*(1), 524–541, doi:10.1016/j.epsl.2005.04.033.

Cook, D. L., R. J. Walker, M. F. Horan, J. T. Wasson, and J. W. Morgan (2004), Pt-Re-Os systematics of group IIAB and IIIAB iron meteorites, *Geochimica et Cosmochimica Acta*, *68*(6), 1413–1431, doi:10.1016/j.gca.2003.09.017.

Cowan, C., F. Reines, F. Harrison, H. Kruse, and A. McGuire (1956a), Detection of the free neutrino: A Confirmation, *Science*, *124*, 103–104, doi:10.1126/science.124.3212.103.

Cowan, C. L., F. Reines, F. B. Harrison, H. W. Kruse, and A. D. McGuire (1956b), Detection of the Free Neutrino: A Confirmation, *Science*, *124*(3212), 103–104, doi:10.1126/science.124.3212.103.

Crane, T., and M. Baker (1991), Neutron Detectors, in *Passive Nondestructive Assay of Nuclear Materials*, edited by D. Reilly, N. Ensslin, and H. Smith, Los Alamos National Laboratory, Los Alamos.

Darling, J. R., C. J. Hawkesworth, C. D. Storey, and P. C. Lightfoot (2010), Shallow impact: Isotopic insights into crustal contributions to the Sudbury impact melt sheet, *Geochimica et Cosmochimica Acta*, *74*(19), 5680–5696, doi:10.1016/j.gca.2010.06.021.

Dauphas, N., and A. Pourmand (2011), Hf-W-Th evidence for rapid growth of Mars and its status as a planetary embryo, *Nature*, *473*, 489 EP–.

Dauphas, N., T. Rauscher, B. Marty, and L. Reisberg (2003), Short-lived p-nuclides in the early solar system and implications on the nucleosynthetic role of X-ray binaries, *Nuclear Physics A*, *719*, C287–C295, doi:10.1016/S0375-9474(03)00934-5.

Davidson, A. (1997), New information on the Grenville Front near Sudbury, in *43rd Annual Institute on Lake Superior Geology*, vol. 43, p. 38.

Davies, G. F. (1980), Thermal histories of convective Earth models and constraints on radiogenic heat production in the Earth, *Journal of Geophysical Research: Solid Earth*, *85*(B5), 2517–2530, doi:10.1029/JB085iB05p02517.

Davies, J. H. (2013), Global map of solid Earth surface heat flow: Global Surface Heat Flow Map, *Geochemistry, Geophysics, Geosystems*, *14*(10), 4608–4622, doi:10.1002/ggge.20271.

Davies, J. H., and D. R. Davies (2010), Earth's surface heat flux, *Solid Earth*, *1*(1), 5–24, doi:10.5194/se-1-5-2010.

de Koker, N., G. Steinle-Neumann, and V. Vlček (2012), Electrical resistivity and thermal conductivity of liquid Fe alloys at high P and T, and heat flux in Earth's core, *Proceedings of the National Academy of Sciences*, *109*(11), 4070–4073, doi:10.1073/pnas.1111841109.

de Meijer, R., F. Smit, F. Brooks, R. Fearick, H. Wortche, et al. (2005), Towards Earth AntineutRino TomagrapHy (EARTH), pp. 193–206.

De Meijer, R. J., and W. Van Westrenen (2008), The feasibility and implications of nuclear georeactors in Earth's core-mantle boundary region : Research article, *South African Journal of Science*, *104*, 111–118.

Delagnes, E., Y. Degerli, P. Goret, P. Nayman, F. Toussenel, and P. Vincent (2006), SAM: A new {GHz} sampling {ASIC} for the H.E.S.S.-II front-end electronics, *Nuclear Instruments and Methods in Physics Research Section A: Accelerators, Spectrometers, Detectors and Associated Equipment*, *567*(1), 21–26, doi:http://dx.doi.org/10.1016/j.nima.2006.05.052, proceedings of the 4th International Conference on New Developments in PhotodetectionBEAUNE 2005Fourth International Conference on New Developments in Photodetection.

Deschamps, F., P. J. Tackley, and T. Nakagawa (2010), Temperature and heat flux scalings for isoviscous thermal convection in spherical geometry, *Geophysical Journal International*, *182*(1), 137–154, doi:10.1111/j.1365-246X.2010.04637.x.

Dey, B., M. Borsato, N. Arnaud, D. Leith, K. Nishimura, et al. (2014), Design and performance of the Focusing DIRC detector, *Nucl.Instrum.Meth.*, *A775*, 112–131, doi:10.1016/j.nima.2014.11.120.

Dwarkadas, V. V., N. Dauphas, B. Meyer, P. Boyajian, and M. Bojazi (2017), Triggered Star Formation inside the Shell of a Wolf–Rayet Bubble as the Origin of the Solar System, *The Astrophysical Journal*, *851*(2), 147.

Dwyer, D., and T. Langford (2015), Spectral Structure of Electron Antineutrinos from Nuclear Reactors, *Phys.Rev.Lett.*, *114*(1), 012,502, doi:10.1103/PhysRevLett.114.012502.

Dye, S., Y. Huang, V. Lekic, W. McDonough, and O. Šrámek (2015), Geo-neutrinos and Earth Models, *Physics Procedia*, *61*, 310–318, doi:10.1016/j.phpro.2014.12.050.

Dye, S. T. (2010), Geo-neutrinos and silicate earth enrichment of U and Th, *Earth and Planetary Science Letters*, *297*(1), 1–9, doi:10.1016/j.epsl.2010.06.012.

Dye, S. T. (2012), Geoneutrinos and the radioactive power of the Earth, *Reviews of Geophysics*, *50*(3), doi:10.1029/2012RG000400.

Dziewonski, A. M., and D. L. Anderson (1981), Preliminary reference Earth model, *Physics of the Earth and Planetary Interiors*, *25*(4), 297–356, doi:10.1016/0031-9201(81)90046-7.

Easton, R. (2000), Variation in crustal level and large-scale tectonic controls on rare-metal and platinum-group element mineralization in the Southern and Grenville provinces, *Ontario Geol. Surv. Open File Rep*, *6032*, 28–21.

Easton, R. (2016), *Geological Guidebook to the Nepewassi Domain, Central Gneiss Belt, Grenville Province*, Ontario Geological Survey Miscellaneous Release-Data 338.

ELJEN (), EJ-254, *Scintillator EJ-254 data sheet*.

Elliott, T., A. Zindler, and B. Bourdon (1999), Exploring the kappa conundrum: The role of recycling in the lead isotope evolution of the mantle, *Earth and Planetary Science Letters*, *169*(1), 129–145.

ENDF (2011), Evaluated Nuclear Data File, *Nuclear Data libraries*.

Engel, K., W. McDonough, and L. Ludhova (2016), Geochemical models of the Earth and the crustal geoneutrino flux, *Geoneutrinos*.

Enomoto, S. (2005), Neutrino Geophysics and Observation of Geo-Neutrinos at KamLAND, Ph.D. thesis, Tohoku University.

Enomoto, S. (2006a), Geoneutrino Spectrum and Luminosity.

Enomoto, S. (2006b), Experimental study of geoneutrinos with KamLAND, *Earth Moon and Planets*, *99*(1-4), 131–146.

Enomoto, S., E. Ohtani, K. Inoue, and A. Suzuki (2007), Neutrino geophysics with KamLAND and future prospects, *Earth and Planetary Science Letters*, *258*(1-2), 147–159, doi:10.1016/j.epsl.2007.03.038.

Farley, T. A. (1960), HALF-PERIOD OF Th232, *Canadian Journal of Physics*, *38*(8), 1059–1068, doi:10.1139/p60-114.

Fields, B. D., and K. A. Hochmuth (2006), Imaging the Earth's Interior: The Angular Distribution of Terrestrial Neutrinos, *Earth, Moon, and Planets*, *99*(1), 155–181, doi:10.1007/s11038-006-9132-4.

Fiorentini, G., M. Lissia, and F. Mantovani (2007a), Geo-neutrinos and earth's interior, *Physics Reports*, *453*(5-6), 117–172, doi:10.1016/j.physrep.2007.09.001.

Fiorentini, G., M. Lissia, and F. Mantovani (2007b), Geo-neutrinos and earth's interior, *Physics Reports*, *453*(5-6), 117–172, doi:10.1016/j.physrep.2007.09.001.

Fiorentini, G., G. L. Fogli, E. Lisi, F. Mantovani, and A. M. Rotunno (2012), Mantle geoneutrinos in KamLAND and Borexino, *Physical Review D*, *86*(3), doi:10.1103/PhysRevD.86.033004.

Flasar, M. F., and F. Birch (1973), Energetics of core formation: A correction, *Journal of Geophysical Research*, *78*(26), 6101–6103, doi:10.1029/JB078i026p06101.

Fogli, G. L., E. Lisi, A. Palazzo, A. M. Rotunno, and A. Palazzo (2007), Geo-Neutrinos: A Systematic Approach to Uncertainties and Correlations, in *Neutrino Geophysics: Proceedings of Neutrino Sciences 2005*, edited by S. T. Dye, pp. 111–130, Springer New York.

French, S., V. Lekic, and B. Romanowicz (2013), Waveform Tomography Reveals Channeled Flow at the Base of the Oceanic Asthenosphere, *Science*, *342*(6155), 227–230, doi:10.1126/science.1241514.

Fukai, R., and T. Yokoyama (2016), Nucleosynthetic Neodymium Isotope Anomalies in Carbonaceous and Ordinary Chondrites, in *Lunar and Planetary Science Conference*, vol. 47, p. 1298.

Gale, A., C. A. Dalton, C. H. Langmuir, Y. Su, and J.-G. Schilling (2013), The mean composition of ocean ridge basalts, *Geochemistry, Geophysics, Geosystems*, *14*(3), 489–518, doi:10.1029/2012GC004334.

Galer, S. J. G., and R. K. O'Nions (1985), Residence time of thorium, uranium and lead in the mantle with implications for mantle convection, *Nature*, *316*(6031), 778–782, doi:10.1038/316778a0.

Gando, A., Y. Gando, K. Ichimura, H. Ikeda, K. Inoue, Y. Kibe, Y. Kishimoto, M. Koga, Y. Minekawa, T. Mitsui, T. Morikawa, N. Nagai, K. Nakajima, K. Nakamura, K. Narita, I. Shimizu, Y. Shimizu, J. Shirai, F. Suekane, A. Suzuki, H. Takahashi, N. Takahashi, Y. Takemoto, K. Tamae, H. Watanabe, B. D. Xu, H. Yabumoto, H. Yoshida, S. Yoshida, S. Enomoto, A. Kozlov, H. Murayama, C. Grant, G. Keefer, A. Piepke, T. I. Banks, T. Bloxham, J. A. Detwiler, S. J. Freedman, B. K. Fujikawa, K. Han, R. Kadel, T. O'Donnell, H. M. Steiner, D. A. Dwyer, R. D. McKeown, C. Zhang, B. E. Berger, C. E. Lane, J. Maricic, T. Miletic, M. Batygov, J. G. Learned, S. Matsuno, M. Sakai, G. A. Horton-Smith, K. E. Downum, G. Gratta, K. Tolich, Y. Efremenko, O. Perevozchikov, H. J. Karwowski, D. M. Markoff, W. Tornow, K. M. Heeger, M. P. Decowski, and M. P. Decowski (2011), Partial radiogenic heat model for Earth revealed by geoneutrino measurements, *Nature Geoscience*, *4*(9), 647–651, doi:10.1038/ngeo1205.

Gando, A., Y. Gando, H. Hanakago, H. Ikeda, K. Inoue, K. Ishidoshiro, H. Ishikawa, M. Koga, R. Matsuda, S. Matsuda, T. Mitsui, D. Motoki, K. Nakamura, A. Obata, A. Oki, Y. Oki, M. Otani, I. Shimizu, J. Shirai, A. Suzuki, Y. Takemoto, K. Tamae, K. Ueshima, H. Watanabe, B. D. Xu, S. Yamada, Y. Yamauchi, H. Yoshida, A. Kozlov, S. Yoshida, A. Piepke, T. I. Banks, B. K. Fujikawa,

K. Han, T. O'Donnell, B. E. Berger, J. G. Learned, S. Matsuno, M. Sakai, Y. Efremenko, H. J. Karwowski, D. M. Markoff, W. Tornow, J. A. Detwiler, S. Enomoto, M. P. Decowski, and KamLAND Collaboration (2013), Reactor on-off antineutrino measurement with KamLAND, *Physical Review D*, *88*(3), doi:10.1103/PhysRevD.88.033001.

Gaschnig, R. M., R. L. Rudnick, W. F. McDonough, A. J. Kaufman, J. W. Valley, Z. Hu, S. Gao, and M. L. Beck (2016), Compositional evolution of the upper continental crust through time, as constrained by ancient glacial diamictites, *Geochimica et Cosmochimica Acta*, *186*, 316–343, doi:10.1016/j.gca.2016.03.020.

Gilligan, A., and K. Priestley (2018), Lateral variations in the crustal structure of the Indo–Eurasian collision zone, *Geophysical Journal International*, *214*(2), 975–989, doi:10.1093/gji/ggy172.

Gilmour, J. D., and S. A. Crowther (2017), The I-Xe chronometer and its constraints on the accretion and evolution of planetesimals, *Geochemical Journal*, *51*(1), 69–80, doi:10.2343/geochemj.2.0429.

Goldstein, J., E. Scott, and N. Chabot (2009), Iron meteorites: Crystallization, thermal history, parent bodies, and origin, *Chemie der Erde - Geochemistry*, *69*(4), 293–325, doi:https://doi.org/10.1016/j.chemer.2009.01.002.

Gomi, H., K. Ohta, K. Hirose, S. Labrosse, R. Caracas, M. J. Verstraete, and J. W. Hernlund (2013), The high conductivity of iron and thermal evolution of the Earth's core, *Physics of the Earth and Planetary Interiors*, *224*, 88–103, doi:10.1016/j.pepi.2013.07.010.

Goorley, T. (2014), MCNP6. 1.1-Beta Release Notes, *Los Alamos National Laboratory Technical Report*.

Gordon, M., P. Goldhagen, K. Rodbell, T. Zabel, H. Tang, J. Clem, and P. Bailey (2004a), Measurement of the flux and energy spectrum of cosmic-ray induced neutrons on the ground, *IEEE Transactions on Nuclear Science*, *51*(6), 3427–3434, doi:10.1109/TNS.2004.839134.

Gordon, M. S., P. Goldhagen, K. P. Rodbell, T. H. Zabel, H. H. K. Tang, J. M. Clem, and P. Bailey (2004b), Measurement of the flux and energy spectrum of cosmic-ray induced neutrons on the ground, *IEEE Transactions on Nuclear Science*, *51*(6), 3427–3434, doi:10.1109/TNS.2004.839134.

Gordon, M. S., P. Goldhagen, K. P. Rodbell, T. H. Zabel, H. H. K. Tang, J. M. Clem, and P. Bailey (2004c), Measurement of the Flux and Energy Spectrum of Cosmic-Ray Induced Neutrons on the Ground, *IEEE Transactions on Nuclear Science*, *51*, 3427–3434, doi:10.1109/TNS.2004.839134.

Gounelle, M., and Meynet, G. (2012), Solar system genealogy revealed by extinct short-lived radionuclides in meteorites, *A&A*, *545*, A4, doi:10.1051/0004-6361/201219031.

Hacker, B. R., P. B. Kelemen, and M. D. Behn (2015), Continental Lower Crust, *Annual Review of Earth and Planetary Sciences*, *43*(1), 167–205, doi:10.1146/annurev-earth-050212-124117.

Hagmann, C., D. Lange, and D. Wright (2007), Cosmic-ray shower generator (CRY) for Monte Carlo transport codes, in *2007 IEEE Nuclear Science Symposium Conference Record*, vol. 2, pp. 1143–1146, doi:10.1109/NSSMIC.2007.4437209.

Hagmann, C., D. Lange, J. Verbeke, and D. Wright (2012a), Cosmic-ray shower Library (CRY), *Technical Report UCRL-TM-229453*.

Hagmann, C., D. Lange, J. Verbeke, and D. Wright (2012b), Cosmic-ray Shower Library (CRY), *Technical Report UCRL-TM-229453*.

Han, R., Y.-F. Li, L. Zhan, W. F. McDonough, J. Cao, and L. Ludhova (2016), Potential of geo-neutrino measurements at JUNO, *Chinese Physics C*, *40*(3), 033,003, doi:10.1088/1674-1137/40/3/033003.

Hanson, A., and D. Diamond (2011), Calculation of Design Parameters for an Equilibrium LEU Core in the NBSR, *Technical Report BNL-96386-2011-IR*.

Hao, M., Q. Wang, Z. Shen, D. Cui, L. Ji, Y. Li, and S. Qin (2014), Present day crustal vertical movement inferred from precise leveling data in eastern margin of Tibetan Plateau, *Tectonophysics*, *632*, 281–292, doi:10.1016/j.tecto.2014.06.016.

Herndon, J. M. (1996), Substructure of the inner core of the Earth, *Proceedings of the National Academy of Sciences*, *93*(2), 646–648, doi:10.1073/pnas.93.2.646.

Hiess, J., D. J. Condon, N. McLean, and S. R. Noble (2012), $^{238}U/^{235}U$ systematics in terrestrial uranium-bearing minerals, *Science (New York, N.Y.)*, *335*(6076), 1610–4, doi:10.1126/science.1215507.

Hofmann, A. (2014), Sampling Mantle Heterogeneity through Oceanic Basalts: Isotopes and Trace Elements, in *Treatise on Geochemistry*, pp. 67–101, Elsevier, doi:10.1016/B978-0-08-095975-7.00203-5.

Hofmann, A. W. (2007), Sampling Mantle Heterogeneity through Oceanic Basalts: Isotopes and Trace Elements, in *Treatise on Geochemistry*, pp. 1–44, Elsevier.

Höink, T., A. Lenardic, and A. M. Jellinek (2013), Earth's thermal evolution with multiple convection modes: A Monte-Carlo approach, *Physics of the Earth and Planetary Interiors*, *221*, 22–26, doi:10.1016/j.pepi.2013.06.004.

Hollenbach, D. F., and J. M. Herndon (2001), Deep-Earth reactor: Nuclear fission, helium, and the geomagnetic field, *Proceedings of the National Academy of Sciences*, *98*(20), 11,085–11,090, doi:10.1073/pnas.201393998.

Huang, Y., V. Chubakov, F. Mantovani, R. L. Rudnick, and W. F. McDonough (2013), A reference Earth model for the heat-producing elements and associated geoneutrino flux, *Geochemistry, Geophysics, Geosystems*, *14*(6), 2003–2029, doi:10.1002/ggge.20129.

Huang, Y., V. Strati, F. Mantovani, S. B. Shirey, and W. F. McDonough (2014), Regional study of the Archean to Proterozoic crust at the Sudbury Neutrino Observatory (SNO+), Ontario: Predicting the geoneutrino flux, *Geochemistry, Geophysics, Geosystems*, *15*(10), 3925–3944, doi:10.1002/2014GC005397.

Iizuka, T., Y.-J. Lai, W. Akram, Y. Amelin, and M. Schonbachler (2016), The initial abundance and distribution of ^{92}Nb in the Solar System, *Earth and Planetary Science Letters*, *439*, 172–181, doi:10.1016/J.EPSL.2016.02.005.

Inman, H. F., and E. L. Bradley Jr. (1989), The overlapping coefficient as a measure of agreement between probability distributions and point estimation of the overlap of two normal densities, *Communications in Statistics - Theory and Methods*, *18*(10), 3851–3874, doi:10.1080/03610928908830127.

Jackson, M. G., J. G. Konter, and T. W. Becker (2017), Primordial helium entrained by the hottest mantle plumes, *Nature*, *542*(7641), 340, doi:10.1038/nature21023.

Jaffey, A. H., K. F. Flynn, L. E. Glendenin, W. C. Bentley, and A. M. Essling (1971), Precision Measurement of Half-Lives and Specific Activities of ^{235}U and ^{238}U, *Physical Review C*, *4*(5), 1889–1906, doi:10.1103/PhysRevC.4.1889.

Jarvis, A., H. I. Reuter, A. Nelson, and E. Guevara (2008), Hole-filled SRTM for the globe Version 4.

Jaupart, C., and J.-C. Mareschal (2014), Constraints on Crustal Heat Production from Heat Flow Data, in *Treatise on Geochemistry*, pp. 53–73, Elsevier, doi:10.1016/B978-0-08-095975-7.00302-8.

Jaupart, C., and J. C. Mareschal (2015), 6.05 - Heat Flow and Thermal Structure of the Lithosphere, in *Treatise on Geophysics (Second Edition)*, edited by G. Schubert, pp. 217–253, Elsevier, Oxford, doi:10.1016/B978-0-444-53802-4.00114-7.

Jaupart, C., S. Labrosse, F. Lucazeau, and J. C. Mareschal (2015), 7.06 - Temperatures, Heat, and Energy in the Mantle of the Earth, in *Treatise on Geophysics (Second Edition)*, edited by G. Schubert, pp. 223–270, Elsevier, Oxford, doi:10.1016/B978-0-444-53802-4.00126-3.

Javoy, M. (1999), Chemical earth models, *Comptes Rendus de l'Académie des Sciences - Series IIA - Earth and Planetary Science*, *329*(8), 537–555, doi:10.1016/S1251-8050(00)87210-9.

Javoy, M., and E. Kaminski (2014), Earth's Uranium and Thorium content and geoneutrinos fluxes based on enstatite chondrites, *Earth and Planetary Science Letters*, *407*, 1–8, doi:10.1016/j.epsl.2014.09.028.

Javoy, M., E. Kaminski, F. Guyot, D. Andrault, C. Sanloup, M. Moreira, S. Labrosse, A. Jambon, P. Agrinier, A. Davaille, and C. Jaupart (2010), The chemical composition of the Earth: Enstatite chondrite models, *Earth and Planetary Science Letters*, *293*(3-4), 259–268, doi:10.1016/j.epsl.2010.02.033.

Jellinek, A. M., and M. G. Jackson (2015), Connections between the bulk composition, geodynamics and habitability of Earth, *Nature Geoscience*, *8*(8), 587, doi:10.1038/ngeo2488.

Jocher, G., et al. (2015), miniTimeCube: Neutron telescope, *paper in progress*.

Jocher, G. R., D. A. Bondy, B. M. Dobbs, S. T. Dye, J. A. Georges, et al. (2013), Theoretical antineutrino detection, direction and ranging at long distances, *Phys.Rept.*, *527*, 131–204, doi:10.1016/j.physrep.2013.01.005.

Kita, N. T., Q.-Z. Yin, G. J. MacPherson, T. Ushikubo, B. Jacobsen, K. Nagashima, E. Kurahashi, A. N. Krot, and S. B. Jacobsen (2013), 26Al-26Mg isotope systematics of the first solids in the early solar system, *Meteoritics & Planetary Science*, *48*(8), 1383–1400, doi:10.1111/maps.12141.

Kleine, T., and R. J. Walker (2017), Tungsten Isotopes in Planets, *Annual Review of Earth and Planetary Sciences*, *45*(1), 389–417, doi:10.1146/annurev-earth-063016-020037.

Kleine, T., M. Touboul, B. Bourdon, F. Nimmo, K. Mezger, H. Palme, S. B. Jacobsen, Q.-Z. Yin, and A. N. Halliday (2009), Hf–W chronology of the accretion and early evolution of asteroids and terrestrial planets, *Geochimica et Cosmochimica Acta*, *73*(17), 5150–5188, doi:https://doi.org/10.1016/j.gca.2008.11.047, the Chronology of Meteorites and the Early Solar System.

Knoll, G. (2000), *Radiation Detection and Measurement*, Wiley.

Kong, F., J. Wu, K. H. Liu, and S. S. Gao (2016), Crustal anisotropy and ductile flow beneath the eastern Tibetan Plateau and adjacent areas, *Earth and Planetary Science Letters*, *442*, 72–79, doi:10.1016/j.epsl.2016.03.003.

Konôpková, Z., R. S. McWilliams, N. Gómez-Pérez, and A. F. Goncharov (2016), Direct measurement of thermal conductivity in solid iron at planetary core conditions, *Nature*, *534*(7605), 99–101, doi:10.1038/nature18009.

Kopeikin, V., L. Mikaelyan, and V. Sinev (2004), Reactor as a source of antineutrinos: Thermal fission energy, *Phys.Atom.Nucl.*, *67*, 1892–1899, doi:10.1134/1.1811196.

Korenaga, J. (2008), Urey ratio and the structure and evolution of Earth's mantle, *Reviews of Geophysics*, *46*(2).

Kruijer, T. S., T. Kleine, M. Fischer-Gödde, C. Burkhardt, and R. Wieler (2014), Nucleosynthetic W isotope anomalies and the Hf–W chronometry of Ca–Al-rich inclusions, *Earth and Planetary Science Letters*, *403*, 317–327, doi:10.1016/j.epsl.2014.07.003.

Kumari, S., D. Paul, and A. Stracke (2016), Open system models of isotopic evolution in Earth's silicate reservoirs: Implications for crustal growth and mantle heterogeneity, *Geochimica et Cosmochimica Acta*, *195*, 142–157, doi:10.1016/j.gca.2016.09.011.

Lane, C., S. Usman, J. Blackmon, C. Rasco, H. Mumm, et al. (2015), A new type of Neutrino Detector for Sterile Neutrino Search at Nuclear Reactors and Nuclear Nonproliferation Applications.

Langford, T. J. (2013), Measurement of the surface and underground fast neutron spectra with the UMD/NIST fast neutron spectrometers, Ph.D. thesis, University of Maryland, College Park.

Langford, T. J., C. D. Bass, E. J. Beise, H. Breuer, D. K. Erwin, C. R. Heimbach, and J. S. Nico (2015), Fast neutron detection with a segmented spectrometer, *Nucl.Instrum.Meth.*, *A771*, 78–87, doi:10.1016/j.nima.2014.10.060.

Laske, G., and T. G. Masters (1997), A global digital map of sediment thickness, *EOS Trans. AGU*, *78*, F483.

Laske, G., G. Masters, Z. Ma, and M. E. Pasyanos (2013), Update on CRUST1.0 - A 1-degree Global Model of Earth's Crust, in *Geophysical Research Abstracts*, *EGU2013-2658*, vol. 15.

Learned, J. G. (2009a), *KamLAND internal memo*.

Learned, J. G. (2009b), High Energy Neutrino Physics with Liquid Scintillation Detectors.

Learned, J. G., S. T. Dye, and S. Pakvasa (2008), Hanohano: A Deep Ocean Anti-Neutrino Detector for Unique Neutrino Physics and Geophysics Studies, *arXiv:0810.4975 [hep-ex, physics:hep-ph]*.

Lenardic, A., C. M. Cooper, and L. Moresi (2011), A note on continents and the Earth's Urey ratio, *Physics of the Earth and Planetary Interiors*, *188*(1), 127–130, doi:10.1016/j.pepi.2011.06.008.

Leutz, H., G. Schulz, and H. Wenninger (1965), The decay of potassium-40, *Zeitschrift für Physik*, *187*(2), 151–164, doi:10.1007/BF01387190.

Li, V. A., R. Dorrill, M. J. Duvall, J. Koblanski, S. Negrashov, M. Sakai, S. A. Wipperfurth, K. Engel, G. R. Jocher, J. G. Learned, L. Macchiarulo, S. Matsuno, W. F. McDonough, H. P. Mumm, J. Murillo, K. Nishimura, M. Rosen, S. M. Usman, and G. S. Varner (2016), Invited Article: miniTimeCube, *Review of Scientific Instruments*, *87*(2), 021,301, doi:10.1063/1.4942243.

Li, V. A., J. Koblanski, R. Dorrill, M. J. Duvall, K. Engel, G. R. Jocher, J. G. Learned, S. Matsuno, W. F. McDonough, H. P. Mumm, S. Negrashov, K. Nishimura, M. Rosen, M. Sakai, S. M. Usman, G. S. Varner, and S. A. Wipperfurth (2018), Studies of MCP-PMTs in the miniTimeCube neutrino detector, *AIP Advances*, *8*(9), 095,003, doi:10.1063/1.5043308.

Li, Z., S. Ni, T. Hao, Y. Xu, and S. Roecker (2012), Uppermost mantle structure of the eastern margin of the Tibetan plateau from interstation Pn traveltime difference tomography, *Earth and Planetary Science Letters*, *335-336*, 195–205, doi:10.1016/j.epsl.2012.05.005.

Lightfoot, P., W. Doherty, K. Farrell, R. Keays, M. Moore, and D. Pekeski (1997), Geochemistry of the main mass, sublayer, offsets, and inclusions from the Sudbury Igneous Complex, Ontario, *Ontario Geological Survey, Open File Report*, *5959*, 231.

Liu, M.-C. (2017), The initial ^{41}Ca/^{40}Ca ratios in two type A Ca–Al-rich inclusions: Implications for the origin of short-lived ^{41}Ca, *Geochimica et Cosmochimica Acta*, *201*, 123–135, doi:10.1016/j.gca.2016.10.011.

Liu, M.-C., L. R. Nittler, C. M. O. Alexander, and T. Lee (2010), Lithium-Beryllium-Boron isotopic compositions in meteoritic hibonite: Implications for origin of ^{10}Be and early Solar System irradiation, *The Astrophysical Journal*, *719*(1), L99–L103, doi:10.1088/2041-8205/719/1/L99.

Liu, Q. Y., R. D. van der Hilst, Y. Li, H. J. Yao, J. H. Chen, B. Guo, S. H. Qi, J. Wang, H. Huang, and S. C. Li (2014), Eastward expansion of the Tibetan Plateau by crustal flow and strain partitioning across faults, *Nature Geoscience*, *7*(5), 361–365, doi:10.1038/ngeo2130.

Long, D. G. F. (2004), The tectonostatigraphic evolution of the Huronian basement and the subsequent basin fill: Geological constraints on impact models of the Sudbury event, *Precambrian Research*, *129*(3–4), 203–223, doi:10.1016/j.precamres.2003.10.003.

Long, D. G. F. (2009), The Huronian Supergroup, in *A Field Guide to the Geology of Sudbury, Ontario*, pp. 14–30., Ontario Geological Survey Open File Report 6243.

Lozza, V. (2016), The SNO+ Experiment for Neutrinoless Double-Beta Decay, *Nuclear and Particle Physics Proceedings*, *273-275*, 1836–1841, doi:10.1016/j.nuclphysbps.2015.09.296.

Lucassen, F., R. Becchio, R. Harmon, S. Kasemann, G. Franz, R. Trumbull, H.-G. Wilke, R. L. Romer, and P. Dulski (2001), Composition and density model of the continental crust at an active continental margin—the Central Andes between 21° and 27°S, *Tectonophysics*, *341*(1), 195–223, doi:10.1016/S0040-1951(01)00188-3.

Lucy, L. B. (1974), An iterative technique for the rectification of observed distributions, *The astronomical journal*, *79*, 745, doi:10.1086/111605.

Ludhova, L., and S. Zavatarelli (2013), Studying the Earth with Geoneutrinos, *Advances in High Energy Physics*, *2013*, e425,693, doi:10.1155/2013/425693.

Mantovani, F., L. Carmignani, G. Fiorentini, and M. Lissia (2004), Antineutrinos from Earth: A reference model and its uncertainties, *Physical Review D*, *69*(1), doi:10.1103/PhysRevD.69.013001.

Mareschal, J.-C., and C. Jaupart (2013), Radiogenic heat production, thermal regime and evolution of continental crust, *Tectonophysics*, *609*, 524–534, doi:10.1016/j.tecto.2012.12.001.

Mareschal, J.-C., C. Jaupart, J. Armitage, C. Phaneuf, C. Pickler, and H. Bouquerel (2017), The Sudbury Huronian heat flow anomaly, Ontario, Canada, *Precambrian Research*, *295*, 187–202, doi:10.1016/j.precamres.2017.04.024.

Marks, N., L. Borg, I. Hutcheon, B. Jacobsen, and R. Clayton (2014), Samarium–neodymium chronology and rubidium–strontium systematics of an Allende calcium–aluminum-rich inclusion with implications for 146Sm half-life, *Earth and Planetary Science Letters*, *405*, 15–24, doi:https://doi.org/10.1016/j.epsl.2014.08.017.

Matthes, M., M. Fischer-Godde, T. S. Kruijer, and T. Kleine (2017), Pd-Ag chronometry of IVA iron meteorites and the crystallization and cooling of a protoplanetary core, *Geochimica et Cosmochimica Acta*, *365*, doi:10.1016/J.GCA.2017.09.009.

McDonough, W. (2014), 3.16 - Compositional Model for the Earth's Core, in *Treatise on Geochemistry (Second Edition)*, edited by H. D. Holland and K. K. Turekian, second edition ed., pp. 559–577, Elsevier, Oxford.

McDonough, W. F. (1990), Constraints on the composition of the continental lithospheric mantle, *Earth and Planetary Science Letters*, *101*(1), 1–18, doi:10.1016/0012-821X(90)90119-I.

McDonough, W. F. (2016), The Composition of the Lower Mantle and Core, in *Deep Earth: Physics and Chemistry of the Lower Mantle and Core*, edited by Hidenori Terasaki and Rebecca A. Fischer, chap. 12, pp. 143–159, John Wiley & Sons, Inc, Washington DC.

McDonough, W. F. (2017), Earth's Core, in *Encyclopedia of Geochemistry*, edited by W. M. White, Encyclopedia of Earth Sciences Series, pp. 1–13, Springer International Publishing, doi:10.1007/978-3-319-39193-9_258-1.

McDonough, W. F., and S.-s. Sun (1995), The composition of the Earth, *Chemical Geology*, *120*(3-4), 223–253, doi:10.1016/0009-2541(94)00140-4.

McDonough, W. F., S. S. Sun, A. E. Ringwood, E. Jagoutz, and A. W. Hofmann (1992), Potassium, Rubidium, and Cesium in the Earth and Moon and the Evolution of the Mantle of the Earth, *Geochimica et Cosmochimica Acta*, *56*(3), 1001–1012.

Meissner, F., W. D. Schmidt-Ott, and L. Ziegeler (1987), Half-life and α-ray energy of146Sm, *Zeitschrift für Physik A Atomic Nuclei*, *327*(2), 171–174, doi:10.1007/BF01292406.

Meldrum, A., A. F. M. Abdel-Rahman, R. F. Martin, and N. Wodicka (1997), The nature, age and petrogenesis of the Cartier Batholith, northern flank of the Sudbury Structure, Ontario, Canada, *Precambrian Research*, *82*(3), 265–285, doi:10.1016/S0301-9268(96)00055-1.

Meng, G.-j., J.-w. Ren, M. Wang, W.-j. Gan, Q. Wang, X.-j. Qiao, and Y.-l. Yang (2008), Crustal deformation in western Sichuan region and implications for 12 May 2008 Ms 8.0 earthquake, *Geochemistry, Geophysics, Geosystems*, *9*(11), doi:10.1029/2008GC002144.

Miao, S. Q., H. P. Li, and G. Chen (2014), Temperature dependence of thermal diffusivity, specific heat capacity, and thermal conductivity for several types of rocks, *Journal of Thermal Analysis and Calorimetry*, *115*(2), 1057–1063, doi:10.1007/s10973-013-3427-2.

Millot, R., C.-J. Allègre, J. Gaillardet, and S. Roy (2004), Lead isotopic systematics of major river sediments: A new estimate of the Pb isotopic composition of the Upper Continental Crust, *Chemical Geology*, *203*(1), 75–90, doi:10.1016/j.chemgeo.2003.09.002.

Monsalve, G., A. Sheehan, C. Rowe, and S. Rajaure (2008), Seismic structure of the crust and the upper mantle beneath the Himalayas: Evidence for eclogitization of lower crustal rocks in the Indian Plate, *Journal of Geophysical Research: Solid Earth*, *113*(B8), doi:10.1029/2007JB005424.

Mooney, W. D., G. Laske, and T. G. Masters (1998), CRUST 5.1: A global crustal model at $5^\circ \times 5^\circ$, *Journal of Geophysical Research: Solid Earth*, *103*(B1), 727–747, doi:10.1029/97JB02122.

Mougeot, X. (2015), Reliability of usual assumptions in the calculation of β and ν spectra, *Physical Review C*, *91*(5), 055,504, doi:10.1103/PhysRevC.91.055504.

Mueller, T., D. Lhuillier, M. Fallot, A. Letourneau, S. Cormon, et al. (2011), Improved Predictions of Reactor Antineutrino Spectra, *Phys.Rev.*, *C83*, 054,615, doi:10.1103/PhysRevC.83.054615.

Mungall, J. E., D. E. Ames, and J. J. Hanley (2004), Geochemical evidence from the Sudbury structure for crustal redistribution by large bolide impacts, *Nature*, *429*(6991), 546–548, doi:10.1038/nature02577.

Nakagawa, T., and P. J. Tackley (2012), Influence of magmatism on mantle cooling, surface heat flow and Urey ratio, *Earth and Planetary Science Letters*, *329-330*, 1–10, doi:10.1016/j.epsl.2012.02.011.

Naumenko-Dèzes, M. O., T. F. Nägler, K. Mezger, and I. M. Villa (2018), Constraining the ^{40}K decay constant with ^{87}Rb-^{87}Sr—^{40}K-^{40}Ca chronometer intercomparison, *Geochimica et Cosmochimica Acta*, *220*, 235–247, doi:https://doi.org/10.1016/j.gca.2017.09.041.

Nimmo, F. (2015), 8.02 - Energetics of the Core, in *Treatise on Geophysics (Second Edition)*, edited by G. Schubert, pp. 27–55, Elsevier, Oxford, doi:10.1016/B978-0-444-53802-4.00139-1.

Novikova, E., M. Strickman, C. Gwon, B. Phlips, E. Wulf, C. Fitzgerald, L. Waters, and R. Johns (2006), Designing SWORD – SoftWare for Optimization of Radiation Detectors, *IEEE Nuclear Science Symposium Conference Record*, *1*, 607–612, doi:10.1109/NSSMIC.2006.356228.

Nyblade, A. A., and H. N. Pollack (1993), A global analysis of heat flow from Precambrian terrains: Implications for the thermal structure of Archean and Proterozoic lithosphere, *Journal of Geophysical Research: Solid Earth*, *98*(B7), 12,207–12,218, doi:10.1029/93JB00521.

Oberla, E., J.-F. Genat, H. Grabas, H. Frisch, K. Nishimura, et al. (2014), A 15 GSa/s, 1.5 GHz bandwidth waveform digitizing ASIC, *Nucl.Instrum.Meth.*, *A735*, 452–461, doi:10.1016/j.nima.2013.09.042.

Ohta, K., Y. Kuwayama, K. Hirose, K. Shimizu, and Y. Ohishi (2016), Experimental determination of the electrical resistivity of iron at Earth's core conditions, *Nature*, *534*(7605), 95–98, doi:10.1038/nature17957.

Olaniyan, O., R. S. Smith, and B. Lafrance (2015), Regional 3D geophysical investigation of the Sudbury Structure, *Interpretation*, *3*(2), SL63–SL81, doi:10.1190/INT-2014-0200.1.

Olive, K., et al. (2014), Review of Particle Physics, *Chin.Phys.*, *C38*, 090,001, doi:10.1088/1674-1137/38/9/090001.

Olugboji, T. M., V. Lekic, and W. F. McDonough (2017), A statistical assessment of seismic models of the U.S. continental crust using Bayesian inversion of ambient noise surface wave dispersion data, *Tectonics*, p. 2017TC004468, doi:10.1002/2017TC004468.

O'Neill, H. S., and H. Palme (2008), Collisional erosion and the non-chondritic composition of the terrestrial planets, *Philosophical Transactions of the Royal Society A: Mathematical, Physical and Engineering Sciences*, *366*(1883), 4205–4238, doi:10.1098/rsta.2008.0111.

Ontario Geologic Survey (2011), 1:250000 Scale Bedrock Geology of Ontario, *Tech. Rep. 126: Revision 1*, Ontario Geologic Survey, Toronto, ON.

Pakiser, L. C., and R. Robinson (1966), Composition and evolution of the continental crust as suggested by seismic observations, *Tectonophysics*, *3*(6), 547–557, doi:10.1016/0040-1951(66)90030-8.

Palme, H., and H. O'Neill (2014), Cosmochemical Estimates of Mantle Composition, in *Treatise on Geochemistry*, pp. 1–39, Elsevier, doi:10.1016/B978-0-08-095975-7.00201-1.

Pasquale, V., M. Verdoya, and P. Chiozzi (2015), Measurements of rock thermal conductivity with a Transient Divided Bar, *Geothermics*, *53*, 183–189, doi:10.1016/j.geothermics.2014.05.008.

Pasyanos, M. E., T. G. Masters, G. Laske, and Z. Ma (2014), LITHO1.0: An updated crust and lithospheric model of the Earth: LITHO1.0, *Journal of Geophysical Research: Solid Earth*, *119*(3), 2153–2173, doi:10.1002/2013JB010626.

Paul, D., W. M. White, and D. L. Turcotte (2003), Constraints on the 232Th/238U ratio (κ) of the continental crust, *Geochemistry, Geophysics, Geosystems*, *4*(12), 1102, doi:10.1029/2002GC000497.

Pawelczak, I., et al. (2014), Boron-loaded plastic scintillator with neutron-gamma pulse shape discrimination capability, *Nucl.Instrum.Meth.*, *A751*, 62–69, doi:10.1016/j.nima.2014.03.027.

Perry, H., J.-C. Mareschal, and C. Jaupart (2009), Enhanced crustal geo-neutrino production near the Sudbury Neutrino Observatory, Ontario, Canada, *Earth and Planetary Science Letters*, *288*(1-2), 301–308, doi:10.1016/j.epsl.2009.09.033.

Phaneuf, C., and J.-C. Mareschal (2014), Estimating concentrations of heat producing elements in the crust near the Sudbury Neutrino Observatory, Ontario, Canada, *Tectonophysics*, *622*, 135–144, doi:10.1016/j.tecto.2014.03.001.

PHOTONIS (2013), Photon detector XP85012 PLANACON, *PLANACON XP85012 data sheet*.

Plank, T. (2014), The Chemical Composition of Subducting Sediments, in *Treatise on Geochemistry*, pp. 607–629, Elsevier, doi:10.1016/B978-0-08-095975-7.00319-3.

Pollack, H. N., and D. S. Chapman (1977), On the regional variation of heat flow, geotherms, and lithospheric thickness, *Tectonophysics*, *38*(3), 279–296, doi:10.1016/0040-1951(77)90215-3.

Pourmand, A., and N. Dauphas (2010), Distribution coefficients of 60 elements on TODGA resin: Application to Ca, Lu, Hf, U and Th isotope geochemistry, *Talanta*, *81*(3), 741–753, doi:10.1016/j.talanta.2010.01.008.

Pozzo, M., C. Davies, D. Gubbins, and D. Alfè (2012), Thermal and electrical conductivity of iron at Earth's core conditions, *Nature*, *485*(7398), 355–358, doi:10.1038/nature11031.

Rasco, B. C., M. Wolińska-Cichocka, A. Fijałkowska, K. P. Rykaczewski, M. Karny, R. K. Grzywacz, K. C. Goetz, C. J. Gross, D. W. Stracener, E. F. Zganjar, J. C. Batchelder, J. C. Blackmon, N. T. Brewer, S. Go, B. Heffron, T. King, J. T. Matta, K. Miernik, C. D. Nesaraja, S. V. Paulauskas, M. M. Rajabali, E. H. Wang, J. A. Winger, Y. Xiao, and C. J. Zachary (2016), Decays of the Three Top Contributors to the Reactor ${\overline{\ensuremath{\nu}}}_{e}$ High-Energy Spectrum, $\hat{92}\mathrm{Rb}$, $\hat{96\mathrm{gs}}\mathrm{Y}$, and $\hat{142}\mathrm{Cs}$, Studied with Total Absorption Spectroscopy, *Physical Review Letters*, *117*(9), 092,501, doi:10.1103/PhysRevLett.117.092501.

Reguzzoni, M., and D. Sampietro (2015), GEMMA: An Earth crustal model based on GOCE satellite data, *International Journal of Applied Earth Observation and Geoinformation*, *35*, 31–43, doi:10.1016/j.jag.2014.04.002.

Reimann, C., and P. Filzmoser (2000), Normal and lognormal data distribution in geochemistry: Death of a myth. Consequences for the statistical treatment of geochemical and environmental data, *Environmental Geology*, *39*(9), 1001–1014, doi:10.1007/s002549900081.

Reines, F., and C. L. Cowan (1956), The neutrino, *Nature*, *178*, 446–449, doi:10.1038/178446a0.

Renne, P. R., G. Balco, K. R. Ludwig, R. Mundil, and K. Min (2011), Response to the comment by W.H. Schwarz et al. on "Joint determination of ^{40}K decay constants and ^{40}Ar*/^{40}K for the Fish Canyon sanidine standard, and improved accuracy for ^{40}Ar/^{39}K geochronology" by P.R. Renne et al. (2010), *Geochimica et Cosmochimica Acta*, *75*(17), 5097–5100, doi:10.1016/j.gca.2011.06.021.

Riller, U. (2009), Felsic Plutons, in *A Field Guide to the Geology of Sudbury, Ontario*, pp. 11–13, Ontario Geological Survey Open File Report 6243.

Ritt, S., R. Dinapoli, and U. Hartmann (2010), Application of the {DRS} chip for fast waveform digitizing, *Nuclear Instruments and Methods in Physics Research Section A: Accelerators, Spectrometers, Detectors and Associated Equipment*, *623*(1), 486–488, doi:http://dx.doi.org/10.1016/j.nima.2010.03.045, 1st International Conference on Technology and Instrumentation in Particle Physics.

Rizo, H., R. J. Walker, R. W. Carlson, M. Touboul, M. F. Horan, I. S. Puchtel, M. Boyet, and M. T. Rosing (2016), Early Earth differentiation investigated through 142Nd, 182W, and highly siderophile element abundances in samples from Isua, Greenland, *Geochimica et Cosmochimica Acta*, *175*(Supplement C), 319–336, doi:10.1016/j.gca.2015.12.007.

Rocholl, A., and K. P. Jochum (1993), Th, U and other trace elements in carbonaceous chondrites: Implications for the terrestrial and solar-system Th/U ratios, *Earth and Planetary Science Letters*, *117*(1), 265–278, doi:10.1016/0012-821X(93)90132-S.

Rodriguez, J. A., D. M. Adler, P. C. Brand, C. Broholm, J. C. Cook, C. Brocker, R. Hammond, Z. Huang, P. Hundertmark, J. W. Lynn, N. C. Maliszewskyj, J. Moyer, J. Orndorff, D. Pierce, T. D. Pike, G. Scharfstein, S. A. Smee, and R. Vilaseca (2008), MACSa new high intensity cold neutron spectrometer at NIST, *Measurement Science and Technology*, *19*(3), 034023, doi:10.1088/0957-0233/19/3/034023.

Rousell, D. H., and K. Card (2009), Geologic Setting, in *A Field Guide to the Geology of Sudbury, Ontario*, pp. 1–6, Ontario Geological Survey Open File Report 6243.

Rudnick, R., and S. Gao (2003), Composition of the Continental Crust, in *Treatise on Geochemistry*, pp. 1–64, Elsevier.

Rudnick, R. L., and D. M. Fountain (1995), Nature and composition of the continental crust: A lower crustal perspective, *Reviews of Geophysics*, *33*(3), 267, doi:10.1029/95RG01302.

Rudnick, R. L., and S. Gao (2014), Composition of the Continental Crust, in *Treatise on Geochemistry*, pp. 1–51, Elsevier, doi:10.1016/B978-0-08-095975-7.00301-6.

Rudnick, R. L., and S. L. Goldstein (1990), The Pb isotopic compositions of lower crustal xenoliths and the evolution of lower crustal Pb, *Earth and Planetary Science Letters*, *98*(2), 192–207, doi:10.1016/0012-821X(90)90059-7.

Ruedas, T. (2017), Radioactive heat production of six geologically important nuclides, *Geochemistry, Geophysics, Geosystems*, *18*(9), 3530–3541, doi:10.1002/2017GC006997.

Sato, J., and T. Hirose (1981), Half-life of ^{138}La, *Radiochemical and Radioanalytical Letters*, *46*(3), 145–152, doi:ISSN 0079-9483.

Schubert, G., D. Stevenson, and P. Cassen (1980), Whole planet cooling and the radiogenic heat source contents of the Earth and Moon, *Journal of Geophysical Research: Solid Earth*, *85*(B5), 2531–2538, doi:10.1029/JB085iB05p02531.

Seagle, C. T., E. Cottrell, Y. Fei, D. R. Hummer, and V. B. Prakapenka (2013), Electrical and thermal transport properties of iron and iron-silicon alloy at high pressure, *Geophysical Research Letters*, *40*(20), 5377–5381, doi:10.1002/2013GL057930.

Shapiro, N. M., and M. H. Ritzwoller (2002), Monte-Carlo inversion for a global shear-velocity model of the crust and upper mantle, *Geophysical Journal International*, *151*(1), 88–105, doi:10.1046/j.1365-246X.2002.01742.x.

Sleep, N. H., D. K. Bird, and M. T. Rosing (2013), Biological effects on the source of geoneutrinos, *International Journal of Modern Physics A*, *28*(30), 1330,047, doi:10.1142/S0217751X13300470.

Söderlund, U., P. J. Patchett, J. D. Vervoort, and C. E. Isachsen (2004), The ^{176}Lu decay constant determined by Lu-Hf and U-Pb isotope systematics of Precambrian mafic intrusions, *Earth and Planetary Science Letters*, *219*(3-4), 311–324, doi:10.1016/S0012-821X(04)00012-3.

Sonley, T. (2009), Measuring atmospheric Neutrinos at the Sudbury Neutrino observatory, in *Proceedings of 31st International Cosmic Ray Conference, Lódz*.

Šrámek, O., Y. Ricard, and F. Dubuffet (2010), A multiphase model of core formation, *Geophysical Journal International*, *181*(1), 198–220, doi:10.1111/j.1365-246X.2010.04528.x.

Šrámek, O., W. F. McDonough, E. S. Kite, V. Lekić, S. T. Dye, and S. Zhong (2013), Geophysical and geochemical constraints on geoneutrino fluxes from Earth's mantle, *Earth and Planetary Science Letters*, *361*, 356–366, doi:10.1016/j.epsl.2012.11.001.

Šrámek, O., B. Roskovec, S. A. Wipperfurth, Y. Xi, and W. F. McDonough (2016), Revealing the Earth's mantle from the tallest mountains using the Jinping Neutrino Experiment, *Scientific Reports*, *6*, 33,034, doi:10.1038/srep33034.

Steinberger, B., and T. W. Becker (2016), A comparison of lithospheric thickness models, *Tectonophysics*, doi:10.1016/j.tecto.2016.08.001.

Strati, V., M. Baldoncini, I. Callegari, F. Mantovani, W. F. McDonough, B. Ricci, and G. Xhixha (2015), Expected geoneutrino signal at JUNO, *Progress in Earth and Planetary Science*, *2*(1), doi:10.1186/s40645-015-0037-6.

Strati, V., S. A. Wipperfurth, M. Baldoncini, W. F. McDonough, and F. Mantovani (2017), Perceiving the Crust in 3-D: A Model Integrating Geological, Geochemical, and Geophysical Data, *Geochemistry, Geophysics, Geosystems*, *18*(12), 4326–4341, doi:10.1002/2017GC007067.

Strati, V., S. A. Wipperfurth, M. Baldoncini, W. F. McDonough, S. Gizzi, and F. Mantovani (2018), Geoneutrinos from the rock overburden at SNO+, *arXiv:1808.03199 [physics]*.

Sturges, H. A. (1926), The Choice of a Class Interval, *Journal of the American Statistical Association*, *21*(153), 65–66.

Sun, Y., J. Liu, K. Zhou, B. Chen, and R. Guo (2015), Crustal structure and deformation under the Longmenshan and its surroundings revealed by receiver function data, *Physics of the Earth and Planetary Interiors*, *244*, 11–22, doi:10.1016/j.pepi.2015.04.005.

Szwillus, W., J. C. C. Afonso, J. Ebbing, and W. D. Mooney (2019), Global crustal thickness and velocity structure from geostatistical analysis of seismic data, *Journal of Geophysical Research: Solid Earth*, *0*(ja), doi:10.1029/2018JB016593.

Tain, J. L., and D. Cano-Ott (2007), Algorithms for the analysis of -decay total absorption spectra, *Nuclear Instruments and Methods in Physics Research Section A: Accelerators, Spectrometers, Detectors and Associated Equipment*, *571*(3), 728–738, doi:10.1016/j.nima.2006.10.098.

Tanaka, H. K. M., and H. Watanabe (2014), 6Li-loaded directionally sensitive antineutrino detector for possible geo-neutrinographic imaging applications, *Scientific Reports*, *4*, doi:10.1038/srep04708.

Tanimizu, M. (2000), Geophysical determination of the ^{138}La b^- decay constant, *Phys. Rev. C*, *62*(1), 017,601, doi:10.1103/PhysRevC.62.017601.

Tatsumoto, M. (1978), Isotopic composition of lead in oceanic basalt and its implication to mantle evolution, *Earth and Planetary Science Letters*, *38*(1), 63–87, doi:10.1016/0012-821X(78)90126-7.

Tatsumoto, M., R. J. Knight, and C. J. Allegre (1973), Time Differences in the Formation of Meteorites as Determined from the Ratio of Lead-207 to Lead-206, *Science*, *180*(4092), 1279–1283, doi:10.1126/science.180.4092.1279.

Therriault, A. M., A. D. Fowler, and R. A. F. Grieve (2002), The Sudbury Igneous Complex: A Differentiated Impact Melt Sheet, *Economic Geology*, *97*(7), 1521–1540, doi:10.2113/gsecongeo.97.7.1521.

Trappitsch, R., P. Boehnke, T. Stephan, M. Telus, M. R. Savina, O. Pardo, A. M. Davis, N. Dauphas, M. J. Pellin, and G. R. Huss (2018), New Constraints on the Abundance of ^{60}Fe in the Early Solar System, *The Astrophysical Journal Letters*, *857*(2), L15.

Trinquier, A., J. L. Birck, C. J. Allègre, C. Göpel, and D. Ulfbeck (2008), ^{53}Mn-^{53}Cr systematics of the early Solar System revisited, *Geochimica et Cosmochimica Acta*, *72*(20), 5146–5163, doi:10.1016/j.gca.2008.03.023.

Tschirhart, P., and B. Morris (2012), Grenville age deformation of the Sudbury impact structure: Evidence from magnetic modelling of the Sudbury diabase dyke swarm, *Terra Nova*, *24*(3), 213–220, doi:10.1111/j.1365-3121.2011.01056.x.

Turcotte, D. L., and G. Schubert (2014), *Geodynamics*, Cambridge University Press.

Turner, G., A. Busfield, S. A. Crowther, M. Harrison, S. Mojzsis, and J. Gilmour (2007), Pu–Xe, U–Xe, U–Pb chronology and isotope systematics of ancient zircons from Western Australia, *Earth and Planetary Science Letters*, (3-4), 491–499, doi:10.1016/J.EPSL.2007.07.014.

Turner, G., S. A. Crowther, J. D. Gilmour, S. P. Kelley, and G. J. Wasserburg (2013), Short lived ^{36}Cl and its decay products ^{36}Ar and ^{36}S in the early solar system, *Geochimica et Cosmochimica Acta*, *123*, 358–367, doi:10.1016/J.GCA.2013.06.022.

Usman, S. M., G. R. Jocher, S. T. Dye, W. F. McDonough, and J. G. Learned (2015), AGM2015: Antineutrino Global Map 2015, *Scientific Reports*, *5*, 13,945, doi:10.1038/srep13945.

Vescovi, D., M. Busso, S. Palmerini, O. Trippella, S. Cristallo, L. Piersanti, A. Chieffi, M. Limongi, P. Hoppe, and K.-L. Kratz (2018), On the Origin of Early Solar System Radioactivities: Problems with the Asymptotic Giant Branch and Massive Star Scenarios, *The Astrophysical Journal*, *863*(2), 115.

Villa, I. M., P. De Bièvre, N. E. Holden, and P. R. Renne (2015), IUPAC-IUGS recommendation on the half life of ^{87}Rb, *Geochimica et Cosmochimica Acta*, *164*, 382–385, doi:10.1016/j.gca.2015.05.025.

Villa, I. M., M. L. Bonardi, P. De Bièvre, N. E. Holden, and P. R. Renne (2016), IUPAC-IUGS status report on the half-lives of ^{238}U, ^{235}U and ^{234}U, *Geochimica et Cosmochimica Acta*, *172*, 387–392, doi:10.1016/j.gca.2015.10.011.

Vogel, P., and J. F. Beacom (1999), Angular distribution of neutron inverse beta decay, anti-neutrino(e) + p —> e+ + n, *Phys.Rev.*, *D60*, 053,003, doi:10.1103/PhysRevD.60.053003.

Vogel, P., L. Wen, and C. Zhang (2015a), Neutrino oscillation studies with reactors, *Nature Communications*, *6*, 6936, doi:10.1038/ncomms7935.

Vogel, P., L. Wen, and C. Zhang (2015b), Neutrino Oscillation Studies with Reactors.

Wang, C.-Y., W.-B. Han, J.-P. Wu, H. Lou, and W. W. Chan (2007), Crustal structure beneath the eastern margin of the Tibetan Plateau and its tectonic implications, *Journal of Geophysical Research: Solid Earth*, *112*(B7), doi:10.1029/2005JB003873.

Wang, M., G. Audi, F. G. Kondev, W. Huang, S. Naimi, and X. Xu (2017), The AME2016 atomic mass evaluation (I). Evaluation of input data; and adjustment procedures, *Chinese Physics C*, *41*(3), 030,002, doi:10.1088/1674-1137/41/3/030002.

Wang, X., G. Zhang, H. Fang, W. Luo, W. Zhang, Q. Zhong, X. Cai, and H. Luo (2014), Crust and upper mantle resistivity structure at middle section of Longmenshan, eastern Tibetan plateau, *Tectonophysics*, *619-620*, 143–148, doi:10.1016/j.tecto.2013.09.011.

Wasserburg, G. J., M. Busso, R. Gallino, and C. M. Raiteri (1994), Asymptotic Giant Branch stars as a source of short-lived radioactive nuclei in the solar nebula, *The Astrophysical Journal*, *424*, 412, doi:10.1086/173899.

Wasserburg, G. J., A. I. Karakas, and M. Lugaro (2017), Intermediate-mass Asymptotic Giant Branch Stars and Sources of 26Al, 60Fe, 107Pd, and 182Hf in the Solar System, *The Astrophysical Journal*, *836*(1), 126.

Watanabe, H. (2010), Toward low energy anti-neutrinos directional measurement, *Neutrino Geoscience 2010, Italy*.

Watanabe, H. (2016), KamLAND, presentation at International Workshop : Neutrino Research and Thermal Evolution of the Earth.

White, W. M., and E. M. Klein (2014), Composition of the Oceanic Crust, in *Treatise on Geochemistry*, pp. 457–496, Elsevier, doi:10.1016/B978-0-08-095975-7.00315-6.

Wilkinson, B. H., B. J. McElroy, S. E. Kesler, S. E. Peters, and E. D. Rothman (2009), Global geologic maps are tectonic speedometers–Rates of rock cycling from area-age frequencies, *Geological Society of America Bulletin*, *121*(5-6), 760–779, doi:10.1130/B26457.1.

Wipperfurth, S. A., M. Guo, O. Šrámek, and W. F. McDonough (2018), Earth's chondritic Th/U: Negligible fractionation during accretion, core formation, and crust–mantle differentiation, *Earth and Planetary Science Letters*, *498*, 196–202, doi:10.1016/j.epsl.2018.06.029.

Wohlers, A., and B. J. Wood (2015), A Mercury-like component of early Earth yields uranium in the core and high mantle ^{142}Nd, *Nature*, *520*(7547), 337, doi:10.1038/nature14350.

Wohlers, A., and B. J. Wood (2017), Uranium, thorium and REE partitioning into sulfide liquids: Implications for reduced S-rich bodies, *Geochimica et Cosmochimica Acta*, *205*, 226–244, doi:10.1016/j.gca.2017.01.050.

Wright, A., P. Mosteiro, B. Loer, and F. Calaprice (2011), A Highly Efficient Neutron Veto for Dark Matter Experiments, *Nucl.Instrum.Meth.*, *A644*, 18–26, doi:10.1016/j.nima.2011.04.009.

Xhixha, G., G. P. Bezzon, C. Broggini, G. P. Buso, A. Caciolli, I. Callegari, S. D. Bianchi, G. Fiorentini, E. Guastaldi, M. K. Xhixha, F. Mantovani, G. Massa, R. Menegazzo, L. Mou, A. Pasquini, C. R. Alvarez, and M. Shyti (2013), The worldwide NORM production and a fully automated gamma-ray spectrometer for their characterization, *Journal of Radioanalytical and Nuclear Chemistry*, *295*(1), 445–457, doi:10.1007/s10967-012-1791-1.

Xhixha, G., M. Alberi, M. Baldoncini, K. Bode, E. Bylyku, F. Cfarku, I. Callegari, F. Hasani, S. Landsberger, F. Mantovani, E. Rodriguez, F. Shala, V. Strati, and

M. X. Kaçeli (2016), Calibration of HPGe detectors using certified reference materials of natural origin, *Journal of Radioanalytical and Nuclear Chemistry*, *307*(2), 1507–1517, doi:10.1007/s10967-015-4360-6.

Young, E. D. (2014), Inheritance of solar short- and long-lived radionuclides from molecular clouds and the unexceptional nature of the solar system, *Earth and Planetary Science Letters*, *392*, 16–27, doi:10.1016/j.epsl.2014.02.014.

Young, G. M. (2013), Precambrian supercontinents, glaciations, atmospheric oxygenation, metazoan evolution and an impact that may have changed the second half of Earth history, *Geoscience Frontiers*, *4*(3), 247–261, doi:10.1016/j.gsf.2012.07.003.

Young, G. M., D. G. F. Long, C. M. Fedo, and H. W. Nesbitt (2001), Paleoproterozoic Huronian basin: Product of a Wilson cycle punctuated by glaciations and a meteorite impact, *Sedimentary Geology*, *141–142*, 233–254, doi:10.1016/S0037-0738(01)00076-8.

Zartman, R. E., and B. R. Doe (1981), Plumbotectonics—the model, *Tectonophysics*, *75*(1), 135–162, doi:10.1016/0040-1951(81)90213-4.

Zhang, Y., J. Teng, Q. Wang, and G. Hu (2014), Density structure and isostatic state of the crust in the Longmenshan and adjacent areas, *Tectonophysics*, *619-620*, 51–57, doi:10.1016/j.tecto.2013.08.018.